



**HAL**  
open science

# Large-Eddy Simulation of combustion in gas turbines

Aleksandra Rezchikova

► **To cite this version:**

Aleksandra Rezchikova. Large-Eddy Simulation of combustion in gas turbines. Fluid Dynamics [physics.flu-dyn]. Université Paris-Saclay, 2022. English. NNT : 2022UPAST126 . tel-04756893

**HAL Id: tel-04756893**

**<https://theses.hal.science/tel-04756893v1>**

Submitted on 28 Oct 2024

**HAL** is a multi-disciplinary open access archive for the deposit and dissemination of scientific research documents, whether they are published or not. The documents may come from teaching and research institutions in France or abroad, or from public or private research centers.

L'archive ouverte pluridisciplinaire **HAL**, est destinée au dépôt et à la diffusion de documents scientifiques de niveau recherche, publiés ou non, émanant des établissements d'enseignement et de recherche français ou étrangers, des laboratoires publics ou privés.

# Large-eddy simulation of two-phase combustion in gas turbines

*Modélisation LES de la combustion dans les  
turbomachines*

## Thèse de doctorat de l'université Paris-Saclay

École doctorale n° 579, Sciences Mécaniques et Energétiques, Matériaux  
et Géosciences (SMEMaG)

Spécialité de doctorat : mécanique des fluides

Graduate School : Sciences de l'ingénierie et des systèmes.  
Réfèrent : CentraleSupElec

Thèse préparée dans l'unité de recherche IFP Energies Nouvelles sous la  
direction de Olivier COLIN, Dr. HDR, et la co-direction de Cédric MEHL, Dr.

Thèse soutenue à l'Université Paris-Saclay,  
le 18 octobre 2022, par

**Aleksandra REZCHIKOVA**

### Composition du jury

<b>Bruno Renou</b> Prof. Dr., INSA Rouen Normandie, CORIA	Président
<b>Christian Hasse</b> Prof. Dr.-Ing., The Technical University of Darm- stadt	Rapporteur & Examineur
<b>Epaminondas Mastorakos</b> Prof. Dr., University of Cambridge	Rapporteur & Examineur
<b>Renaud Mercier</b> Dr., SAFRAN Tech	Examineur
<b>Olivier COLIN</b> Dr. HDR, IFP Energies nouvelles	Directeur de thèse
<b>Cédric Mehl</b> Dr., IFP Energies nouvelles	Encadrant de thèse

Titre : Modélisation LES de la combustion dans les turbomachines

Mots clés : Modélisation, combustion, turbomachine, écoulements diphasiques, Simulations aux Grandes Echelles

Résumé : L'augmentation constante du trafic aérien et les réglementations environnementales strictes exigent d'améliorer les systèmes de propulsion modernes. Actuellement, les avions civils sont propulsés par des turbines à gaz, où le carburant est injecté sous forme liquide pour assurer leur fonctionnement en toute sécurité. La mécanique des fluides numérique (CFD, "Computational Fluid Dynamics") joue un rôle essentiel dans le développement des chambres de combustion des turbines à gaz, car les simulations numériques sont beaucoup moins coûteuses que les essais expérimentaux. Par conséquent, la simulation précise de la combustion en écoulement diphasique est cruciale pour la conception des chambres de combustion aéronautiques. Afin de mieux comprendre les interactions complexes entre la flamme, l'écoulement et la phase liquide, le présent travail porte sur la modélisation de la combustion pour les simulations aux grandes échelles (LES, "Large Eddy Simulation") d'écoulements diphasiques turbulents. Les tailles de cellule LES généralement utilisées sont supérieures à l'épaisseur de la flamme. Comme la combustion a généralement lieu au niveau de la sous-maille, elle nécessite un traitement spécifique. Le modèle de flamme épaissie (TFM, "Thickened Flame Model") est l'une des approches robustes et bien connues pour calculer les flammes turbulentes. Pour résoudre une flamme sur les mailles LES, le modèle TFM applique un épaississement artificiel du front de flamme tout en préservant la vitesse de la flamme. Le modèle TFM couplé au raffinement de maillage adaptatif (AMR, "Adaptive Mesh Refinement") fournit des résultats de haute précision sans coûts de calcul prohibitifs et donne lieu à l'approche de modélisation TFM-AMR étudiée dans ce travail. Le modèle TFM a été initialement conçu

pour des flammes prémélangées, qui ne sont pas toujours représentatives de la combustion ayant lieu dans les sprays. De plus, l'évolution des gouttelettes de combustible liquide est suivie dans un cadre lagrangien séparément de la phase gazeuse. Par conséquent, l'approche de modélisation doit être adaptée pour inclure l'effet de l'épaississement de la phase moyenne sur la phase dispersée afin de garantir une évaporation et une propagation correctes du spray. Les approches existantes de l'extension du modèle TFM aux écoulements diphasiques sont d'abord examinées. Elles sont explorées dans le contexte du TFM-AMR et validées sur les différentes configurations de flamme diphasique, y compris deux brûleurs bien caractérisés fonctionnant dans des conditions ambiantes. L'extension TFM-AMR sur les flammes diphasiques a démontré un bon potentiel dans les calculs. En particulier, il a été démontré qu'elle reproduit bien l'extinction de la flamme d'un brûleur à l'échelle du laboratoire. Cependant, l'approche de modélisation existante nécessitait des ajustements supplémentaires lors du calcul de configurations de flammes complexes et diphasiques, car TFM est basé sur des propriétés de flamme prémélangée tabulées, qui peuvent s'écarter considérablement dans de tels cas. Par conséquent, une nouvelle approche de modélisation est proposée, qui ne nécessite pas l'utilisation des propriétés tabulées des flammes prémélangées et qui est donc mieux adaptée aux calculs diphasiques. Les tests de validation effectués sur les configurations de flammes simples unidimensionnelles et sur deux brûleurs à diphasiques montrent des résultats prometteurs. Néanmoins, la stratégie de modélisation proposée nécessite une étude plus approfondie dans le contexte des brûleurs diphasiques fonctionnant à des températures et des pressions élevées.

Title :Large-Eddy Simulation of combustion in gas turbines

Keywords :Modeling, combustion, gasturbine, two-phase flows, Large Eddy Simulation

Abstract : Constantly growing air traffic and strict environmental regulations require to improve modern propulsion systems. Currently, civil aircraft are powered by gas turbines, where fuel is injected in a liquid form to ensure their safe operation. Computational fluid dynamics (CFD) plays an essential role in developing gas turbine combustors since numerical simulations are much cheaper than costly experimental tests. Therefore, the accurate simulation of two-phase flow combustion is crucial for designing aeronautical combustion chambers. In order to gain insight into the complex interactions between the flame, the flow, and the liquid phase, the present work addresses combustion modeling for Large Eddy Simulation (LES) of turbulent two-phase flows. Typically used LES cell sizes are larger than the flame thickness. Since the combustion usually takes place at the sub-grid level, it requires specific treatment. The Thickened Flame Model (TFM) is one of the robust and well-known approaches to compute turbulent flames. To resolve a flame on the LES grids, TFM applies an artificial flame front thickening while preserving the flame speed. TFM coupled to Adaptive Mesh Refinement (AMR) provides high accuracy results without prohibitive computational costs and results in the TFM-AMR modeling approach investigated in this work. TFM has been initially designed for premixed flames, which are not always representative of the combustion taking place in sprays. Additionally, the evo-

lution of liquid fuel droplets is tracked within a Lagrangian framework separately from the gaseous phase. Therefore, the modeling approach has to be adapted to include the effect of mean phase thickening on the dispersed phase to ensure correct spray evaporation and propagation. The existing approaches of extending the TFM onto two-phase flows are investigated first. These are explored in the context of TFM-AMR and validated on the different spray flame configurations, including two well-characterized spray burners operated at ambient conditions. The TFM-AMR extension on two-phase flames demonstrated a good potential in computing spray flames. In particular, it is shown to reproduce the lean blowout of a laboratory scale burner well. However, the existing modeling approach required additional adjustments when computing complex and spray flame configurations since TFM is based on tabulated premixed flame properties, which can significantly deviate in such cases. Therefore, a new modeling approach is proposed which does not require the use of tabulated properties of premixed flames and, thus, is better adapted for the two-phase computations. The validation tests performed on the simple one-dimensional flame configurations and two spray burners demonstrate promising results. Nevertheless, the proposed modeling strategy requires further investigation in the context of spray burners operated at high temperatures and pressures.

# Contents

<b>1</b>	<b>Introduction</b>	<b>17</b>
1.1	Aeronautical gas turbines . . . . .	18
1.1.1	Fuel injection . . . . .	19
1.1.2	Two-phase combustion . . . . .	20
1.2	Numerical simulations of gas turbines . . . . .	22
1.2.1	Combustion modeling . . . . .	24
1.2.2	TFM application in the context of two-phase flows . . . . .	28
1.3	Goal and objectives of this work . . . . .	31
<b>2</b>	<b>TFM modeling approach for two-phase flames</b>	<b>33</b>
2.1	Carrier phase . . . . .	33
2.2	Dispersed phase . . . . .	36
2.2.1	Equation of motion . . . . .	36
2.2.2	Evaporation . . . . .	38
2.3	Thickened Flame Model . . . . .	40
2.3.1	Flame sensor . . . . .	40
2.3.2	Flame thickening factor . . . . .	42
2.3.3	Stretched flames . . . . .	42
2.3.4	TFM formulation for the liquid phase . . . . .	43
2.4	Conclusion . . . . .	45
<b>3</b>	<b>Modeling approach validation. 1D Configuration</b>	<b>47</b>
3.1	High-volatile fuel (N-Heptane flames) . . . . .	49

3.1.1	Chemistry modelling . . . . .	49
3.1.2	Numerical setup . . . . .	51
3.1.3	Simulation domain and settings . . . . .	52
3.1.4	Non-thickened spray flame . . . . .	54
3.1.5	Constant spray flame thickening . . . . .	57
3.1.6	Dynamic spray flame thickening . . . . .	59
3.2	Low-volatile fuel (N-Dodecane flames) . . . . .	64
3.2.1	Chemistry modelling . . . . .	64
3.2.2	Simulation domain and settings . . . . .	65
3.2.3	Non-thickened spray flame . . . . .	66
3.2.4	Dynamic spray flame thickening . . . . .	72
3.3	Conclusions . . . . .	78
<b>4</b>	<b>CORIA burner</b>	<b>81</b>
4.1	Experimental facility . . . . .	81
4.2	CORIA burner: State of the art . . . . .	83
4.3	CORIA burner: LES . . . . .	87
4.3.1	Numerical setup . . . . .	87
4.3.2	Fuel injection . . . . .	88
4.3.3	Non-reacting flow validation . . . . .	90
4.3.4	Reacting flow results . . . . .	94
4.4	Conclusions . . . . .	101
<b>5</b>	<b>DLR burner</b>	<b>103</b>
5.1	Experimental facility . . . . .	104
5.2	DLR burner: State of the art . . . . .	105
5.3	DLR burner LES: reference flame conditions . . . . .	107
5.3.1	Numerical setup and geometry . . . . .	107
5.3.2	Non-reacting flow validation . . . . .	112
5.3.3	Reacting flow: reference configuration . . . . .	113
5.3.4	Reacting flow: the effect of spray/flame orientation . . . . .	125

5.3.5	Reacting flow: the effect of radiative heat losses . . . . .	126
5.3.6	Reacting flow: the effect of refinement . . . . .	129
5.4	DLR burner LES: lean blowout . . . . .	133
5.4.1	Numerical setup . . . . .	135
5.4.2	Results . . . . .	137
5.5	Conclusions . . . . .	141
<b>6</b>	<b>Geometrical formulation of the thickened flame model</b>	<b>143</b>
6.1	Geometrical formulation of the thickened flame model: formulation .	144
6.1.1	Generic methodology to transfer information from the reaction zone . . . . .	145
6.1.2	Flame indicator . . . . .	148
6.1.3	Flame properties . . . . .	149
6.2	Geometrical formulation of the thickened flame model: 1D Configuration	158
6.2.1	Verification of model assumptions . . . . .	158
6.2.2	Gaseous flame validation . . . . .	160
6.2.3	Spray flame validation . . . . .	164
6.2.4	Conclusions . . . . .	171
6.3	Geometrical formulation of the thickened flame model: CORIA burner	173
6.3.1	Numerical settings . . . . .	173
6.3.2	LES results . . . . .	175
6.3.3	Conclusions . . . . .	183
6.4	Geometrical formulation of the thickened flame model: DLR burner .	185
6.4.1	Numerical settings . . . . .	185
6.4.2	LES results . . . . .	187
6.4.3	Conclusions . . . . .	192
	<b>Conclusions</b>	<b>195</b>
	<b>Synthèse</b>	<b>205</b>



# List of Figures

1-1	Oil demand in the transport sector in 2050 [4] . . . . .	18
1-2	Gas turbine . . . . .	18
1-3	Sketched liquid fuel injection [37] . . . . .	20
1-4	Interaction diagram between dispersed and gaseous phases [37] . . . . .	20
1-5	Spray-flame interaction. Left: Pre-vaporized flame. Middle: Homogeneous combustion. Right: Heterogeneous combustion [77]. . . . .	21
1-6	Model validation workflow. . . . .	32
3-1	N-heptane flame properties at $T = 298K$ , $p = 1bar$ as a function of fuel/air equivalence ratio. . . . .	49
3-2	Simulation domain sketch. Laminar spray flame configuration. . . . .	52
3-3	Laminar burning velocity as a function of flame resolution. $\bullet$ : non-oscillatory solution; $\circ$ : oscillatory solution . . . . .	53
3-4	1-D spray flame profiles. Reference solution. $F = 1$ , $D_d = 10 - 90 \mu m$ . (a): gaseous temperature; (b): gaseous temperature vs normalized droplet diameter; (c): gaseous fuel/air equivalence ratio; (d): heat release rate; (e): Species mass fractions. Solid line: $nC_7H_{16}$ Dashed line: $O_2$ ; (f): fuel reaction rate . . . . .	56
3-5	The effect of Lagrangian corrections on the spray flame burning velocity. $\blacksquare$ : Reference, $\bullet$ : C5m0, $\blacktriangledown$ : C5m1, $\blacklozenge$ : C5m2, $\circ$ : C20m0, $\nabla$ : C5m1, $\diamond$ : C20m2. . . . .	57

3-6	1-D spray flame profiles. Constant thickening $F = 5$ with fixed droplet size $D_d = 90 \mu m$ for different correction strategies of spray equations: -x-: reference, —: m0, —: m1, —: m2. (a): gaseous temperature; (b): gaseous temperature vs normalized droplet diameter; (c): gaseous fuel/air equivalence ratio; (d): gaseous and spray velocities; (e): Species mass fractions. Solid line: $nC_7H_{16}$ Dashed line: $O_2$ ; (f): heat release rate . . . . .	58
3-7	1-D spray flame profiles. Dynamic thickening $F = F(\phi)$ with fixed droplet size $D_d = 90 \mu m$ for different grid settings. —: reference, —: D5m2, —: D20m2. (a): gaseous temperature; (b): gaseous fuel/air equivalence ratio; (c): Solid line: gaseous temperature, Dashed line: sensor $\hat{S}$ ; (d): heat release rate; (e): Solid line: gaseous temperature, Dashed line: thickening factor $F$ ; (f): Species mass fractions. Bottom: $nC_7H_{16}$ Top: $O_2$ . . . . .	60
3-8	1-D spray flame profiles. Dynamic thickening $F = F(\phi)$ with AMR and fixed droplet size $D_d = 90 \mu m$ for different grid settings. —: reference, —: D10AMRm2, —: D40AMRm2. (a): gaseous temperature; (b): gaseous fuel/air equivalence ratio; (c): Solid line: gaseous temperature, Dashed line: sensor $\hat{S}$ ; (d): heat release rate; (e): Solid line: gaseous temperature, Dashed line: thickening factor $F$ ; (f): Species mass fractions. Bottom: $nC_7H_{16}$ Top: $O_2$ . . . . .	62
3-9	Dynamically thickened spray flame burning velocity. ■: Reference, ▼: D5m2, ●: D20m2, ▽: D10AMRm2, ○: D40AMRm2. . . . .	63
3-10	Flame properties at $T = 323K$ , $p = 1bar$ as a function of fuel-equivalence-ratio. Solid lines: 43-species reduced mechanism. Dashed line: skeletal 180-species mechanism. . . . .	65
3-11	1-D n-dodecane spray flame properties. No thickening. (a): Flame speed; (b): Flame thickness . . . . .	66
3-12	1-D n-dodecane spray flame profiles. Reference solution. $F = 1$ , $D_d = 0 - 40 \mu m$ . (a): gaseous temperature; (b): normalized droplet diameter; (f): progress variable; (d): gaseous fuel/air equivalence ratio; (e): heat release rate; (f): fuel reaction rate . . . . .	68
3-13	1-D n-dodecane spray flame profiles. Reference solution. $F = 1$ , $D_d = 0 - 40 \mu m$ . (a): Sum of $CO$ and $CO_2$ mass fractions; (b): Fuel mass fraction . . . . .	69

3-14	Dilution fraction: 1-D n-dodecane spray flame profiles, $D_d = 40 \mu m$ , no thickening. (a): gaseous temperature; (b): normalized droplet diameter; (c): heat release rate: instantaneous - dots, tabulated - solid lines; (d): gaseous fuel/air equivalence ratio; (e): Sum of $CO$ and $CO_2$ mass fractions; (f): progress variable. . . . .	70
3-15	1-D n-dodecane spray flame profiles for different Jaravel sensor parameters, $D_d = 40 \mu m$ , TFM-AMR $\Delta_x = 0.5mm$ . (a): gaseous temperature (line-points), Final flame sensor $\hat{S}$ (solid line); (b): gaseous fuel/air equivalence ratio, Thickening factor $F$ (solid line). . . . .	73
3-16	1-D n-dodecane spray flame profiles for different Jaravel sensor parameters, $D_d = 40 \mu m$ , TFM-AMR $\Delta_x = 0.5mm$ . Instantaneous heat release rate profiles scaled with $F$ . (a): $\beta = 5$ , $\alpha_{cold} = 0.05$ , $\alpha_{hot} = 0.005$ ( $S > 0.9$ in yellow); (b): $\beta = 30$ , $\alpha_{cold} = 0.05$ , $\alpha_{hot} = 0.05$ ( $S > 0.9$ in red). . . . .	73
3-17	1-D n-dodecane spray flame profiles, $D_d = 0 - 40 \mu m$ , TFM-AMR $\Delta_x = 0.5mm$ . (a): thickening factor; (b): gaseous fuel/air equivalence ratio. . . . .	75
3-18	1-D n-dodecane spray flame profiles, TFM-AMR $\Delta_x = 0.5mm$ . $D_d = 20 \mu m$ - left column, $D_d = 40 \mu m$ - right column. (a,b): gaseous temperature, sensor (solid lines); (c,d): heat release rate; (e,f): gaseous fuel/air equivalence ratio, thickening factor (solid lines); (g,h): Sum of $CO$ and $CO_2$ mass fractions. . . . .	76
3-19	N-dodecane flame burning velocity as a function of droplet diameter. TFM-AMR, $\Delta_x = 0.5mm$ . . . . .	77
4-1	CRSB burner. [77] . . . . .	82
4-2	CRSB flame topology computed in [73] for the resolved flame with global chemistry description. Left: Takeno flame index with stoichiometric mixture fraction isoline. Right: Takeno index isolines. Gray: premixed flames (Takeno = 1), black: diffusion flames (Takeno = 1). . . . .	83
4-3	Droplet diameter computed in [14]. Left: refined mesh; right: coarse mesh. . . . .	85
4-4	LES simulation domain. . . . .	87
4-5	Fuel injection. Top: CRSB [77]. Bottom left: injection sketch; bottom right: simplified injection sketch (adapted from [33]). . . . .	89

4-6	Rosin-Rammler distribution at the injection plane. . . . .	91
4-7	Droplet size radial distribution at $Z = 13 \text{ mm}$ . $-\blacksquare-$ , $-\text{---}$ (PDF): experiments [77]; $-\text{---}$ , $-\text{---}$ (PDF): LES . . . . .	92
4-8	Carrier phase at non-reacting conditions: axial mean and RMS velocities. $-\text{---}$ : LES mean $z$ -velocity, $-\text{---}$ : LES RMS $z$ -velocity, $\bullet$ : EXP mean $z$ -velocity [77], $\blacklozenge$ : EXP RMS $z$ -velocity [77]. . . . .	93
4-9	Dispersed phase at non-reacting conditions: axial velocities (left) and droplet size (right) radial distributions. $-\bullet-$ : experiments with error bars proportional to measured RMS-values [77]. LES: $\bullet$ $D < 15 \text{ }\mu\text{m}$ , $\bullet$ $15 \text{ }\mu\text{m} \leq D < 30 \text{ }\mu\text{m}$ , $\bullet$ $D \geq 30 \text{ }\mu\text{m}$ . . . . .	93
4-10	Instantaneous heat release scaled with the thickening factor (left), instantaneous thickening factor with AMR (middle), instantaneous fuel/air equivalence ratio (right). Takeno index iso-contours: $-0.2$ black, $0.2$ white . . . . .	95
4-11	Carrier phase at reacting conditions: axial mean and RMS velocities. $-\text{---}$ : LES mean $z$ -velocity, $-\text{---}$ : LES RMS $z$ -velocity, $\bullet$ : EXP mean $z$ -velocity [77], $\blacklozenge$ : EXP RMS $z$ -velocity [77]. . . . .	96
4-12	Dispersed phase at reacting conditions: axial velocities (left) and droplet size (right) radial distributions. $-\bullet-$ : experiments with error bars proportional to measured RMS-values [77]. LES: $\bullet$ $D < 15 \text{ }\mu\text{m}$ , $\bullet$ $15 \text{ }\mu\text{m} \leq D < 30 \text{ }\mu\text{m}$ , $\bullet$ $D \geq 30 \text{ }\mu\text{m}$ . . . . .	97
4-13	Mean LES OH mass-fraction on the left-hand side, experimental OH-PLIF on the right [51] . . . . .	98
4-14	Reduced temperature and species mass fractions profiles at $Z = 43 \text{ mm}$ . $-\text{---}$ : $T/T_{max}$ , $-\text{---}$ : $Y_{OH} \times 10^2$ , $-\text{---}$ : $Y_{H_2} \times 10$ , $-\text{---}$ : $Y_{C_2H_2}$ , $-\text{---}$ : $Y_{C_2H_4}$ , $-\text{---}$ : $Y_{nC_7H_{16}}$ , $-\text{---}$ : $Y_{HC}$ , $-\text{---}$ : $Y_{O_2}$ . The colored regions correspond to different combustion modes defined with Takeno index $\mathcal{T}$ : blue – premixed mode with $\mathcal{T} > 0.2$ , orange – non-premixed $\mathcal{T} < -0.2$ . . . . .	99
4-15	Gaseous temperature versus gaseous fuel/air equivalence ratio at $Z = 43 \text{ mm}$ . The points are colored with heat release values scaled with thickening factor values $w_T F$ , and are divided into four characteristic flame zones (see Fig. 4-14) marked with symbols: $\diamond$ : B1-P, $\square$ : B1-D, $\circ$ : B2-P, $\nabla$ : B2-D. . . . .	100

5-1	Gas-Turbine Model Combustor [31]: rig with superimposed n-dodecane flame photograph (left); nozzle (right). . . . .	105
5-2	Characteristic zones in the Gas-Turbine Model Combustor defined by Eckel et al. in [21]. Instantaneous temperature field (grey scale contour plot), mixture fraction (colored lines). . . . .	106
5-3	Simulation domain (left); Mesh with fixed embeddings (middle); Mesh with fixed embeddings and AMR (right). . . . .	108
5-4	Gaseous mean temperature radial profiles obtained experimentally for kerosene and n-dodecane flames. . . . .	109
5-5	Temperature boundary conditions. Left: 1D temperature profile prescribed at the walls. Right: burner walls with assigned temperatures. . . . .	111
5-6	Average velocity field of a non-reacting flow: experiments (left); LES simulations (right) . . . . .	112
5-7	Mean velocity components at $Z = 1/15/35/55/125mm$ : radial (left), circumferential (middle), axial (right). Non-reacting case. . . . .	114
5-8	Rms velocity components at $Z = 1/15/35/55/125mm$ : radial (left), circumferential (middle), axial (right). Non-reacting case. . . . .	115
5-9	DLR-rc-ref case. Total power. . . . .	116
5-10	DLR-rc-ref case. Instantaneous fields: gaseous temperature, heat release rate, gaseous fuel/air equivalence ratio, efficiency factor with superimposed mesh, thickening factor, tabulated laminar flame thickness. . . . .	117
5-11	Gaseous temperature profiles at $Z = 15/25/35mm$ : mean (top); RMS (bottom) . .	118
5-12	Averaged temperature field: experiments versus numerical results (left); instantaneous temperature field (right). . . . .	119
5-13	CH* chemiluminescence and Mie scattering(left); averaged heat release rate field (right). . . . .	120
5-14	Averaged profiles ( $D_{32}$ and velocity components) of dispersed phase: $Z = 15mm$ (left); $Z = 25mm$ (right) . . . . .	123
5-15	Left: experimental conditional liquid loading. Right: LES fraction of evaporated liquid fuel. . . . .	124

5-16	Gaseous temperature radial profiles at $Z = 15/25/35mm$ : mean (top); RMS (bottom).	126
5-17	Averaged profiles ( $D_{32}$ and velocity components) of dispersed phase: $Z = 15mm$ (left); $Z = 25mm$ (right).	127
5-18	Gaseous temperature radial profiles at $Z = 15/25/35mm$ : mean (top); RMS (bottom).	128
5-19	Gaseous temperature axial profiles at $X = -20mm$ and $X = 0mm$ : mean (top); RMS (bottom).	128
5-20	Averaged profiles ( $D_{32}$ and velocity components) of dispersed phase: $Z = 15mm$ (left); $Z = 25mm$ (right).	129
5-21	Instantaneous fields : gaseous temperature, heat release rate, thickening factor, mesh refinement. DLR-rc-ref: left column); DLR-rc-amr: right column.	131
5-22	Gaseous temperature radial profiles at $Z = 15/25/35mm$ : mean (top); RMS (bottom).	132
5-23	Gaseous temperature axial profiles at $X = -20mm$ and $X = 0mm$ : mean (top); RMS (bottom).	132
5-24	Averaged profiles ( $D_{32}$ and velocity components) of dispersed phase: $Z = 15mm$ (left); $Z = 25mm$ (right).	133
5-25	LES fraction of evaporated liquid fuel.	134
5-26	Lean blowout experimental results at $T = 323K$ [32].	135
5-27	Temperature boundary conditions with applied scaling.	137
5-28	Total power during DLR-lbo simulation sequence	138
5-29	Instantaneous heat release rate and temperature fields at $\phi = 0.80$ (top) and $\phi = 0.44$ (bottom).	139
5-30	Instantaneous heat release rate and temperature fields (left), burner total power (right): $\phi = 0.52$ (top), $\phi = 0.48$ (middle) and $\phi = 0.44$ (bottom).	140
6-1	Transported variables, their source terms and use.	156
6-2	Flame thickening algorithm. Left: standard sensor formulation; right: geometrical sensor formulation.	157
6-3	1-D n-dodecane progress variable profiles versus $C^*$ function, $D_d = 0 - 40 \mu m$ , no TFM. (a): gaseous and $D_d = 10 \mu m$ ; (b): $D_d = 30 \mu m$ ; (c): $D_d = 20 \mu m$ (d): $D_d = 40 \mu m$ .	159

6-4	1-D n-dodecane gaseous flame profiles, TFM-AMR with geometrical sensor. (a): gaseous temperature; (b): heat release rate; (c): progress variables: computed $C$ - dashed lines with points, actual $C$ - solid lines; (d): fuel reaction rate; (e): gaseous and reaction fuel/air equivalence ratio; (f): fuel mass fraction. . . . .	161
6-5	1-D n-dodecane gaseous flame profiles, TFM-AMR with geometrical sensor. (a): progress variables: computed $C$ - dashed lines with points, actual $C$ - solid lines; (b): indicator $\psi$ ; (c): final sensor $\hat{S}$ ; (d): thickening factor $F$ ; (e): flame thickness $\delta_L^0$ ; (f): laminar flame speed $S_L^0$ . . . . .	162
6-6	1-D n-dodecane 40 $\mu m$ spray flame profiles, GS-sL-TFM-AMR. (a): gaseous temperature; (b): heat release rate; (c): progress variables: computed $C$ - dashed lines with points, actual $C$ - solid lines; (d): sum of $CO$ and $CO_2$ mass fractions; (e): gaseous fuel/air equivalence ratio; (f): normalized droplet diameter. . . . .	165
6-7	1-D n-dodecane 40 $\mu m$ spray flame profiles, GS-sL-TFM-AMR. (a): progress variables: computed $C$ - dashed lines with points, actual $C$ - solid lines; (b): indicator $\psi$ ; (c): final sensor $\hat{S}$ ; (d): thickening factor $F$ ; (e): flame thickness $\delta_L^0$ ; (f): laminar flame speed $S_L^0$ . . . . .	166
6-8	1-D n-dodecane 40 $\mu m$ spray flame profiles, GS-phi-TFM-AMR. (a): gaseous temperature; (b): heat release rate; (c): reacting fuel/air equivalence ratio; (d): gaseous fuel/air equivalence ratio; (e): sum of $CO$ and $CO_2$ mass fractions; (f): normalized droplet diameter. . . . .	169
6-9	1-D n-dodecane 40 $\mu m$ spray flame profiles, GS-phi-TFM-AMR (a): progress variables: computed $C$ - dashed lines with points, actual $C$ - solid lines; (b): indicator $\psi$ ; (c): final sensor $\hat{S}$ ; (d): thickening factor $F$ ; (e): flame thickness $\delta_L^0$ ; (f): laminar flame speed $S_L^0$ . . . . .	170
6-10	1-D n-dodecane burning velocity as a function of droplet diameter. TFM-AMR with geometrical sensor, S-TFM-phi-ext configuration . . . . .	171
6-11	1-D n-dodecane flame profiles, $D_d = 0 - 40 \mu m$ , TFM-AMR. Top: SS-TFM-AMR, bottom: GS-TFM-AMR (S-TFM-phi-ext configuration). Left: Thickening factor, right: Gaseous fuel/air equivalence ratio . . . . .	172
6-12	CRSB LES global parameters. . . . .	174

6-13	Instantaneous $\hat{S}$ fields. Left: GS-sL-TFM-AMR $\beta = 1$ ; right: GS-sL-TFM-AMR $\beta = 10$ . . . . .	175
6-14	Instantaneous temperature and heat release rate fields. Left: SS-TFM-AMR; middle:GS-sL-TFM-AMR; right: GS-phi-TFM-AMR . . . . .	176
6-15	Instantaneous fields of final flame sensor $\hat{S}$ , thickening factor $F$ and gaseous fuel/air equivalence ratio. Top: SS-TFM-AMR; bottom: GS-sL-TFM-AMR . . . . .	177
6-16	SS-TFM-AMR VS GS-sL-TFM-AMR. Instantaneous fields of temperature, thickening factor $F$ , efficiency factor $E$ , flame thickness $\delta_L^0$ and AMR . . . . .	177
6-17	GS-sL-TFM-AMR (left) VS GS-phi-TFM-AMR (right). Instantaneous fields of temperature, thickening factor $F$ , flame thickness $\delta_L^0$ , progress variable $C$ , efficiency factor $E$ , and laminar flame speed . . . . .	178
6-18	GS-phi-TFM-AMR: gaseous fuel/air equivalence ratio (left), reacting gaseous fuel/air equivalence ratio (right) . . . . .	179
6-19	Radial profiles; gaseous phase; SS-TFM-AMR (—: mean, —: rms); GS-sL-TFM-AMR (—: mean, —: rms); GS-phi-TFM-AMR (—: mean, —: rms); experiments (o: mean, x: rms). Left: radial velocity component; middle: axial velocity component; right: temperature. . . . .	181
6-20	Mean radial profiles; dispersed phase; —: SS-TFM-AMR; —: GS-sL-TFM-AMR; —: GS-phi-TFM-AMR; -●-: experiments with error bars proportional to measured RMS-values [77]. Left: droplet diameter (solid lines), gaseous temperature (dashed lines); middle: radial velocity component; right: axial velocity component. . . . .	182
6-21	Mean $Y_{OH}$ fields. Left: SS-TFM-AMR; middle: GS-sL-TFM-AMR right: GS-phi-TFM-AMR . . . . .	183
6-22	Instantaneous fields. . . . .	188
6-23	Instantaneous fields of the flame sensor $\hat{S}$ , thickening factor $F$ , and efficiency factor $E$ with AMR. Top: SS-TFM-AMR (DLR-rc-ref case), bottom: GS-TFM-AMR. Elevation is based on the temperature field. . . . .	190
6-24	GS-phi-TFM-AMR. Gaseous fuel/air equivalence ratio (left), reacting gaseous fuel/air equivalence ratio (right). Elevation is based on the sensor field. . . . .	191

6-25	Temperature radial profiles at $Z = 15mm$ , $Z = 25mm$ and $Z = 35mm$ ; GS-TFM-AMR vs SS-TFM-AMR. . . . .	191
6-26	Temperature axial profiles at $X = -20mm$ and $X = 0mm$ ; GS-TFM-AMR vs SS-TFM-AMR. . . . .	192
6-27	Averaged axial profiles of droplet diameter $D_{32}$ and spray velocity components: radial $U$ , circumferential $V$ , axial $W$ ; $Z = 15mm$ and $Z = 25mm$ ; GS-TFM-AMR vs SS-TFM-AMR. . . . .	193
6-28	Instantaneous fraction of evaporated liquid fuel; GS-TFM-AMR vs SS-TFM-AMR.	194



# List of Tables

3.1	1-D laminar spray flame configurations. . . . .	54
5.1	Computed flame configurations at reference conditions. . . . .	116
5.2	Computed LBO sequences. . . . .	136
6.1	Computed 1D gaseous flame configurations. . . . .	160
6.2	Computed 1D spray $D_d = 0 - 40 \mu m$ flame configurations. . . . .	164
6.3	The main CRSB flame characteristics, inner reaction zone, $Z < 60mm$ . . . . .	178



# Chapter 1

## Introduction

The World Energy Outlook (WEO) is conducted annually and provides an extensive analysis of the energy market. The future trends in this study are usually given under the assumption of different scenarios. The "Current Policies Scenario" stands for the case when the current trends are projected for the future with no additional regulations being applied. The "Stated Policies Scenario" (STEPS) and "Sustainable Development Scenario" (SDS) are the corrected estimations. The first one considers the announced improvement policies to be implemented. The second one assumes significant changes in line with reaching a global "net-zero" carbon dioxide emissions goal in 2070.

Energy-related  $CO_2$  emissions are expected to rise in the Stated Policies Scenario, with aviation being a massive contributor to this growth. Currently, 1 Gt of  $CO_2$  is only emitted by aviation, and passenger activity is expected to double in the next 20 years [4]. Due to the significant growth in activity in the transport sector, the oil demand will rise in 2050 according to STEPS, as illustrated in Fig. 1-1. The use of alternative fuels and the efficiency improvements of current technologies are considered the main possible ways to reduce emissions in such a hard-to-abate sector as aviation.

Constantly growing air traffic and strict environmental regulations require the improvement of modern propulsion systems. In order to reach higher fuel and thermal efficiency and the reduction of pollutants emissions, the operating conditions have

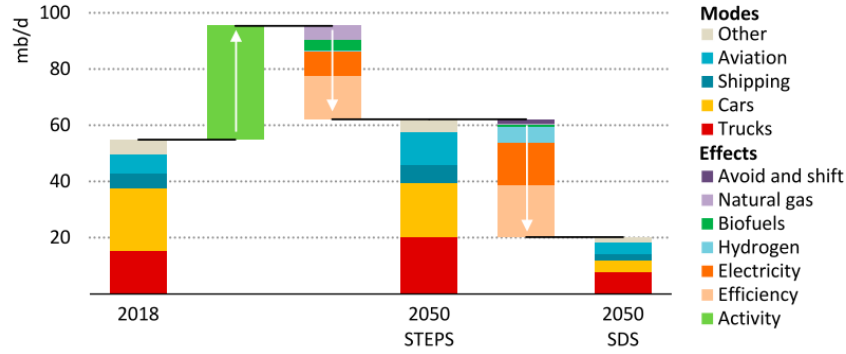


Figure 1-1: Oil demand in the transport sector in 2050 [4]

experienced a dramatic change over the past half-century. Operating pressures have increased from 5 to 50 atmospheres, inlet air temperatures from 450 to 900 K, and outlet temperatures from 1100 to 1850 K [42]. Moreover, the life expectancy of aero-engine liners has risen from just a few hundred hours to many tens of thousands of hours due to the travelers' demand.

## 1.1 Aeronautical gas turbines

Figure 1-2a illustrates a typical gas turbine. The main goal of an aircraft engine operation is to accelerate the air that passes through it. To achieve this, the pressure is increased before entering the combustion chamber. Then, the energy released from air/fuel combustion is converted to kinetic energy when the air undergoes the expansion in the turbine and is accelerated through the nozzle (see Fig.1-2a).

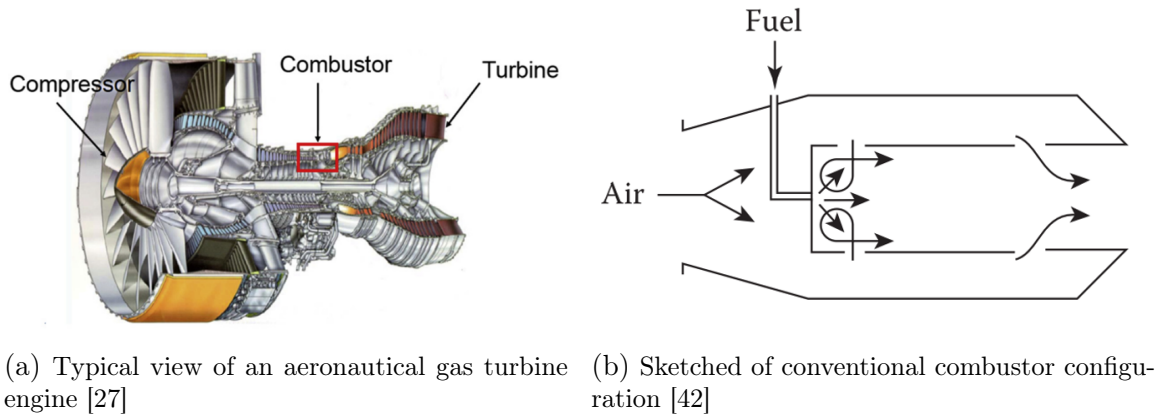


Figure 1-2: Gas turbine

Generally, new gas turbine developments aim to reduce current combustors' size and weight. Regardless of the engine type, the requirements of low fuel consumption and low pollutant emissions are paramount.

A conventional combustor is sketched in Fig. 1-2b. For safety reasons, the liquid fuel is stored separately and is injected directly into the combustor in the form of a well-atomized spray to ensure its better mixing. To reduce pollutant emissions, the combustors are operated with high air/fuel ratios [42]. In order to ensure stable combustion in such lean operating conditions, a recirculatory motion is usually desired within the combustion chamber to promote fuel mixing and thus better fuel consumption. The air inlets downstream, which can be seen in Fig. 1-2b, serve to reduce the temperature to a value that is not detrimental to the turbine.

As mentioned above, gas turbines are usually operated with liquid fuel. Therefore it is essential to improve our understanding of two-phase flow combustion, which includes multi-scale physical and chemical processes taking place concurrently. Before the discussion of numerical aspects, we will briefly summarize some essential physical phenomena related to the fuel injection and two-phase combustion

### 1.1.1 Fuel injection

The fuel is commonly injected in liquid form in the stationary and aeronautical gas turbine combustors. Once the liquid fuel is injected into the gaseous atmosphere, it undergoes subsequent atomization, as shown in Fig. 1-3.

Close to the injector, the liquid breaks down into ligaments and large droplets, called primary atomization. A further disintegration into smaller ligaments and fragments occurs during the secondary atomization. At these stages, the atomization process dominates, and the droplets can collide and merge after collisions. As the volume fraction of the dispersed phase drops below  $10^{-3}$ , we transit to the dilute regime where the droplet interaction can be neglected.

The exact reproduction of liquid fuel injection is a complex task that deserves special attention. The main focus of this work lies in the modeling of dilute spray combustion. Unlike the very diluted regime, where the volume fraction of the dis-

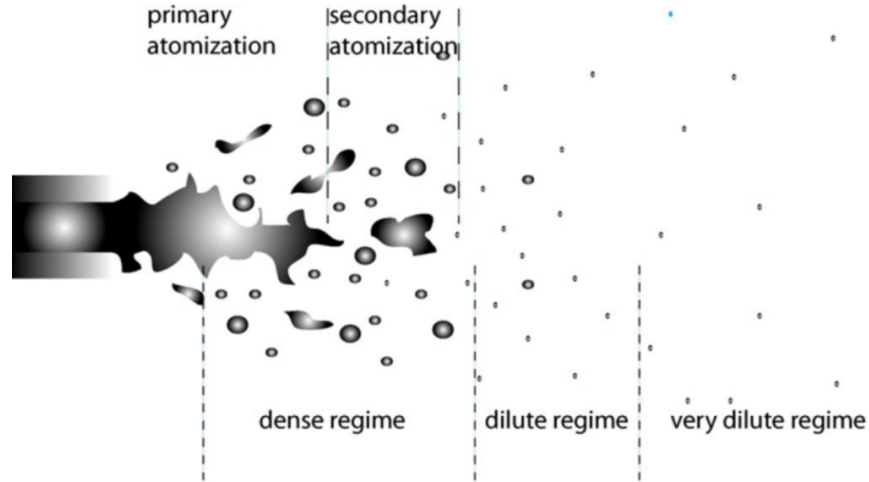


Figure 1-3: Sketched liquid fuel injection [37]

persed phase lies below  $10^{-6}$ , the influence of the dispersed phase on the mean phase is still significant in the diluted regime.

### 1.1.2 Two-phase combustion

Two-phase combustion involves the simultaneous presence of different combustion modes, turbulence-chemistry, and droplet-flame interactions. The diagram in Fig. 1-4 demonstrates how complex the interaction between spray and gaseous reacting flow can be.

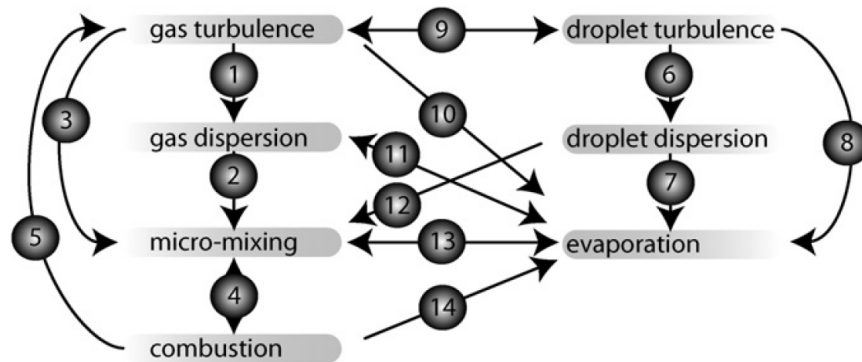


Figure 1-4: Interaction diagram between dispersed and gaseous phases [37]

The turbulence alters the species diffusion directly (arrow 3) or through gaseous macro-mixing (arrow 2) by promoting scalar gradients. Besides, the species diffu-

sion into the reaction zone (arrow 4) and the local mixture composition affect the combustion. Moreover, turbulence can influence flame propagation by wrinkling its surface. At the same time, the chemical reactions within the flame front raise the temperature locally and induce strong gradients, which promote the diffusion processes (reverse arrow 4). In addition, the flame modifies the mean flow due to the burned gas expansion (arrow 5).

The momentum exchange at the droplet interface (arrow 9) couples the turbulence of the mean flow with the droplets' turbulence. The relative velocity between gas and droplets (arrows 7,8,10) enhances the evaporation rates, promoting the diffusion processes (arrow 13). The elevated temperatures in the flame vicinity (arrow 14) and low fuel concentrations (arrows 11,13) also intensify the droplet evaporation.

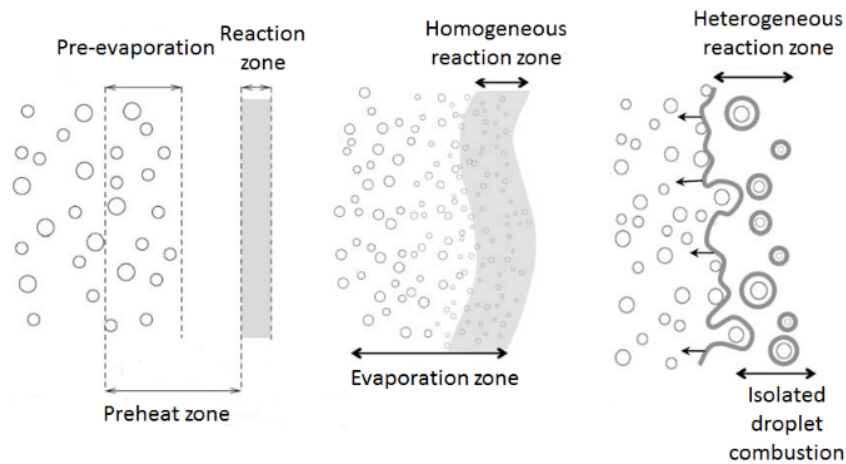


Figure 1-5: Spray-flame interaction. Left: Pre-vaporized flame. Middle: Homogeneous combustion. Right: Heterogeneous combustion [77].

A lot of work has been done to characterize the combustion of droplets [61]. These efforts led to the definition of several spray-flame combustion regimes that are summarized in Fig. 1-5. The first regime, illustrated on the left of Fig. 1-5, describes the pre-vaporized flame. Here, all the liquid fuel evaporates in the preheat zone before entering the flame front, such that the spray evaporation and flame propagation can be studied separately.

Heterogeneous combustion represents the opposite case and is shown on the right of Fig.1-5. Here, the droplets do not have sufficient time for evaporation and enter the

flame modifying its structure. It has been observed experimentally that the presence of the spray can enhance flame speed propagation [77]. This effect was attributed to the increase of the flame surface caused by the wrinkling induced by the spray-flame interactions.

In the homogeneous regime, the spray is sufficiently dense and homogeneous to feed the flame uniformly, as illustrated in the middle of Fig. 1-5. In this case, the flame interaction with the spray is moderate compared to the heterogeneous regime [58]. Nevertheless, this interaction can result in flame characteristics that deviate from the purely gaseous flame burning at the same fuel/air equivalence ratio.

In the following, we consider only the spray flame that burns either pre-vaporized or in the homogeneous regime. The investigation of heterogeneous spray combustion, in which the flame can emerge around the droplet, is outside the scope of this study.

## 1.2 Numerical simulations of gas turbines

Computational fluid dynamics (CFD) plays an essential role in the development of gas turbine combustors. Numerical simulations are much cheaper to run compared to costly experimental tests. While the experiments provide only global information about engine performance, simulations grant access to valuable information about the processes that take place inside the combustion chamber, which can not be measured otherwise. With an improved understanding of internal processes, the operating point can be adjusted so that the devices can be run at optimal conditions. Moreover, with the use of CFD, changes in the combustor design can be evaluated with less effort.

Several techniques are used to perform the simulation of turbulent flow and include RANS (Reynolds Averaged Navier-Stokes) simulations, Large Eddy Simulations (LES), and Direct Numerical Simulations (DNS). While the RANS modeling deals with the time-averaged flow properties, LES is a powerful approach that can correctly address the unsteady nature of flows in gas turbine combustion chambers. Compared to Direct Numerical Simulations, where all the characteristic scales are resolved, in Large Eddy Simulations (LES), only the part containing the spectrum's largest and

most energy-containing scales is resolved explicitly. In LES, the remaining scales are filtered out and require specific modeling. In practice, the filtering procedure is done implicitly with an effective filter size proportional to the cell size. Thus, the level of mesh refinement dictates the level of scale resolution, the amount of introduced modeling, and, finally, computational costs.

The "CFD Vision 2030 Study" project contracted by NASA aims to estimate the progress in CFD development in aerospace applications. This study defines future objectives and milestones in physical modeling, algorithms, geometry modeling and mesh generation, knowledge extraction, and multidisciplinary analysis and optimization. Here, the progress in LES and combustion modeling is enclosed within the physical Modeling section. According to this study, RANS modeling is the most mature and widespread approach in industrial applications) [53]. At the same time, LES becomes affordable for industrial applications as computational power increases. However, typical LES cell sizes are larger than the flame thickness. Thus, combustion is taking place at the sub-grid level and requires specific sub-grid scale models. As stated in the roadmap, the technology readiness level (TRL) of combustion modeling remains at a low level at the current moment. This indicates that combustion modeling approaches for LES have to be improved in the future to be used in industrial applications. Therefore, this study will focus on two-phase combustion modeling in the context of LES.

While the most accurate two-phase flow representation is to track the liquid-gas interface, it would set enormous requirements on resolution, making such computation not feasible for practical applications. Instead, a point droplet approximation is commonly used to overcome this issue. In this case, the droplets can be viewed as the continuum (Eulerian-Eulerian approach), or they can be seen as the particles whose evolution in time is tracked separately by solving an ordinary differential equation system (Eulerian-Lagrangian approach). In this work, the Eulerian-Lagrangian framework is chosen to perform two-phase simulations, which details are given in Chapter 2.

It is mentioned above that the influence of the dispersed phase on the gaseous

phase is still significant in the considered diluted spray regime. Therefore, this interaction between the phases is achieved by a two-way coupling in the simulations, as explained in Chapter 2.

In the cases where a fraction of droplets that burn in isolated mode is high in the spray, it might be important to include this issue into modeling consideration, as it has been done, for example, in [58] in the context of LES. However, the isolated droplet combustion and the flame front wrinkling induced by the spray-flame interactions require an additional modeling effort on the LES grids and are neglected in this study.

The essential aspects related to the combustion modelling, such as the choice of chemistry description and the turbulence-flame interactions, are discussed in the following section.

### **1.2.1 Combustion modeling**

In order to reproduce a combustion process numerically, one will need a suitable chemical reaction scheme that includes all the species and reactions to describe kinetic processes. Additionally, a turbulent combustion model is required to provide a closure for the filtered equations since the flame thickness is usually much smaller than the practical LES grid cell size. Moreover, a turbulent combustion model should ensure a proper flame/turbulence modeling because a part of the flame wrinkling induced by the turbulence takes place at the sub-grid level and is not resolved. Both these modeling aspects are addressed in the following.

#### **Chemistry description**

The detailed reaction mechanisms that can carefully describe a chemically reacting system may include thousands of species and are highly non-linear. Therefore, such a chemistry description can not be integrated directly into the LES simulations since it requires tremendous computational efforts. Nevertheless, there are multiple ways to include the chemistry computations in the LES simulations. These include using

globally fitted simple chemical kinetics models, chemistry tabulations techniques, and reduced chemistry. The complexity of the chemistry modeling will dictate, in turn, the properties of interest that can be reproduced by such simulation.

**Global chemistry.** The globally fitted simple chemical kinetics models [38] can include a few several main species and are not very computationally intensive. However, such simulations provide a very crude approximation and are usually limited to the specific range of operating conditions. Moreover, a physical process description that requires intermediate species, such as the pollutant formation, becomes impossible with global mechanisms [28].

**Tabulated chemistry.** Another classical solution for chemistry incorporation is to tabulate flamelet properties using a detailed mechanism [25]. As with the globally fitted chemical kinetics, such simulations are not very expensive for simple flame configurations. However, as the complexity of a considered flame raises, it increases the number of parameters needed to determine a thermo-chemical state. Moreover, the presence of the spray and its evaporation introduces a non-monotonicity of the mixture fraction and requires an additional adjustment of look-up tables. All these factors increase the dimensionality of the look-up tables, making such computations not essentially straightforward.

**Reduced chemistry.** An accurate chemistry description is essential for computing unsteady phenomena such as flashback, lean blow-out, and ignition. Understanding these physical processes is critical to the gas turbine design and choosing optimal operating conditions. Moreover, detailed kinetics is needed to evaluate the performance of alternate fuels compared to conventional ones.

Unfortunately, the use of detailed chemical mechanisms remains unfeasible nowadays because hundreds of species have to be transported, which requires long run times. Nevertheless, the use of reduced mechanisms can be viewed as the best compromise because they retain the most important species and reactions to represent the desired physical properties of interest. Different approaches exist to reduce the

number of species in the chemical mechanism. The graph methods belong to the most commonly used ones and aim to remove the species with the weakest global interaction. The recently developed Analytically Reduced Chemistries allow getting even compacter mechanisms that retain only the most relevant kinetic information and are non-stiff by the construction [29].

The main challenge in the design of modern aero-engines remains the formation of the pollutant. Therefore, the recent combustion modeling trends focus on the approaches that allow for the online chemistry computations to capture the transient evolution of species [28]. This allows not only to capture the local mixture evolution more precisely, which is beneficial for the unsteady physical phenomena but also helps to avoid additional modeling assumptions related to the different time scales involved in the pollutant formation process. For this reason, only the combustion models that can employ direct chemistry computations are considered in the following. Additionally, new approaches to make the computations more efficient continue to be devised, allowing to increase the complexity of the used chemistry description at a reasonable cost. For example, the methods using artificial intelligence are currently gaining popularity since they allow to reduce CPU times significantly [78, 70, 15, 8].

## **Turbulent combustion**

While combustion usually takes place at the sub-grid level in a turbulent environment, a combustion model should provide a closure for turbulent combustion. However, no additional modeling is required if the flame is sufficiently resolved. This strategy will be referred to as NCM (No Combustion Model), and such numerical studies can be found in [59, 26, 73]. In other cases, attention should be paid to the choice of the combustion model since its applicability is often limited to a specific combustion mode, such as fully premixed or non-premixed. In premixed flames, fuel and oxidizer are mixed before reacting, making the species and temperature transport important only in the vicinity of the flame.

On the contrary, fuel and oxidizer are separated in diffusion flames. Therefore the molecular and turbulent transport in the diffusive region control the reaction rate

and the thickness of such flames. Unlike the premixed flames, the diffusion flames do not propagate and therefore do not feature a fixed reference burning velocity.

In practical systems, however, non-premixed combustion tends to be avoided since it leads to higher temperatures that promote the production of pollutants. In gas turbines, the so-called partially premixed flames are often observed. These flames can not be characterized as purely premixed or non-premixed. Therefore, the classical combustion models devised either for purely premixed or diffusion flames should be used with care unless specially adapted [27].

Following the combustion model classification proposed by Veynante and Vervisch [39], the modeling approaches can be divided into two main categories: the geometrical and statistical ones.

In the statistical approaches, the main modeling challenge lies in determining the probability density function (PDF) to recover the statistical information lost due to the filtering operation. The dimensionality of the space describing the chemical state of the system usually includes the temperature and the mass fractions of the species involved in the chemical mechanism and affects the complexity of PDF computation.

The probability density function can be presumed, as in [40] or transported depending on the modeling approach. The work done in [56], where different spray evaporation models were investigated in the context of a non-swirling jet flame, can be an example of the transported PDF modeling approach. The Conditional Moment Closure (CMC) falls in the category of presumed PDF methods, where the flame properties are conditioned on the mixture fraction or the progress variable, as it is done in [74]. With the PDF knowledge, the mean correlations can be obtained for any location within the flow.

PDF calculation becomes more prohibitive as the number of species in the considered mechanism increases. In presumed PDF approaches, the presence of spray or considering other effects, such as radiation or heat losses, demands additional modeling. Despite the modeling complexity and relatively high computational costs, the statistical approaches provide rather good simulation results.

**Thickened Flame Model.** This work will focus on the Thickened Flame Model (TFM) belonging to the geometrical methods. In this approach, the flame is thickened artificially to resolve a flame on the LES grid while preserving the flame speed. Here, the unresolved flame wrinkling is introduced by the sub-grid efficiency model [16, 13]. Although TFM can be combined practically with any chemistry description (simplified, reduced, tabulated), we will consider the direct chemistry computations for the above reasons. This allows accounting better for the local mixture composition without further modeling effort.

Initially, TFM was introduced for laminar premixed flames in [11]. Later, it was extended to turbulent premixed flames [16], and then improved in [44] so that it can be successfully applied on practical combustors operated in a non-premixed or partially-premixed regime [36, 23, 22, 24]. Although TFM provides reasonable results in these cases, no theoretical proof of the TFM validity in the non-premixed regime has been provided in the literature [61]. The advantage of TFM in the non-premixed regime is that it allows the use of reduced chemistry. With this level of chemistry description, the mixture composition can be better predicted, which is essential for a non-premixed flame.

It has been shown recently that high accuracy can be achieved without prohibitive computational cost by coupling TFM with Adaptive Mesh Refinement (AMR). The TFM-AMR model has demonstrated a good agreement with experimental data on a stratified gaseous burner, as was shown in [47].

### 1.2.2 TFM application in the context of two-phase flows

The first extension of the Thickened Flame Model for spray flames was proposed for LES in [10] in the context of the Eulerian-Eulerian framework. The proposed model called TP-TFLES (Two-Phase Thickened Flame for LES) was based on a dimensional analysis and included the modification of the evaporation and drag terms for the dispersed phase. However, the modification of the drag term was omitted to avoid the modifications of spray trajectories. The author highlighted the influence of the dispersed phase on the flame, in particular the role of the evaporation process.

The Thickened Flame Model adaptation was proposed by Damien Paulhiac [58] within the Lagrangian-Eulerian framework. In this study, the evaporation and drag terms were modified in the dispersed phase equations accounting for the thickening factor. This modeling approach, also referred to as TP-TFLES, was validated in a two-phase laminar 1D flame configuration. While the drag corrections showed minor influence on the results in the cases where the relative velocity between the phases was low, it had a pronounced effect in the cases with significant relative velocities. It was shown that the corrections introduced by the TP-TFLES model are necessary for the spray thickened flames to get the flame characteristics of the reference non-thickened two-phase flames.

The TP-TFLES model was then validated in the context of the Cambridge burner [12] designed to study confined turbulent swirling premixed and non-premixed spray flames. The burner was operated with n-heptane at atmospheric conditions. The n-heptane chemistry was described through a global two-step mechanism. Despite the simplified chemistry description, the results obtained numerically matched well the experimental data.

Another attempt to adapt TFM onto two-phase flows was made by Sacomano Filho et al. in [24]. Here, similar modifications as in [58] were applied to the Lagrangian equations to include the effect of the mean phase thickening onto the dispersed phase. However, the modification of the drag terms was put aside to keep the computation of droplet movement unchanged. On one-dimensional spray flame configurations, it was demonstrated that these modifications are essential to get the correct spray evaporation rates in the thickened two-phase flames.

The TFM modeling approach (here called Artificially Thickened Flame or ATF) coupled to the tabulated chemistry and adapted to two-phase flames was then investigated by authors in [24] in the context of lean partially pre-vaporized burner [60]. Here, the premixed turbulent n-heptane spray flames are studied at ambient temperature and pressure conditions. The applied modeling strategy showed a great capacity for predicting such flames providing an overall good agreement with the available experimental data. However, the authors note that considering heat losses and detailed

chemistry aspects could improve the prediction of such flame configurations.

To avoid any thickening outside the flame region, the studies mentioned above used the dynamic flame thickening approach [44], where the flame front was detected by comparing the local flow characteristic with the tabulated values of laminar premixed flames. However, the variations of local conditions, complex flame configurations, and dispersed phase presence can make this flame detection not essentially straightforward, requiring a model parameter tuning.

For this reason, Bastien Rochette suggested a generic and self-adapting method for flame detection in [69] that TFM can use. In the proposed modeling approach, the flame thickness and, therefore, the required flame thickening is deduced from the curvature of the test function that associates a bell-curve shape to a flame front, eliminating the use of tabulated premixed flame properties. This approach was first validated on the premixed laminar flames using a two-step global mechanism and then on a propane-air turbulent premixed flame.

Finally, the proposed generic method for the flame detection was compared to the standard one that uses pre-tabulated flame properties in the context of the HERON burner (High prEssure facility for aeRO-eNgines). This test rig can be equipped with aircraft and helicopter injectors and was designed in the CORIA laboratory to study high temperature high-pressure lean combustion [2, 5]. The computed mean flow velocities were similar for both modeling approaches and demonstrated some mismatches with the experimental results. Moreover, none of the modeling approaches could predict the shape of the flame observed experimentally. These discrepancies were attributed to the fact that the spray injection was not sufficiently parameterized, which did not allow for setting up correctly the boundary conditions for the dispersed phase. Nevertheless, the proposed generic approach reduced the applied thickening factors, providing a more realistic flame thickness estimation than the standard approach.

## 1.3 Goal and objectives of this work

The main focus of this work is the investigation of two-phase flow combustion modeling using the TFM-AMR approach in the context of LES. Therefore, it is essential to understand how the thickening procedure can affect a spray flame in order to extend the existing TFM-AMR approach to two-phase flows. The first part of this work aims to assess the state-of-the-art models which involve the use of laminar premixed flame characteristics. We will explore how to improve the existing methods in the second part.

To achieve this goal, the following objectives should be met:

1. First, the validity of TFM-AMR application in two-phase flow combustion should be verified and investigated on simple laminar spray flame configurations.
2. Then, the performance of two-phase flow TFM-AMR should be evaluated in the context of a simple burner geometry.
3. Gradually increasing the complexity level, the modeling approach should be investigated in more complex cases.
4. Propose a novel TFM modeling approach to compute complex flames, including spray.
5. Similarly to the validation of the existing approach described in steps 1-3, evaluate the new model.

The simplified burner geometry investigated first in this work is unconfined which results in a nearly laminar jet flame. This burner, as well as the more complex configuration studied next are operated in atmospheric conditions. Contrarily to the first burner, the second investigated burner is confined and leads to a more complex combustion process, including a recirculation of burned gases. Moreover, the lean blowout limit is evaluated for the second configuration.

The computation of realistic gas turbine configurations and burners at elevated temperatures and pressures is outside the scope of the study. As illustrated in the model validation workflow in Fig. 1-6, we focus on the configurations enclosed in the green rectangle.

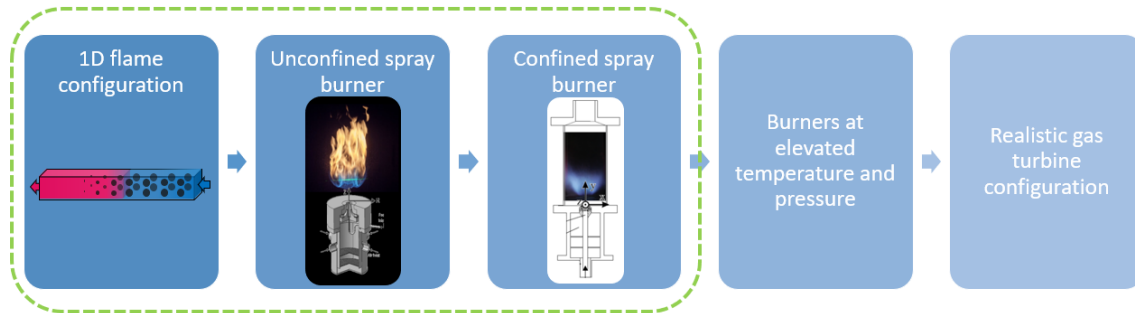


Figure 1-6: Model validation workflow.

First, the existing TFM-AMR modeling approach and its extension to two-phase flames are described in Chapter 2. Then, the analysis of the TFM-AMR performance on simple laminar gaseous and spray flames is presented in Chapter 3. After the modeling approach is validated on the 1D configurations, the TFM-AMR modeling approach is investigated in the context of an atmospheric unconfined academic burner in Chapter 4. Next, the behaviour of TFM-AMR is explored in the context of an atmospheric confined burner that features characteristics of real aero-engines in Chapter 5.

The limitations of the existing modeling approach were noted and discussed during this work. Therefore, a new TFM-AMR modeling approach is proposed in the final chapter, Chapter 6, that attempts to overcome these issues. In particular, Chapter 6 includes the validation of the proposed modeling approach on the 1D flames, as well as the simulation results for both burner configurations mentioned above.

# Chapter 2

## TFM modeling approach for two-phase flames

### 2.1 Carrier phase

The Eulerian-Lagrangian framework is selected to describe the gaseous and liquid phases, respectively. The gaseous phase is governed by filtered compressible Navier-Stokes equations, where spatial averaged and Favre averaged quantities are indicated with over-bars and tildes, respectively. In the framework of the TFM model presented in Sec. 2.3, the conservation equations for mass, momentum, species mass fraction and specific internal energy write:

$$\frac{\partial \bar{\rho}}{\partial t} + \frac{\partial \bar{\rho} \tilde{u}_i}{\partial x_i} = S_{mass}^{l \rightarrow g} \quad , \quad (2.1)$$

$$\frac{\partial \bar{\rho} \tilde{u}_i}{\partial t} + \frac{\partial \bar{\rho} \tilde{u}_i \tilde{u}_j}{\partial x_j} = -\frac{\partial \bar{p}}{\partial x_i} + \frac{\partial}{\partial x_j} (\bar{\tau}_{ij} + \bar{\tau}_{ij}^{sgs}) + S_{mom,i}^{l \rightarrow g} \quad , \quad (2.2)$$

$$\frac{\partial \bar{\rho} \tilde{Y}_m}{\partial t} + \frac{\partial \bar{\rho} \tilde{u}_j \tilde{Y}_m}{\partial x_j} = \frac{\partial}{\partial x_j} \left( [\hat{S}(EF - 1) + 1] \bar{J}_{m,j} + [1 - \hat{S}] \bar{J}_{m,j}^{sgs} \right) + \frac{E}{F} \bar{\dot{\omega}}_m + S_{mf,m}^{l \rightarrow g} \quad , \quad (2.3)$$

$$\frac{\partial \bar{\rho} \tilde{e}}{\partial t} + \frac{\partial \bar{\rho} \tilde{u}_j \tilde{e}}{\partial x_j} = \frac{\partial}{\partial x_j} \left( \tilde{u}_i (-\bar{p} \delta_{ij} + \bar{\tau}_{ij} + \bar{\tau}_{ij}^{sgs}) + [\hat{S}(EF - 1) + 1] \bar{Q}_j + [1 - \hat{S}] \bar{Q}_j^{sgs} \right) + \frac{E}{F} \bar{\omega}_T + S_{en}^{l \rightarrow g}, \quad (2.4)$$

where  $\rho$  is the gas density,  $u_i$  is the  $i^{th}$ -component of the velocity,  $p$  is the pressure, and  $\tau_{ij}$  is the viscous stress tensor. The viscous stress tensor  $\tau_{ij}$  is computed using  $\tau_{ij} = \mu \left( \frac{\delta u_i}{\delta x_j} + \frac{\delta u_j}{\delta x_i} \right) - \frac{2}{3} \mu \left( \frac{\delta u_k}{\delta x_k} \delta_{ij} \right)$ , where  $\mu$  is the dynamic viscosity and  $\delta_{ij}$  is the Kronecker delta. The LES sub-grid terms are denoted with superscript *sgs*.

The species equation Eq.(2.3) is solved for each species  $m$  present in the chemical mechanism.  $Y_m$  is the mass fraction of species  $m$ , and  $\dot{\omega}_m$  is its reaction rate. The species diffusive flux is defined using Hirschfelder and Curtiss approximation as  $J = \rho D_m \frac{\partial Y_m}{\partial x_j}$ , where  $D_m$  is the species diffusion coefficient.

In a multi-component mixture with  $M$  species in total, the Hirschfelder and Curtiss approximation allows to avoid solving at each point and at each time instant a linear system of size  $2^M$ . However, to eliminate the error introduced by the approximated diffusion velocities, and to ensure the global mass conservation, a correction velocity is included in Eq.(2.3) and Eq.(2.4). Additional details may be found in [61].

Heat flux is defined by  $Q = \lambda \frac{\partial T}{\partial x_j} + \rho \sum_m D_m h_m \frac{\partial Y_m}{\partial x_j}$ , where  $\lambda$  is the thermal conductivity, and  $h_m$  is species  $m$  enthalpy. The first term here describes a heat diffusion expressed by Fourier's Law, while the second term is related to the heat transfer due to the enthalpy transport induced by the diffusion of species.

The heat release rate due to the chemical reactions appears as a source term in the energy equation, and is defined using  $\dot{\omega}_T = -\sum_m \Delta h_{f,m}^0 \dot{\omega}_m$ , where  $\Delta h_{f,m}^0$  is the mass formation enthalpy. If any external energy is deposited into the system, e.g. ignition energy, an additional source term emerges on the RHS of Eq.(2.4).

$\hat{S}$ ,  $F$  and  $E$  which arise in Eq.(2.3) and in Eq.(2.4) are the terms introduced by the TFM. These are the flame sensor, the thickening and the efficiency factors, respectively. The flame thickening procedure is presented in detail in Section 2.3.

The contribution of droplets to the gaseous conservation equations is given by the source terms in mass, energy, species mass fractions and momentum equations which

are presented by the terms  $S_{mass}^{l \rightarrow g}$ ,  $S_{en}^{l \rightarrow g}$ ,  $S_{mf}^{l \rightarrow g}$  and  $S_{mom}^{l \rightarrow g}$  respectively in Eqs.(2.18, 2.20, 2.18, 2.21).

In this work, the ideal gas law is used to relate density, pressure, and temperature. Molecular species diffusion due to temperature gradients, or the Soret effect, and the heat flux due to species mass fraction gradients, or the Dufour effect, are both considered to be negligible.

As it has been already mentioned, typical LES cell sizes are larger than the flame thickness. In that case, combustion is taking place entirely at the sub-grid level and requires specific sub-grid scale models and turbulence is under-resolved.

**Unresolved Reynolds stresses.** With the eddy-viscosity assumption, the sub-grid stress tensor  $\tau_{ij}^{sgs}$  is computed similarly to  $\tau_{ij}$ , but with turbulent viscosity  $\mu_t$  instead of the molecular one. In this work, we employ the Sigma model proposed in [55], in which the turbulent viscosity is related to the singular values of the resolved velocity gradient tensor.

Similarly to the standard Smagorinsky model, it has a case-specific constant, but is suitable for transitioning flows and for wall turbulence treatment. By construction, the sub-grid stresses vanish when the flow is two-component or two-dimensional, and in case of pure axisymmetric or isotropic contraction/expansion. It has been shown analytically in [55], that the model has a cubic behavior in the vicinity of solid boundaries, and thus does not require any ad-hoc treatment in these regions. The authors in [55] and later in [68] have demonstrated that the results with the Sigma model are comparable to the dynamic Smagorinsky model for most of the settings at significantly lower computational costs.

**Unresolved scalar transport.** In this work, the unresolved scalar transport is described using a gradient assumption. According to this approach, the molecular transport coefficients in the species diffusive flux  $J_m$  and in the heat flux  $Q$  are replaced with the turbulent quantities leading to  $J_m^{sgs}$  and  $Q^{sgs}$ , respectively.

The transport coefficients are modeled by introducing turbulent Prandtl and

Schmidt numbers,  $Pr_t = 0.9$  and  $Sc_t = 0.78$ . Then, the turbulent mass diffusion coefficient is computed from  $D_t = \mu_t / (\rho Sc_t)$  using turbulent viscosity provided by the closure for sub-grid stress tensor. Similarly, the turbulent conductivity is obtained with  $\lambda_t = c_p \mu_t / Pr_t$ , where  $c_p$  is the specific heat capacity.

## 2.2 Dispersed phase

Within the Lagrangian framework, droplets are approximated as evolving mass points tracked separately from the continuous phase. A two-way coupling in the Eulerian-Lagrangian approach is ensured by interpolating gaseous quantities to the droplets position, and by introducing the spray source term  $S^{l \rightarrow g}$  (see Section 2.3.4) into the gaseous equations (2.1-2.4).

Such droplet representation is based on the assumption that the spray is diluted and consists of sufficiently small droplets with high surface tension forces. Then, considering the droplets to be isolated, small-scale models must account for the momentum, mass, and heat exchange at the phase interfaces. These are discussed in this section.

### 2.2.1 Equation of motion

The position of the droplets is updated based on their velocities that are governed by:

$$\frac{du_{d,i}}{dt} = \frac{1}{m_d} F_{ex,i} = \frac{1}{m_d} (F_{drag,i} + F_{\nabla p} + F_{g,i}),$$

where  $m_d$  is the mass of the droplet,  $\mathbf{u}_d$  is its velocity and  $\mathbf{F}_{ex}$  is the external force acting on this droplet. In the following, we assume the effect of gravitational force  $\mathbf{F}_g$  to be negligible, and since the liquid density is sufficiently higher than the gaseous one, the force induced by the pressure gradients  $\mathbf{F}_{\nabla p}$  can also be neglected. With all these assumptions, the droplet velocity evolution is affected only by the drag force

$\mathbf{F}_{drag}$  and simplifies to:

$$\begin{aligned}
\frac{du_{d,i}}{dt} &= \frac{1}{m_d} F_{drag,i} \\
&= \frac{1}{m_d} C_{drag} A_d \rho_g \frac{|\mathbf{u}_{rel}| u_{rel,i}}{2} \\
&= \frac{1}{\tau_d} u_{rel,i} \text{ ,}
\end{aligned} \tag{2.5}$$

where  $A_d$  is the drop's cross-section and  $C_{drag}$  is the drag coefficient. The relative velocity between the droplet and the gas phase is computed using  $\mathbf{u}_{rel} = \mathbf{u}_{g@d} - \mathbf{u}_d$ , with  $\mathbf{u}_{g@d}$  being the velocity of the gas interpolated at the droplet's location.

The subscript  $d$  addresses the droplets' characteristics, and the subscripts  $g$  and  $l$  indicate the properties that correspond to the gaseous and liquid phases, respectively. The subscript  $s$  denotes the gaseous characteristics at the droplets' surface which are estimated using 1/3 - rule, i.e. at the reference temperature  $T_s = (2T_d + T_g)/3$ .

In this work, we assume the droplets to be perfectly spherical, and use the droplet drag coefficient proposed in [45]:

$$C_{drag} = \begin{cases} 0.424 & Re_d > 1000 \\ \frac{24}{Re_d} \left(1 + \frac{1}{6} Re_d^{2/3}\right) & Re_d \leq 1000 \end{cases}$$

where  $Re_d$  is a Reynolds number based on the droplet's radius, the relative velocity between the droplet and the gas, and the gas properties, such that:  $Re_d = \frac{2R_d \rho_g |\mathbf{u}_{rel}|}{\mu_s}$ .

The droplet relaxation time  $\tau_d$  that arises in Eq.(2.5) can be defined by:

$$\tau_d = \frac{4}{3} \frac{\rho_l}{\rho_g} \frac{2R_d}{C_{drag} |\mathbf{u}_{rel}|} \tag{2.6}$$

This information is often provided by defining the non-dimensional Stokes number as  $St_d = \tau_d / \tau_g$ , where  $\tau_g$  is the characteristic time of the mean flow. When  $St_d$  is small, droplets relax quickly towards the gaseous velocity and follow the streamlines of the mean flow, which corresponds to the perfect advection. In the case of large  $St_d$ , the droplet's inertia dominates so that the droplet moves along its initial trajectory.

## 2.2.2 Evaporation

As was mentioned above, the droplet is considered to be spherical. Additionally, we assume that the fuel is a pure liquid with a well-defined boiling point, and we neglect the radiative heat transfer. Generally, these assumptions are considered to be acceptable, except for highly luminous flames and at very low pressures [43].

The process of droplet evaporation, which is suddenly immersed in the hot gaseous medium, can be divided into two stages. In the beginning, the mass transfer from the droplet is low since the concentration of fuel vapor at the liquid surface is low at normal fuel injection temperatures. At this stage, almost all supplied heat is used to raise the temperature of the droplet, where a part of it goes on the liquid vaporization. As the droplet temperature reaches its wet-bulb value, all the transferred heat is used to vaporize the liquid [43].

If we additionally consider the conductivity within the droplet to be infinite, then the droplet evaporation is governed by a set of two ordinary differential equations.

The temporal change of a droplet's radius  $R_d$  is described by the Frossling correlation [6]:

$$\frac{dR_d}{dt} = - \frac{(\rho_g D_F)|_s}{2R_d \rho_l} \ln(1 + B_d) Sh, \quad (2.7)$$

where  $Sh$  is the Sherwood number,  $B_d$  is the transfer number, and  $(\rho_g D_F)|_s$  are the gaseous density and a mass diffusion coefficient of a liquid vapor at the droplet surface. Here,  $D_F$  is estimated from the empirical correlation  $(\rho_g D_F)|_s = \rho_0 D_0 (T_s/T_0)^{n_0-1}$ . For n-heptane and  $\rho_0 = 1.293$  and  $T_0 = 273$ , the experimentally defined values are  $D_0 = 5.94e - 06$  and  $n_0 = 1.6$ . For n-dodecane, these values are set to  $D_0 = 4.16e - 06$  and  $n_0 = 1.6$ .

The transfer number  $B_d = (Y_F^* - Y_F)(1 - Y_F^*)$  represents the driving force for the evaporation process and is defined based on the fuel mass fraction  $Y_F$  and the vapor mass fraction at the droplets surface  $Y_F^*$  computed with:

$$Y_F^* = \frac{W_F}{W_F + W_{mix} \left( \frac{p}{p_{vapor}} - 1 \right)}, \quad (2.8)$$

where  $W_F$  and  $W_{mix}$  are the molecular weights of liquid fuel and mixture, respectively. The value of saturated vapor pressure  $p_{vapor}$  is obtained based on the reference temperature  $T_s$ .

When the droplet evaporates under quiescent conditions, the heat transfer proceed primarily through the thermal conduction, while the relative motion between the gas and the droplet enhances the evaporation rates. The latter effects are included into the equations (2.7) and (2.10) through the Sherwood and Nusselt numbers, respectively. These are obtained using Ranz-Marshall correlations [64]:

$$\begin{aligned} Nu &= 2.0 + 0.6 Re_d^{1/2} Pr^{1/3} \\ Sh &= 2.0 + 0.6 Re_d^{1/2} Sc^{1/3}, \end{aligned} \tag{2.9}$$

where  $Pr$  is obtained with mean flow quantities, whereas for the computation of Schmidt number  $Sc = \frac{\mu_s}{(\rho_g D_F)_s}$  the gaseous values are used, which are estimated on the droplet surface.

The fuel mass flow rate  $\dot{m}_d$  is defined based on the radius change computed in Eq.(2.7). Here, we consider  $\dot{m}_d$  to be always negative, meaning there is no condensation taking place.

The evolution of the droplet's temperature in time is given by:

$$\begin{aligned} c_{p,l} m_d \frac{dT_d}{dt} &= Q_{tot} \\ &= Q_{cond} + Q_{vap} \\ &= A_d \frac{\lambda_s}{2R_d} (T_g - T_d) Nu \frac{\log(1 + B_d)}{B_d} + \dot{m}_d h_{vap} \end{aligned} \tag{2.10}$$

where  $h_{vap}$  is the latent heat of vaporization,  $c_{p,l}$  is the liquid specific heat capacity, both estimated at the reference temperature  $T_s$  [6]. The term  $Q_{cond}$  describes the heat flux from the gaseous to the liquid phase, and is proportional to the droplet surface  $A_d$  and to the temperature difference between the phases.  $Q_{vap}$  stands for the heat required to vaporize the fuel with a mass flow rate  $\dot{m}_d$ . Therefore, Eq (2.10) states that the heat transferred to the droplet  $Q_{cond}$  will either heat up the droplet or supply

heat for vaporization  $Q_{vap}$ .

The Lagrangian source terms in the mean flow equations (2.1-2.4) and the effect of the flame thickening on these terms are discussed in Section 2.3.4 after introduction of TFM in the next section.

## 2.3 Thickened Flame Model

As the flame thickness is usually much smaller than the cell size, the TFM introduces artificial flame thickening to ensure a correct resolution of the flame on a coarse mesh. The flame is thickened by a factor  $F$  through the coordinate transformation  $x \rightarrow Fx$  and  $t \rightarrow Ft$ , which in practice is achieved by multiplying thermal and molecular diffusivities by  $F$ , and dividing reaction rates by  $F$ . It guarantees that the laminar flame speed of the resulting thickened flame remains unchanged [11].

The Charlette [13] efficiency function  $E$  is introduced in the species mass fractions and energy equations to model turbulence-flame interactions at the sub-filter level. Similarly to LES models using flame surface density, the efficiency function corrects the loss of flame surface due to the under-resolution and the thickening by enhancing the reaction rates and diffusivities.

### 2.3.1 Flame sensor

To avoid thickening outside the flame region, where pure mixing is taking place, the dynamic version of the TFM is considered in this work [44]. The flame sensor  $S$  is used to detect the flame front. Similarly to the sensor formulation in [36], the sensor in Eq.(2.11) takes the value of one in zones where reactions take place, and falls to zero outside.

$$S = \max \left[ \min \left( \beta \max \left\{ \frac{\omega_T}{\omega_{T1D}^{max}(\phi)}, 0 \right\} - 1; 1 \right); 0 \right], \quad (2.11)$$

where  $\beta$  is the parameter controlling the sensibility of the sensor,  $\phi$  is a local fuel/air equivalence ratio,  $w_T$  and  $w_{T1D}^{max}$  are the local and the reference heat release values respectively.

Here and in the following, the reference values of the heat release  $w_{T1D}^{max}(\phi, T_u, p)$ , the flame thickness  $\delta_L^0(\phi, T_u, p)$ , the burning velocity  $S_L^0(\phi, T_u, p)$  are tabulated using 1-D laminar premixed flames.

The sensor  $S$  is extended towards fresh and burned gases to enclose the reactive region completely. The extended sensor  $\hat{S}$  is obtained following the methodology proposed in [36], where an indicator function  $\psi$  is defined to filter the sensor. The transport equation for the indicator function is given by:

$$\frac{\partial \rho \psi}{\partial t} + \frac{\partial \rho u_j \psi}{\partial x_j} = \frac{\partial}{\partial x_j} \left( [\hat{S}(EF - 1) + 1] \Psi_j + [1 - \hat{S}] \Psi_j^{sgs} \right) + \frac{E}{F} \dot{\omega}_\psi, \quad (2.12)$$

where the diffusive indicator flux is defined by  $\Psi_j = \rho D_\psi \frac{\partial \psi}{\partial x_j}$ . The diffusion coefficient  $D_\psi = \mu / (\rho Sc_\psi)$  is obtained using a Schmidt number, set here at a value  $Sc_\psi = 0.7$ . Similarly to the scalar transport, the sub-grid scale flux  $\Psi^{sgs}$  is computed using turbulent diffusion coefficient  $D_t = \mu_t / (\rho Sc_t)$ . The indicator source term value is based on the flame sensor  $S$ :

$$\dot{\omega}_\psi = \begin{cases} \rho \frac{\psi_0 - \psi}{\tau_0} & S > 0.8 \\ \rho \frac{0 - \psi}{\tau_1} & S < 0.05 \end{cases}$$

Here  $\psi_0 = 20$  is the maximum value that the indicator can attain [36]. The relaxation time is set to a small value  $\tau_0 = 5\Delta t$  in the active sensor regions  $S > 0.8$ , so that the indicator quickly reaches its peak value. Outside the region detected by the sensor, the indicator is relaxed towards zero in a time proportional to the laminar flame time  $\tau_1 = \alpha \tau_{chem}$ , so that the flame extension is based on a characteristic physical scale. The characteristic chemical time is estimated based on local conditions from tabulated reference 1D flame characteristics  $\tau_{chem} = \delta_L^0 / S_L^0$ . Here, the parameter  $\alpha$  can take different values on the unburned  $\alpha_{cold}$  and on the burned  $\alpha_{hot}$  sides, with their standard values  $\alpha_{cold} = 0.05$  and  $\alpha_{hot} = 0.005$ .

The flame sensor  $\hat{S}$  which is finally used in all scalar transport equations is defined

by:

$$\hat{S} = \max \left( \min(\psi; 1); S \right) \quad (2.13)$$

### 2.3.2 Flame thickening factor

The flame thickening factor used in all scalar transport equations is obtained from:

$$F = 1 + (F_{max} - 1)\hat{S}, \quad (2.14)$$

where  $F_{max}$  is the maximum thickening factor estimated from the cell size  $\Delta_x$  and the laminar flame thickness  $\delta_L^0$ :

$$F_{max} = \frac{n_{res}\Delta_x}{\delta_L^0(\phi)}, \quad (2.15)$$

where  $n_{res}$  is the TFM parameter to impose a desired flame front resolution and is given in points per laminar flame thickness.

The accuracy of simulations is here increased by coupling TFM with AMR. Indeed, in TFM-AMR [47], AMR is used to reduce by a factor  $2^n$  the cell size in the flame front, thus reducing by the same factor  $2^n$  the thickening factor, therefore improving the flame dynamics. In practice, a target value of thickening  $F_{target}$  is given by the user, and the level of AMR  $n_{amr}$  is adjusted automatically by the model using:

$$n_{amr} = \text{int} \left[ \frac{1}{\log(2)} \left( \frac{n_{res}\Delta_x^{base}}{\delta_L^0(\phi)F_{target}} \right) \right], \quad (2.16)$$

where  $n_{amr}$  is rounded up to the larger integer,  $\Delta_x^{base}$  is the base cell size, i.e. the maximum cell size in the domain.

### 2.3.3 Stretched flames

Pierre Quillatre investigated in his thesis [62] the propagation of spherical flames using realistic transport (non-unity Le). It was shown that the thickening amplifies the effects of stretch and leads to a significant underestimation of consumption rates

and burned temperatures in the thickened flames.

As explained in [62], the thickening procedure modifies the flame thickness and thus the Markstein length, which affects resulting consumption rates. To reproduce stretch effects correctly in the thickened flames, it was proposed to adjust the Schmidt numbers in the following way:

$$Sc_k^* = Pr + \frac{Sc_k - Pr}{F}, \quad (2.17)$$

where Prandtl number is constant and equals to  $Pr = 0.7$ , and  $Sc_k$  is the Schmidt number of species  $k$ .

### 2.3.4 TFM formulation for the liquid phase

The spray is considered to be diluted and is represented by Lagrangian particles, whose evolution is tracked separately from the gaseous phase. To include the effect of thickening on the gaseous phase, the disperse Lagrangian equations need to be corrected as proposed in [58].

For a given computational cell with a volume  $V_{cell}$ , the source term in the mass fraction conservation equation is computed from the mass flow rate  $\dot{m}_d$  (calculated using the method described in [17]), induced by the  $k^{th}$ -droplet evaporation, which is then summed over all  $n_d$  droplets present in the cell:

$$S_{mf}^{l \rightarrow g} = S_{mass}^{l \rightarrow g} = -\frac{1}{V_{cell}} \sum_{k=1}^{n_d} \dot{m}_{d,k}^*, \quad (2.18)$$

As shown in [58], the mass flow rate  $\dot{m}_d$  needs to be written as  $\dot{m}_d^* = \frac{1}{F} \dot{m}_d$ , which states that evaporation must be slowed down  $F$  times in the thickened regions.

Similarly to  $\dot{m}_d$ , which appears in the source terms of the mean equations,  $Q_{tot}$  in the droplet temperature equation also arises within a source term in the energy equation and has to be scaled with the  $1/F$  factor [58]. Then the modified evolution

of droplets' temperature introduced previously, see Eq.(2.10), reads:

$$c_{p,l}m_d \frac{dT_d}{dt} = Q_{tot}^* = Q_{cond}^* + Q_{vap}^* = \frac{1}{F}Q_{cond} + \dot{m}_d^* h_{vap}, \quad (2.19)$$

The heat consumed on evaporation  $Q_{vap}$  already takes into account flame thickening because it depends on the corrected mass flow rate  $\dot{m}_d^*$ . Therefore, in order to get properly scaled  $Q_{tot}$ , the resulting heat that penetrates the liquid phase, we still have to correct the diffusive heat flux from the gaseous to the liquid phase  $Q_{cond}$ , as it is shown in Eq.(2.19). All these corrections lead to the modified Lagrangian source term in the gaseous energy equation Eq.(2.4):

$$S_{en}^{l \rightarrow g} = \frac{1}{V_{cell}} \sum_{k=1}^{n_d} (h_d \dot{m}_{d,k}^* - Q_{tot,k}^*), \quad (2.20)$$

where  $h_d$  is the enthalpy of the evaporated fuel.

The remaining Lagrangian source term in momentum equation Eq.(2.2) is computed as follows:

$$S_{mom,i}^{l \rightarrow g} = \frac{1}{V_{cell}} \sum_{k=1}^{n_d} (u_{d,i} \dot{m}_{d,k}^* - F_{drag,i,k}^*), \quad (2.21)$$

where  $F_{drag,i}^* = u_{rel,i} / \tau_d^*$  is the force responsible for the droplet-gas momentum exchange, and  $\tau_d^* = F\tau_d$  is the corrected droplet relaxation time computed using  $\tau_d$  defined in Eq.(2.6).

In Chapter 3, we assess the effect of these modifications on the spray flame propagation by comparing the cases without any corrections in the Lagrangian equations to the cases where the whole set of corrections is included. Additionally, we investigate the modeling approach that keeps the droplet relaxation time  $\tau_d$  unaffected by the thickening to assess the impact of the drag correction in the Lagrangian equations.

### Projection correction

Flame thickening implies a coordinate transformation in the direction normal to the flame front. In two-phase flames, droplets can enter the thickened flame at a different angle. Therefore, droplets' paths can be elongated in the direction orthogonal to the

flame and parallel to it, resulting in an altered mixture composition.

A correction of heat and mass transfer through the definition of an effective thickening  $F_{eff}$  was proposed by Dressler et al. in [20] and was referred to as projection correction.  $F_{eff}$  limits the effect of the flame thickening to the droplets moving in the direction normal to the flame front and is defined by:

$$F_{eff} = 1 + \left| \frac{\nabla C}{|\nabla C|} \cdot \frac{\mathbf{u}_d}{|\mathbf{u}_d|} \right| (F - 1), \quad (2.22)$$

where  $C$  stands for the progress variable and its gradients define the orientation of the flame, while the movement direction of the droplet is defined by its normalized velocity vector  $\mathbf{u}_d/|\mathbf{u}_d|$ .

$F_{eff}$  takes the values between unity and  $F$  and can be viewed as a combination of the standard liquid phase thickening approach described above and introducing no corrections due to the thickening. When the droplet enters the flame front perpendicularly,  $\nabla C$  and  $\mathbf{u}_d$  are co-linear and  $F_{eff} = F$  corresponding to the standard spray thickening approach. When the droplet's trajectory lies parallel to the flame, no thickening is accounted for and  $F_{eff} = 1$ .

The effective thickening factor replaces  $F$  in Eq.(2.19),  $\dot{m}_d^* = \frac{1}{F_{eff}} \dot{m}_d$  and  $\tau_d^* = F_{eff} \tau_d$ . Compared to the standard spray thickening, the projection correction changes the vapor release along the droplet path that does not move normal to the flame front, leading to a reduction of its lifetime.

## 2.4 Conclusion

This chapter summarizes the modeling framework used in this work to compute turbulent spray flames within the LES context.

First, we introduced the governing equations for the gaseous and liquid phases in Sections 2.1 and 2.2. Then the TFM-AMR modeling approach was presented in Sec. 2.3. In the described thickening procedure, we use the Jaravel sensor formulation detailed in Sec. 2.3.1 to detect the flame front. The TFM modification that also allows use in spray flame configurations is detailed in Sec. 2.3.4.

The described TFM-AMR model is investigated in Chapter 3 on simple one-dimensional spray flames. Then, it is evaluated in the context of turbulent spray flames of two different burner geometries in Chapters 4 and 5.

# Chapter 3

## Modeling approach validation. 1D

### Configuration

The necessity of the Lagrangian corrections for thickened flames has been already demonstrated in [58, 24] on the laminar two-phase flames. The simulations in [58] were performed in the context of dynamically thickened flames using two-step chemistry. However, only two configurations were investigated: with and without relative droplet motion, with multiple parameters changed at the same time. Later, a more detailed study on validation of corrected droplet equations was done in [24], but in a slightly different context. There, the authors used TFM together with chemical reactions described by the Flamelet Generated Manifold (FGM) chemistry reduction method. Moreover, the droplets' equation of motion Eq.(2.5) was left unchanged and not affected by the thickening (the correction of  $\mathbf{F}_{drag}$ ).

Despite the differences in their setups, both studies showed significant differences in the flame structure when TFM corrections are not introduced into the spray equations.

A 1D spray flame configuration without thickening which is similar to the one used below and described in Section 3.1.3 has already been investigated numerically. It was studied first using a detailed mechanism in [54]. For n-heptane, the simulations were performed under atmospheric conditions for a wide range of overall fuel/air equivalence ratios  $0.6 < \phi_o < 6$  with droplet diameter ranging from  $5 \mu m$  to  $140 \mu m$ .

To assess the influence of the droplet residence time, the study of Neophytou et al. [54] proposed to vary the distance between the flame front and the point of injection. Although the resulting flame speed highly depends on the size of injected droplets and overall fuel/air equivalence ratio, the obtained results show that  $S_L$  is enhanced with an increased residence time, which can be explained by the fact that the droplets have more time to evaporate.

The droplet residence time, its diameter, and the overall fuel/air equivalence ratio, all affect the gaseous fuel/air equivalence ratio observed within the flame-front. This gaseous fuel/air equivalence ratio that characterizes the reacting zone is referred to as an effective fuel/air equivalence ratio  $\phi_{eff}$  in [54]. However, it was demonstrated in [54] that the burning velocities are only marginally correlated with  $\phi_{eff}$ . High flame speeds were more likely to occur when  $\phi_{eff}$  was closer to unity. Simulations in [54] have also confirmed the experimental observations, that the spray flame at certain conditions can propagate faster than the pure gaseous flame with the same  $\phi_o$ . It was observed in cases where the droplets evaporating behind the reaction zone produce gaseous fuel, which pyrolyses in the absence of oxygen. Then, the intermediate pyrolysis products, mainly  $H_2$ ,  $C_2H_2$ , and  $C_2H_4$ , diffuse back towards the reaction zone and enhance the flame propagation.

The effect of relative velocity between liquid and gaseous phases was investigated in [69] using a simplified 2-step mechanism. Depending on the initial conditions ( $\phi_o$  lean/rich, droplet size), larger velocity differences can either enhance or slow down the flame propagation speeds. On the one hand, higher relative velocities enhance the evaporation rates, and on the other, decrease the droplet residence time within the flame-front.

In the present study, we will consistently evaluate the modifications applied to the spray equations in one-dimensional configurations using reduced chemistry. The modeling strategy described in Sec. 2.3.4 is first validated on a simple 1-D flame propagating in a mono-disperse droplet mist.

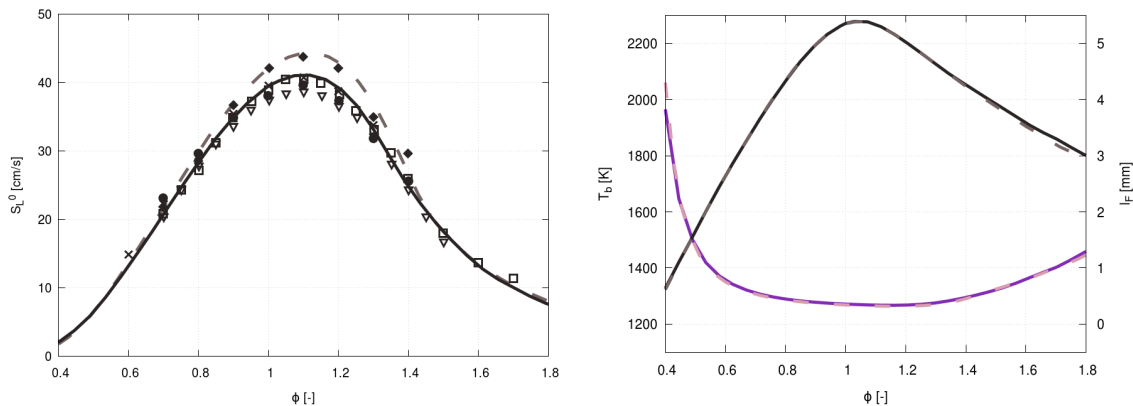
Three different TFM setups with increasing complexity are investigated in Sec. 3.1 in the context of n-heptane spray flames: (i) TFM using a constant thickening factor

in the whole domain; (ii) Dynamic thickening; (iii) Dynamic thickening with AMR. Then, the validated modelling approach will be applied to low-volatile n-dodecane fuel and explored in a more challenging flame configuration in Sec. 3.2.

## 3.1 High-volatile fuel (N-Heptane flames)

### 3.1.1 Chemistry modelling

Complex fuels are often approximated by a mono-component primary reference fuel to study combustion modeling. N-heptane is often used as a representative fuel in chemical kinetics modeling because it is a part of a Toluene Reference Fuel surrogate model for gasoline. It has also been chosen as one of the surrogates by the Engine Combustion Network (ECN). Moreover, n-heptane is a typical fuel with high volatility. Thus, it has a higher evaporation rate than other less volatile fuels, which is favorable when studying combustion systems as the fuel needs to vaporize before burning.



(a) Laminar burning velocity. Solid line: 36-species reduced mechanism. Dashed line: skeletal 99-species mechanism. Experiments: □: [18], ●: [34], ◆: [41], ×: [76], ▽: [19].

(b) Burned temperature (grey scale) and flame thickness (in color). Solid line: 36-species reduced mechanism. Dashed line: skeletal 99-species mechanism.

Figure 3-1: N-heptane flame properties at  $T = 298K$ ,  $p = 1bar$  as a function of fuel/air equivalence ratio.

The number of species, even for mono-component fuels, might exceed hundreds in detailed mechanisms. However, such large mechanisms are prohibitive in terms of computational resources. Therefore, the detailed mechanisms, which are usually

valid for a wide range of temperatures and pressures, are reduced for a specific range of operating conditions. An atmospheric operating point has been chosen as a target since the selected academic burner investigated in Chapter 4 is operated with n-heptane at  $1\text{ bar}$  and  $298 \pm 2\text{ K}$ .

A skeletal 99-species chemical kinetic mechanism [75], which has been derived from the Lawrence Livermore detailed mechanisms, is further reduced using the CONVERGE reduction tool. The reduction leads to 36 species and is based on a Directed Relation Graph with Error Propagation and Sensitivity Analysis (DRGEP-SA) [63].

As seen in Fig. 3-1a, the complete mechanism agrees very well with the experiments [19, 76, 41, 34, 18] over a wide range of fuel/air equivalence ratios at  $p = 1\text{ atm}$  and  $T = 300\text{ K}$ . The reduced mechanism slightly under-predicted the velocities obtained with the complete mechanism, but those are still in very good agreement with the experiments.

The thermal flame thickness  $l_F$  is estimated from the temperature profile as the ratio of the difference of its burned  $T_b$  and unburned  $T_u$  values and its maximum gradient value over the flame front as  $l_F = (T_b - T_u)/|\partial T/\partial x|_{max}$ . The values of burned temperatures and the resulting flame thicknesses obtained with the reduced mechanism match very well the values of skeletal 99-species mechanism and are shown in Figure 3-1b.

A combustible mixture can be characterized by a single Lewis number, the effective Lewis number  $Le_{eff}$ , which is related to the fuel and oxidizer Lewis numbers as explained in [46] and simplifies to just an average between those  $Le$  once a mixture is stoichiometric  $Le_{eff} = (Le_{Ox} + Le_{Fuel})/2$ .  $Le_{eff}$  can significantly deviate from unity and is usually larger than one for a lean mixture of heavy fuels, such as n-heptane.

With the corresponding Lewis numbers obtained with Cantera, we get  $Le_{eff} = (Le_{O_2} + Le_{nC_7H_{16}})/2 = 1.35$  for the stoichiometric n-heptane flame in atmospheric conditions. The effective Lewis number larger than unity indicates that the thermal diffusion in this mixture dominates over the mass diffusion, adding a negative correction to the overall burning rate. In this case, the temperature is convected faster from the burning zone than the fuel molecules can diffuse into it.

### 3.1.2 Numerical setup

The CONVERGE CFD solver [17] is selected to perform simulations. It features a fully automatic generation of orthogonal structured grids, and the mesh-generation is done at run-time using a triangulated surface constructed from the burner geometry. Additionally, the solver features an adaptive mesh refinement algorithm, which enables the refinement of the grid dynamically in the region of interest.

The pressure-velocity coupling is achieved using a modified Pressure Implicit with Splitting of Operators (PISO) method [35]. All transported quantities are collocated at the center of cells, and the use of Rhie-Chow interpolation scheme [65] helps to eliminate undesirable checkerboarding effects. Conservation equations are solved using second-order accuracy in both space and time.

While the CFD solver solves the transport equations, the detailed chemical kinetics solver SAGE [71] is employed to calculate the reaction rates for each elementary reaction. The chemistry description is provided in the form of CHEMKIN-formatted input files.

To accelerate chemistry calculations, the adaptive zoning [7] available in CONVERGE was adopted in this work. According to this method, similar computational cells are grouped together, and the chemistry solver is then invoked once per group rather than once per cell. The zoning in our simulations is done based on the temperature and the fuel/air equivalence ratio in the cells, with bin sizes of  $5K$  and  $0.01$ , respectively.

The species diffusion coefficients are computed using constant non-unity Schmidt numbers with  $D_m = \mu/(\rho Sc_m)$ , where the species Schmidt numbers are pre-computed for the given conditions and provided as an input.

Regarding spray modeling, droplets are approximated as point sources, which are then treated in the Lagrangian framework (see Sec. 2.2). To reduce the computational effort, droplets are grouped into parcels. In that way, each parcel can be viewed as a group of droplets sharing the same characteristics so that the whole set of parcels statistically represents the entire spray field.

### 3.1.3 Simulation domain and settings

Laminar flame propagation in the presence of droplets is investigated for a fresh mixture at 300 K and 1 bar, wherein the overall fuel/air equivalence ratio  $\phi_o = 1$  is kept constant for all 1-D configurations. It is computed using  $\phi_o = s(\dot{m}_F^l + \dot{m}_F^g)/\dot{m}_{Ox}^g$ , where  $s$  is the mass stoichiometric ratio,  $\dot{m}$  is the mass flow-rate, subscripts  $F$  and  $Ox$  indicate the fuel and the oxidizer, and superscripts  $g$  and  $l$  are the gas and the liquid phase respectively. The gaseous fuel/air equivalence ratio in the fresh gases  $\phi_g = s \dot{m}_F^g/\dot{m}_{Ox}^g$  is also kept constant and contains 20% of the total injected fuel to ensure the simulation stability.

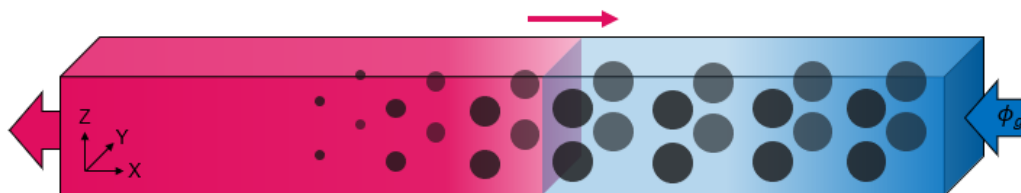


Figure 3-2: Simulation domain sketch. Laminar spray flame configuration.

The simulation domain is a long rectangular box with a square cross-section in  $YZ$ -plane and a flame propagating in  $X$ -direction and is shown in Fig. 3-2. The outlet with zero-gradient boundary conditions is located on the left and the inlet with Dirichlet boundary conditions on the right. All cells in the domain have the same aspect ratio.

In order to choose the reference cell size  $\Delta_x^{base}$ , a grid convergence test has been carried out for the thinnest flame computed in the present study, which is the purely gaseous flame at  $\phi = 1$ . In Fig. 3-3, the burning velocity of the gaseous n-heptane stoichiometric mixture is shown as a function of the flame resolution  $n_{res} = l_F/\Delta_x$ . The reference burning velocities are computed using the Cantera solver. A value of five for  $n_{res}$  is generally considered as a required minimum. However, in this particular setup, such a flame resolution leads to an oscillating laminar flame speed in time. These periodic oscillations disappear when we decrease the cell size.

For the non-thickened configuration, the selected reference cell size is equal to  $\Delta_x^{base} = 40\mu m$ . With these grid settings, the flame is resolved with  $n_{res} = 8.9$ , and the

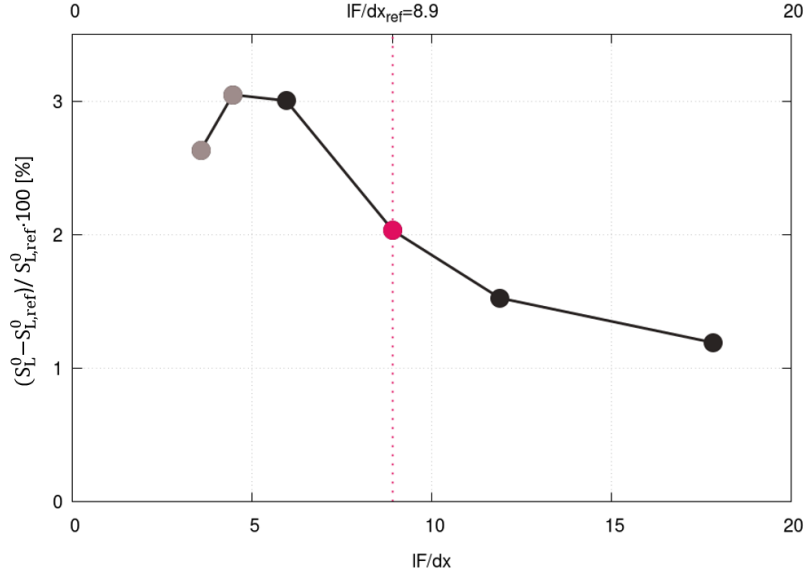


Figure 3-3: Laminar burning velocity as a function of flame resolution. ●: non-oscillatory solution; ●: oscillatory solution

burning velocity deviation from the reference Cantera solution is acceptable (around 2%). The mesh is kept constant when varying the droplet size.

N-heptane parcels are injected with the same velocity as the gaseous mixture. The parcel injection frequency is chosen so that at least five parcels are present within a reference cell. In reality, droplet evaporation also takes place in the unburned gases, in the so-called primary evaporation zone. The variation of droplets' diameter and the level of flame thickening would lead to a different flame position, which would affect the length of the primary evaporation zone and, therefore, the gaseous fuel mass fractions at the base of the flame, making the comparison impossible. To avoid this issue, we allow the droplets to evaporate only when they have reached the base of the flame, here defined as the condition  $T > T_u + 10 K$ .

In the following, the laminar flame speed is defined as the consumption flame speed, i.e., the speed at which the flame burns the reactants:

$$S_L^0 = \frac{-1}{\rho_u(Y_{F,u} - Y_{F,b})A} \int_V \dot{w}_F dV , \quad (3.1)$$

where  $A$  is the domain cross-section area and  $V$  is its total volume. The fuel reaction

Configuration	Mesh size	Model	Stat./Dyn.	$D_d$ [ $\mu m$ ]
Reference	$\Delta_x^{base}$	-	-	10 – 120
C5m0 / C20m0	$5\Delta_x^{base} / 20\Delta_x^{base}$	m0	F=5 / 20	10 – 90
C5m1 / C20m1	$5\Delta_x^{base} / 20\Delta_x^{base}$	m1	F=5 / 20	10 – 90
C5m2 / C20m2	$5\Delta_x^{base} / 20\Delta_x^{base}$	m2	F=5 / 20	10 – 90
D5m2	$5\Delta_x^{base}$	m2	$\hat{S}$	10 – 120
D20m2	$20\Delta_x^{base}$	m2	$\hat{S}$	10 – 120
D10AMRm2	$10\Delta_x^{base}$ $\Delta_x MIN = 5\Delta_x^{base}$	m2	$\hat{S}$	10 – 120
D40AMRm2	$40\Delta_x^{base}$ $\Delta_x MIN = 20\Delta_x^{base}$	m2	$\hat{S}$	10 – 120

Table 3.1: 1-D laminar spray flame configurations.

rate  $\dot{w}_F$  is integrated over the whole simulation domain. The mixture density  $\rho_u$  is the density of the fresh gaseous mixture, the fuel mass fraction  $Y_{F,u}$  corresponds to the amount of the injected fuel, and  $Y_{F,b}$  is the remaining fuel at the outlet, which is equal to zero in our cases.

Table 3.1 summarizes the parameters of all the presented laminar spray flame configurations. For each case, first letter C or D stands for Constant or Dynamic TFM model, the number that follows characterizes the mesh size, and finally, the employed model m0, m1 or m2 is specified.

### 3.1.4 Non-thickened spray flame

In the selected setup,  $\phi_o$  and  $\phi_g$  are fixed parameters, and the droplets are injected with the same velocity as the gas. Moreover, we allow the droplets to evaporate only when they reach the flame base. Thus, the fuel/air equivalence ratio within the flame front is controlled solely by the size of injected droplets. The effective fuel/air equivalence ratio  $\phi_{eff}$  decreases for larger droplets, while it attains the value of the pure gaseous flame at  $\phi = 1.0$  for smaller droplets with  $D_d = 10 \mu m$  (see Fig. 3-4c), since all the droplets evaporate before reaching the reaction zone (see Fig. 3-4b).

The profiles of non-thickened flames when varying the size of the injected droplets are demonstrated in Fig. 3-4. The resulting profiles and burning velocities are then considered as the reference solutions for the thickened flames discussed later (see Table 3.1). In order to simplify the comparison, the profiles are shifted, so that the origin is placed at the location of maximum heat release rate (see Fig. 3-4d).

In Fig. 3-4c we can observe a peak in the the fuel/air equivalence ratio where  $\phi_g$  raises from 1.0 up to 1.3 for the pure gaseous flame. This peak appears close to the maximum heat release rate location and is explained by the preferential diffusion of intermediate combustion products from the reaction zone. When the same case is computed with unity Lewis numbers, this local  $\phi_g$  increase is no longer seen without preferential diffusion.

In the cases where  $D_d > 10 \mu m$  the droplets continue to evaporate through the flame front (see Fig. 3-4b), where there is still enough oxidizer to complete combustion (see Fig. 3-4e), the resulting mixture burns at slower rates (see Fig. 3-4d).

For the purely gaseous flame and the  $10 \mu m$  spray flame, the maximum heat is released right after almost all fuel is consumed, resulting in a slight shift between the maximum fuel reaction rate and the location of the maximum heat release rate (the coordinate origin).

With the increasing droplet size, chemical reactions are activated at lower  $\phi_g$  triggering the start of the fuel consumption, the point where the fuel reaction rate starts to drop. Approaching the heat release rate peak, the net reaction rate of the fuel tends to zero in Fig. 3-4f, meaning that the fuel from the droplets that continue to evaporate does not accumulate but is immediately consumed.

As we mentioned, the mesh size is kept constant when varying the droplet size. Such settings lead to a better flame front resolution for larger droplets since these are characterized by larger flame thickness values. This can also be seen in the zoomed temperature profiles demonstrated in Fig. 3-4a.

In Fig. 3-5, the burning velocities are provided as a function of the droplet size, which varies from  $10 \mu m$  to  $90 \mu m$ . When looking at the reference non-thickened cases (black squares), a slowly burning lean flame is observed for the larger droplets. Con-

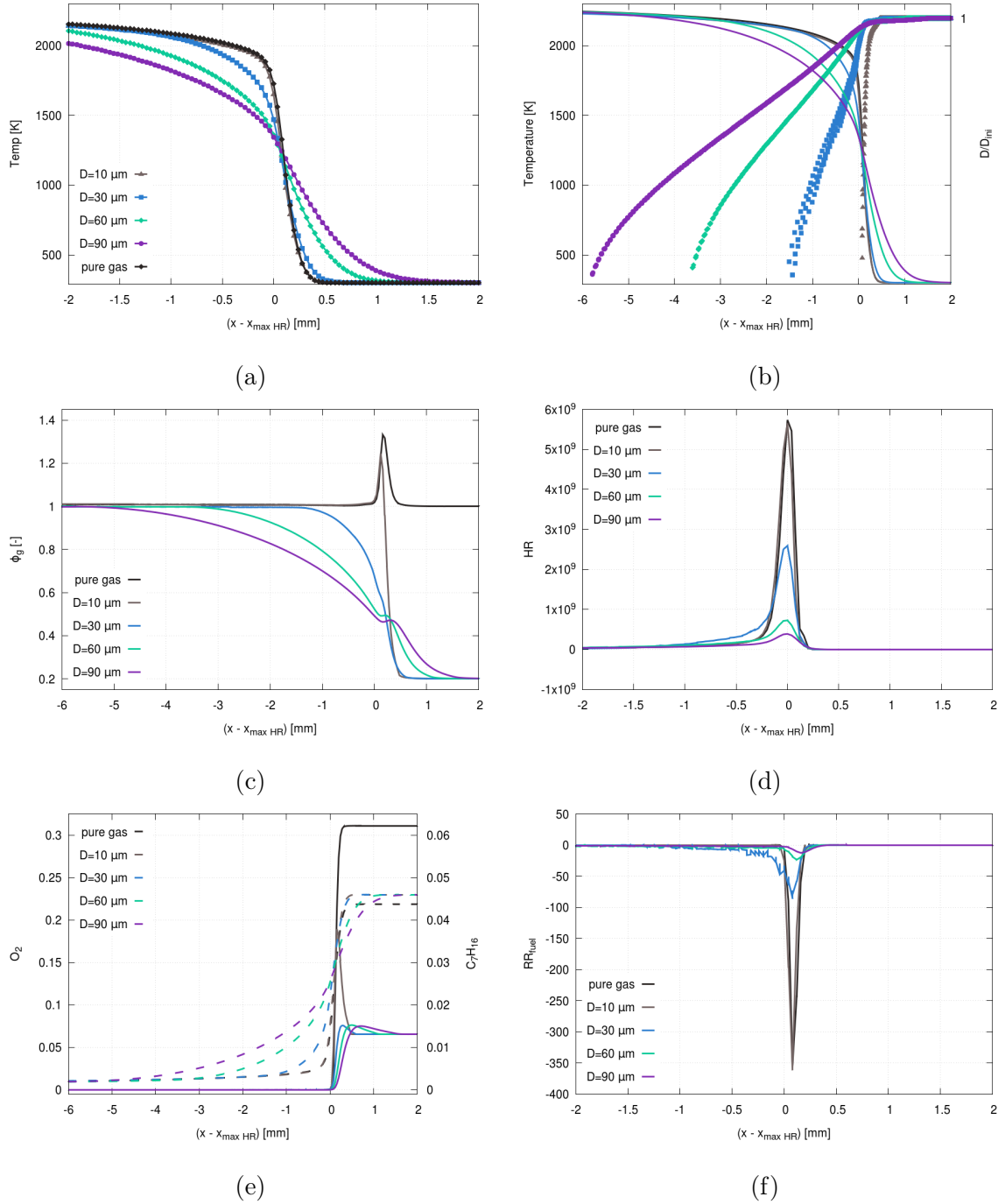


Figure 3-4: 1-D spray flame profiles. Reference solution.  $F = 1$ ,  $D_d = 10 - 90 \mu\text{m}$ . (a): gaseous temperature; (b): gaseous temperature vs normalized droplet diameter; (c): gaseous fuel/air equivalence ratio; (d): heat release rate; (e): Species mass fractions. Solid line:  $n\text{C}_7\text{H}_{16}$  Dashed line:  $\text{O}_2$ ; (f): fuel reaction rate

versely, in the case of  $10 \mu\text{m}$  droplets, almost all the fuel evaporates before reaching the reaction zone, leading to a flame structure close to the purely gaseous stoichio-

metric flame and slightly lower burning velocities due to the evaporative cooling.

### 3.1.5 Constant spray flame thickening

Thickened laminar spray flames are studied first by considering a constant flame thickening, i.e.,  $F(x) = F$ . These simulations are carried out to validate the re-scaling of the Lagrangian equations by the thickening factor.

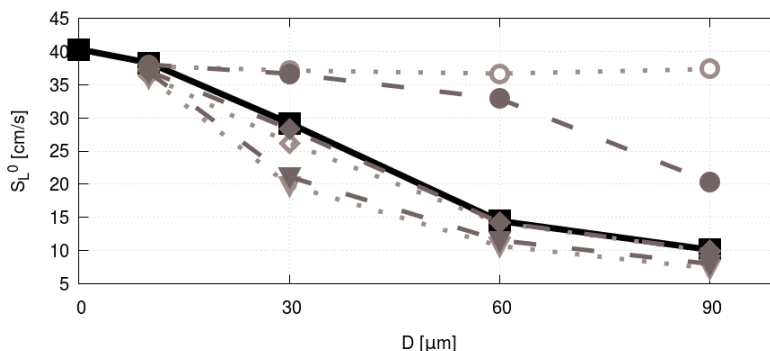


Figure 3-5: The effect of Lagrangian corrections on the spray flame burning velocity. ■: Reference, ●: C5m0, ▼: C5m1, ◆: C5m2, ○: C20m0, ▽: C5m1, ◇: C20m2.

In order to assess the effect of the Lagrangian equations correction for thickened flames, the simulations were performed with constant thickening factor  $F$ , whereas the cell size was increased by a factor  $F$ , such that  $\Delta_x = F\Delta_x^{base}$ . Two different values of  $F$  have been investigated: a thickening factor representative of academic burner configurations ( $F = 5$ ) and a thickening factor more relevant to industrial applications ( $F = 20$ ). Details are provided in Table 3.1.

As shown in Fig. 3-5 for cases C5m0 and C20m0, without any corrections to the Lagrangian equations the difference in laminar flame speed with the non-thickened reference solution exceeds 100% for the droplet diameters larger than  $30 \mu m$  for both thickening factors. The over-estimation of flame speeds is due to excessive droplet evaporation, which leads to mixtures closer to stoichiometry, and is especially pronounced for large thickening factors (see configuration C20m0 in Fig. 3-5).

For configurations C5m2 and C20m2, which includes the whole set of corrections introduced in Sec. 2.3.4, a perfect agreement is obtained for the flame speed prediction at any droplet size (see Fig. 3-5).

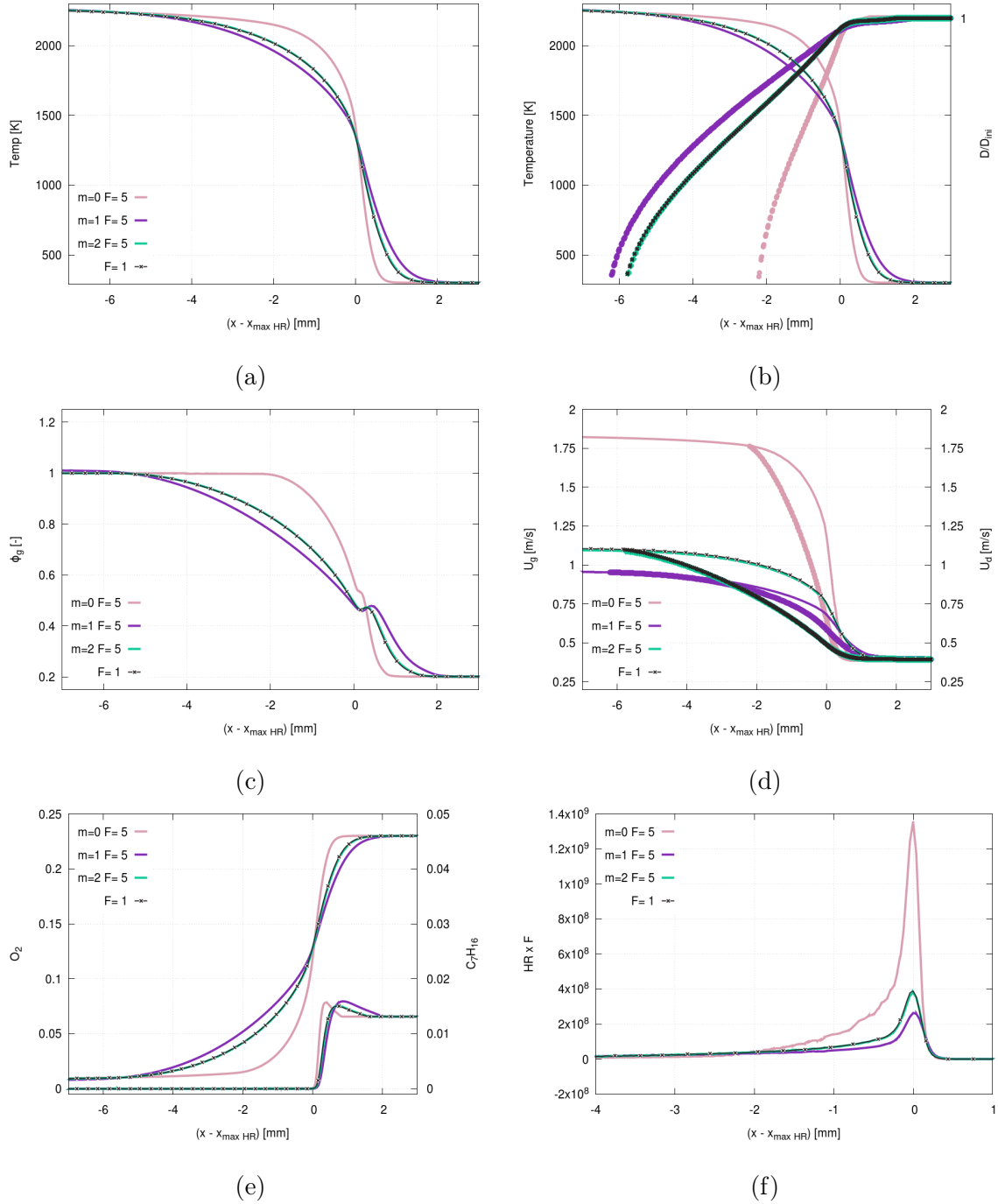


Figure 3-6: 1-D spray flame profiles. Constant thickening  $F = 5$  with fixed droplet size  $D_d = 90 \mu m$  for different correction strategies of spray equations: -x-: reference, —: m0, —: m1, —: m2. (a): gaseous temperature; (b): gaseous temperature vs normalized droplet diameter; (c): gaseous fuel/air equivalence ratio; (d): gaseous and spray velocities; (e): Species mass fractions. Solid line:  $nC_7H_{16}$  Dashed line:  $O_2$ ; (f): heat release rate

To demonstrate the effect of constant thickening on the flame profiles, we have selected the case with the largest droplets  $D_d = 90 \mu m$ , since the presence of the

spray is more pronounced here compared to cases with smaller spray diameter sizes. To allow the comparison with the non-thickened reference solution, the thickened flame profiles and the positions of spray particles in Fig. 3-6 are scaled spatially with respect to the local thickening factor, which is  $F(x) = 5$  for all thickened cases presented on this plot. For the same reason, the heat release rate is also multiplied by the thickening factor  $F$  in Fig. 3-6f.

As was mentioned, without any corrections applied to the spray equations (model  $m0$ ), the droplets in the thickened regions evaporate too fast. This can be seen in Fig. 3-6b. Therefore, the resulting gaseous fuel/air equivalence ratios are significantly higher compared to the ones observed in the reference case (see Fig. 3-6c). For that reason, the heat release rate (Fig. 3-6f) and finally the flame speed (Fig. 3-5), are not recovered correctly.

Compared to the setups C5m2 and C20m2 with the whole set of corrections, in C5m1 and C20m1 performed with model  $m1$ , we do not correct the droplet drag force. In this case, the droplets crossing the flame relax faster towards the gaseous velocity, which significantly increases from fresh to burned gases. This can be seen when looking at the gaseous and spray velocity profiles in Fig. 3-6d. As a result, the relative velocity between the gas and the droplets is under-estimated. This leads in turn to the under-estimation of the evaporation rate, which can be deduced from the longer droplet lifetime in Fig. 3-6b. The mixture is then leaner (see  $\phi_g$  Fig. 3-6c) and the flame speed is lower (see Fig. 3-5).

### 3.1.6 Dynamic spray flame thickening

In the LES simulation discussed in Sec. 4.3, the flame front is detected with a flame sensor defined in Eq.(2.11) and is refined using AMR. In order to validate the dynamic TFM-AMR approach for two-phase flows and ensure a correct prediction of the flame propagation, mono-dimensional cases are simulated first.

In order to assess the dynamic thickening procedure independently from AMR, the 1D flames presented in Sec. 3.1.5 are computed first without using AMR. In all configurations with dynamic thickening, the desired flame resolution  $n_{res}$  is set to 9,

and only the model  $m2$  is considered, as it led to the best results in cases with a constant thickening.

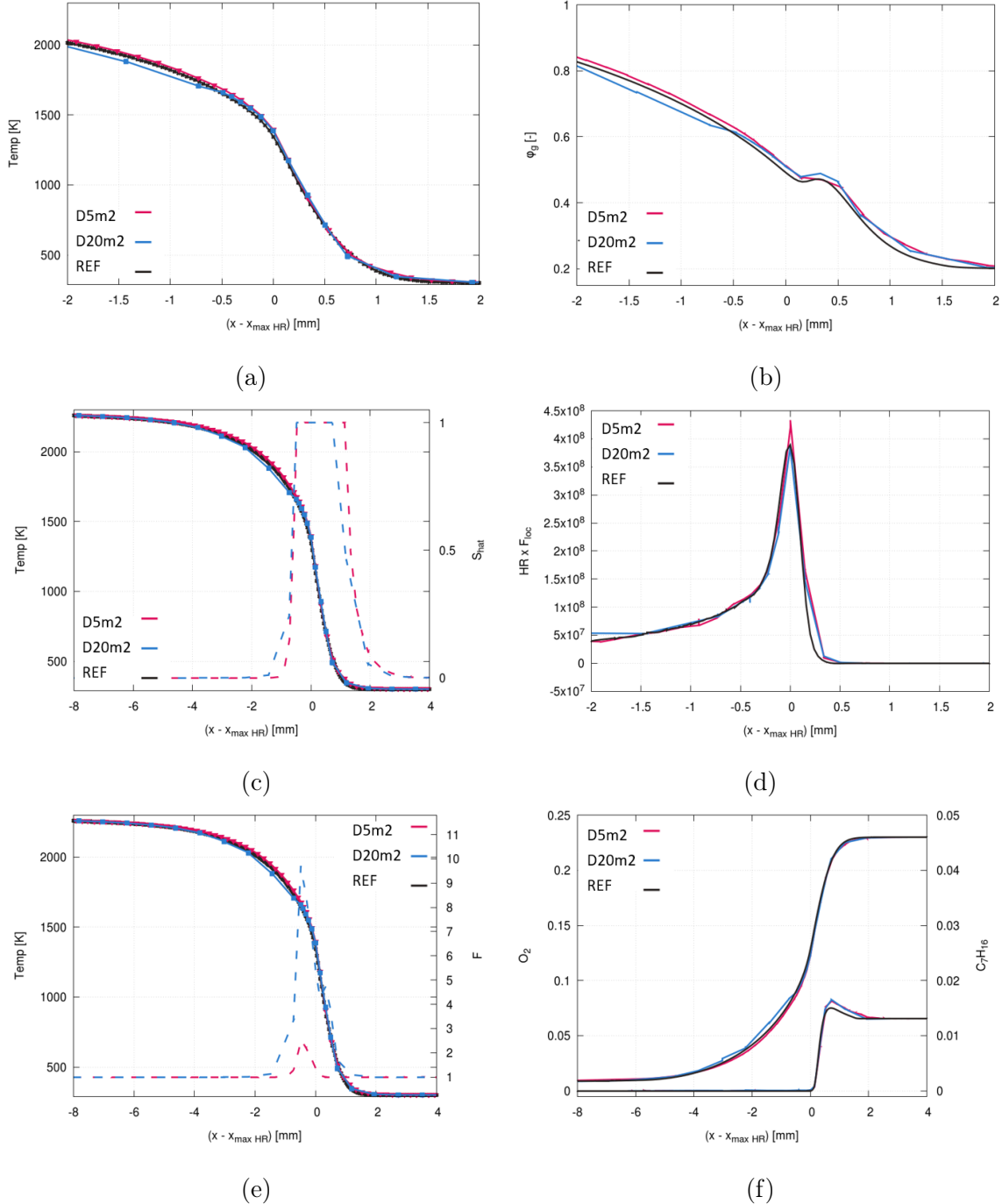


Figure 3-7: 1-D spray flame profiles. Dynamic thickening  $F = F(\phi)$  with fixed droplet size  $D_d = 90 \mu\text{m}$  for different grid settings. —: reference, —: D5m2, —: D20m2. (a): gaseous temperature; (b): gaseous fuel/air equivalence ratio; (c): Solid line: gaseous temperature, Dashed line: sensor  $\hat{S}$ ; (d): heat release rate; (e): Solid line: gaseous temperature, Dashed line: thickening factor  $F$ ; (f): Species mass fractions. Bottom:  $nC_7H_{16}$  Top:  $O_2$

In cases D5m2 and D20m2 we use different meshes with cell sizes equal to  $\Delta_x = 5\Delta_x^{base}$  and  $\Delta_x = 20\Delta_x^{base}$ , respectively. The resulting flame profiles are shown for the droplets with  $D_d = 90 \mu m$  in Fig. 3-7. All profiles are scaled with respect to the local thickening factor values  $F = F(\phi)$ .

The flame sensor detects the flame front based on the local heat release rate as described in Section 2.3.1, the region corresponding to the steepest temperature gradients, see Fig. 3-7c. Then, the thickening factor  $F$  is computed based on the local fuel/air equivalence ratio, as explained in Section 2.3. As we can see in Fig. 3-7e, the region detected by the sensor is broader than the region where the thickening is applied. This can be explained by the fact that the mixture is very lean at the base of the flame, even below the flammability limit (see  $\phi_g$  in Fig. 3-7b). The tabulated values indicate a thick flame or an infinite thickness when approaching the flammability limit. The infinite thickness is an arbitrary choice made for the cases when we reach the end of the table. Therefore,  $F$  remains equal to one at these locations.

Note that with increasing cell size, the thickened flame thickness increases as  $F$  increases. Since the mesh in D20m2 is four times coarser than in D5m2, the maximum thickening factor in case D20m2 is approximately four times higher as well, see Fig. 3-7e.

Good overall agreement with the reference solution is found for the flame profiles obtained with dynamic TFM.

Next, two configurations D10AMRm2 and D40AMRm2, are performed on grids two-times coarser than in D5m2 and D20m2, and with one additional level of AMR applied in the flame reaction zone. As a consequence, the thickening factor will be the same as in D5m2 and D20m2 (see Table 3.1). The corresponding profiles can be seen in Fig. 3-8 for droplets with  $D_d = 90 \mu m$ .

To increase the simulation stability and obtain non-oscillatory flame speed, which is computed based on the integrated fuel reaction rate, see Eq.(3.1), the sensor is extended towards the burned side by setting larger  $\alpha_{hot}$  values. With this, the sensor coverage becomes larger in the high-temperature regions characterized by a larger

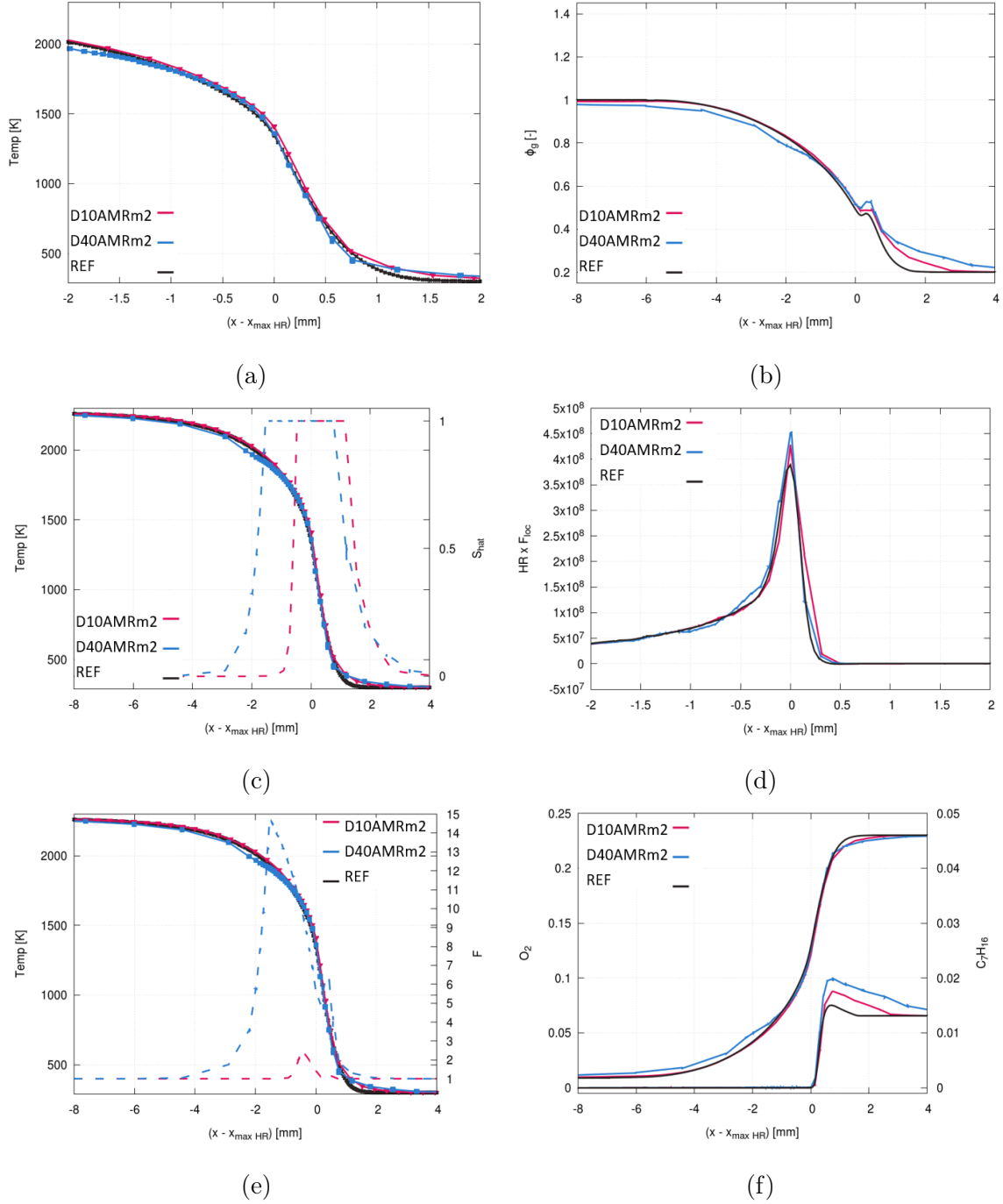


Figure 3-8: 1-D spray flame profiles. Dynamic thickening  $F = F(\phi)$  with AMR and fixed droplet size  $D_d = 90 \mu\text{m}$  for different grid settings. —: reference, —: D10AMRm2, —: D40AMRm2. (a): gaseous temperature; (b): gaseous fuel/air equivalence ratio; (c): Solid line: gaseous temperature, Dashed line: sensor  $\hat{S}$ ; (d): heat release rate; (e): Solid line: gaseous temperature, Dashed line: thickening factor  $F$ ; (f): Species mass fractions. Bottom:  $n\text{C}_7\text{H}_{16}$  Top:  $\text{O}_2$

amount of evaporated fuel and thus higher values of  $\phi_g$ . Since the flame thickness in the lookup tables is a function of gaseous fuel/air equivalence ratio  $\delta_L^0(\phi)$ , and while

it decreases as  $\phi_g$  grows, the resulting thickening factor values in Fig. 3-8e are slightly larger compared to the cases D5m2 and D20m2 in Fig. 3-7e.

Towards the unburned gases, low  $\phi_g$  values lead to large flame thickness estimation based on tabulated  $\delta_L^0(\phi)$ . In this situation, the thickening factor approaches unity, leading to an under-resolution in this region. Therefore, we can observe a slight discrepancy for  $\phi_g$  and  $Y_F$  profiles on the fresh side in Figures 3-7b and 3-7f.

Overall good agreement is found between the reference solution and the flame profiles obtained with TFM-AMR. The over-estimation of the fuel mass fraction at the flame base in both Fig. 3-7f and Fig. 3-8f can be explained by the condition on droplet evaporation, which is allowed when  $T > T_u + 10 \text{ K}$ . Thus, the position where this condition is fulfilled depends on the temperature resolution and affects the amount of fuel vapor present in the cell. This, however, has little effect on the global flame characteristics in the current setup.

The resulting flame speeds for all configurations with dynamic TFM / TFM-AMR are shown in Figure 3-9, and are found to be in very good agreement with the non-thickened spray flame values, demonstrating the correct flame detection by the sensor.

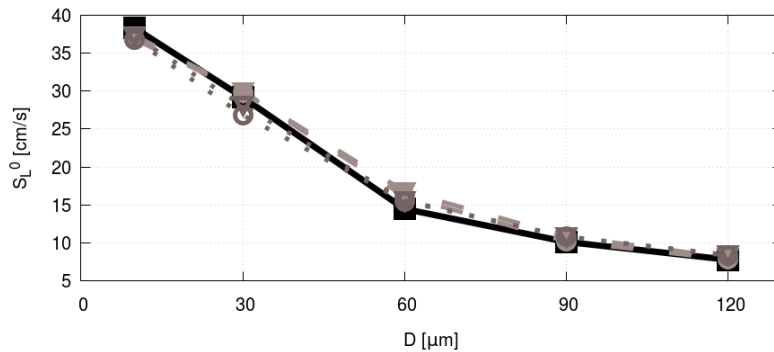


Figure 3-9: Dynamically thickened spray flame burning velocity. ■: Reference, ▽: D5m2, ●: D20m2, ▽: D10AMRm2, ○: D40AMRm2.

The great performance of dynamic flame detection coupled to AMR justifies the use of this modeling approach in 3-D simulations. This will be demonstrated in Chapters 4 and 5.

## 3.2 Low-volatile fuel (N-Dodecane flames)

Jet A-1 fuel is considered to be a standard fuel in the aviation industry. Therefore it is used as a reference fuel in a gas turbine model combustor investigated later in Chapter 5 of this work. Additionally, the experimental measurements of the dispersed and the mean phases show that kerosene flames are similar to flames operated with n-dodecane [1]. N-dodecane is, therefore, selected in this study to reduce the modeling complexity associated with multi-component fuel use.

N-dodecane belongs to a group of low-volatile fuels and is characterized by lower evaporation rates when compared to n-heptane used in Sec. 3.1. Therefore, in the cases with a low fuel pre-evaporation and large droplet diameters, we might face difficulties related to the use of tabulated properties that rely on the gaseous fuel/air equivalence ratio.

In this section, we will explore the characteristics of two-phase flames in the conditions of interest. In particular, we will investigate a mismatch between tabulated properties and actual spray flames. This analysis will help us to correctly set up the TFM model for the gas turbine model combustor studied in Chapter. 5.

In gas turbine combustors, flames are often stabilized by a swirling flow, which leads to the recirculation of burned gases in the flame region. For this reason, we will assess in Sec. 3.2.3 to which extent a dilution with burned products might affect a spray flame.

### 3.2.1 Chemistry modelling

For the n-dodecane flame simulations, we will use a reduced mechanism which includes 43 species and 235 reactions to reduce the computational effort.

Similarly to the n-heptane reduced mechanism described in Sec. 3.2.1, the n-dodecane reduced mechanism was obtained from a skeletal 180-species chemical kinetic mechanism [52] using CONVERGE reduction tool, which is based on a directed relation graph with error propagation and sensitivity analysis (DRGEPSA) [63].

To reduce the original mechanism, the operating conditions of the gas turbine

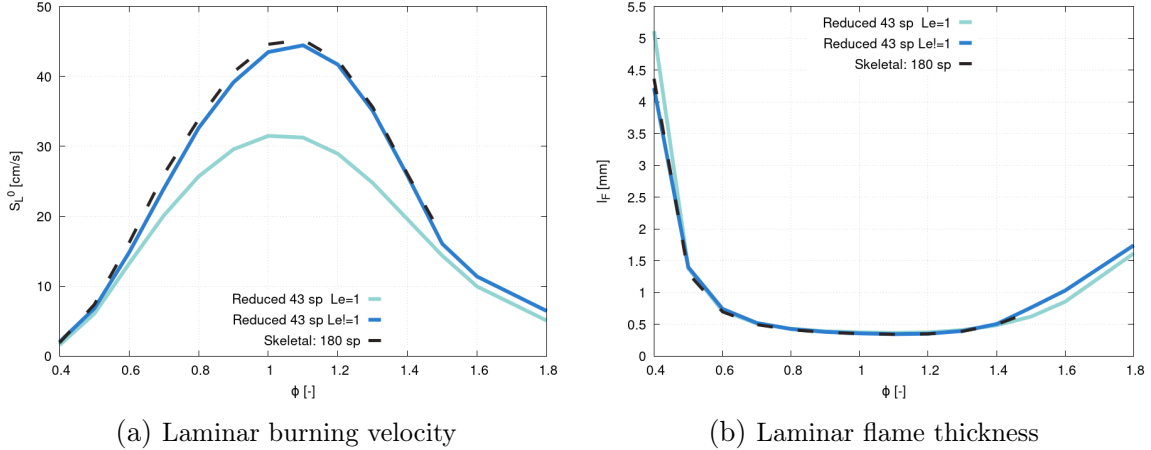


Figure 3-10: Flame properties at  $T = 323K$ ,  $p = 1bar$  as a function of fuel-equivalence-ratio. Solid lines: 43-species reduced mechanism. Dashed line: skeletal 180-species mechanism.

model combustor were selected as a target and correspond to  $T = 323K$  and  $p = 1bar$ .

In terms of laminar flame speed and flame thickness, the reduced mechanism agrees very well with the original skeletal mechanism over a wide range of fuel/air equivalence ratios, as it can be seen in Fig.3-10.

For lean mixtures of heavy fuels like n-dodecane, the effective Lewis number is greater than unity, and for the stoichiometric mixture it is  $Le_{eff} = (Le_{O_2} + Le_{nC_{12}H_{26}})/2 = 1.64$ .  $Le_{eff}$  indicates that the thermal diffusion in this mixture dominates over the mass diffusion in n-dodecane flames. The effect of preferential diffusion has a strong impact on the burning velocities, see Fig. 3-10a blue solid line versus light blue computed with unity Lewis assumption. Hence, the preferential diffusion is considered in computations by setting Lewis numbers constant but not equal to unity.

### 3.2.2 Simulation domain and settings

In the following, we will investigate the laminar flame propagating in an n-dodecane spray mist at  $T = 323K$ ,  $p = 1bar$  and  $\phi_o = 0.8$ , which corresponds to the reference operating conditions of the gas turbine model combustor investigated in [1].

To compute one-dimensional n-dodecane spray flames, we will use the same numerical setup as for n-heptane 1D flames detailed in Sec. 3.1.2. The simulation domain and the fuel injection strategy are adapted from 1D n-heptane flames, which

are detailed in Sec. 3.1.3.

As we saw in Sec. 3.1.6, spray flame thickening, especially when thickening factors are high, can lead to an under-resolution of the flame on the fresh gas side, where  $\phi_g$  is low. Therefore, the most challenging case from the perspective of combustion modeling corresponds to the one with low content of gaseous fuel on the fresh side. It becomes especially true when considering low-volatile fuels such as dodecane, which evaporate slowly. Thus, it is interesting to investigate such cases by setting  $\phi_g$  to zero at the inlet, meaning that we inject pure air, and all the fuel will come from the evaporated spray.

### 3.2.3 Non-thickened spray flame

#### Effect of droplet size on the flame structure

N-dodecane flames are computed first without any thickening for droplet diameters ranging from 0  $\mu m$  (purely gaseous case  $\phi_g = 0.8$ ) to 40  $\mu m$ , which corresponds to the characteristic droplet size observed in the gas turbine model combustor configuration (see Chap. 5). During the cell size variation, the cell size is kept constant.

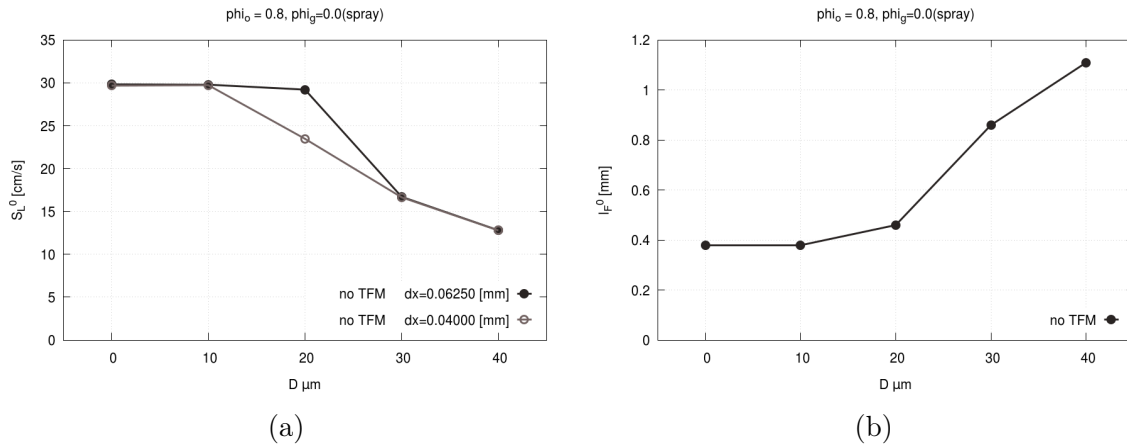


Figure 3-11: 1-D n-dodecane spray flame properties. No thickening. (a): Flame speed; (b): Flame thickness

Burning velocities are computed using Eq.(3.1) and shown in Fig. 3-11a for  $\Delta x = 0.0625mm$  and  $\Delta x = 0.04mm$ . The mesh size was continuously reduced until no change was seen in the computed  $S_L^0$ . Whereas  $\Delta x = 0.0625mm$  is sufficient to resolve

most of the flames and corresponds to  $n_{res} = 6$  within the thinnest flame, the  $20 \mu m$  spray flame required  $n_{res}$  of 11. Cutting the cell size up below  $40 \mu m$  did not modify further the resulting burning velocity for  $20 \mu m$  spray flame.

Flame thicknesses in Fig. 3-11b are estimated from the gradient of the progress variable  $C$  as:  $l_F = 1/|\nabla C|_{max}$ . Here, the progress variable is computed based on the mass-fractions of a carbon monoxide and carbon dioxide as  $C = (Y_{CO} + Y_{CO2})/(Y_{CO} + Y_{CO2})|_{max}$ .

In Fig. 3-11 we can observe that for small droplet sizes  $D = 10 \mu m$ , burning velocities, as well as flame thicknesses remain very similar to that of the purely gaseous flame. However, when the spray size reaches  $40 \mu m$ , the burning velocity drops by a factor of two, and the flame becomes almost three times thicker.

The instantaneous non-thickened flame profiles in Fig. 3-12 and Fig. 3-13 are presented with an abscissa offset such that the maximum heat release rate is located at  $x = 0$ , as can be observed on heat release profiles in Fig. 3-12e. Different colors indicate different spray diameters on these plots. In particular, black color represents the purely gaseous flame.

When plotting temperature profiles (see Fig. 3-12a) over the spatial coordinate we can clearly observe how they broaden for droplet diameters larger than  $20 \mu m$ , while the profiles remain almost identical to the gaseous flame for spray sizes below  $20 \mu m$ . The same tendency can be observed for the progress variable profiles shown in Fig. 3-12c.

Such similarities in temperature and progress variable profiles of spray flames with droplet sizes below  $20 \mu m$  with the gaseous flame are consistent with the resulting similar values for burning velocities and flame thicknesses we have seen in Fig. 3-11.

Especially for smaller droplets, we can recognize a major difference between gaseous and spray flames on the plots of gaseous fuel/air equivalence ratio (Fig. 3-12d) and a fuel mass-fraction (Fig. 3-13b).

In the spray flame with  $10 \mu m$  sized droplets (green lines), all the fuel is evaporated before reaching the maximum heat release rate point (see the droplet size evolution in Fig. 3-12b). Then, all profiles merge with the ones of the gaseous flame. For spray

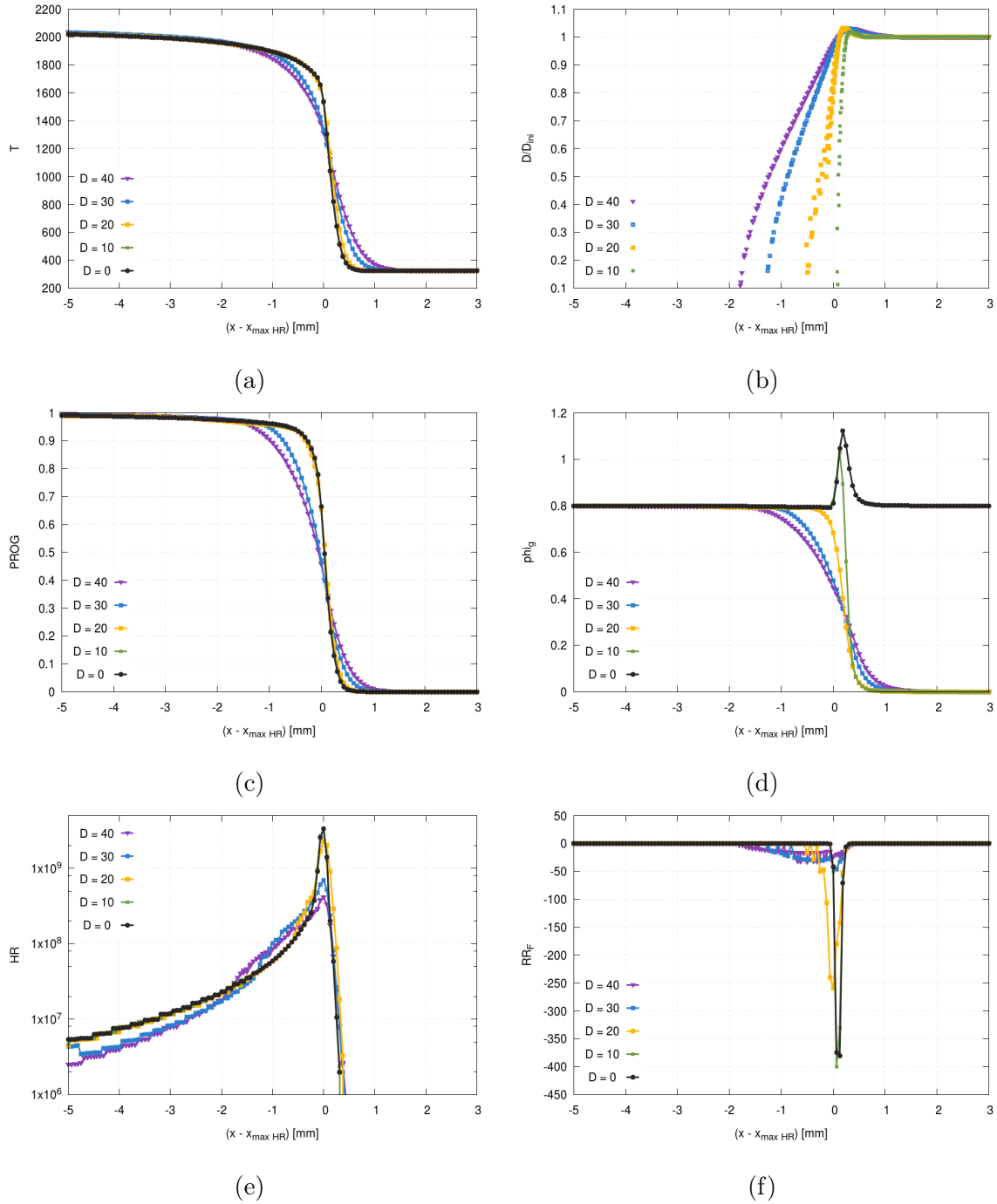


Figure 3-12: 1-D n-dodecane spray flame profiles. Reference solution.  $F = 1$ ,  $D_d = 0 - 40 \mu m$ . (a): gaseous temperature; (b): normalized droplet diameter; (f): progress variable; (d): gaseous fuel/air equivalence ratio; (e): heat release rate; (f): fuel reaction rate

flames with droplet sizes larger than  $10 \mu m$ , the evaporated fuel is directly consumed after its production, as can be observed in Fig. 3-13b.

In the cases with  $D > 20 \mu m$ , the gaseous fuel/air equivalence ratio (Fig. 3-12d)

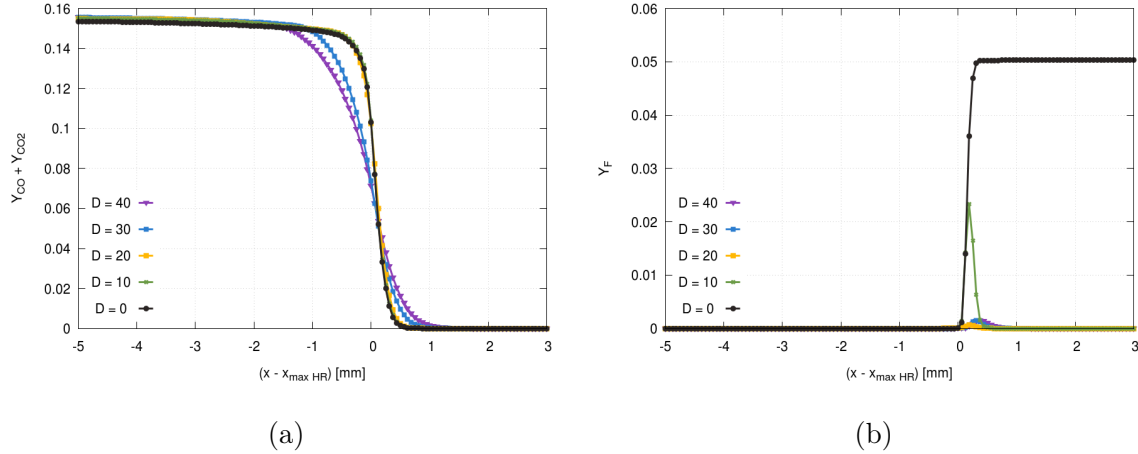


Figure 3-13: 1-D n-dodecane spray flame profiles. Reference solution.  $F = 1$ ,  $D_d = 0 - 40 \mu\text{m}$ . (a): Sum of  $CO$  and  $CO_2$  mass fractions; (b): Fuel mass fraction

only reaches a value of around 0.4 at the heat release rate peak and continues to increase further downstream. As a consequence, the maximum heat release rate in such flames is almost one order of magnitude lower than the one of the gaseous flame (see Fig. 3-12e). Compared to the purely gaseous configuration, the presence of droplets also extends the region with high heat release rates on the burned side.

### Effect of dilution on the flame structure

A reactant's dilution with burned products can take place in recirculating regions of gas turbine combustors. It is, for instance, the case in the gas turbine model combustor investigated in Chapter 5. Therefore, we will assess in this section to which extent a dilution might affect a spray flame.

In Fig. 3-14 the flame profiles are given for  $40\mu\text{m}$  n-dodecane spray flames at four different dilution ratios  $X_{dil}$  corresponding to 0, 5, 15 and 20 percent of dilution. In particular, zero dilution level indicates the reference case without dilution, which was discussed above in the context of droplet size variation. Unlike the cases without dilution where pure air is injected at the inlet, the air is mixed here with burned products.

The temperature and mixture composition were adjusted at the inlet to match the dilution ratio  $X_{dil}$ , such that  $T_{inlet} = (1 - X_{dil})T_u + X_{dil}T_b$  and  $Y_{m,inlet} = (1 - X_{dil})Y_{m,air} +$

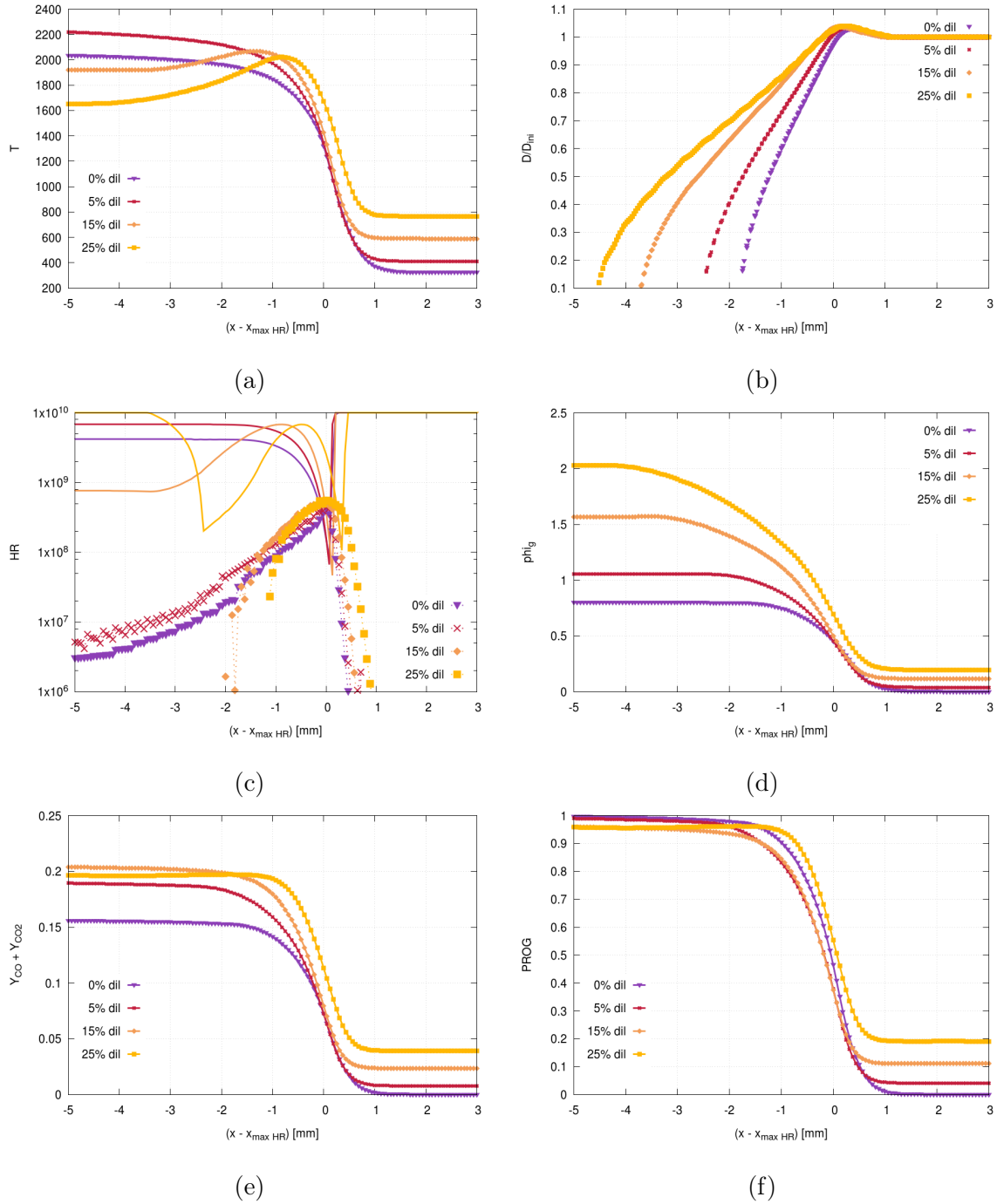


Figure 3-14: Dilution fraction: 1-D n-dodecane spray flame profiles,  $D_d = 40 \mu m$ , no thickening. (a): gaseous temperature; (b): normalized droplet diameter; (c): heat release rate: instantaneous - dots, tabulated - solid lines; (d): gaseous fuel/air equivalence ratio; (e): Sum of  $CO$  and  $CO_2$  mass fractions; (f): progress variable.

$X_{dil}Y_{m,b}$ . Sub-scripts  $u$  and  $b$  indicate the temperature and the species mass fractions of a gaseous flame at  $\phi_g = 0.8$  at the unburned and the burned sides respectively.

As done for previous flames, the temperature threshold above which the droplets are allowed to evaporate is adjusted to be  $10K$  above  $T_{inlet}$ . Similarly to the flames without dilution, it is done to avoid spray evaporation upstream of the flame-front to facilitate the comparison between the cases. The liquid fuel mass flow rate is kept unchanged for all computations and corresponds to the undiluted reference case.

As a consequence of the described dilution procedure, the temperature of the reactants rises as  $X_{dil}$  increases, as seen in the right part of Fig. 3-14a. The gaseous fuel/air equivalence ratio is computed based on an atomic balance, and as a result, it also becomes higher on the fresh side and the burned of the diluted flames ( see Fig. 3-14d ).

We can notice in Fig. 3-14b that the lifespan of the droplets within the flame increases with the dilution level. This can be explained by the different mixture composition and the temperature drop after the flame front induced by the endothermic pyrolysis reactions.

The diluted flames can be generally characterized by higher burning velocities and less steep progress variable profiles ( Fig. 3-14f ) leading to twenty percent larger flame thickness compared to the undiluted flame.

Despite all the differences listed above, the peak heat release rate remains mainly unchanged for all dilution levels. The instantaneous heat release rate is given in Fig. 3-14c by the lines with dots, whereas the corresponding tabulated heat release rates  $\omega_{T1D}^{max}(\phi)$  is plotted with solid lines. Here, the tabulated values of  $10^{10}$  tell us that we have reached the table limits. When the thickening is done using the Jaravel sensor formulation, these tabulated values are compared to the instantaneous ones in Eq.(2.11). We detect the flame if the local heat release rate is close to the tabulated maximum heat release rate. Usually, the region seen by the sensor does not include the entire chemically active area, but only a very limited region around the heat release rate peak, even in the flames without dilution. Significant dilution levels also enhance the discrepancy with tables in the vicinity of the maximum heat release, as it can be seen in Fig. 3-14c. Therefore, we might need to increase the sensor sensitivity to detect the diluted flames correctly.

Figure 3-14c also illustrates that the difference between the tabulated and instantaneous values might be one order of magnitude below  $\omega_T^{max}$ . The sensor might have difficulties identifying the entire flame region in such conditions. However, it might not be a problem when the tail of the flame is not thickened since the progress variable is above 0.9 and the gradients are much lower than in the main reaction zone.

Although tabulating laminar two-phase flames and diluted flames would improve the match with tabulated values, it would require additional computational expenses and significantly increase the tables' complexity. Since no simple better solution was found, the tabulated values of premixed flames will be used in the computations presented below in this chapter and in Chapters 4 and 5. This is also the reason why the new modeling approach presented in Chapter 6 has its goal to suppress the use of tabulated properties of premixed flames.

### 3.2.4 Dynamic spray flame thickening

To analyze how the thickening procedure affects the spray-flame configuration presented in Sec. 3.2.2 we will use a mesh with a cell size of  $\Delta_x = 0.5mm$ , which is at least eight times larger than the mesh used to computed non-thickened flames in Sec. 3.2.3. Furthermore, we will use one additional level of AMR, so that the resolution within the flame-front reaches  $\Delta_{x,AMR} = 0.25mm$ . In the following we will target a flame resolution of nine points per flame thickness. These meshing settings were selected to resemble the ones adopted in the gas turbine model combustor in Chapter 5.

To allow a fair comparison between the profiles of thickened flames and a reference non-thickened solution, the coordinates are divided by the thickening factor  $F$ , and the source terms are multiplied by  $F$ , unless stated otherwise. Similar to the previous plots, the maximum heat release rate is located at  $x=0$ .

#### Flame sensor parameters

The flame sensor parameters involved in Eq.(2.11) include the sensor sensitivity  $\beta$  and the relaxation time coefficients on both flame sides. In the following, we will compare

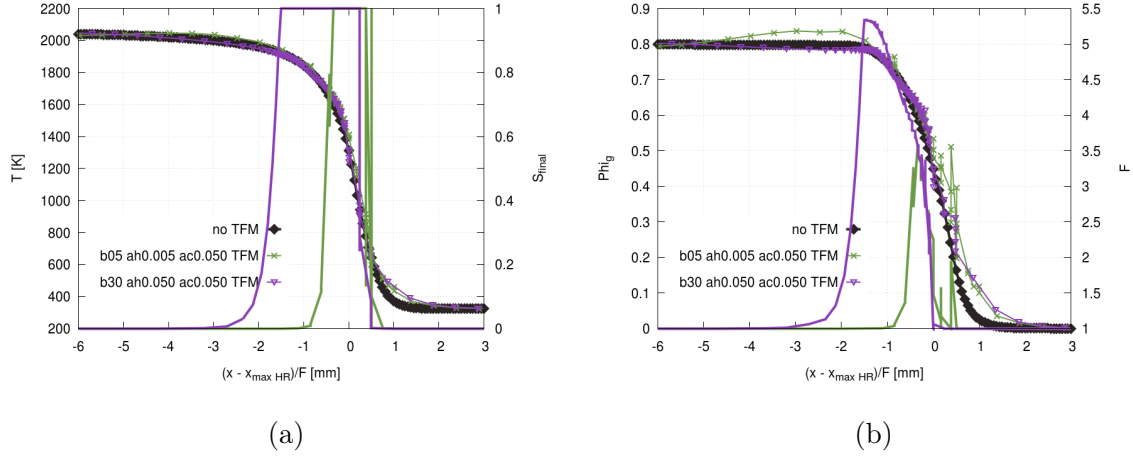


Figure 3-15: 1-D n-dodecane spray flame profiles for different Jaravel sensor parameters,  $D_d = 40 \mu m$ , TFM-AMR  $\Delta_x = 0.5 mm$ . (a): gaseous temperature (line-points), Final flame sensor  $\hat{S}$  (solid line); (b): gaseous fuel/air equivalence ratio, Thickening factor  $F$  (solid line).

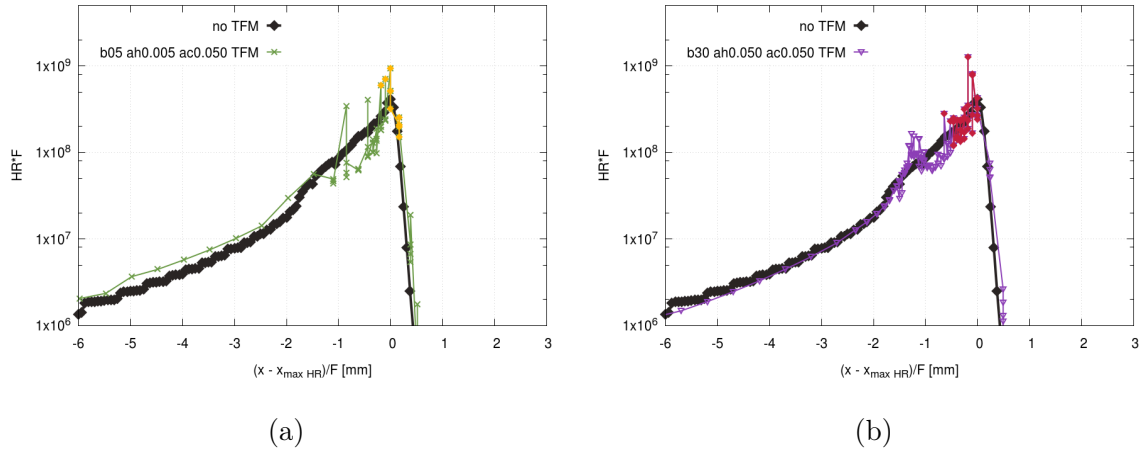


Figure 3-16: 1-D n-dodecane spray flame profiles for different Jaravel sensor parameters,  $D_d = 40 \mu m$ , TFM-AMR  $\Delta_x = 0.5 mm$ . Instantaneous heat release rate profiles scaled with  $F$ . (a):  $\beta = 5$ ,  $\alpha_{cold} = 0.05$ ,  $\alpha_{hot} = 0.005$  ( $S > 0.9$  in yellow); (b):  $\beta = 30$ ,  $\alpha_{cold} = 0.05$ ,  $\alpha_{hot} = 0.05$  ( $S > 0.9$  in red).

two different parameter setups: a standard and an extended one. The standard sensor parameters are set to  $\beta = 5$ ,  $\alpha_{cold} = 0.05$ ,  $\alpha_{hot} = 0.005$ , while the extended sensor will be defined with  $\beta = 30$ ,  $\alpha_{cold} = 0.05$ ,  $\alpha_{hot} = 0.05$ .

Thickened spray flame profiles obtained for  $D = 40 \mu m$  are compared against the reference non-thickened solution in Figures 3-15 and 3-16, where the reference solution is shown in black. The reference solution was discussed in Sec. 3.2.3 and is plotted in Figures 3-12 and 3-13. The reference solution also corresponds to the case with zero dilution shown in Fig. 3-14.

When looking at the temperature profiles in Fig. 3-15a with superimposed flame sensor profiles (solid lines), we can notice that the region identified by the sensor with standard parameters (in green) only partially covers the flame front. At the same time, the extended sensor (in purple) encompasses well the flame tail on the burned side. The additional simulation performed with the standard sensor sensitivity and 10 times larger  $\alpha_{hot}$  ( $\beta = 5$ ,  $\alpha_{cold} = 0.05$ ,  $\alpha_{hot} = 0.05$ ) did not enlarge the sensor active region and is not plotted in the figures above. Therefore, in the case of the extended sensor, the larger spreading of the sensor is mainly due to the multiplication by a factor 6 of the sensitivity  $\beta$ .

The instantaneous heat release obtained with the standard sensor parameters is shown on the left of Fig. 3-16, while the heat release obtained with the extended sensor parameters is given on the right. The highlighted regions on the instantaneous heat release rate plots correspond to the heat release rate detected by the flame sensor where  $S > 0.9$ . The increased sensor sensitivity enlarges this region allowing better spreading of the final sensor  $\hat{S}$ , as shown in Fig. 3-16b. Therefore, a solution to tackle the large differences between the instantaneous heat release rate and the tabulated heat release rate is to increase the sensor sensitivity.

The model is designed so that the final sensor relaxes very fast towards zero outside the table limit by (below  $\phi_g = 0.4$ ). Therefore, the sensor (given with solid lines in Fig. 3-15a) struggles to cover the base of the flame despite different sensor parameters. The sensor could be extended by extrapolating the tabulated values on the lean side. In this particular case, however, it would not enlarge the thickening at the base because the flame thickness tends to  $5mm$  when approaching  $\phi_g = 0.4$ , and it is sufficient to resolve the flame with the employed  $\Delta_x$  and targeted  $n_{res}$ .

The thickening factor, shown with solid lines in Fig.3-15b, is not uniform over the flame front as it raises with the increasing fuel/air equivalence ratio due to the droplet's evaporation, which is promoted as the temperature increases. With a reference flame thickness of  $1.1mm$  for the case with  $D_d = 40 \mu m$  droplets (see Fig.3-11b), the thickening in the refined regions should reach 2. However, we can observe that the thickening factors are significantly overestimated in both computed cases behind

the heat release rate peak on the burned side. It happens since the thickening factor estimation relies on the tabulated flame thickness of premixed flames, which are thinner compared to spray flames when burning at the same overall  $\phi_g$ .

### Droplet size variation

Although the profiles obtained with standard sensor parameters looked reasonably good when compared to the non-thickened solution, such limited flame-front coverage with the flame sensor observed in Fig. 3-15a can lead to larger discrepancies at higher thickening factors. Moreover, the use of extended sensor parameters makes this computation more stable. For all these reasons, the extended sensor settings are adopted to perform simulations of the thickened configurations.

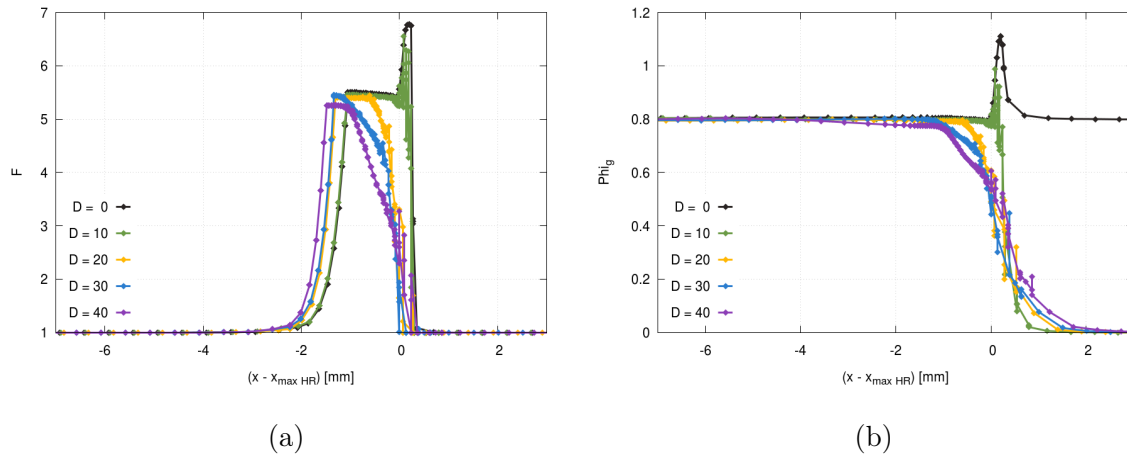


Figure 3-17: 1-D n-dodecane spray flame profiles,  $D_d = 0 - 40 \mu\text{m}$ , TFM-AMR  $\Delta_x = 0.5\text{mm}$ . (a): thickening factor; (b): gaseous fuel/air equivalence ratio.

The thickened flame configuration was computed for the gaseous case, as well as for droplet diameter sizes: 10, 20, 30, 40  $\mu\text{m}$ , as it was done for the non-thickened flames in Sec. 3.2.3. During the results' discussion Sec. 3.2.3, it was mentioned that flames fed with small droplets behave similarly to the purely gaseous flame. Thus, we observe also that the thickening of 10 $\mu\text{m}$  spray flame is comparable to the thickening applied in the purely gaseous case, as shown in Fig. 3-17a.

When the droplet size increases, the droplets evaporate more gradually, and this slows down the accumulation of gaseous fuel/air equivalence ratio, as illustrated in

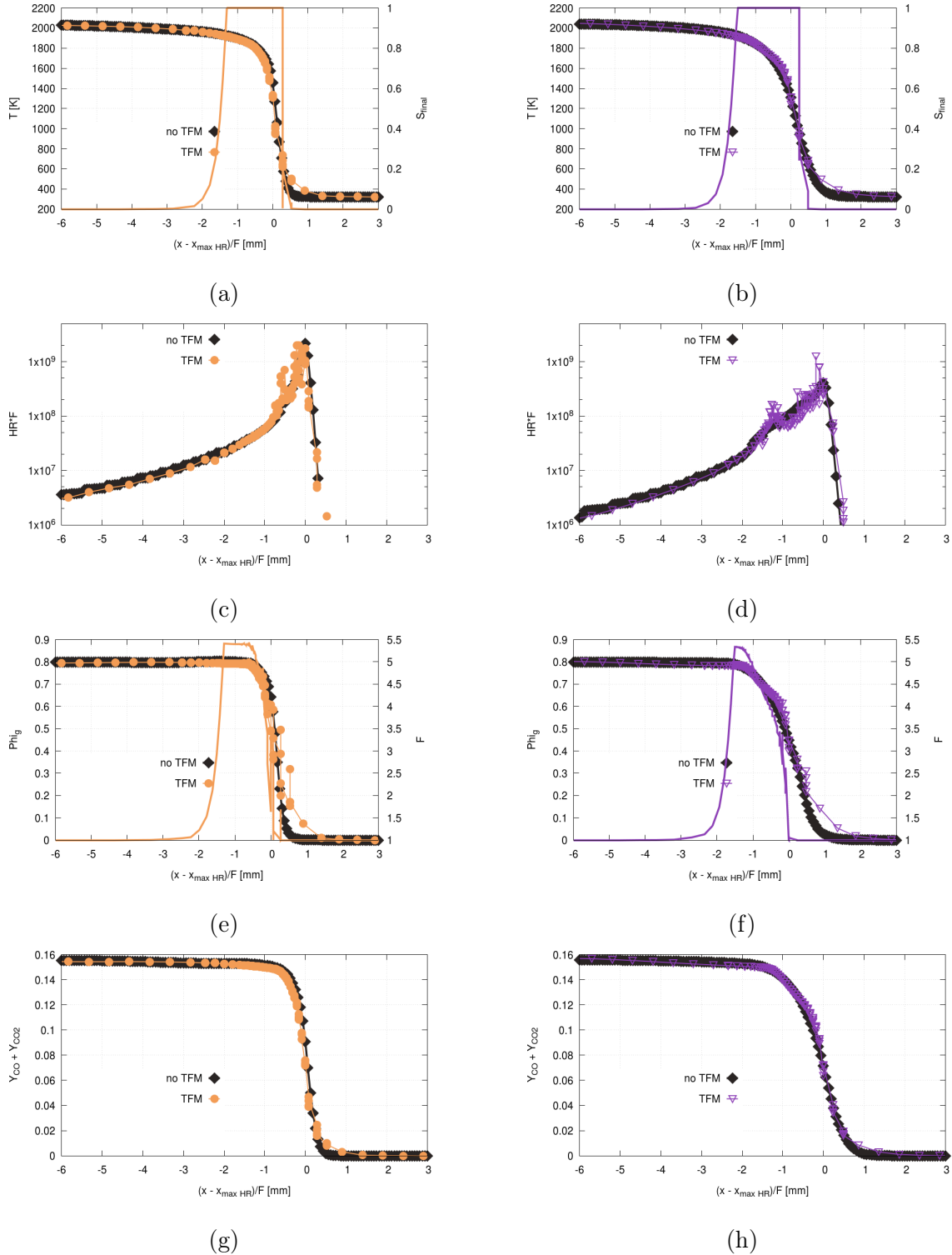


Figure 3-18: 1-D n-dodecane spray flame profiles, TFM-AMR  $\Delta_x = 0.5\text{mm}$ .  $D_d = 20 \mu\text{m}$  - left column,  $D_d = 40 \mu\text{m}$  - right column. (a,b): gaseous temperature, sensor (solid lines); (c,d): heat release rate; (e,f): gaseous fuel/air equivalence ratio, thickening factor (solid lines); (g,h): Sum of  $CO$  and  $CO_2$  mass fractions.

Fig. 3-17b. Compared to the gaseous flames, the location of maximum heat release ( $x = 0$ ) can be shifted towards lower  $\phi_g$  values in the spray flames depending on the size of the droplets.

Figure 3-17a shows that the thickening reaches the same level in all cases. Considering the reference flame thicknesses given in Fig. 3-11b, such thickening is excessive for  $D_d \geq 20 \mu m$ . Such behavior is observed because the current modeling approach relies on the 1D premixed tables as a function of the local gaseous fuel/air equivalence ratio. Since the overall gaseous fuel/air equivalence ratio is set to the same value for all configurations, and the entire liquid fuel evaporates completely in all cases, the thickening factor reaches the same level.

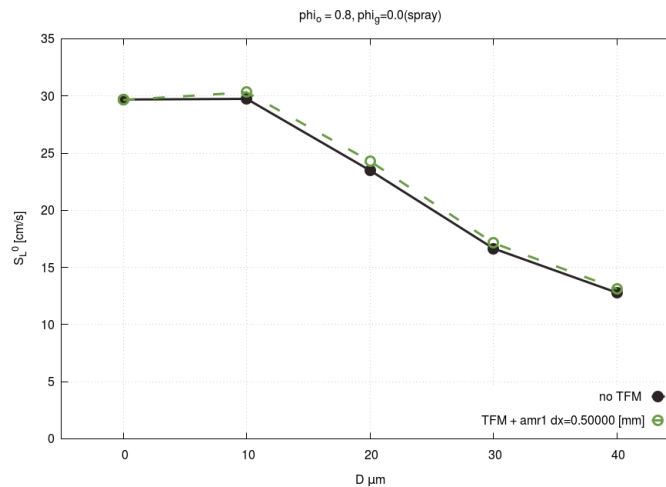


Figure 3-19: N-dodecane flame burning velocity as a function of droplet diameter. TFM-AMR,  $\Delta x = 0.5mm$

For the sake of brevity, the comparison of thickened spray flame profiles with the reference resolved solutions are given only for two droplet sizes: for  $D_d = 20 \mu m$  (left column in Fig. 3-18) and for  $D_d = 40 \mu m$  (right column in Fig. 3-18).

We can observe a relatively good agreement of thickened profiles compared to the fully resolved flames for both droplet sizes.

As already mentioned above, the sensor defined as in Sec. 2.3.1 can face difficulties in identifying the base of the spray flames at certain conditions. This sensor limitation is illustrated on the temperature plots in Fig. 3-18a and in Fig. 3-18b. The main deviation from the reference solution can be seen when looking at the gaseous fuel/air

equivalence ratios on the fresh side in Fig. 3-18g and Fig. 3-18h. Since the fraction of gaseous fuel at the inlet is set to zero in these cases, the fuel/air equivalence ratio reaches the values around 0.5 at the maximum heat release location. In our case, the tabulation starts at 0.4, and the sensor is designed to relax quickly outside the tables. Therefore, the base of the computed thickened flames is slightly under-resolved.

Figure 3-19 shows that the burning velocities of the thickened spray flames computed using Eq.(3.1) agree well with the reference values computed for the non-thickened flames.

### 3.3 Conclusions

In this chapter, the extension of the TFM-AMR to two-phase flows described in Sec. 2.3.4 was validated on one-dimensional two-phase laminar flame cases. Two different fuels were examined in Sections 3.1 and 3.2: high-volatile n-heptane used as a fuel in the academic burner configuration discussed in Chapter 4, and a low-volatile n-dodecane used in the gas turbine model combustor configuration investigated in Chapter 5.

On one-dimensional two-phase n-heptane laminar flame cases, it was shown in Sec. 3.1 that the TFM spray source terms proposed by Paulhiac in [58] allow us to recover the non-thickened flame results accurately. An excellent agreement with the reference non-thickened solutions was demonstrated first for the constant thickening and a static mesh, then for the dynamic thickening and a static mesh, and finally for the dynamic thickening with AMR.

While the fraction of gaseous fuel was set at 20% at the inlet in the n-heptane configurations, it was reduced down to zero in the n-dodecane laminar flames investigated in Sec. 3.2. This, together with the lower volatility of the n-dodecane fuel, revealed some possible deficiencies of the TFM-AMR modeling approach when applied to the spray flame.

First, we have observed that the heat release within a spray flame might deviate from the heat release values tabulated for premixed flames. Therefore, the sensor can

have difficulties to cover the entire flame front. A reactant's dilution with burned products, commonly encountered in gas turbines, can amplify the discrepancies with the tabulated values. A possible solution in such a case would be to increase the sensitivity of the sensor. Nevertheless, this solution is not robust as the value of the sensor sensitivity will be case dependent, and a more systematic solution will be investigated in Chapter 6.

Second, low premixing levels in combination with large droplets of low-volatile fuel can lead to low fuel/air equivalence ratios at the base of the flame. Thus, the sensor can struggle to cover the base of the flame despite re-adjusted sensor parameters.

Third, we have seen that the thickening is non-uniform and raises over the flame front as the fuel/air equivalence ratio increases. Moreover, the thickening in the spray flames might be overestimated, especially when approaching the burned side.

In the following chapters, the objective is to investigate the capability of the modeling strategy described in Chapter 2 to handle complex turbulent cases. To take a step forward towards the simulation of industrial systems, the TFM-AMR modeling approach is investigated in the context of atmospheric academic burner configurations of increasing complexity in Chapter 4 and Chapter 5.



# Chapter 4

## CORIA burner

To the best of our knowledge, well-instrumented experimental data on complex industrial two-phase flow gas turbines are scarce and limited today. This is why we propose here as a first step the application of TFM on an academic ambient pressure two-phase flow burner from CORIA [77], which features an extensive database for validation purposes. The selected experimental facility called CRSB (CORIA Rouen spray burner) is an academic atmospheric unconfined burner with well-defined boundary conditions. The burner is operated with liquid fuel so that it leads to a turbulent spray jet flame.

In this chapter, the details of the experimental facility are given first, followed by a summary of the numerical studies already done on this burner configuration. Then, the LES results obtained using the TFM-AMR modeling approach described in Chapter 2 are discussed in detail.

### 4.1 Experimental facility

Recent work has been conducted at the CORIA laboratory to study spray combustion and build a validation database for turbulent spray combustion models. The CRSB burner, shown in Fig. 4-1a, features an external annular non-swirling air co-flow and a pressurized swirl injector operated with n-heptane (Danfoss,  $1.35 \text{ kg/h}$ , hollow cone with half-angle of  $40^\circ$ ). The outer diameter of the air inlet is  $20 \text{ mm}$ , and the inner

diameter, which has a rounded edge, is around 10 *mm*. For the reference operating point considered here, fuel and air are injected at 298 *K* with mass flow rates of 6 *g/s* and 0.28 *g/s*, respectively. Further details about the burner geometry can be found in the literature [77].

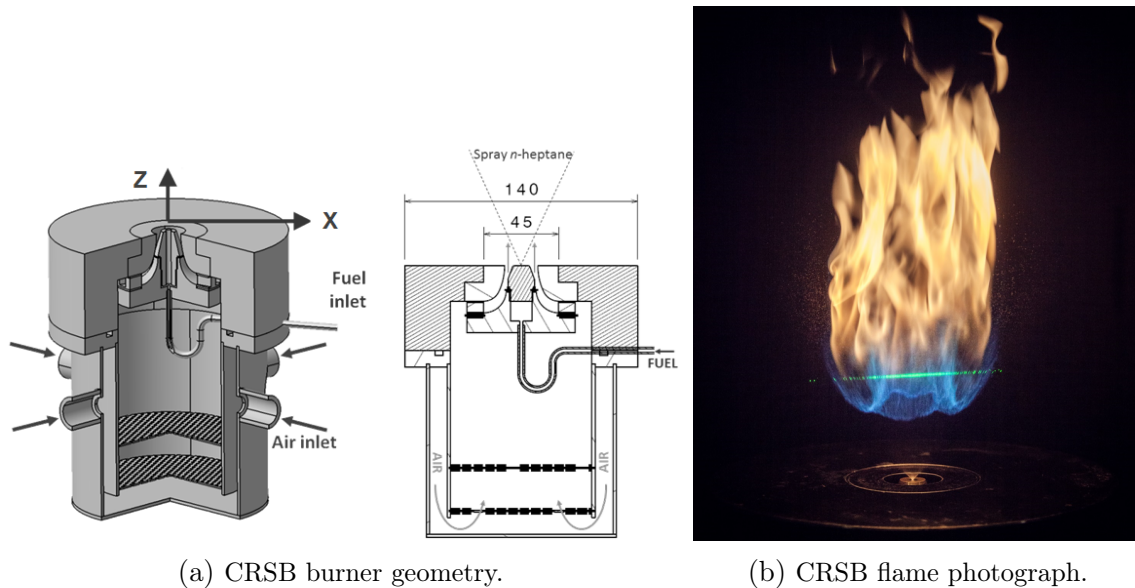


Figure 4-1: CRSB burner. [77]

The resulting flame is lifted, and the atomized liquid phase is composed of  $2 \mu m \leq D_{10} \leq 80 \mu m$  sized fuel droplets, which are distributed over a hollow cone shape with an opening angle of  $80^\circ$ .

The experimental data is obtained using several measurement techniques for both reacting and non-reacting conditions. The phase Doppler anemometry (PDA) enables to measure droplet size distributions and their velocities, as well as the velocity of the carrier phase. Planar Laser-Induced Fluorescence of OH radical (OH-PLIF and HS-OH-PLIF) has been applied to characterize the flame structure. Additionally, the temperature of droplets has been measured by means of the Global Rainbow refractometry Technique (GRT) [77].

The CRSB database is being continuously updated. Recently published measurements [49, 50, 51] include instantaneous and mean nitric oxide (NO) concentrations, flame-front (OH), quantitative soot volume fraction and soot-precursor marked by smaller (2–4 ring) polycyclic aromatic hydrocarbons (PAH). This extensive data con-

tributes to a better understanding of this specific flame structure and can be further used to validate turbulent spray combustion models.

## 4.2 CORIA burner: State of the art

The selected experimental facility has already been studied numerically by other teams. All of them have used a Lagrangian description for the spray while applying different approaches for the sub-grid scale combustion modeling.

CRSB was first investigated numerically in [73] using two-step chemistry in the limit of a resolved flame so that no sub-grid scale combustion modeling is needed. The flame has been analyzed using Takeno index [79] and is shown in Fig. 4-2. Takeno index compares the gradients of an oxidizer and a fuel, whereby its negative values indicate the non-premixed regime and its positive values mark the premixed flame zones.

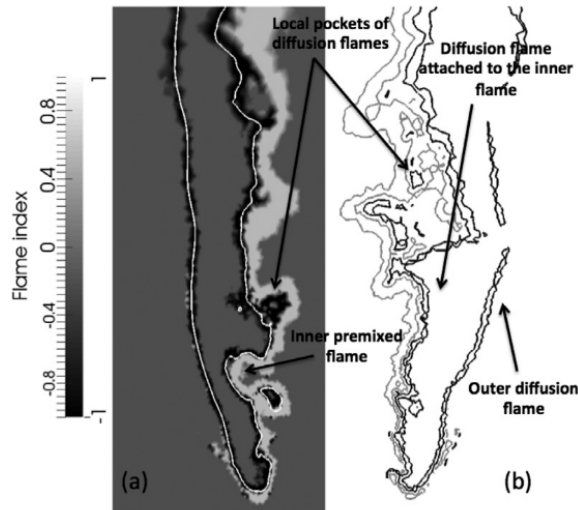


Figure 4-2: CRSB flame topology computed in [73] for the resolved flame with global chemistry description. Left: Takeno flame index with stoichiometric mixture fraction isoline. Right: Takeno index isolines. Gray: premixed flames (Takeno = 1), black: diffusion flames (Takeno = -1).

The inner flame branch is highly wrinkled and possesses a double flame structure, as illustrated in Fig. 4-2. In this region, the diffusion flame comes after the premixed one as we move towards the outer flame branch. At the same time, the outer flame

branch is mainly laminar and burns predominantly in the diffusion mode. The region of hot gases is enclosed between the two flame branches. It corresponds to the fuel-rich zone, since the evaporation rate of larger droplets, which survive the inner reaction zone, is enhanced in this high-temperature region. The flame structure will be discussed in Section 4.3.4 in more detail.

It has been shown that the position of the flame base depends strongly on the spatial droplet distribution and its evaporation rate since a clear correlation between the gaseous fuel/air equivalence ratio and flame stabilization point was observed.

At high temperatures, n-heptane molecules are broken down into smaller species due to pyrolysis. Since the global chemistry description does not capture the pyrolysis effects in the hot gas region, another simulation was conducted on the same setup but with a reduced mechanism to evaluate the drawbacks of simplified chemistry use. Some of its results are briefly summarized in [72], and some are shown later in the context of experimental work [49].

With reduced chemistry, the endothermic pyrolysis reactions lower the temperatures in the hot gas region, but also the temperatures within the inner flame branch. Therefore, the use of simplified chemistry might lead to the overestimation of spray evaporation rates and thus affect the flame stabilization. However, the flame lift-off length (LOL) was not changed with the increased level of chemistry description; in both cases, the flame stabilization height was significantly under-predicted.

The results of LES with Filtered Tabulated Chemistry for LES (F-TACLES) were presented in [14]. Here, the use of tabulated chemistry allows to avoid solving the transport of each species (as in Eq. 2.3) and replaces it with the transport of a progress variable. In order to take into account the presence of the liquid phase, the transport of the mixture fraction is solved with a source term corresponding to the evaporated fuel.

First, this modeling approach has been tested on the same mesh as in [72] without any SGS combustion modeling to verify the ability of the chemistry tabulation to capture the flame structure. Then, the same setup was performed on a coarser mesh to evaluate the use of F-TACLES with SGS flame wrinkling represented with Charlette

efficiency function [13]. It was shown that in both cases, the global structure of the flame is well captured.

The lift-off length, which is measured based on the OH-PLIF signal experimentally, is estimated here using the iso-contour of the temperature. For both cases, the obtained LOL values are in a pretty good agreement with experimental data.

However, when looking at the mean  $OH$  mass-fraction, one can notice that the flame on the finer mesh appears to be narrower than in the experiments. The smaller hot region zone might be explained by the use of a chemistry description that relies on look-up tables composed of premixed flames.

At the same time, on the coarser mesh, the resulting flame is broader, and the droplets are exposed to the high temperatures longer. Since no additional corrections are introduced into the Lagrangian equations, the spray evaporation rates might be over-predicted in the filtered flame, which is illustrated by Figure 4-3. It can be seen that the largest droplets are able to cross the outer flame branch when computed on the fine mesh, which is also observed experimentally (see Fig. 4-1b), whereas no spray droplets can be found behind the flame in the case performed on the coarser mesh.

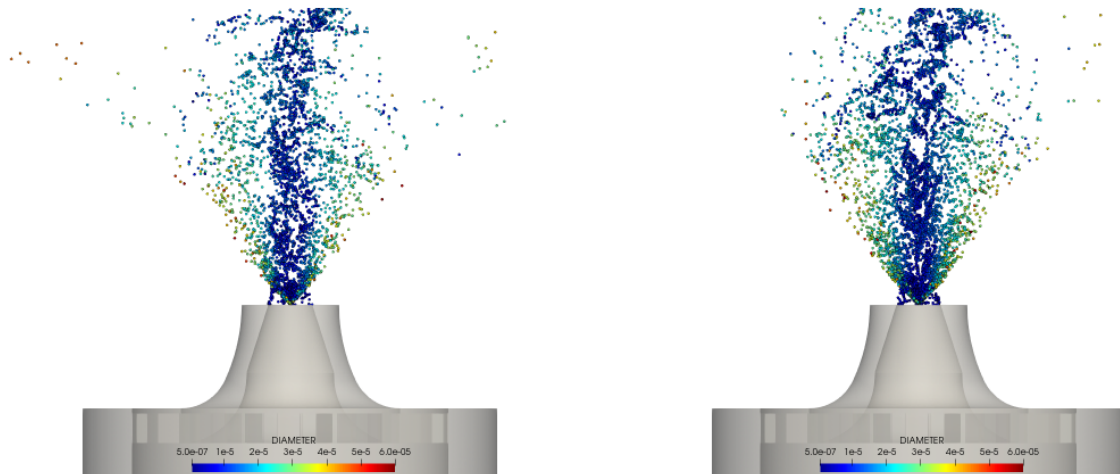


Figure 4-3: Droplet diameter computed in [14]. Left: refined mesh; right: coarse mesh.

LES has also been performed using Doubly Conditional Moment Closure (DCMC) in the work of Sitte et al. in [74]. DCMC belongs to the statistical combustion modeling approaches and is an extension of Conditional Moment Closure. Unlike CMC,

DCMC can be applied in the cases where both the premixed and the non-premixed modes co-exist within a single flame. This is achieved by the space parametrization done with two quantities: the mixture fraction and the reaction progress variable. Additionally, the unity Lewis number is assumed throughout this work so that the preferential diffusion effects are not accounted for.

The mean and disperse phase profiles match the experiments well. Although the LOL was also found to be in good agreement with the measured value, the resulting flame shape slightly deviates from the experimental one. Based on the flame base analysis, it has been shown, that the non-premixed burning modes and its correct prediction play an unimportant role in the flame stabilization.

Another statistical approach to model combustion at the sub-grid level, which is based on the transported probability density functions, is used in [56]. This study focused on the evaluation of different evaporation models in the context of the CRSB burner.

Unlike previously mentioned LES setups, the authors use a stochastic dispersion and a stochastic break-up formulation for the spray evolution in this study. In this case, the maximum droplet diameter corresponds to the diameter of injected droplets that equals  $43.5 \mu m$ . As the experimental diameters lie between  $2 \mu m$  and  $80 \mu m$ , these LES thus ignores the presence of larger droplets from  $43 \mu m$  and  $80 \mu m$ . Since the liquid fuel mass in this LES is concentrated within the droplets of smaller radius that evaporate faster, it might explain why the LOL is under-predicted in these simulations.

The analysis of different evaporation models reveals no significant difference between the costly non-equilibrium model and the commonly used Abramzon-Sirignano model, whereas the use of a classical, rapid mixing evaporation model leads to the lowest flame stabilization point. All the LES presented above showed the highest values of OH in the outer flame branch, which is not what is observed experimentally where the highest OH values are found close to the flame stabilization point. This issue, as well as the flame tip form, will be discussed later in Sec. 4.3.4.

In Section 4.3 we present the first LES performed with the TFM-AMR modeling

approach (see Sec. 2.3) and reduced chemistry. As we saw in the previous studies, the droplet distribution plays an important role in the flame stabilization mechanism. Therefore, the fuel injection parameters will be carefully validated in Sec. 4.3.3.

## 4.3 CORIA burner: LES

### 4.3.1 Numerical setup

The LES computational domain size was chosen to be large enough to allow for air entrainment and has a diameter of 400 *mm* and a height of 600 *mm*. The simulation domain includes the air plenum and the inlet tubes and is shown in Fig. 4-4. An air co-flow of 0.1 *m/s* is added around the burner geometry to allow an easier evacuation of the flame products towards the outlet.

A static mesh refinement is used to get a 4.0 *mm* cell size in the far-field down to 0.5 *mm* in the flame region. One additional AMR level is used in the flame front leading to a minimum cell size of 0.25 *mm* (see Fig. 4-4). In the plenum close to the walls of the inlet tubes, as well as in the cylinder close to the fuel injections, the minimum  $\Delta_x$  reaches 0.125 *mm*. This grid setting leads to 10.4 million cells for the non-reacting configuration and approximately 14.2 million cells in the reacting case.

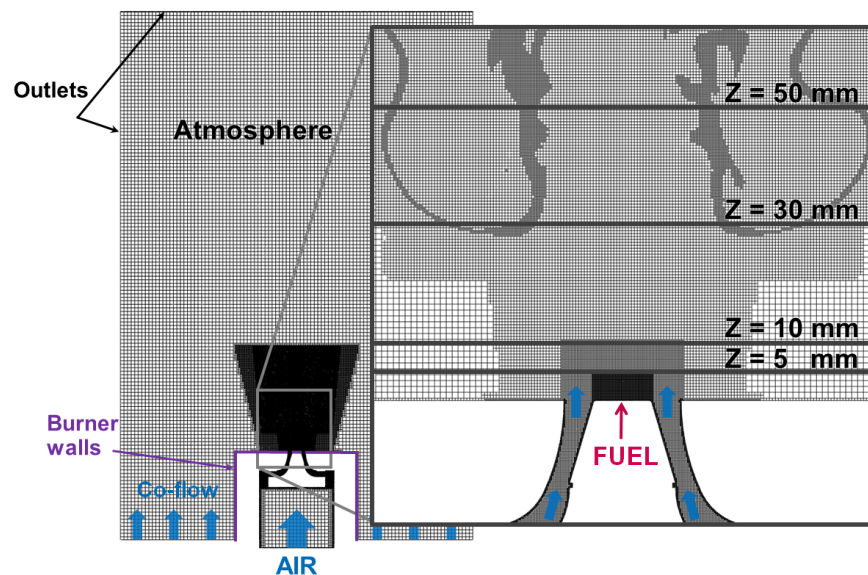


Figure 4-4: LES simulation domain.

The Sigma model [55] with value of 1.5 for the model constant is selected to model unresolved turbulent stresses, while combustion is modeled by the TFM approach presented previously in conjunction with Charlette efficiency function [13]. The flame front is detected based on local heat release values as described in Sec. 2.3 with parameters that were previously validated on the 1-D simulations.

In reality, the droplets' shape can deviate from a sphere, and if it is not taken into account, it might lead to some under-prediction of computed drag forces. However, the dynamic drag model [57], which accounts for variations in the drop shape through a drop distortion parameter, has been tested and has shown only a negligible effect in this particular setup.

### 4.3.2 Fuel injection

The exact reproduction of realistic liquid fuel injection and atomization is a complex task that requires sophisticated break-up models. In this study, we have implemented the simplified injection model proposed in [33].

An instantaneous snapshot of the fuel injection in the CRSB is shown at the top of Fig. 4-5, while its sketch and its approximated form are given at the bottom of Fig. 4-5. Unlike realistic fuel injection, where the liquid close to the injector is present in the form of the liquid film and then is broken down into smaller particles, spherical droplets are here directly injected at the injection nozzle exit.

The liquid film thickness, which is formed within the injector (see the injection sketch in Fig. 4-5), can be computed as the difference between the orifice radius  $R_o$  and the radius of the air cone  $R_a$  developed at the injector outlet. The resulting film thickness directly affects the axial velocity of the injected droplets  $u_{ax}$  that is deduced from the mass conservation as:

$$u_{ax} = \frac{\dot{m}_F}{\rho_l \pi (R_o^2 - R_a^2)}, \quad (4.1)$$

where  $\dot{m}_F$  the mass flow-rate of the fuel.

According to the simplified model proposed by Guedot et al. in [33], the film

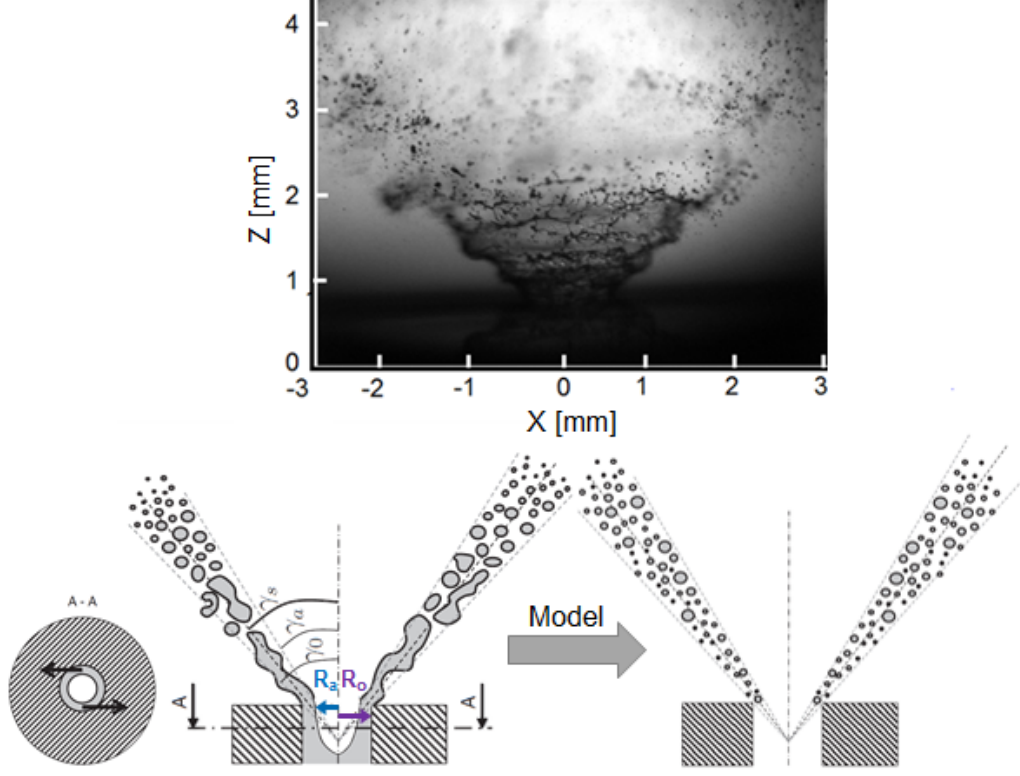


Figure 4-5: Fuel injection. Top: CRBSB [77]. Bottom left: injection sketch; bottom right: simplified injection sketch (adapted from [33]).

thickness is estimated from the orifice radius and the cone half-angle  $\gamma_s$  as:

$$R_a = C_{inj} R_o^2 \sqrt{\frac{\sin^2(\gamma_s)}{1 + \cos^2(\gamma_s)}} \quad (4.2)$$

Since  $R_a$  is difficult to measure experimentally and because of its crucial role in defining the velocity of the droplets, we introduce a third parameter  $C_{inj}$  to account for the uncertainty in  $R_a$  computation. Then, the constant  $C_{inj}$  can be adjusted based on the available downstream experimental data.

Assuming a perfectly inertial spray particle, the droplet's initiating position  $X = R_{inj}$  affects its trajectory, and is set within the liquid film thickness  $R_a < R_{inj} < R_o$ . The half-cone angle for the injected droplet  $\gamma$  can be estimated using  $\tan\gamma = R_{inj}/R_s \tan\gamma_s$ , where  $R_s = 0.5(R_a + R_o)$ . Finally, the tangential velocity of this droplet is given by  $u_{tan} = u_{ax}\gamma$ . The radial velocity component in this derivation is considered to be constant and equals to zero.

To ensure a poly-disperse description of the spray cloud, droplet radii are prescribed by a Rosin-Rammler distribution at the injection plane, also known as Weibull distribution [48]. The Rosin-Rammler correlation is defined by two parameters: its spreading factor  $q$  and a representative diameter  $D_{rr}$  as follows:

$$Q = 1 - \epsilon^{(D_{rr})^q}, \quad (4.3)$$

where  $Q$  is the fraction of total volume contained in droplets of diameter less than  $D$ . The characteristic size  $D_{rr}$  can be obtained from Sauter Mean Diameter (SMD) using:

$$\frac{D_{rr}}{SMD} = \Gamma\left(1 - \frac{1}{q}\right). \quad (4.4)$$

The value of the spreading factor  $q$  lies typically between 1.5 and 4 [43] for most of the sprays, whereby the spray becomes more uniform if the spreading factor  $q$  is increased.

Therefore, the use of the presented simplified injection model allows to describe the hollow-cone liquid fuel injection with three macroscopic characteristics of the injector (the mean cone half-angle  $\gamma_s$ , the orifice radius  $R_o$ , the mass flow-rate of the fuel  $\dot{m}_F$ ), the introduced parameter  $C_{inj}$ , and the Rosin-Rammler distribution.

### 4.3.3 Non-reacting flow validation

For the non-reacting case, the simulations include the data collected and averaged over 13.5 flow-through-times (FTT), after a steady state is attained. FTT is defined as the time that the bulk air takes to reach the highest plane for which we have experimental data, and is equal to  $2.3ms$ . In the experiments, a minimum of 500 droplets is used to compute the statistics. Similarly, in the simulations, we use a minimum of 500 parcels for statistic computation. The experimental measurement volume is a cylinder with a diameter of  $120 \mu m$ , and a height of  $200 \mu m$ , and the same probes were set in simulations to track the parcels.

## Injection model validation

Fuel injection parameters for CRSB are chosen to fit the experimental data. The value  $C_{inj}$  is selected to fit the droplet velocity profiles so that the resulting axial velocities of the droplets are increased by a factor of 1.3. The initial Rosin-Rammler distribution is defined with a  $SMD = 25 \mu m$  and  $q = 2.5$ , and generates droplets with a maximum diameter of around  $80 \mu m$ , as it can be seen in Fig. 4-6.

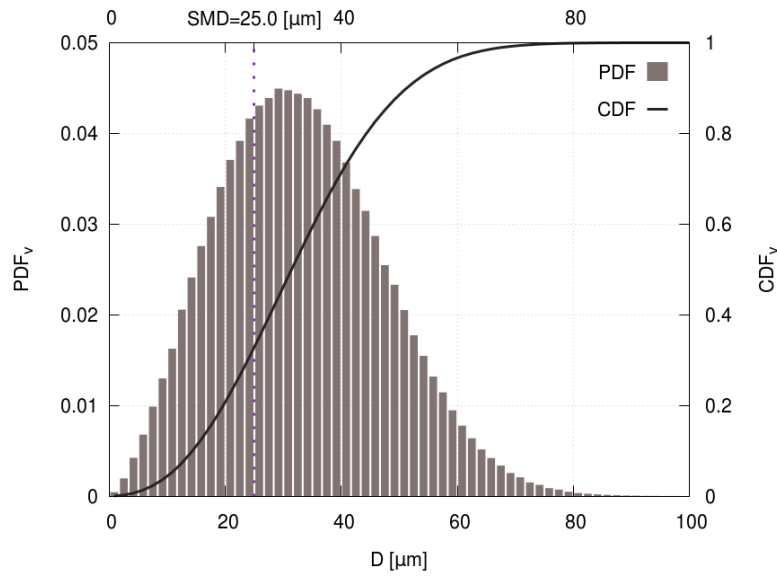


Figure 4-6: Rosin-Rammler distribution at the injection plane.

The liquid injection strategy implies strong simplifications, and for this reason, the resulting droplet distribution has to be verified first. The axial plane  $Z = 13 \text{ mm}$  is selected to evaluate the prescribed boundary conditions, which is the best compromise between the proximity to the injector and the results accuracy [77].

As seen in Fig. 4-7, an overall good agreement is reached for the average droplet diameter  $D_{10}$  radial distribution, but also for the local droplet size distribution, characterized with volumetric probability density functions. The selected radial locations correspond to the middle part of the spray cone, which is the region with the highest concentration of mass-containing droplets.

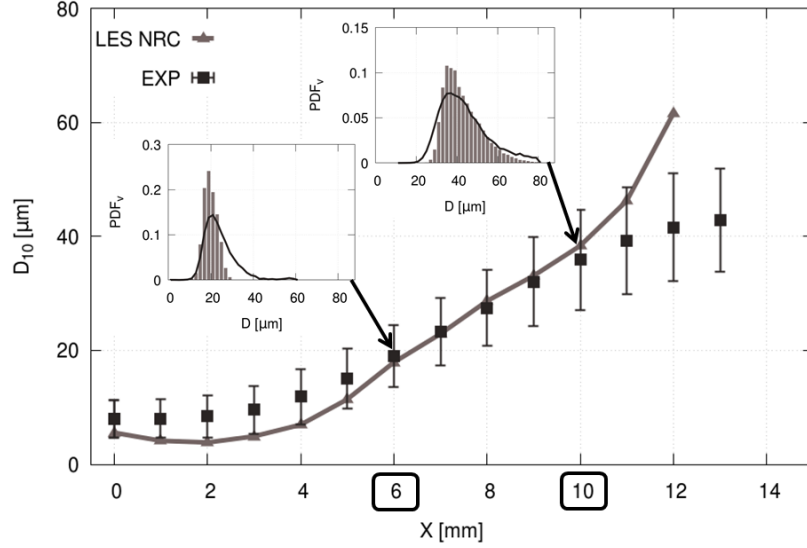


Figure 4-7: Droplet size radial distribution at  $Z = 13 \text{ mm}$ .  $\blacksquare$ ,  $\text{---}$  (PDF): experiments [77];  $\text{---}$ ,  $\text{---}$  (PDF): LES

### Cold flow velocity profiles

The mean velocity components of the gas phase show a good agreement with the experimental data. The axial velocity component is shown on the left side of Fig. 4-8 for three different axial positions downstream the injection plane (see Fig. 4-4). The annular co-flow at the injection plane induces an air bulk velocity of  $20.5 \text{ m/s}$ , and the maximum axial velocity of air at the point of injection exceeds the value of  $30 \text{ m/s}$ . The negative axial velocities at the  $5 \text{ mm}$  plane indicate the presence of a recirculation zone close to the injection plane and are accurately resolved by the simulation. LES correctly captures the typical double-peak velocity profile induced by the annular co-flow. However, we observe a slight velocity underestimation in the middle of the jet.

Radial profiles of the axial root mean square (RMS) velocity of the carrier phase are illustrated on the right side of Fig. 4-8. The shape matches well the experimental results. As we only account for resolved scales in the RMS velocity calculation, a slight under-prediction compared to experiments is expected.

Regarding the dispersed phase analysis, we will only consider the planes above  $10 \text{ mm}$  since an increase in the experimental measurement error was reported below

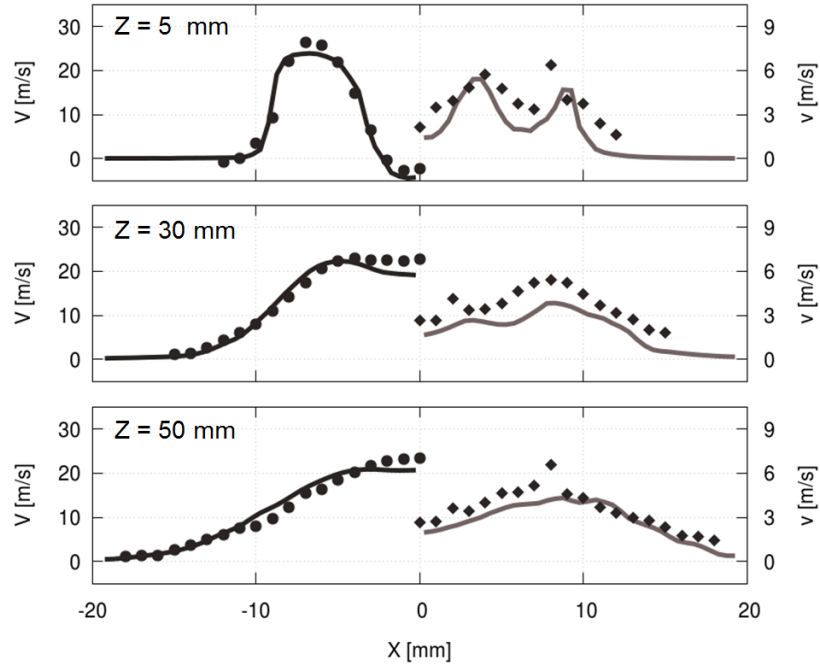


Figure 4-8: Carrier phase at non-reacting conditions: axial mean and RMS velocities. —: LES mean z-velocity, —: LES RMS z-velocity, •: EXP mean z-velocity [77], ♦: EXP RMS z-velocity [77].

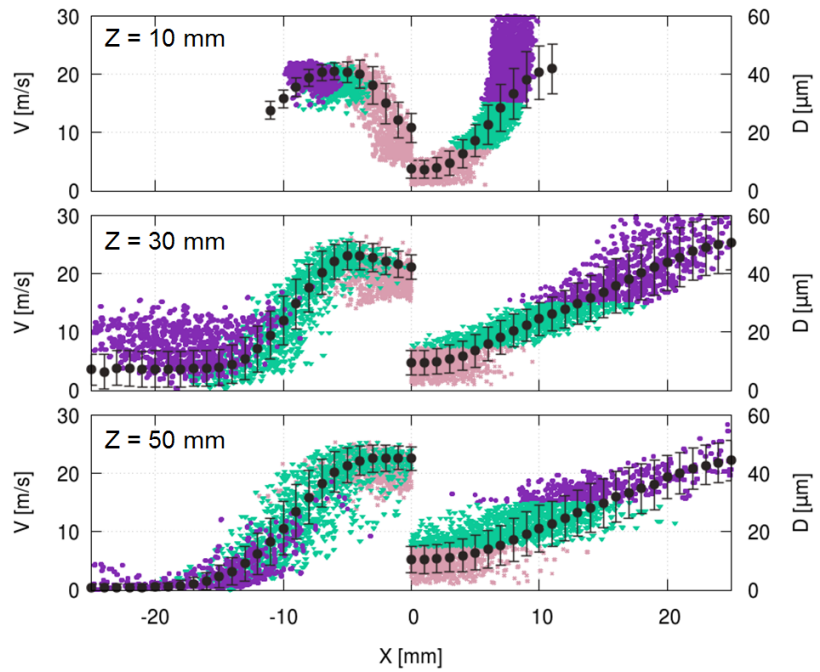


Figure 4-9: Dispersed phase at non-reacting conditions: axial velocities (left) and droplet size (right) radial distributions. —•: experiments with error bars proportional to measured RMS-values [77]. LES: •  $D < 15 \mu\text{m}$ , •  $15 \mu\text{m} \leq D < 30 \mu\text{m}$ , •  $D \geq 30 \mu\text{m}$ .

this value, corresponding to the dense spray region [77]. Figure 4-9 illustrates the evolution of the radial distribution of droplet diameter, wherein the droplets are divided into three groups based on their size that are colored differently. We observe minor discrepancies close to the injection plane, while an almost perfect match with experiments is obtained downstream. Smaller droplets concentrate in the middle of the jet, while larger droplets are detected at the outer part of the spray cone. An overall very good agreement is found for the droplet velocities (see Fig. 4-9) with slightly underestimated axial velocities that are noticed near the burner center-line. This under-prediction is explained by the fact that these droplets having a small Stokes number follow rapidly the carrier phase, which was found to be under-predicted (see Fig. 4-8).

#### 4.3.4 Reacting flow results

In the reacting simulations, n-heptane chemistry is described through the reduced 36 species mechanism also used for 1-D simulations in Sec. 3.1, and combustion is modeled with TFM-AMR. To reduce computational costs, the chemistry calculations are omitted above  $120mm$ , the downstream flame region not covered by the experiments.

After a stable lifted flame is reached, the averaging is performed over  $16.5 FTT$ . The instantaneous LES fields (see Fig. 4-10) demonstrate a complex structure of the resulting flame. The region C filled with hot gases (see heat release in Fig. 4-10), is enclosed between the inner reaction zone B1 and the outer reaction zone B2. The elevated temperatures in the region C enhance the evaporation rate of the larger droplets, which cross the flame branch B1. Then, the evaporated fuel, being exposed to high temperatures and in the absence of an oxidizer, starts to decompose into intermediate products. This endothermic process lowers the temperature in the middle of C to around  $1100K$  and is characterized by negative values of the heat release. The flame in the branch B1 is highly wrinkled due to the high turbulence intensity induced by the annular air injection, while in the branch B2 the flame remains essentially laminar. The flame structure is in good agreement with experimental and previous LES results.

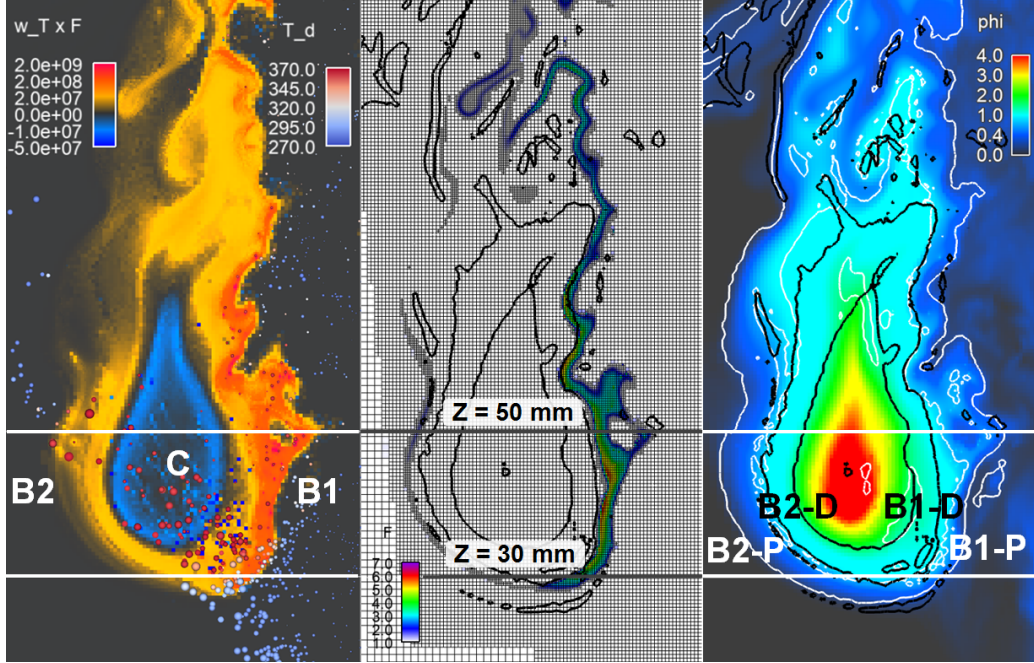


Figure 4-10: Instantaneous heat release scaled with the thickening factor (left), instantaneous thickening factor with AMR (middle), instantaneous fuel/air equivalence ratio (right). Takeno index iso-contours:  $-0.2$  black,  $0.2$  white .

The iso-contours in Fig. 4-10 indicate the regions of different combustion modes, estimated with the Takeno index [79]. The Takeno index is here defined using  $Y_{HC}$  instead of  $Y_{Fuel}$ , where  $Y_{HC}$  is the sum of all hydrocarbon species:

$$\mathcal{I}_t = \frac{\nabla Y_{HC} \cdot \nabla Y_{O_2}}{|\nabla Y_{HC}| \cdot |\nabla Y_{O_2}|} \quad (4.5)$$

This definition is beneficial when using reduced mechanisms, which include intermediate hydrocarbon species. The flame index takes values between minus one and one, corresponding to the non-premixed and premixed zones, respectively. The double flame structure in the inner reaction zone reported in the literature is well captured, identifying first a premixed flame B1-P, followed by a non-premixed one B1-D. As we move from the region of hot gases C towards the outer reaction zone B2, we observe a diffusion flame B2-D and then a premixed flame B2-P.

The efficiency function, as well as the thickening factor, reach their maximum level within zone B1. In the presented simulations, no specific adaptation of TFM is used for the diffusion flame regions. However, considering Fig. 4-10, where we show

the thickening factor with iso-contours corresponding to the most probable location of the diffusion flame, it can be seen that no thickening is applied in this zone. The reason for this is that the flame sensor  $S$  in Eq.(2.11) remains close to zero in this region because the heat release rate  $\omega_T$  is much smaller than the peak heat release rate  $w_{T1D}^{max}$  given by the table, based on premixed flames calculations.

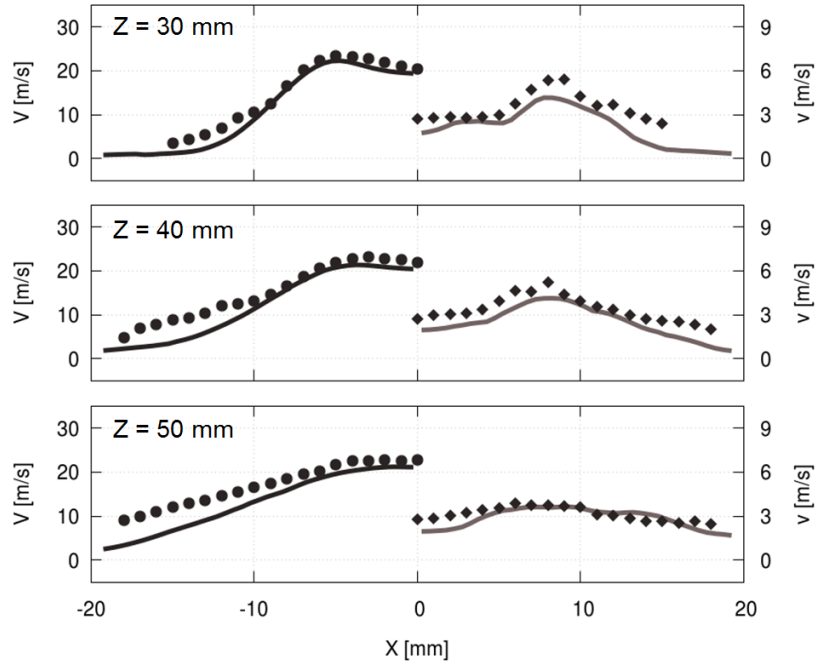


Figure 4-11: Carrier phase at reacting conditions: axial mean and RMS velocities. —: LES mean z-velocity, —: LES RMS z-velocity, •: EXP mean z-velocity [77], ♦: EXP RMS z-velocity [77].

When looking at the velocity axial profiles in Fig. 4-11, we notice the effect of thermal expansion at the outer part of the jet, where we observe larger velocities compared to the non-reactive case. In this region, a slight underestimation might be explained by the minor overestimation of the lift-off length discussed below. Very good overall agreement with experiments is found for the mean and RMS velocities of the gaseous phase, as well as for the velocity and size distributions of the dispersed phase as shown in Fig. 4-12.

A lift-off length (LOL) of 28 *mm* is obtained in the LES based on the mean *OH* mass-fraction (see Fig. 4-13). This value is in good agreement with the 25 *mm* measured experimentally and is also among the most accurate reported values [72, 74, 56, 14]. One possible explanation for the minor LOL misprediction may be the

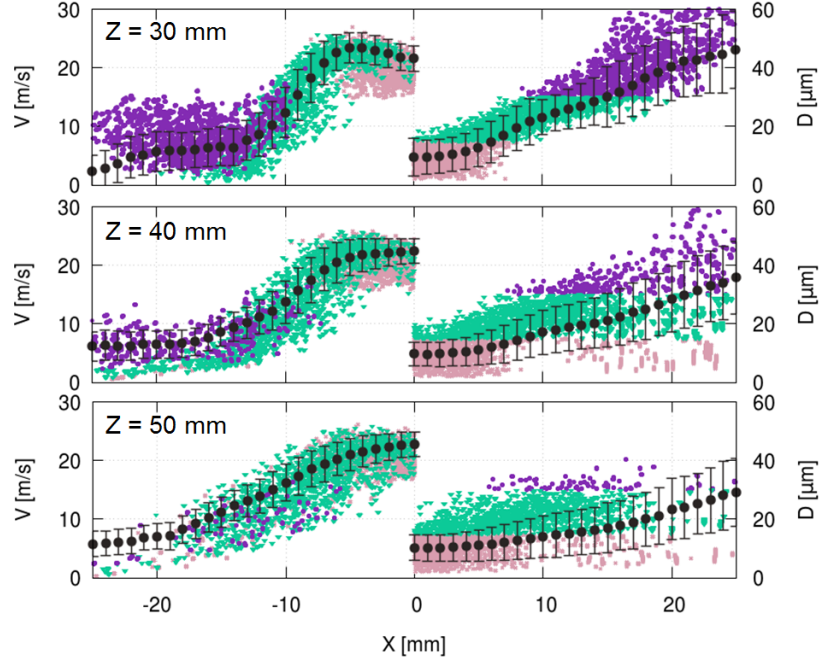


Figure 4-12: Dispersed phase at reacting conditions: axial velocities (left) and droplet size (right) radial distributions.  $\bullet\text{--}\bullet$ : experiments with error bars proportional to measured RMS-values [77]. LES:  $\bullet$   $D < 15 \mu\text{m}$ ,  $\bullet$   $15 \mu\text{m} \leq D < 30 \mu\text{m}$ ,  $\bullet$   $D \geq 30 \mu\text{m}$ .

simplified injection model employed here. During a simulation run-time, we observe a constant spray opening mean angle, whereas it varies in the experimental images, probably due to the interaction of the liquid fuel sheet with the mean flow in the recirculating region close to the injector. Thus, the local mixture composition may be altered, affecting the stabilization point of the flame.

Another global flame shape characteristic, the merging point position of B1 and B2 branches, is properly recovered by LES and is located around  $Z = 70 \text{ mm}$  as in experiments [51]. At the same time, we obtain a flame tip with a larger mean radius than in the experiment. The larger radius might be caused by the flame thickening employed in this region. However, since it can also be observed in other published LES studies with flame resolved simulations or with completely different approaches, we conclude that this might have another explanation.

The experimental  $OH$ -PLIF, when compared to LES, shows a weaker  $OH$  signal at the tip of the flame and above  $40 \text{ mm}$  in the branch B2. The latter one was explained in [77] by a locally rich mixture composition, induced by the larger droplets,

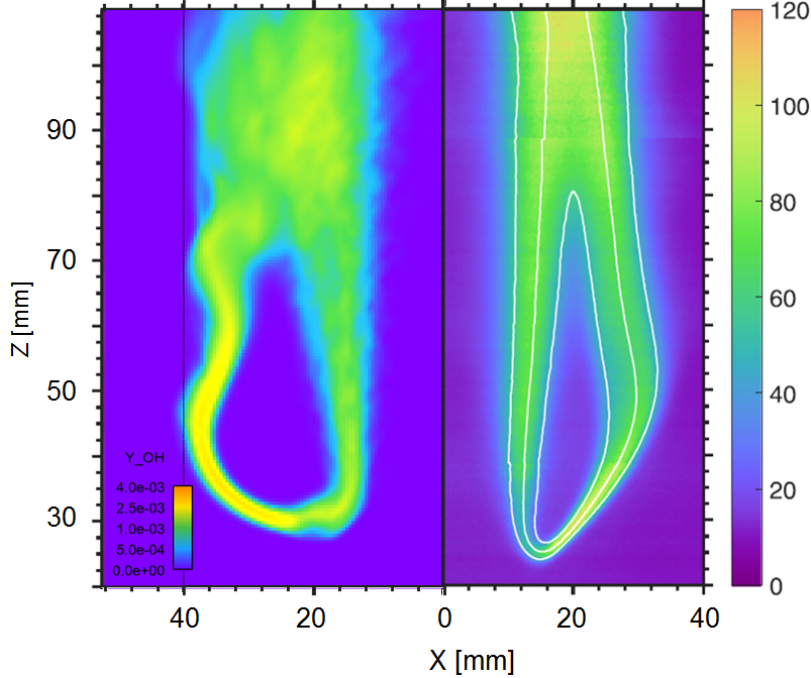


Figure 4-13: Mean LES OH mass-fraction on the left-hand side, experimental OH-PLIF on the right [51]

which continue to evaporate crossing B2. The weaker  $OH$  signal close to the flame stabilization point was related to the evaporation of droplets, which create strong local heat sinks when they cross the flame [77]. Since mass and energy sources are dispatched uniformly on the considered cell, and due to the statistical droplet representation by parcels, we cannot observe such strong local inhomogeneities. Recovering this local effect would require to avoid thickening, that is to turn to a high-resolution LES, which is not the objective of this study. The major question is whether such an effect is also observed in real gas turbines showing higher turbulence and possibly very different spray characteristics.

Downstream of the stabilization point in region B1, the flame thickening is responsible for the broader  $OH$  profile compared to the experiment. Another explanation for the differences in  $OH$  intensity compared to the experiment might come from the absence of soot modeling in the present LES. Indeed, soot formation observed experimentally 15  $mm$  downstream of the stabilization point, is accompanied with soot oxidation by  $OH$ , the latter thus being strongly reduced in this process. Thus, the absence of soot formation mechanism might be a reason for the broader and more

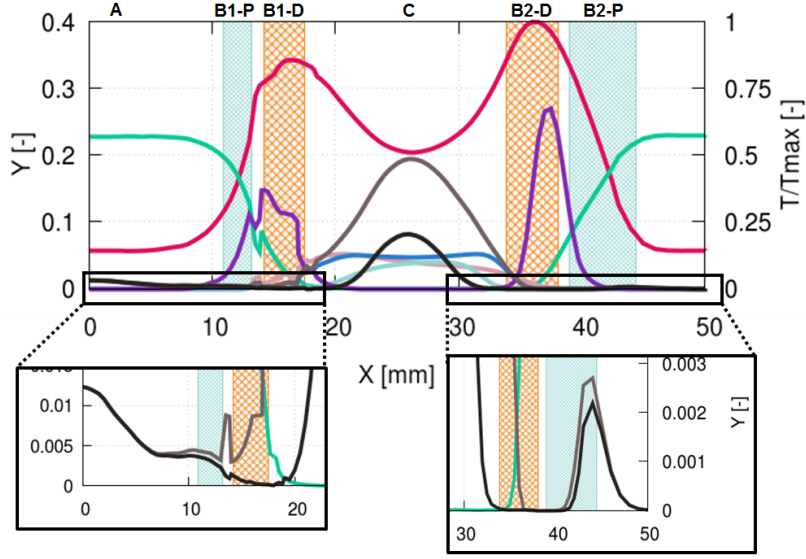


Figure 4-14: Reduced temperature and species mass fractions profiles at  $Z = 43 \text{ mm}$ . —:  $T/T_{max}$ , —:  $Y_{OH} \times 10^2$ , —:  $Y_{H_2} \times 10$ , —:  $Y_{C_2H_2}$ , —:  $Y_{C_2H_4}$ , —:  $Y_{nC_7H_{16}}$ , —:  $Y_{HC}$ , —:  $Y_{O_2}$ . The colored regions correspond to different combustion modes defined with Takeno index  $\mathcal{T}$ : blue – premixed mode with  $\mathcal{T} > 0.2$ , orange – non-premixed  $\mathcal{T} < -0.2$ .

intense  $OH$  profiles in the B2 branch above  $Z = 40 \text{ mm}$ , also observed by other numerical teams using different combustion approaches [72, 74, 56, 14].

Fig. 4-14 shows average radial profiles of the reduced temperature and of the main species at  $Z = 43 \text{ mm}$ , which is  $15 \text{ mm}$  above the LOL, to further analyze the flame structure. The main n-heptane pyrolysis products, which enhance flame propagation, according to [54] are:  $C_2H_2$ ,  $C_2H_4$ ,  $H_2$ , and are primarily found in region C (see Fig. 4-14). Acetylene is among these species and plays an important role in the soot formation mechanism.

On the left side of Fig. 4-14, the lean premixed flame B1-P is seen to be fed by fuel and oxidizer from region A, where the smaller droplets evaporate. Region B2-P shows lower values of  $Y_{HC}$  giving a fuel/air equivalence ratio globally below the lean flammability limit and much-reduced heat release rates compared to B1-P. Region B2-P is, therefore, probably not a self-sustained flame but rather an oxidation zone sustained by the hot products of diffusion flame B2-D. This premixed region was not observed in [73], and experimental measurements do not allow to ascertain its existence. In our LES, this zone is fed by the fuel evaporated from the largest droplets

that cross the zone B2, which were also observed experimentally. The uncertainty, therefore, concerns the importance of the fuel mass flux brought by these droplets.

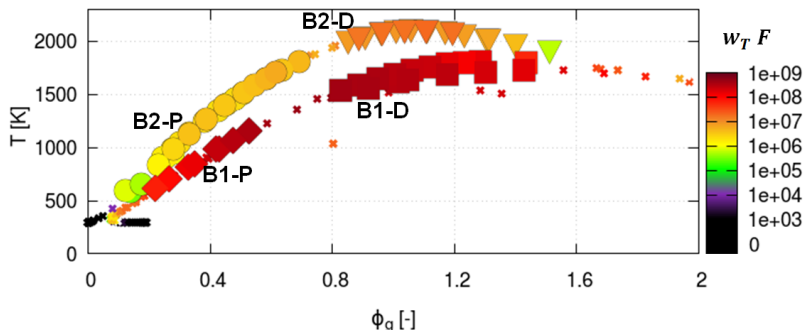


Figure 4-15: Gaseous temperature versus gaseous fuel/air equivalence ratio at  $Z = 43 \text{ mm}$ . The points are colored with heat release values scaled with thickening factor values  $w_T F$ , and are divided into four characteristic flame zones (see Fig. 4-14) marked with symbols:  $\diamond$ : B1-P,  $\square$ : B1-D,  $\circ$ : B2-P,  $\nabla$ : B2-D.

The temperature profile in Fig. 4-14 exhibits two picks in B1-D and B2-D and attains its maximum in B2-D, similar to Fig. 6 in [49], but in our case with the second peak located further away from the jet axis. This difference might be explained by a quite under-predicted LOL obtained in [72], and thus sharper spray trajectory angles, which affect the shape of the resulting flame. Another reason for such a thin flame, as mentioned in [49], could also be the insufficient domain size, which is, in our case, 1.5 times larger.

The peak temperature in zone B1 is found to be lower than the peak in zone B2, which is in agreement with the reduced mechanism simulation of [72]. This lower temperature is explained by intense endothermic reactions caused by the fuel pyrolysis, which is confirmed by 2-step simulation of [72], which shows a much higher peak temperature in zone B1.

In Fig. 4-15, the two branches B1 and B2 can be clearly distinguished. Both detected premixed regions B1-P and B2-P establish in lean zones, while diffusion flames B1-D and B2-D are mainly found between  $\phi = 0.8$  and 1.5. Although the outer branch B2 is characterized by higher temperatures, the heat release is two orders of magnitude lower compared to the inner reaction zone B1, probably due to the low turbulence intensity, and to the endothermic reactions, which continue to take place

in the outer reaction zone.

## 4.4 Conclusions

The TFM-AMR modeling approach described in Chapter 2 and validated first on the 1D n-heptane flames in Sec. 3.1 was applied here to a lab-scale academic two-phase burner as a first step toward the usage of TFM-AMR in real industrial gas turbines.

The LES correctly captures the gas and droplet velocities as well as the droplet size distribution for both cold and reacting cases. The lift-off length and the global flame shape are correctly recovered. Only the upstream part of the flame presents an excessive radius of curvature. This observation, shared with LES of other research groups, is not understood today and requires further investigation. A possible explanation would be the absence of soot description in all LES performed so far, which might strongly affect the flame dynamics.

Although the present flame is stabilized by a premixed flame, non-premixed combustion significantly contributes to the whole heat release. In the present LES, TFM predicts no thickening in non-premixed flame regions and still shows a correct agreement with the experiment. However, this configuration does not allow us to conclude TFM validity in the non-premixed regime. For this purpose, a setup showing a more turbulent diffusion flame would be necessary. It is also probable that a specific formulation of TFM is required for this regime that needs to be developed in future studies.

The simplified configuration of the CORIA burner does not possess some important characteristics of an industrial burner. To pursue the testing of the TFM model, a swirl stabilized burner is investigated in the next chapter.



# Chapter 5

## DLR burner

The TFM-AMR modeling approach was validated first on the 1D spray flames in Chapter 3. In Chapter 4 we applied TFM-AMR in the context of the CRSB burner and obtained accurate predictions of the main flame characteristics observed experimentally, such as the flame topology, the flame lift-off, the mean gaseous, and the mean spray profiles. However, unlike real aero-engines, the CRSB burner is unconfined, operated at the atmospheric conditions, and the air co-flow is not swirled. Despite all these simplifications, this was an essential step in the model validation procedure since the CRSB burner is well documented and offers an extensive database to assess the performance of spray flame modeling strategies.

Our next goal is to verify the TFM-AMR modeling approach in a more complex configuration. Nowadays, high-pressure and high-temperature burner measurements remain pretty challenging, and therefore very few experimental datasets are available in the literature. Compared to the CRSB flame, a flame within a confined burner with a swirled air co-flow has a different topology and characteristics. Therefore, we made a choice to investigate such a configuration first.

The Gas-Turbine Model Combustor configuration designed by Grohmann et al. in [31] is selected as a validation target for the TFM-AMR model. We begin this chapter with the description of the experimental facility in Sec. 5.1. Section 5.1 then provides next a summary of the numerical studies of this burner configuration. A stable flame at reference conditions is investigated next in Sec. 5.3, followed by a lean

blowout studied in Sec. 5.4.

## 5.1 Experimental facility

The Gas-Turbine Model Combustor is a laboratory-scale burner that features real aero-engines characteristics, such as prefilming airblast atomizer and confined geometry. The combustor was designed by Grohmann et al. in [31] to study swirl-stabilized spray flames at atmospheric conditions and offers validation data for CFD simulations.

The Gas-Turbine Model Combustor's measurement database includes stereo particle image velocimetry (PIV),  $CH$  radical chemiluminescence, Mie scattering of the fuel droplets, and temperature measurements by means of vibrational coherent anti-stokes Raman spectroscopy (CARS). A series of experiments were also performed to identify a fuel/air equivalence ratio at which the flame extinguishes by keeping an air mass flow rate constant and slowly reducing a fuel supply. The flame extinction, the lean blowout (LBO), was determined by eye.

Along with the reference kerosene Jet A-1 fuel, multiple single-component fuels, such as toluene, cyclohexane, iso-octane, n-dodecane, n-nonane, and n-hexane, were considered to investigate the fuel influence on the flame characteristics. Since kerosene flames are similar to flames operated with n-dodecane, n-dodecane is selected for the present study to avoid complexities related to multi-component fuel use, which is not the focus of this thesis. The experimental rig with the superimposed photo of the n-dodecane flame is shown in Fig.5-1 (left).

The reference n-dodecane flame is defined at a global equivalence ratio of  $\phi = 0.8$  with an air mass flow rate of  $\dot{m}_{air} = 4.3g/s$ , introducing a liquid mass flow rate of  $\dot{m}_{fuel} = 0.23g/s$ . This reference configuration results in a thermal power of  $P_{th} = 10.12kW$ .

The nozzle of the combustor, shown in Fig.5-1 (right), consists of an inner swirler with  $8mm$  diameter and an outer swirler with  $11.6mm$  diameter. An annular ring with a sharp edge separates two resulting air co-axial, co-rotating swirling air flows.

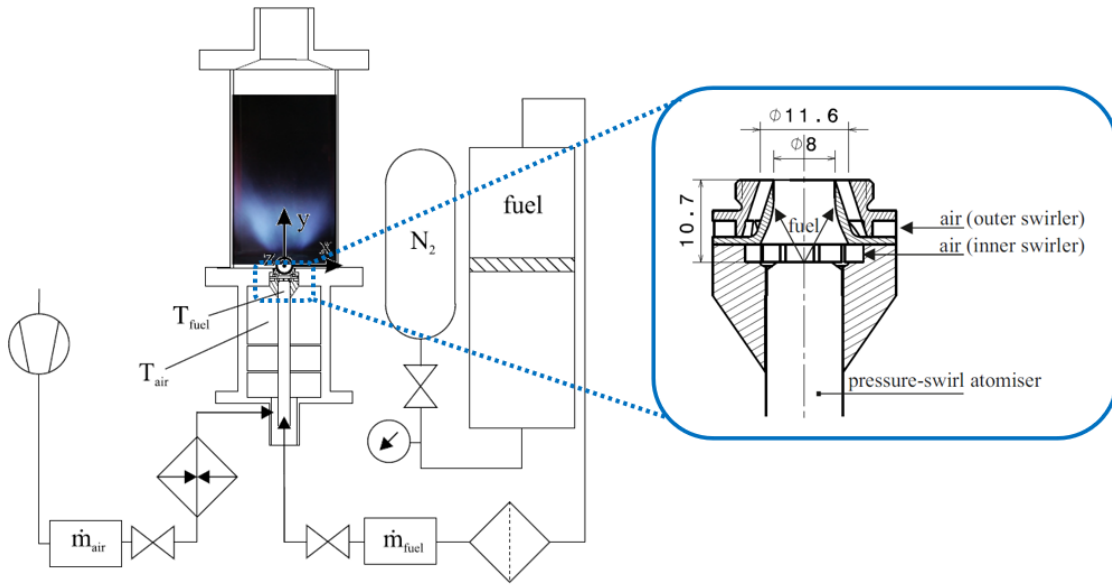


Figure 5-1: Gas-Turbine Model Combustor [31]: rig with superimposed n-dodecane flame photograph (left); nozzle (right).

Both swirlers are fed from the same air plenum where the temperature is kept constant and is equal to  $T_{air@inlet} = 323K$ . The Reynolds number based on the outer swirler diameter is  $Re \approx 25000$ .

The temperature of the liquid fuel is also kept constant at a value  $T_{fuel@injector} = 303K$ . First, the liquid fuel is injected through a pressure-swirl atomizer resulting in a hollow spray cone. The liquid fuel forms a thin liquid film inside the nozzle, sprayed onto the annular ring's surface. This film is then transported towards the ring's lip, which is finally re-atomized when entering the combustion chamber.

For more details about the combustor geometry and its configuration, please refer to [31].

## 5.2 DLR burner: State of the art

To the best of our knowledge, the DLR model combustor was investigated numerically only by Eckel et al. in [21]. In this work, the authors target a burner operated with the Jet-A1 fuel at the reference conditions, a configuration which is pretty similar to

the one investigated below with n-dodecane. The chemical surrogate for kerosene used in this study consists of four species and is described with a chemical mechanism that includes 80 species. Here, the chemistry is integrated directly without any specific sub-grid combustion treatment.

The authors in [21] identified five distinct zones within the burner that are illustrated and numbered in Fig. 5-2. The highest temperatures were detected in zone 2, or the Flame zone, where the mixture fraction values lie close to the stoichiometry, indicated with the green lines. On the contrary, the lowest temperatures are found in the first zone, which was referred to as Unmixed air stream. Hot gases together with unburned droplets recirculate in zone 5, also called Upper mixed zone. These hot gases mix with the air stream in zone 4, Lower central mixing zone. The hot recirculating zones enclosed between the combustion chamber walls, the flame zone, and the air stream, zone 3 or Lower external zones transport combustion products towards fresh gases. The detailed description of the flow can be found in [21].

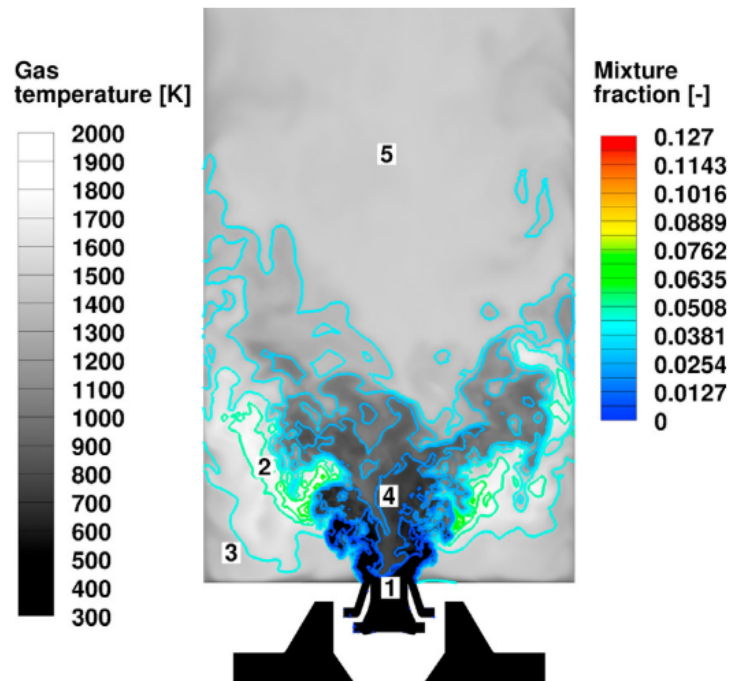


Figure 5-2: Characteristic zones in the Gas-Turbine Model Combustor defined by Eckel et al. in [21]. Instantaneous temperature field (grey scale contour plot), mixture fraction (colored lines).

The obtained results revealed that evaporation and mixing are the rate controlling

steps in the flame zone. However, the authors point out the importance of the use of finite chemistry in this burner configuration since the finite rate chemistry effects dominate in zones outside the main flame region.

Overall, a good agreement was demonstrated between the measurements and LES results, with some discrepancies observed in the mean temperature profiles. The computed temperatures in the middle of the domain were about  $400K$  lower than those obtained experimentally. Moreover, the maximum temperatures within the burner found downstream of the flame were slightly lower than in the experiments. This inaccuracy of numerical results was attributed to the excessive heat losses caused by the Dirichlet boundary conditions imposed on the walls. Another source of uncertainty mentioned in the study is the simplified fuel injection model used in this study.

A DLR team performed the lean blowout simulations within the JETSCREEN project to investigate fuel dependency. The obtained results were briefly presented during the project report. While visible fuel effects were detected under stable conditions, the influence of the fuel on LBO was not captured. Although a flame extinction was captured numerically, the predicted LBO limits were too low compared to the experiments.

## 5.3 DLR burner LES: reference flame conditions

A stable flame at the reference conditions defined in Sec. 5.1 is investigated using the TFM-AMR modeling approach in this section. The numerical settings are summarized in Sec. 5.3.1 and are followed by the non-reacting flow validation in Sec. 5.3.2. The results of the reacting flow are then presented in Sections 5.3.3 - 5.3.6.

### 5.3.1 Numerical setup and geometry

The CONVERGE CFD solver [67] is employed to perform all the simulations in this study. The computations are done using a Cartesian mesh, while complex geometry is simulated with a cut-cell approach. Further numerical settings have already been detailed in Sections 3.2.2 and 4.3.1

The LES computational domain, shown in Fig.5-3, includes an air plenum with inlet tubes, and a combustion chamber. A cylindrical domain is added downstream the burner in order to impose the correct acoustic impedance at the burner outlet. At the bottom of this cylinder, an air co-flow is added to facilitate the evacuation of the flame products towards the outlet.

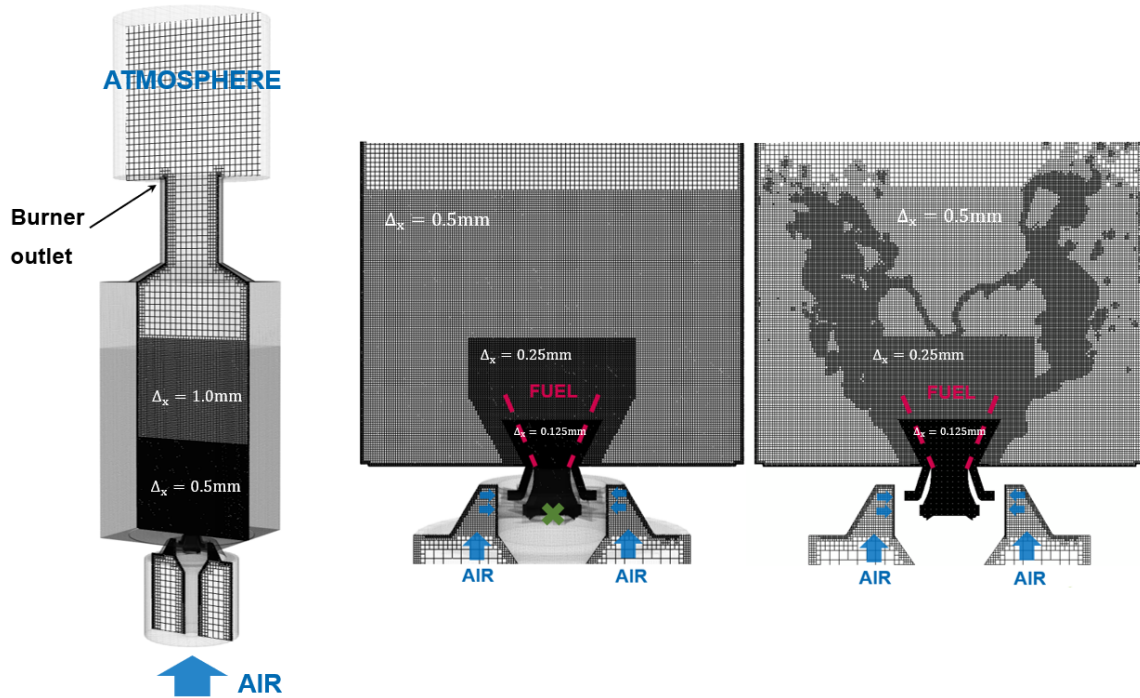


Figure 5-3: Simulation domain (left); Mesh with fixed embeddings (middle); Mesh with fixed embeddings and AMR (right).

A static mesh shown in the middle of Fig.5-3 is achieved through fixed, refined regions and is used in the non-reacting configuration, whereas the same mesh but with AMR shown on the right of Fig.5-3 is used for reacting simulations. The cell size reaches its minimum of  $0.125\text{mm}$  near the injector and within the burner nozzle. With one additional AMR level, we obtain  $\Delta_x = 0.25\text{mm}$  within the flame front. These settings result in  $16.5 \times 10^6$  cells for the non-reacting configuration and approximately  $22 \times 10^6$  cells in the reacting case with active AMR.

A similar modeling strategy to the one used for CRSB computations, described in Sec. 4.3.1, is adopted below to model unresolved turbulent stresses, unresolved scalar transport, and spray combustion.

It was shown in Sec. 3.2.3 that dilution has an impact on the heat release rate peak, which requires the use of a higher flame sensitivity TFM parameter to detect the flame front properly. In the Gas-Turbine Model Combustor, recirculating zones induce a mixing with burned products; therefore, we use a higher value for the sensor sensitivity  $\beta$ , which equals 30. The sensor relaxation times parameters are set to  $\alpha_{hot} = 0.05$  and  $\alpha_{cold} = 0.005$ .

In the simulations presented below, the behavior of thickened flames under stretch conditions is corrected according to the model proposed in Sec. 2.3.3.

The reduced n-dodecane mechanism presented in Sec. 3.2.1 is used in reacting cases and contains 43 species and 235 reactions.

### Thermal boundary conditions

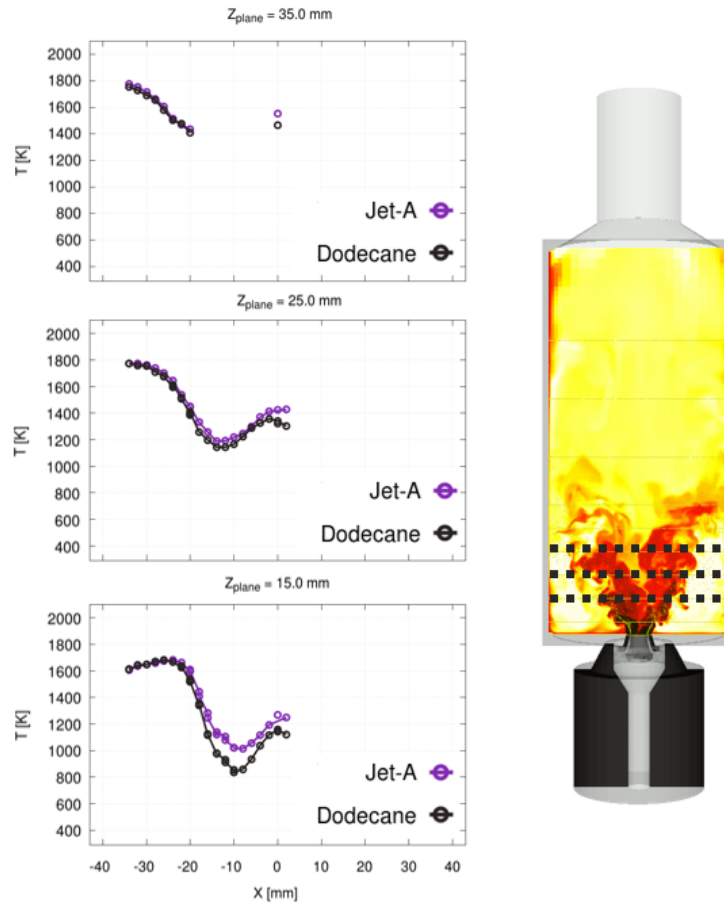


Figure 5-4: Gaseous mean temperature radial profiles obtained experimentally for kerosene and n-dodecane flames.

To provide boundary conditions for numerical simulations, the wall temperatures were measured inside the combustion chamber using phosphor thermometry. However, such measurements were performed only for the reference Jet A-1 flame. On the other hand, mean flow temperature measurements within the combustion chamber, which were done using single-shot broadband shifted vibrational coherent anti-Stokes Raman spectroscopy (SV-CARS), are available for both kerosene and n-dodecane flames operated at  $\phi = 0.8$  and shown in Fig.5-4. Temperature radial profiles are available for the planes indicated with black dashed lines on the burner sketch, as represented on the right-hand side of Fig.5-4, located  $15mm$ ,  $25mm$  and  $35mm$  downstream the nozzle. Since both kerosene and n-dodecane flames demonstrate significant similarities when approaching the burner walls, we impose the temperatures measured for the Jet A-1 flame in our simulations.

The wall temperatures were measured along the combustion chamber at  $X = -20mm$ ,  $X = 0mm$ , and  $X = 20mm$ . Although a slight asymmetry can be observed between these three axial profiles, which can be explained by the flow asymmetry [30], the resulting profiles are very close to each other.

The numerical study of Eckel et al. highlighted the importance of using adequate thermal boundary conditions at the walls [21]. In this study, an average temperature of all measured points  $T = 1205K$  is imposed at the walls. Such settings were mentioned as one of the possible reasons for the temperature underestimation observed within the combustion chamber because it could potentially result in excessive cooling at the walls. Also, setting up the adiabatic simulation would probably lead to largely over-predicted temperatures due to non-negligible heat transfers at the walls.

Instead of setting one temperature value at the sidewalls, we prescribe a 1-dimensional temperature profile at the combustion chamber walls as shown on the right side in Fig. 5-5. This average 1-dimensional temperature profile plotted as a function of the axial coordinate on the left in Fig. 5-5 is obtained from the averaging of experimental profiles. These profiles were measured at the planes located at  $X = -20mm$ ,  $X = 0mm$ , and  $X = 20mm$ , shown with red dashed lines in Fig. 5-5.

The maximum wall temperature of  $1400K$  can be found at  $Z = 50mm$  and is due

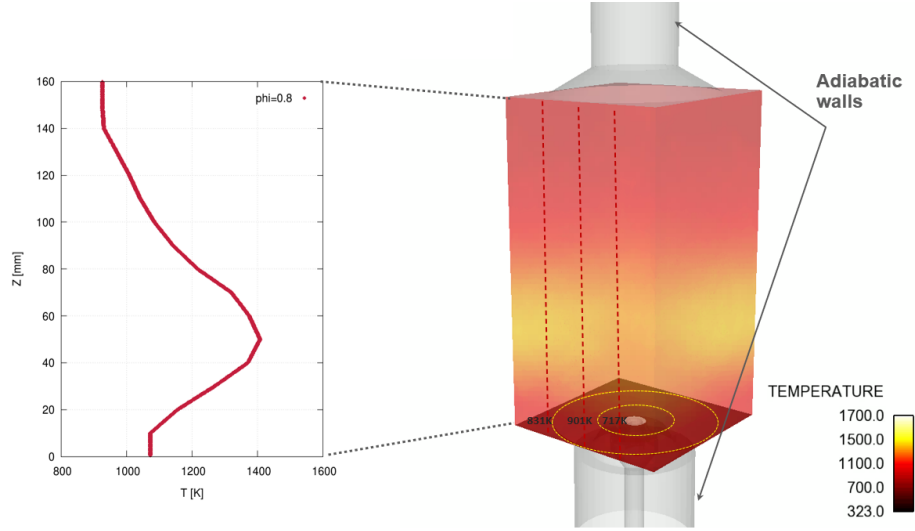


Figure 5-5: Temperature boundary conditions. Left: 1D temperature profile prescribed at the walls. Right: burner walls with assigned temperatures.

to the presence of the flame. As it can be seen in Fig. 5-5, the wall temperatures decrease upstream and downstream in the measured range to approx.  $900K - 1000K$ .

At the burner's bottom plate, the temperature of the glowing ring, the area enclosed between yellow dashed lines in Fig. 5-5, is set to  $901K$ . Temperatures decrease outside the glowing ring and are set to  $717K$  in the nozzle's vicinity and  $831K$  in the region closer to the chamber walls. The walls within the air plenum and at the outlet are considered adiabatic.

## Fuel injection

The combustor configuration includes prefilming airblast atomization, for which the realistic representation requires a significant modeling and computational effort and has not been widely studied in the literature so far. Since it is not the focus of this study, we adopt a simplified model for the fuel injection used in CRSB computations.

Instead of injecting the liquid fuel right in the nozzle, represented by a green cross in Fig.5-3, we inject fuel droplets directly at the nozzle's exit, over the prefilmer lip perimeter. The actual fuel injection locations correspond to the base of the red dashed lines in Fig.5-3.

The original simplified fuel injection model described in Sec. 4.3.2 was designed

for pressure-swirl atomizers and required an orifice radius  $R_o$  as an input parameter replaced here with the radius of the inner swirler. The liquid film thickness calculated from the difference between  $R_o$  and the air cone radius  $R_a$  is not anymore provided by the model but is a fixed quantity to ensure a reasonable ring thickness over which the droplets are introduced into the computations domain. The liquid film thickness is chosen to be  $120\mu m$ , a value close to the largest injected droplet diameter.

The Rosin-Rammler distribution is prescribed at the injection plane and ensures a polydisperse description of the spray cloud. The distribution is defined with a  $15\mu m$  Sauter mean diameter and a spreading factor  $q = 1.8$ , the values fitted using experimental measurements.

### 5.3.2 Non-reacting flow validation

Non-reacting simulations are conducted first to ensure that the flow field is correctly predicted. In the following, we define a flow-through-time  $FTT=4.2ms$  from the combustion chamber's length  $169mm$  and the average axial velocity  $38m/s$  established at the nozzle outlet.

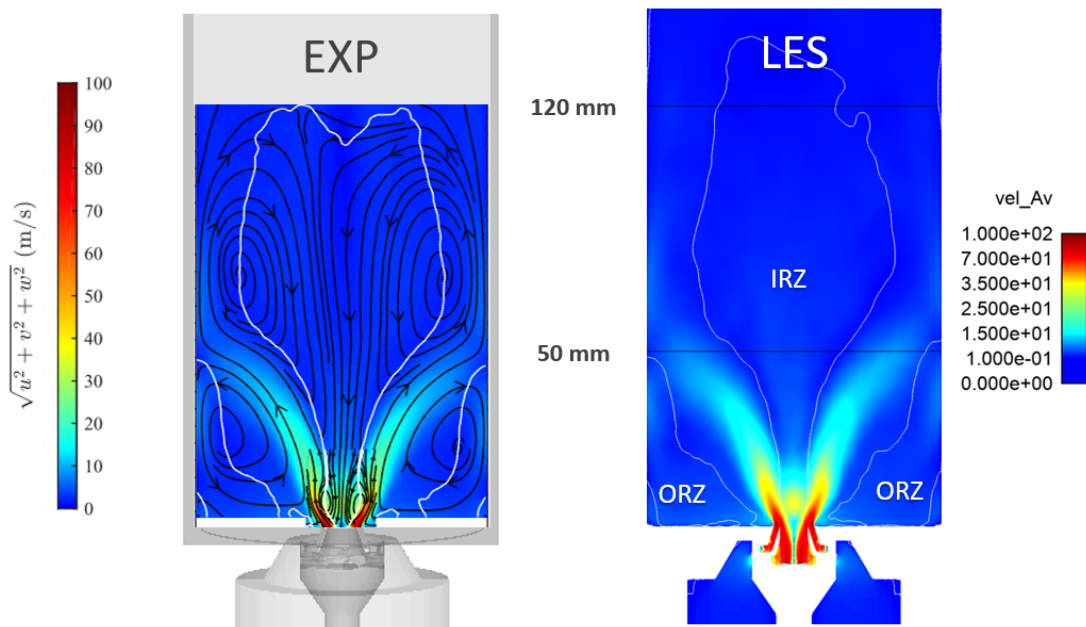


Figure 5-6: Average velocity field of a non-reacting flow: experiments (left); LES simulations (right)

To compute an average velocity field the data was collected and averaged over 33 FTT after a steady state was attained. Figure 5-6 compares the average velocity field obtained experimentally and the one extracted from the LES simulation. The white lines correspond to the zero mean axial velocity component and indicate the locations of the recirculation zone boundaries: the inner recirculation zone (IRZ) and two outer recirculation zones (ORZ).

Mean and RMS radial velocity profiles are given in Figures 5-7 and 5-8 respectively, where the three velocity components (radial, circumferential and axial) are displayed using three columns. Each line in the Figures 5-7 and 5-8 represents an axial plane located  $1mm$ ,  $15mm$ ,  $35mm$ ,  $55mm$  and  $125mm$  downstream the nozzle. The y-scale on the plots decreases while moving away from the injection plane  $Z = 0mm$ , since the velocities drop from approximately  $100m/s$  in the vicinity of the nozzle down to almost zero at the end of the combustion chamber.

Both the mean and the fluctuating velocity components are reproduced well in the entire domain.

At the plane  $Z = 1mm$  in Fig. 5-7, located close to the nozzle, we can clearly distinguish four peaks introduced by the inner and the outer swirlers. Downstream these four peaks merge into two, as seen at  $Z = 15mm$ .

Negative velocities at the middle of the domain indicate the presence of a strong inner recirculation zone that extends into the nozzle. It is also visible in Fig.5-6.

Figures 5-6, 5-7 and 5-8 confirm that LES accurately predicts the velocities in the simulation domain, as well as the locations of the inner and the outer recirculation zones.

### 5.3.3 Reacting flow: reference configuration

Reference flame conditions were defined in Sec. 5.1 with the global equivalence ratio of  $\phi = 0.8$  and with the air mass flow rate of  $\dot{m}_{air} = 4.3g/s$ . This reference flame serves as a starting point for a series of LBO simulations discussed below in Sec. 5.4 and should be analyzed in the first place.

This section deals with an investigation of the resulting flame at the reference

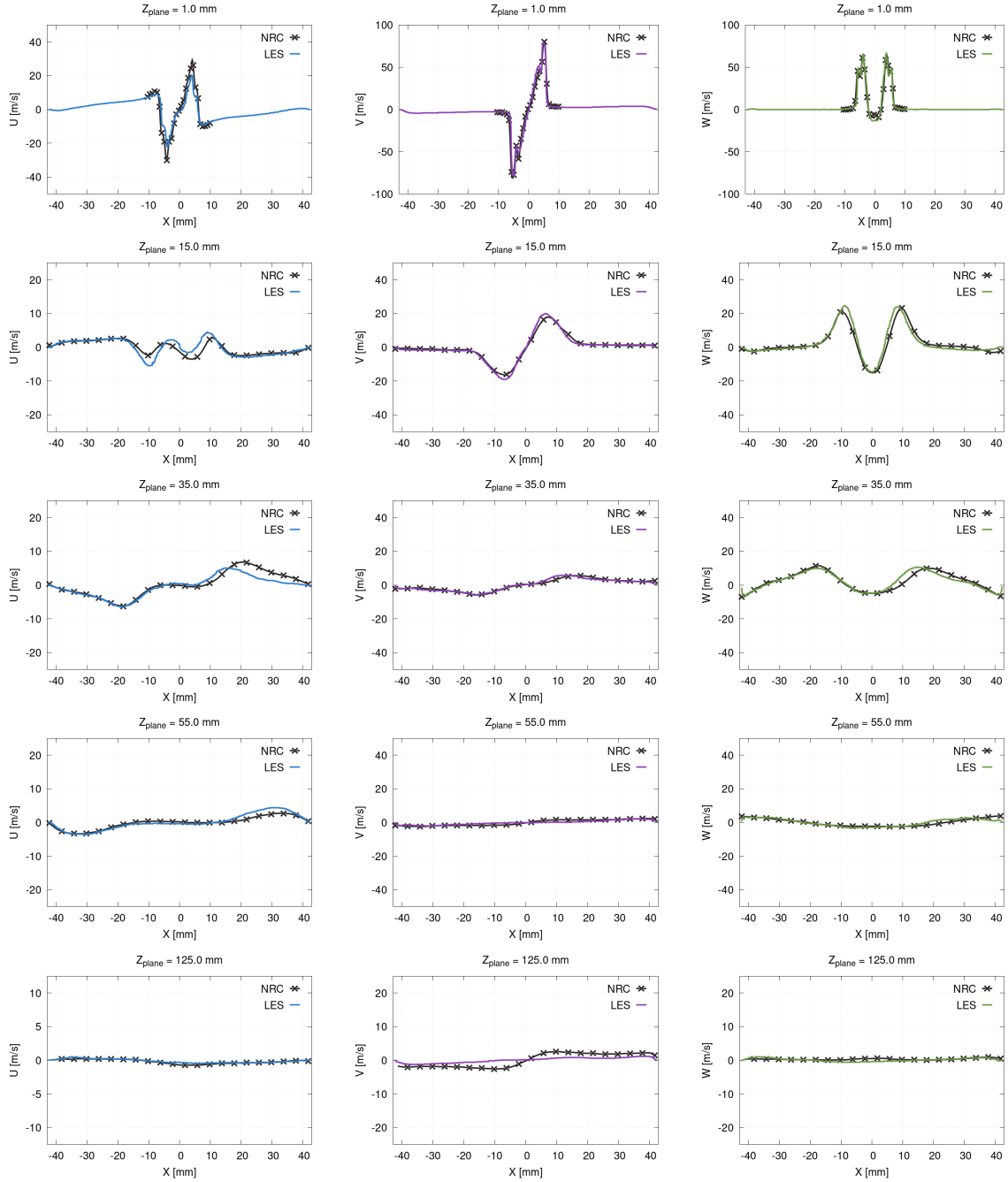


Figure 5-7: Mean velocity components at  $Z = 1/15/35/55/125\text{mm}$ : radial (left), circumferential (middle), axial (right). Non-reacting case.

conditions. Additionally, we will assess the impact of the correction due to the parcel/flame orientation introduced in Sec. 2.3.4, of the refinement, and of the radiative heat losses on the simulation results.

All the cases considered in this section are listed in Table 5.1. We will start the

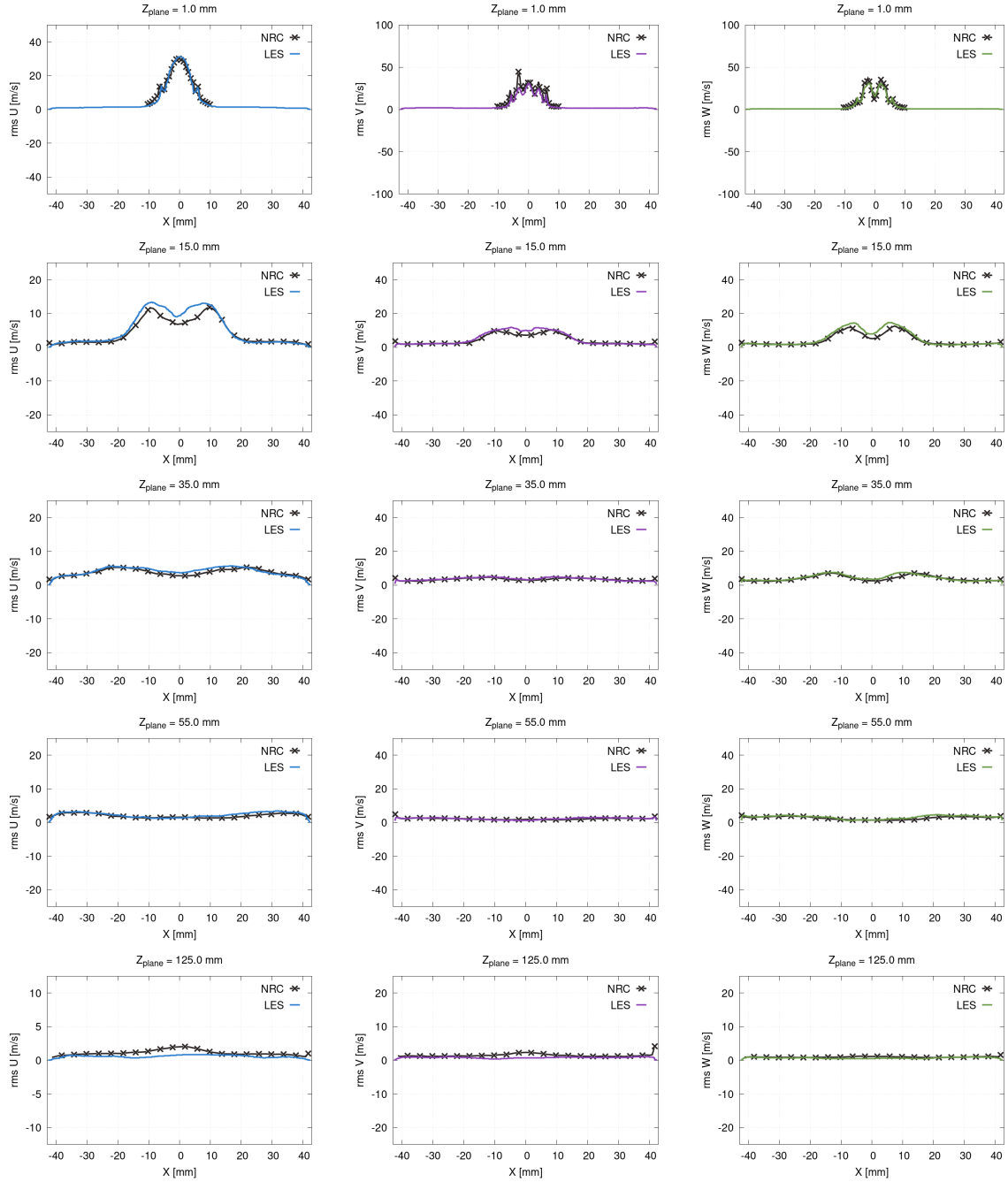


Figure 5-8: Rms velocity components at  $Z = 1/15/35/55/125\text{mm}$ : radial (left), circumferential (middle), axial (right). Non-reacting case.

results' discussion by presenting the results of a reference case, denoted as DLR-rc-ref in Table 5.1.

In the reference DLR-rc-ref case, the TFM-AMR target thickening factor, as defined in Eq.(2.16), is set to 5. Here, the use of one additional level of AMR leads to

Configuration	$\Delta_x$ within flame	Stretch correction	Orientation correction	Radiation	Target thickening
DLR-rc-ref	$0.25mm$	+	+	-	$F_{target} = 5$
DLR-rc-noCorr	$0.25mm$	+	-	-	$F_{target} = 5$
DLR-rc-rad	$0.25mm$	+	+	+	$F_{target} = 5$
DLR-rc-amr	$0.125mm$	+	-	-	$F_{target} = 1$

Table 5.1: Computed flame configurations at reference conditions.

the cell size of  $0.25mm$  within the flame front.

The computed thermal power is given as a function of time in Fig. 5-9, while the burner's thermal power of  $P_{th} = 10.12kW$  is represented with the black horizontal line. Figure 5-9 shows that a steady state is successfully reached and, as the averaged power closely matches the experimental value, that the incoming fuel is correctly burned.

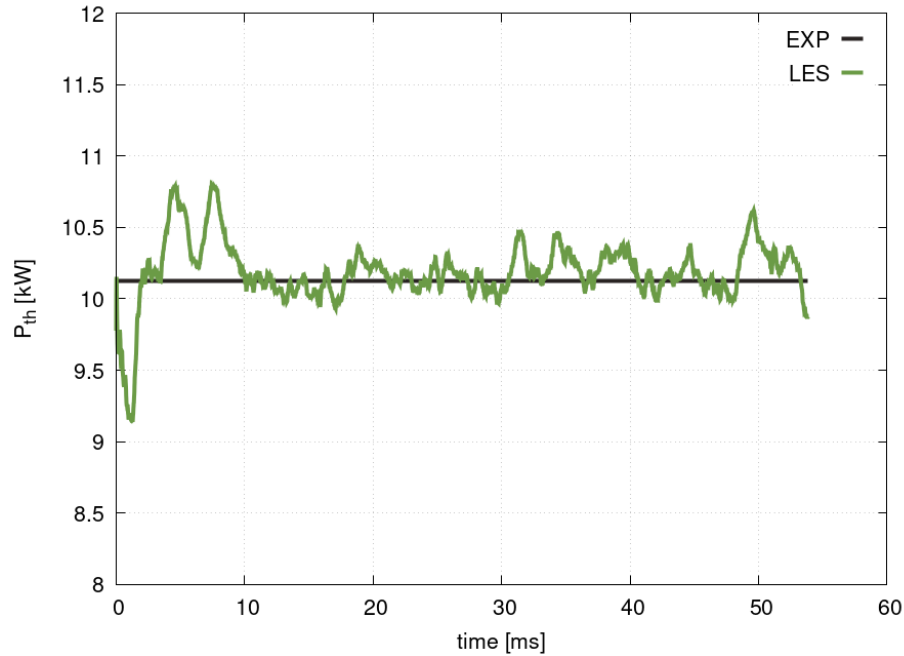


Figure 5-9: DLR-rc-ref case. Total power.

Figure 5-10 shows instantaneous variables representative of the combustion process and the TFM modeling.

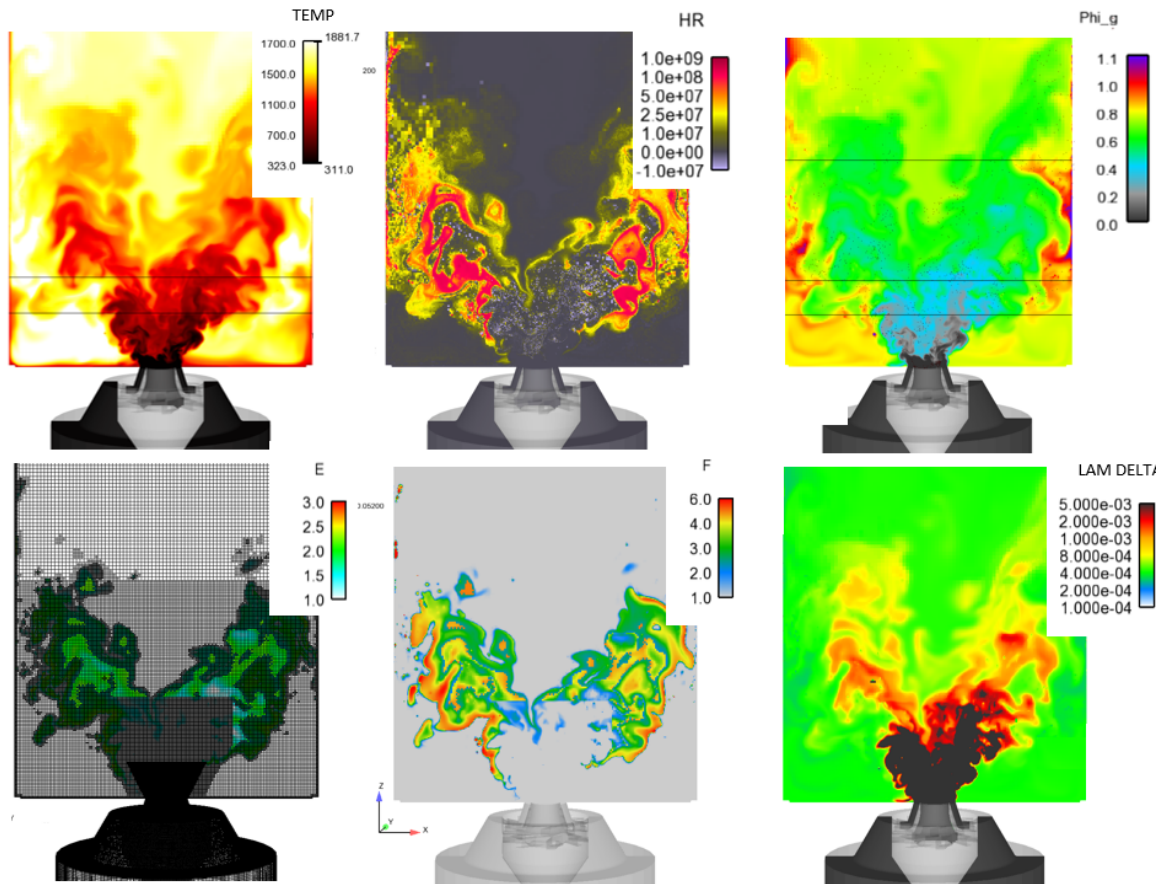


Figure 5-10: DLR-rc-ref case. Instantaneous fields: gaseous temperature, heat release rate, gaseous fuel/air equivalence ratio, efficiency factor with superimposed mesh, thickening factor, tabulated laminar flame thickness.

The instantaneous heat release rate field reveals a highly wrinkled flame hitting the sidewalls of the combustion chamber. The computed flame has a clearly defined V-shape, which is consistent with the experimental findings of Grohmann et al. [1].

The inner recirculation zone (IRZ) and the outer recirculation zones (ORZ) are all characterized by high temperatures. At the same time, the heat release rate field reveals no up to moderate chemical activity in these regions.

While the global gaseous fuel/air equivalence ratio is 0.8, the maximum local gaseous fuel/air equivalence ratio values exceed unity in the ORZ where burned gases are recirculating. Therefore, laminar flame thicknesses retrieved from the table (tabulated laminar flame thickness in Fig. 5-10), which are based on the local equivalence ratio, are smaller in the ORZ. The TFM thickening is thus higher in these regions than in the central part of the domain, as visible in the corresponding instantaneous

$F$  field in Fig. 5-10. For this reason, the mesh refinement is first applied at outer flame portions where the thickening factor exceeds the target of five.

### Flow variables averaging

At the reacting conditions, the data was averaged over 10.3 FTT after the steady-state was reached.

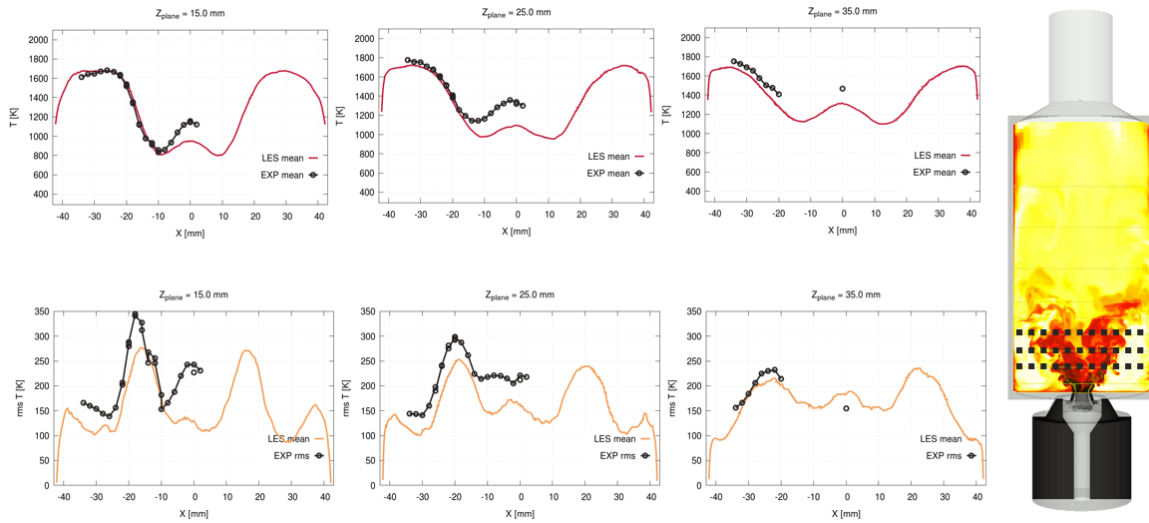


Figure 5-11: Gaseous temperature profiles at  $Z = 15/25/35mm$ : mean (top); RMS (bottom)

The radial temperature profiles are compared against the experiments in Fig. 5-11. Mean temperatures and their fluctuating component are available for three axial planes located at  $15mm$ ,  $25mm$ , and  $35mm$  above the nozzle's exit. The burner with superimposed instantaneous temperature field is also shown in Fig. 5-11 to illustrate the location of considered axial planes shown with black dashed lines.

Figure 5-11 demonstrates that the location of the flame front and the resulting temperature profiles are accurately predicted by LES. Under-predicted mean temperatures in the central region defined by  $|X| < 10mm$  indicate that hot burned gases in the central region are not extended enough towards the nozzle in the LES. The discrepancy with experimental values reaches its maximum of around  $200K$  along the axial line. This could be potentially due to a weak swirl motion that does not sufficiently promote the central recirculation of burned gases. These discrepancies

could also result from low thickening levels in the central region, which can lead to insufficient mixing.

We can also note that the temperature fluctuations at the center are lower than the ones observed experimentally. A possible explanation for the under-predicted RMS values might be related to the under-prediction of mean temperatures since the plotted RMS profiles represent the absolute values and not the relative ones.

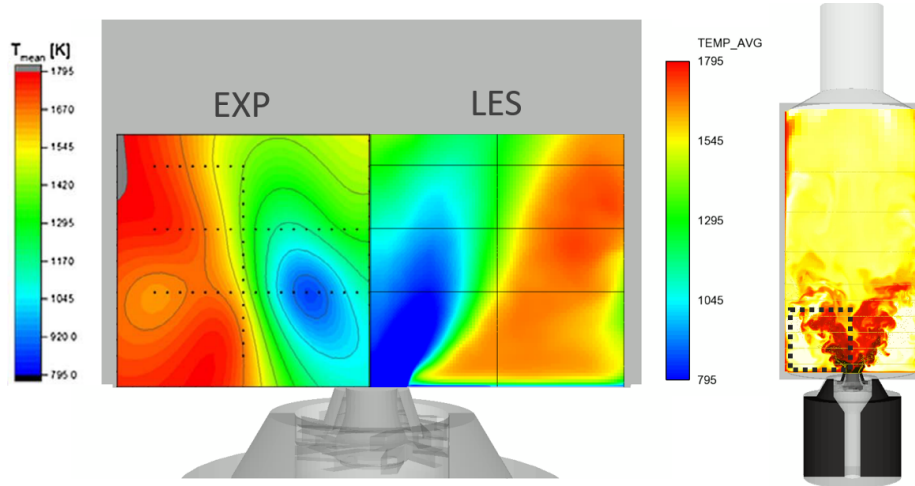


Figure 5-12: Averaged temperature field: experiments versus numerical results (left); instantaneous temperature field (right).

Figure 5-12 provides the comparison of averaged temperature field obtained experimentally with the LES results on a 2D slice. In the experimental results, the locations of the actual measurements are marked with black dots, while the other data points are obtained through extrapolation. The compared region is highlighted on the burner sketch with a dashed square.

In line with the observations made in Fig. 5-11, Fig. 5-12 illustrates that the computed temperatures are underestimated at the center-line, while the other regions show a good agreement between LES and experiments. However, it should be noted that the extrapolated experimental temperatures in the vicinity of the nozzle can be completely wrong and should not be compared with the LES results.

The hydroxyl radical  $\text{OH}^*$  is often measured as a heat release rate marker. Although  $\text{CH}^*$  chemiluminescence does not rigorously correspond to the heat release rate, such comparison can give a rough estimate of whether the LES flame shape is

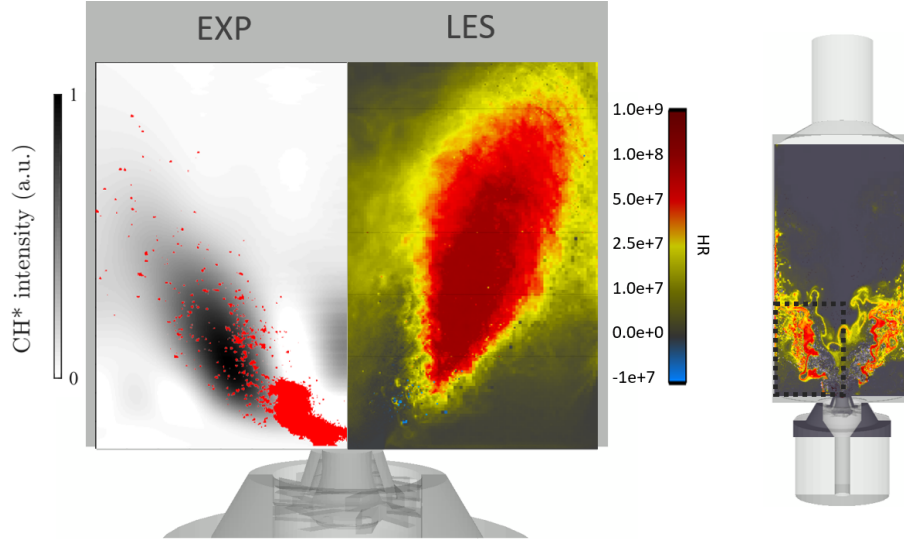


Figure 5-13:  $\text{CH}^*$  chemiluminescence and Mie scattering(left); averaged heat release rate field (right).

similar to the experimental one.

Figure 5-13 presents the averaged Abel-deconvoluted  $\text{CH}^*$  chemiluminescence signal adapted from [3], where red points correspond to the overlaid Mie scattering signal. The averaged heat release rate extracted from LES is shown on the right in the same figure. The burner with the superimposed instantaneous heat release rate is also sketched to highlight the comparison region with black dashed lines.

Looking at Fig. 5-13 we can observe notable similarities between the regions of the maximum heat release rate and the maximum  $\text{CH}^*$  intensity. However, the computed flame stabilizes slightly higher and has a broader shape. The latter may have multiple explanations. The broader flame can be directly linked to the flame thickening applied in this region. Moreover, using TFM might result in an under-estimation of mixing in the highly turbulent region close to the inlet, which could then affect the stabilization height. The simplified fuel injection strategy could also cause these discrepancies since the fuel is injected directly at the prefilmer lip and follows the prescribed droplet size distribution, not within the nozzle, as done in the experiment. In the experiment, a certain amount of the liquid fuel enclosed in small droplets can be entrained by the flow within the nozzle and evaporate later. This behavior can not be reproduced in the computations with the selected fuel injection strategy. Therefore, the simplified

fuel injection can result in a misprediction of the fuel content and can finally affect the flame shape.

### Lagrangian particles averaging

All spray radial profiles presented in Chapter 4 were obtained by setting the probes in the same way as done experimentally and averaging all the droplets that cross the probe locations. Here, the averaging of dispersed phase data is done following the procedure described below to decrease the computational costs.

To obtain time-averaged profiles characterizing the dispersed phase, cell averaged spray properties were collected during the simulation run-time to compute final averaged values at the end of the simulation.

Within one computational cell, several parcels can be present simultaneously. Therefore, we compute cell averaged properties at each time step. With the initial values set to zero, the spray velocity components  $\tilde{u}_j$  are accumulated each time step  $dt_i$  using:

$$\tilde{u}_j = \sum_{t_{start}}^{t_{end}} \frac{\sum_{n_p=1}^{n_{p,tot}} u_i n_{d@p}}{\sum_{n_p=1}^{n_{p,tot}} n_{d@p}} dt_i, \quad (5.1)$$

where  $n_{p,tot}$  is the number of parcels within the considered cell,  $n_{d@p}$  is the number of droplets within the parcel,  $t_{start}$  is the starting time of the averaging procedure, and  $t_{end}$  its ending time.

We perform multiplication with the time step interval  $dt_i$  when  $\tilde{u}_j$  is updated to exclude cells that do not contain any parcel from the averaging procedure. At the same time, the variable  $\tilde{dt}$  is updated for each cell in case there is a parcel, such that  $\tilde{dt} = \sum_{t_{start}}^{t_{end}} dt_i$ . Finally, the average spray velocity can be computed at the post-processing step from the  $\tilde{u}_j$  and  $\tilde{dt}$  ratio as  $\bar{u}_j = \tilde{u}_j / \tilde{dt}$ .

The Sauter mean diameter (SMD) is computed in a similar way:

$$\tilde{D}_{32} = \sum_{t_{start}}^{t_{end}} \frac{\sum_{n_p=1}^{n_{p,tot}} D^3 n_{d@p}}{\sum_{n_p=1}^{n_{p,tot}} D^2 n_{d@p}} dt_i, \quad (5.2)$$

where  $D$  stands for the parcel's diameter. Then, the averaged parcel's Sauter mean diameter is estimated as  $\bar{D}_{32} = \tilde{D}_{32}/\tilde{dt}$ .

Spray measurements in the nozzle vicinity are limited and inaccurate due to the high fuel density, the presence of fuel ligaments, and the non-sphericity of the droplets. The measurements which are the nearest to the injection plane are taken  $15mm$  downstream of the nozzle. The spray distribution parameters in the simplified injection model are tuned to match the experimental spray characteristics at this location. The details about the injection model can be found in Sec. 4.3.3 and Sec. 5.3.1. For this purpose, we conducted a parameter search manually by running reacting simulations until we reached a good agreement with the experiments. The final Rosin-Rammler distribution is defined with a  $15\mu m$  Sauter mean diameter and a spreading factor  $q = 1.8$ .

The variation of prescribed Rosin-Rammler distribution parameters primarily affects the droplet's Sauter mean diameter while leaving all three velocity components practically unchanged. The latter is explained by the fact that the droplets have a low Stokes number and follow the mean flow motion, which is characteristic for such injection systems [43].

The experimental spray data is available for two axial planes, located  $15mm$  and  $25mm$  downstream the nozzle. These planes are marked with dashed white lines on the burner's sketch in Fig.5-14. Average radial profiles are shown in Fig.5-14, and four lines correspond to the droplet's Sauter Mean Diameter and the three velocity components of the droplets.

Numerical results reveal that the droplet diameter ranges from  $20\mu m$  up to  $40\mu m$  and agrees well with the measured data. At the  $Z = 15mm$  plane,  $D_{32}$  increases as we move away from the center line and then drops to zero above  $X = 30mm$  due to the absence of droplets. While maximum diameter values are well reproduced in the simulation, their locations are shifted approximately  $5mm$  closer to the centerline. A diameter plateau followed by an increase is observed experimentally at the  $Z = 25mm$  plane and can also be seen in the computed values. At the same time, we can notice a similar shift towards the center as at  $Z = 15mm$ .

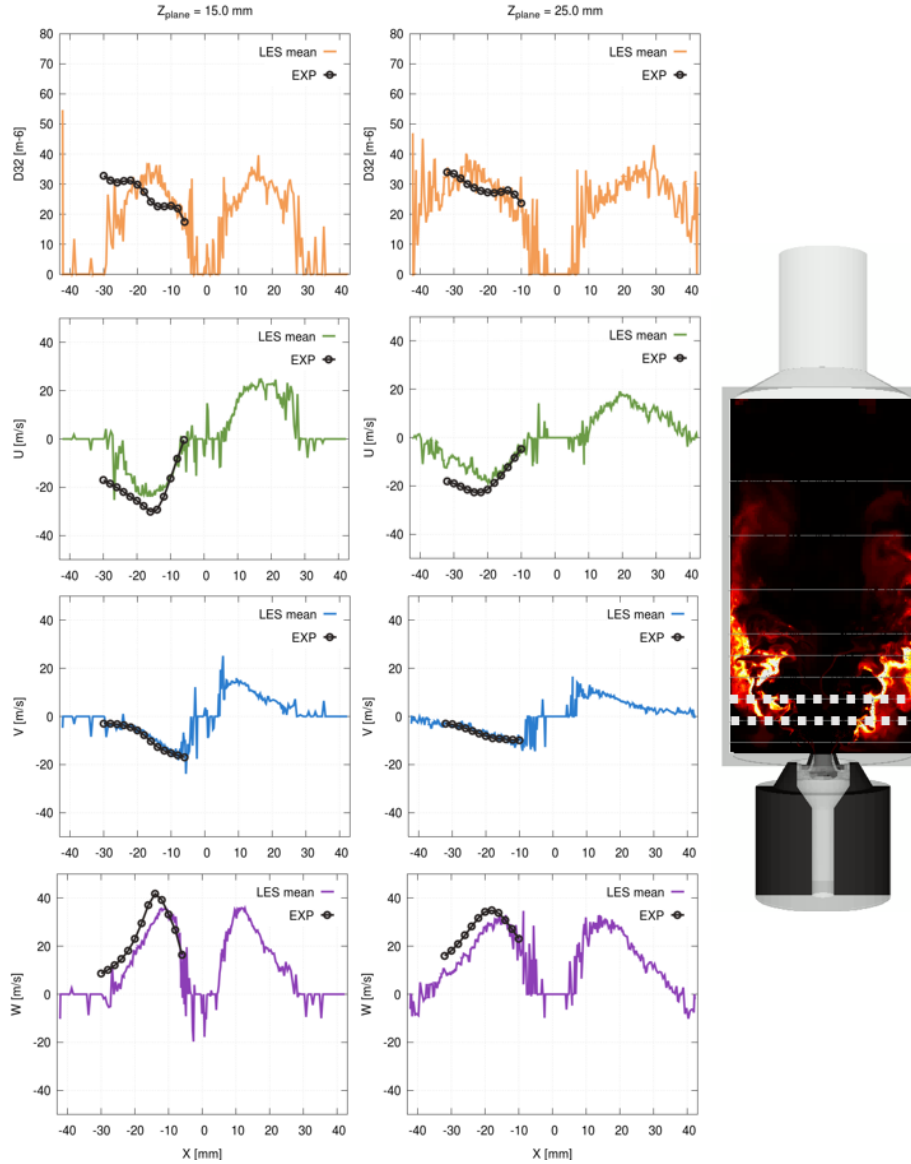


Figure 5-14: Averaged profiles ( $D_{32}$  and velocity components) of dispersed phase:  $Z = 15mm$  (left);  $Z = 25mm$  (right)

The droplet's radial velocity component is slightly underestimated compared to the experiments. While the maximum of the droplet's axial component is well reproduced, its location is slightly shifted towards the centerline.

Unfortunately, no mean velocity measurements of the gas phase are available for the n-dodecane flames. However, the underestimation of spray velocities and droplets' strong dependence on the mean flow characteristics reveal that the gaseous velocities could also be slightly underestimated in the corresponding regions.

Noisy averaged data correspond to the regions where a few particles are included in the averaging procedure. Experimentally, no droplets are observed in the center and closer to the walls for  $X > 30mm$ . It correlates very well with the numerical results since the averaged data in these regions also becomes quite noisy.

Despite the employed simplified injection model, the velocities and the characteristic diameters of the dispersed phase are globally in good agreement with experiments.

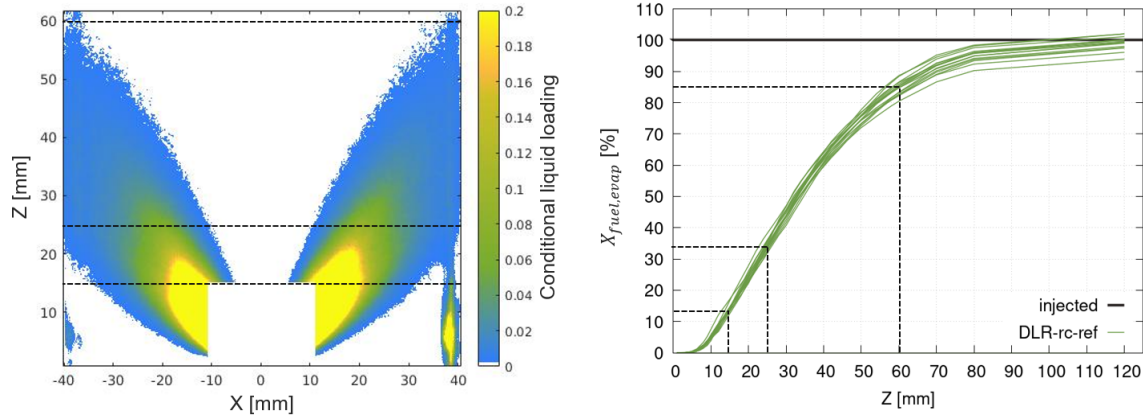


Figure 5-15: Left: experimental conditional liquid loading. Right: LES fraction of evaporated liquid fuel.

The conditional liquid loading shown in Fig. 5-15 represents the probability of finding fuel in the liquid state at a certain point. It is obtained from the Mie scattering data using the procedure described by Grohmann et al. in [1]. Whereas the maximum probability of droplets' presence at  $Z = 15mm$  reaches 20%, it drops almost twice at  $Z = 25mm$ .

The fraction of evaporated liquid fuel is defined as  $X_{fuel, evap} = \dot{m}_{evap} / \dot{m}_{fuel} \times 100\%$ , where  $\dot{m}_{evap}$  is the computed instantaneous parcels' evaporation rate and  $\dot{m}_{fuel}$  is the total injection rate of the liquid fuel. The fraction of evaporated liquid fuel is given as a function of the axial coordinate next to the conditional liquid loading in Fig. 5-15, where the discussed axial planes located at  $Z = 15mm$ ,  $Z = 25mm$ , and  $Z = 60mm$  are marked with black dashed lines. As we can see by looking at  $X_{fuel, evap}$ , approximately 15% of injected liquid fuel evaporates at  $Z = 15mm$ , and the amount of evaporated fuel doubles at  $Z = 25mm$ , reaching a value above 30%.

It was observed experimentally that n-dodecane droplets reach the combustion

chamber walls. The conditional liquid loading records some fuel droplets that can be found even above  $60mm$ , while other fuels considered in the experimental campaign evaporate earlier due to their higher volatility. LES results show that 15% of the injected fuel remains in the liquid form above  $60mm$ , and almost all fuel evaporates at  $120mm$ .

While the simulation results follow the general experimental trends given by the conditional liquid loading, it is hard to draw precise conclusions on whether the spray in LES is evaporated at a correct rate since the conditional liquid loading provides only a qualitative information.

Numerically we observed that the droplets could hit the walls up to approximately  $Z = 60mm$ , where 15% of fuel still exists in its liquid form. In the LES, no specific spray treatment is applied at the walls so that the parcels hitting the wall undergo a perfectly elastic reflection. Due to that simplification, we might expect discrepancies between the real and the computed flames because a non-negligible amount of fuel is still not evaporated at these heights. Nevertheless, the spray treatment at the walls should not affect too much the central flame's behavior where the analysis is done.

### 5.3.4 Reacting flow: the effect of spray/flame orientation

In order to consider the effect of thickening on the evaporation of droplets, we need to modify the Lagrangian equations as explained in Sec. 2.3.4. However, the coordinate transformation introduced by the thickening implies changes in the direction normal to the flame front. The TFM correction due to the spray/flame orientation, described in detail in Sec. 2.3.4, suggests applying the modification of Lagrangian equations only for the droplets that mainly move orthogonally to the flame front. Depending on the flame configuration, this correction due to the spray/flame orientation might significantly impact the results. Therefore, we compare in this section cases with and without this correction, denoted as DLR-rc-ref and DLR-rc-noCorr (see Table 5.1), to verify if it affects Gas-Turbine Model Combustor simulations.

With the averaging done over 12.3 FTT, the resulting gaseous temperature profiles for the DLR-rc-noCorr case (red lines in Fig. 5-16) are compared to the ones obtained

for DLR-rc-ref that included the spray/flame orientation correction (green lines).

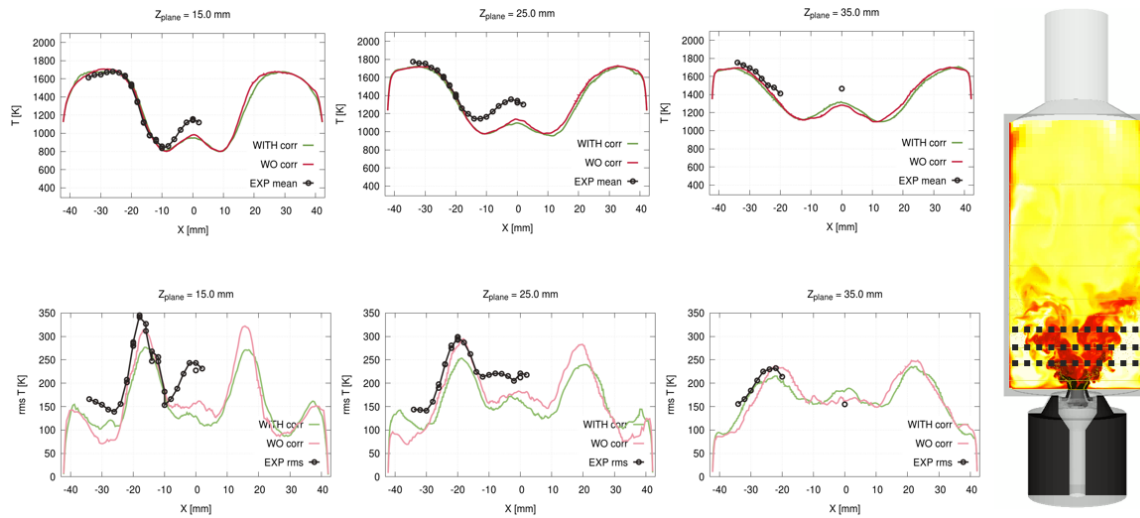


Figure 5-16: Gaseous temperature radial profiles at  $Z = 15/25/35\text{mm}$ : mean (top); RMS (bottom).

In Fig. 5-16 we can hardly see any difference between DLR-rc-ref and DLR-rc-noCorr in the mean temperature profiles. While the shape of temperature's fluctuating component profiles is quite similar in both cases, DLR-rc-noCorr demonstrates more pronounced peaks that match the experimental results better.

The averaged spray data shown in Fig. 5-17 is similar in the DLR-rc-ref and DLR-rc-noCorr cases. In addition, no notable difference is observed in evaporation rates between DLR-rc-ref and DLR-rc-noCorr.

The spray/flame orientation correction has a negligible effect on the simulation results in this particular setup. First, the angle at which droplets enter the flame is not sharp enough to reduce the applied thickening significantly. In addition, the temperature is elevated in the entire domain so that the droplets evaporate not solely in the thickened regions. Since no difference is observed between the DLR-rc-ref and DLR-rc-noCorr cases, we can conclude that the thickened zones are not the principal region where droplets' evaporation occurs.

### 5.3.5 Reacting flow: the effect of radiative heat losses

While keeping other parameters constant, an optically thin radiation model is adopted in the DLR-rc-rad case, see Table 5.1, to determine the effect of radiative heat losses.

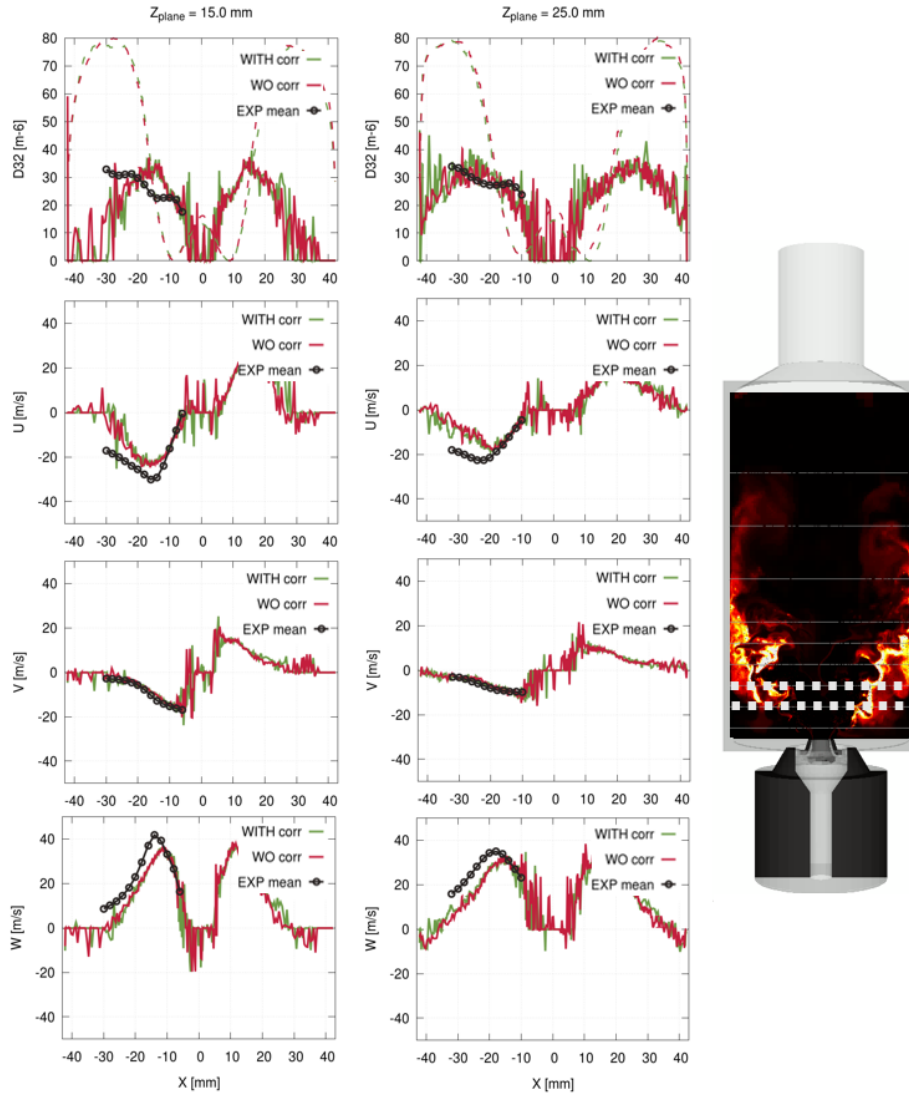


Figure 5-17: Averaged profiles ( $D_{32}$  and velocity components) of dispersed phase:  $Z = 15mm$  (left);  $Z = 25mm$  (right).

The averaging in the DLR-rc-rad case over 4.6 FTT was sufficient to see the main trend that the radiative heat loss leads to a temperature reduction in the entire simulation domain, but mainly in the central region. The radial temperature profiles of the DLR-rc-rad and DLR-rc-ref cases are given in Fig. 5-18.

When we plot the gaseous temperature as the function of axial coordinate in Fig. 5-19, we can clearly observe a temperature drop due to the radiative heat losses. Compared to the reference case, temperatures at the centerline become from  $50K$  up to  $200K$  lower. At the same time, the temperature drop due to the radiation at

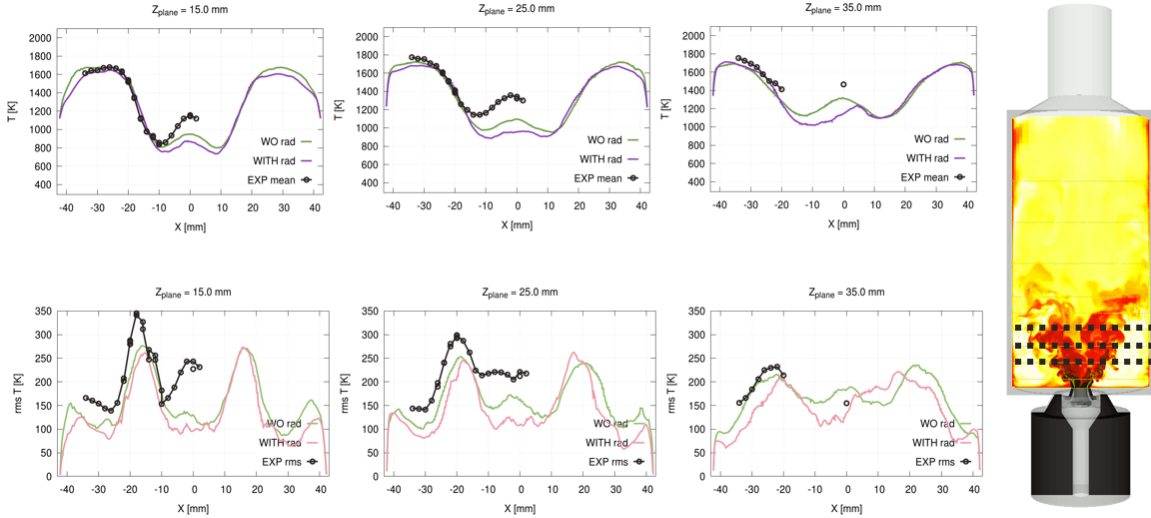


Figure 5-18: Gaseous temperature radial profiles at  $Z = 15/25/35\text{mm}$ : mean (top); RMS (bottom).

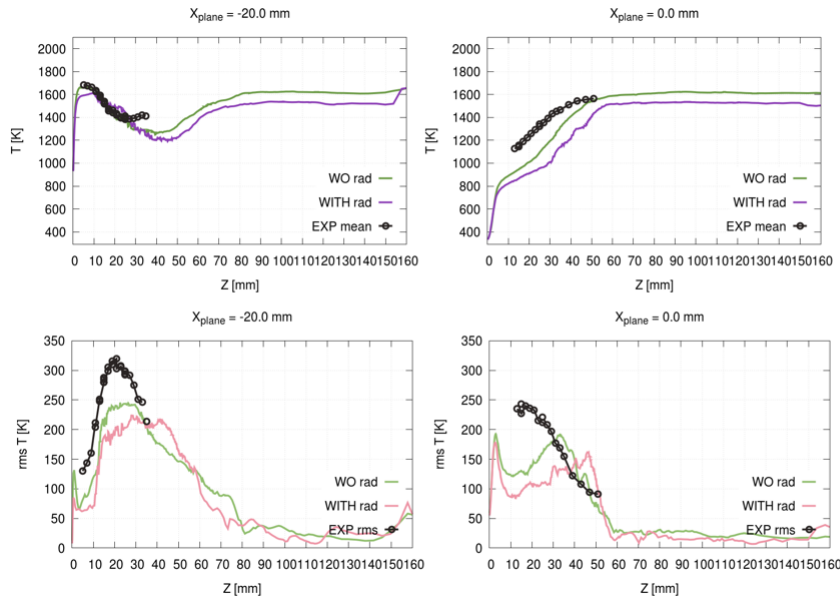


Figure 5-19: Gaseous temperature axial profiles at  $X = -20\text{mm}$  and  $X = 0\text{mm}$ : mean (top); RMS (bottom).

$X = -20\text{mm}$  is less pronounced (left column in Fig. 5-19).

Since the droplets are concentrated mainly in the outer regions where the radiative heat loss does not notably alter the temperatures, the averaged spray data in DLR-rc-rad and DLR-rc-ref is very much alike. Therefore, a negligible difference in the droplet evaporation rates is observed between the cases in Fig. 5-20.

Although the radiative heat losses have a considerable effect on the simulation

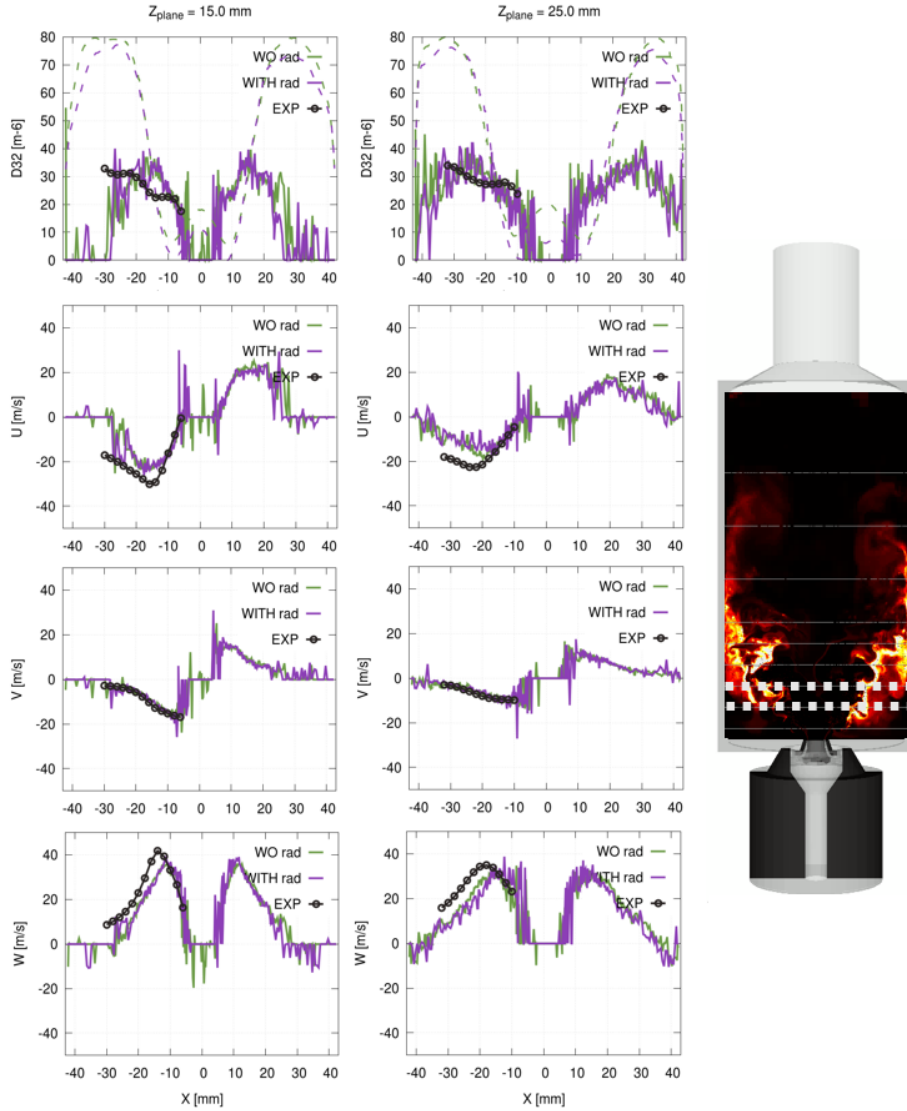


Figure 5-20: Averaged profiles ( $D_{32}$  and velocity components) of dispersed phase:  $Z = 15mm$  (left);  $Z = 25mm$  (right).

results, other simulations were done without radiative heat losses taken into account. Since the selected radiative model is very crude, additional work could be done to investigate the effect of more advanced models in this burner configuration.

### 5.3.6 Reacting flow: the effect of refinement

In order to investigate how the thickening affects the simulation results, a simulation is conducted with one additional level of AMR leading to  $\Delta_x = 0.125mm$  within the flame. This case is referred in Table 5.1 as DLR-rc-amr. Compared to the reference

solution DLR-rc-ref, in the DLR-rc-amr configuration, the number of cells rises from 22 to 40 million, raising computational costs. Nevertheless, the increase of cells is moderate, given that we are able to refine the flame by a factor of 2.

In DLR-rc-amr, the spray/flame orientation is not employed. This fact does not affect the comparison with the DLR-rc-ref case as it was demonstrated in Sec. 5.3.4 that it has a negligible impact on the results.

Figure 5-21 displays the instantaneous fields obtained in the reference case, shown on the left, and the fields of the refined configuration shown in the right column. Compared to DLR-rc-ref, the flame computed in DLR-rc-amr demonstrates more refined flame structures, while the thickened areas are smaller, and the thickening is divided by 2.

Due to a larger computational cost, DLR-rc-amr data was averaged over 4.6 FTT after the steady-state was reached. The resulting radial temperature profiles are compared to the reference DLR-rc-ref case and are given in Fig. 5-22. The comparison of the axial profiles can be seen in Fig. 5-23. The green lines indicate the reference DLR-rc-ref case with  $\Delta_x = 0.25$  within the flame, and the blue lines stand for DLR-rc-amr.

Figure 5-23 shows that the maximum temperature at  $X = 0mm$  which is found above  $60mm$  is well reproduced by both simulations. The refinement does not improve the mean temperature underestimation of approximately  $200K$  below  $40mm$ . This suggests that the misprediction could be due to errors made in the flow prediction.

At  $X = -20mm$  plane, we can observe a slight mean temperature increase due to the refinement in the flame front at the  $25 < Z < 60mm$  height, but the rest of the domain appears to be very similar to the reference case.

As expected for the DLR-rc-amr case, one additional level of AMR positively impacts the temperature's fluctuating component. The profiles in Fig. 5-23 are improved and follow better the experimental trends.

Figure 5-24 shows that the spray characteristics at  $Z = 15mm$  and  $Z = 25mm$  remain similar to the reference DLR-rc-ref solution. However, when looking at the planes located further away from the injector, we can see in Fig. 5-25 that the evap-

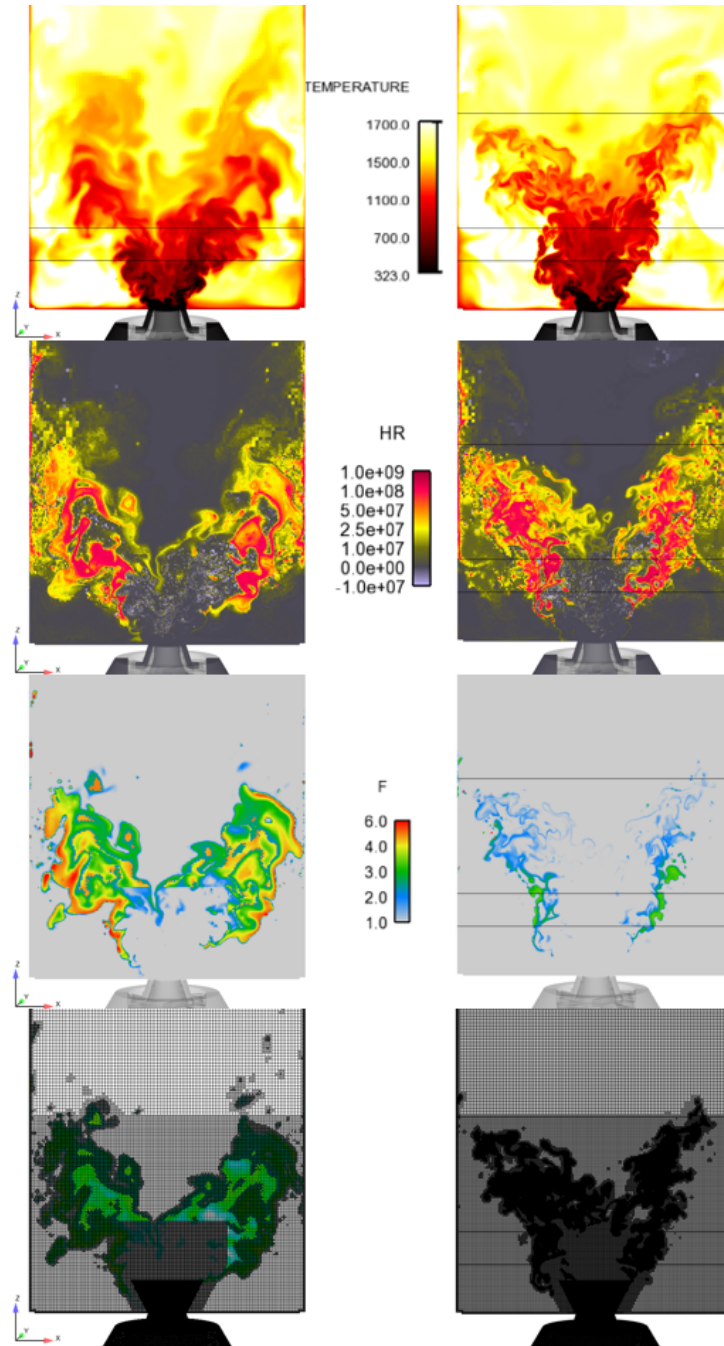


Figure 5-21: Instantaneous fields : gaseous temperature, heat release rate, thickening factor, mesh refinement. DLR-rc-ref: left column); DLR-rc-amr: right column.

oration rate increases by 5 percent.

While one additional level of AMR only slightly refines the results, it significantly increases the computational costs. The similar results obtained with  $\Delta_x = 0.125mm$  and  $\Delta_x = 0.25mm$  indicate that the TFM-AMR modeling approach is robust, as it

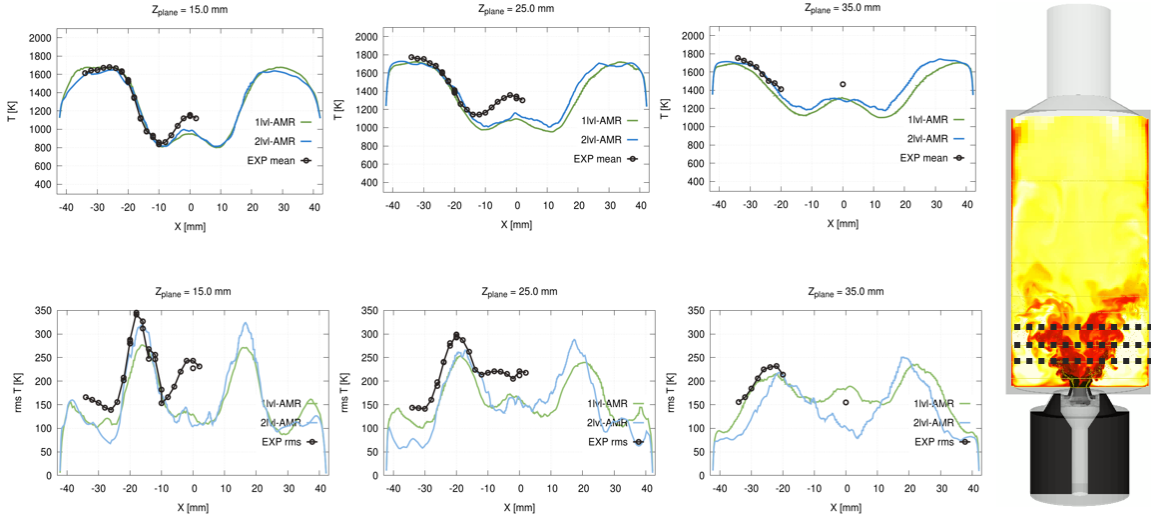


Figure 5-22: Gaseous temperature radial profiles at  $Z = 15/25/35mm$ : mean (top); RMS (bottom).

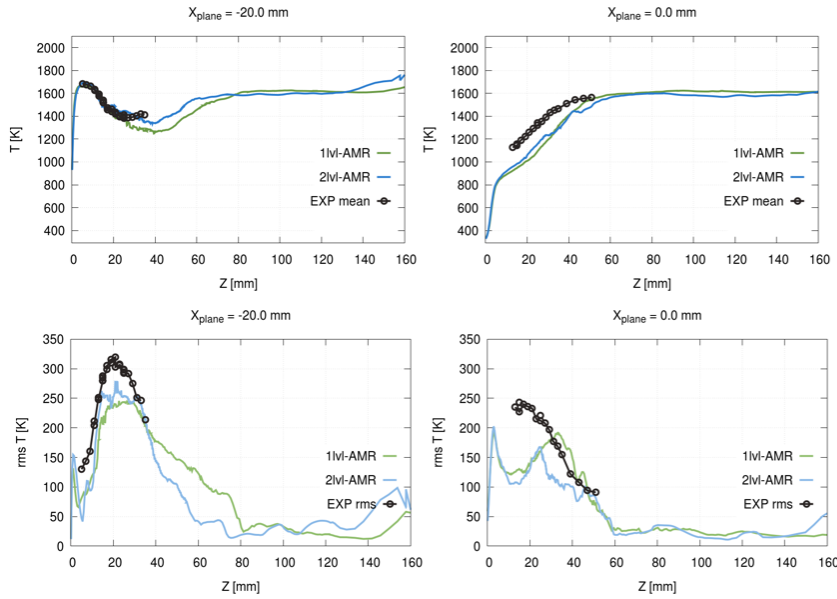


Figure 5-23: Gaseous temperature axial profiles at  $X = -20mm$  and  $X = 0mm$ : mean (top); RMS (bottom).

enables to get correct results with  $\Delta_x = 0.25mm$ . Therefore, we consider that using TFM-AMR with  $\Delta_x = 0.25mm$  is justified in this case.

A generally good agreement was reached for both gaseous and liquid phases between the experimental and the numerical results for the reference operating conditions. The steady-state results presented in this section will serve as the starting point for the lean blowout simulations presented in the next section.

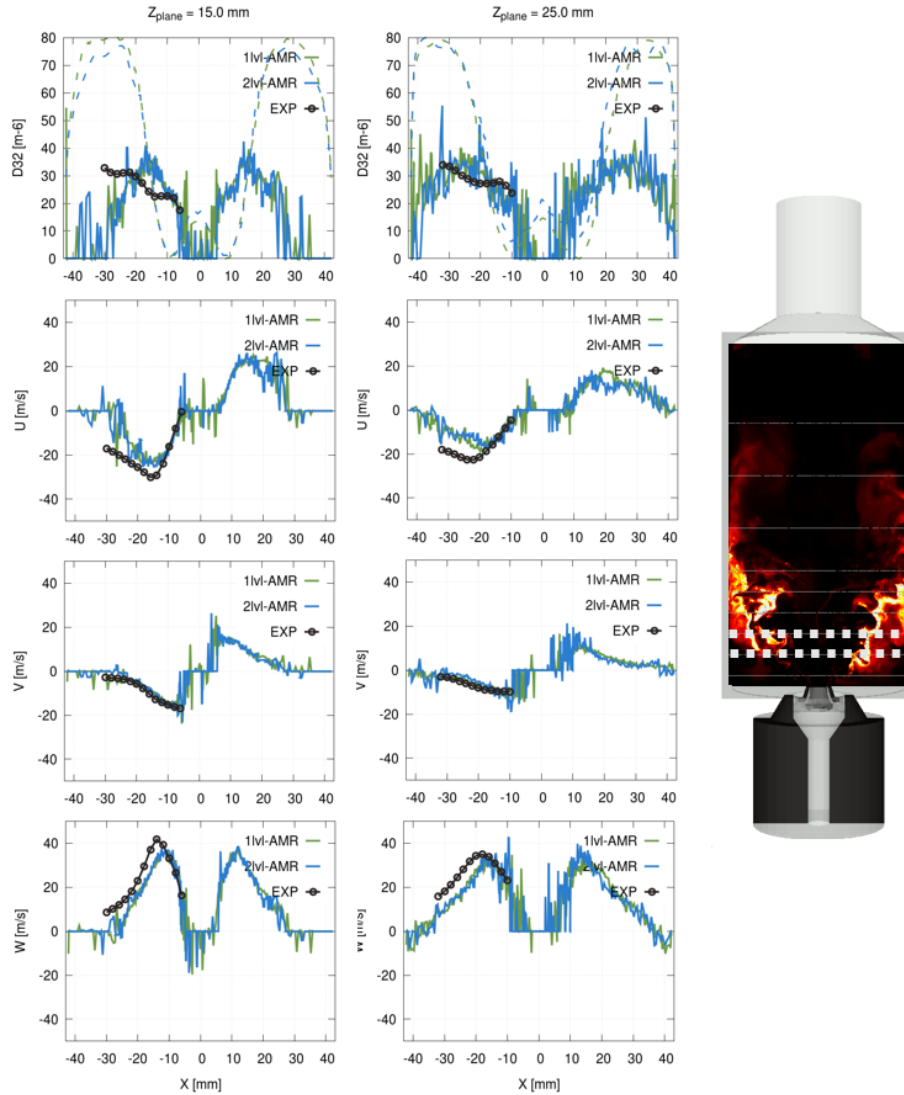


Figure 5-24: Averaged profiles ( $D_{32}$  and velocity components) of dispersed phase:  $Z = 15mm$  (left);  $Z = 25mm$  (right).

## 5.4 DLR burner LES: lean blowout

Stringent emission standards promoting leaner operating conditions and alternative fuel use require a deeper understanding of conditions that lead to the extinction of the flame in the combustion chamber. Lean blowout (LBO) limit is a critical safety characteristic essential in industrial gas turbine design. Therefore, a robust combustion model capable of accurately estimating the limits at which a flame blows off is of great importance to the industry.

The TFM-AMR modeling approach managed to accurately predict the stable

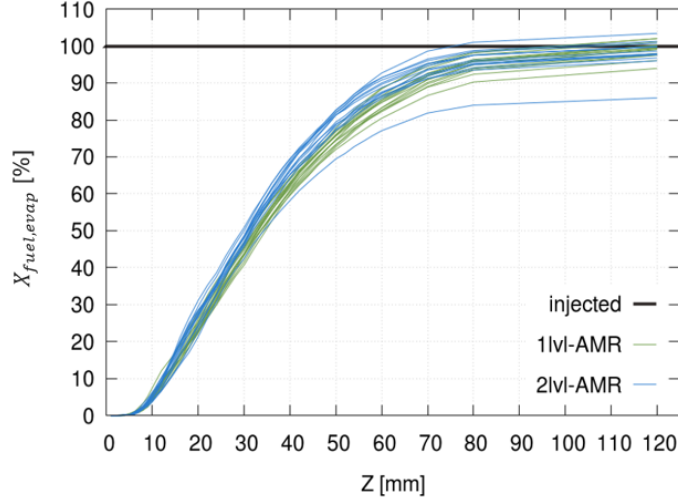


Figure 5-25: LES fraction of evaporated liquid fuel.

swirl-stabilized spray flame in the context of the model combustor operated at the reference conditions. In this section, we would like to investigate the ability of the TFM-AMR modeling approach to predict the lean blowout correctly.

The flame extinction in the Gas Turbine Model Combustor was explored experimentally by Grohmann et al. in [32]. The experiment was conducted for different fuels by keeping the air mass flow rate constant and decreasing the fuel mass flow rate until the extinction of the flame was visually detected. Once the flame blew off, the corresponding global gaseous air/fuel equivalence ratio  $\phi_{LBO}$  was measured. Repeating this experiment for different air mass flow rates,  $\phi_{LBO}$  can be plotted as a function of air mass flow rate as shown in Fig. 5-26.

The experimental results reveal that the global gaseous air/fuel equivalence ratio at which the flame blows off goes down when  $\dot{m}_{air}$  increases up to  $6g/s$ . This tendency can be observed for all considered fuels and is explained by the promoted atomization and mixing. However, a further increase of  $\dot{m}_{air}$  leads to a rise of  $\phi_{LBO}$ . Larger air velocities at the nozzle outlet are promoted by the increase of  $\dot{m}_{air}$  and lead to the decrease of residence times and higher strain rates which destabilize the flame [32].

To observe the lean flame blowout experimentally, the burner is first thermally stabilized at  $\phi = 0.6$ . Then, the fuel flow rate is reduced so that the global gaseous air/fuel equivalence ratio becomes nearly 0.56. Afterwards,  $\dot{m}_{fuel}$  is slowly reduced

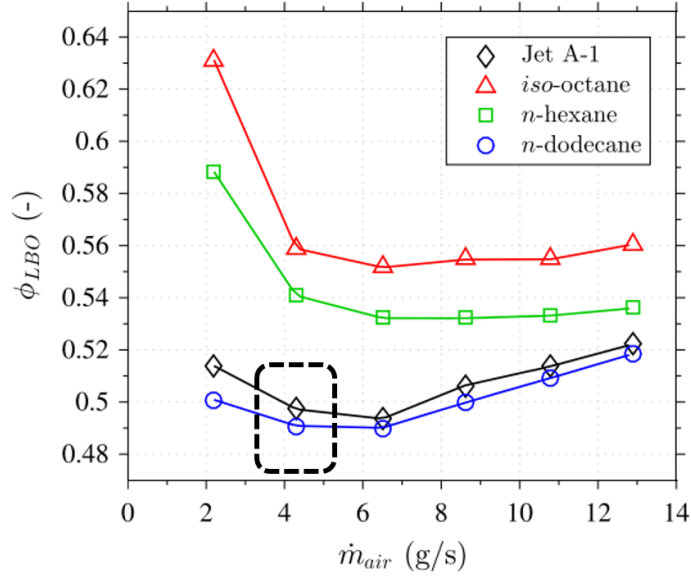


Figure 5-26: Lean blowout experimental results at  $T = 323K$  [32].

until the lean blowout is detected with a constant rate of  $0.00014g/s/s$  corresponding to a global gaseous air/fuel equivalence ratio reduction in the order of  $0.0011/s$ .

### 5.4.1 Numerical setup

The lean blowout simulations presented in this section are performed for the burner operated with n-dodecane at  $\dot{m}_{air} = 4.3g/s$  and  $T = 323K$ . At the investigated operating point, the flame blows off experimentally at approximately  $\phi_{LBO} = 0.49$ . As we can see in Fig. 5-26, the n-dodecane flame extinction behavior lies close to the LBO of Jet-A1 and is thus representative of practical conditions.

To reproduce the LBO numerically, the same numerical setup as described in Sec. 5.3.1 is adopted here. In this setup, radiative heat losses and the spray/flame orientation correction are neglected.

The flame at the reference conditions, extensively discussed in Sec. 5.3.3, serves as the starting point of the LBO simulation sequence. The global gaseous fuel/air equivalence ratio is reduced step-wise: from 0.8 to 0.6 at the first step, and gradually with a step size of 0.04 afterward. Table 5.2 summarizes the simulation sequences presented in this section.

Configuration	$\Delta_x$ within flame	Stretch correction	Orientation correction	Radiation	Wall temperature
DLR-lbo	0.25mm	+	-	-	$T_w = const$
DLR-lbo-scaled	0.25mm	+	-	-	$T_w = f(\phi)$

Table 5.2: Computed LBO sequences.

Unfortunately, the wall temperature measurements were not updated during the lean blowout experiment. The only available wall temperature measurements were taken at the reference conditions, at  $\phi = 0.8$ , and only for Jet-A1 fuel as it was mentioned in Sec. 5.3.1.

In order to investigate the importance of assigned boundary conditions at the walls, two LBO simulation sequences are performed. In the first sequence, referred to as the DLR-lbo sequence in Table 5.2, the wall temperatures obtained for the flame operated at the reference conditions are used for the entire LBO simulation sequence. In the second sequence, DLR-lbo-scaled, the wall temperatures are scaled with respect to the global gaseous fuel/air equivalence ratio each time it was decreased.

The way how the wall temperatures are prescribed at the reference operating conditions is discussed in detail in Sec. 5.3.1 and is illustrated in Fig. 5-5. Since we do not have any information on the wall temperatures during the LBO experiment, our best guess is to scale the temperatures measured at the reference conditions  $T_w$  using the adiabatic flame temperature at the different equivalence ratios. The scaled wall temperatures  $T_w^*$  are obtained with:

$$T_w^*(\phi) = T_u + (T_w - T_u) \frac{T_b(\phi) - T_u}{T_b(\phi = 0.8) - T_u}, \quad (5.3)$$

where  $T_u$  stands for the unburned temperature and  $T_b$  is the burned temperature of a 1D flame that can be tabulated as a function of  $\phi$ .

In the DLR-lbo-scaled sequence, the temperatures at the bottom plate, as well as the temperature profile assigned at the walls, are computed using Eq.(5.3). On the left-hand side in Fig. 5-27 the reference profile corresponding to  $\phi = 0.8$  is plotted

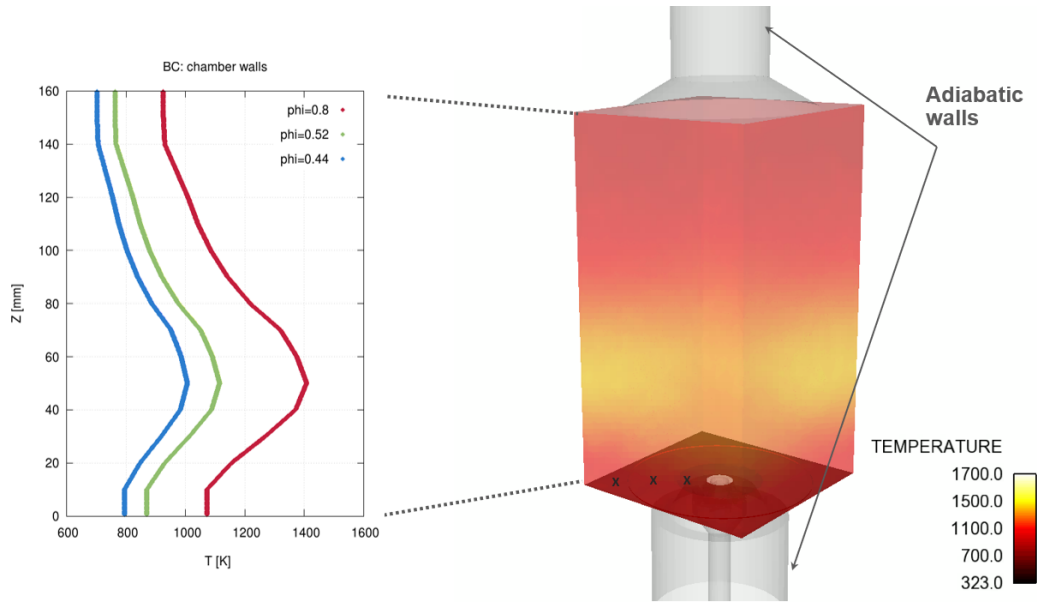


Figure 5-27: Temperature boundary conditions with applied scaling.

together with the scaled profiles computed for  $\phi = 0.52$  and  $\phi = 0.44$ . Following this scaling procedure, the maximum temperature at the wall drops from  $1400K$  to approx.  $1000K$ , when the global gaseous fuel/air equivalence ratio becomes two times lower.

## 5.4.2 Results

During the LBO simulation sequence, the resulting total power of the combustor drops as the global gaseous fuel/air equivalence ratio decreases. Figure 5-28 illustrates how the total power goes down step-wise over the run-time during the DLR-lbo sequence. These steps correspond to the global gaseous fuel/air equivalence ratio's step-wise reduction, which goes down from 0.8 to 0.4. Dashed lines on the plot indicate the theoretical burner power attained when all the fuel at the corresponding  $\phi$  is burned.

As  $\phi$  drops below  $\phi_{LBO} = 0.49$ , the amplitude of total power oscillation grows, but the mean power remains still close to the theoretical value. Although the flame becomes less stable, no blowout is observed numerically.

The snapshots of the instantaneous temperature and heat release fields are given in Fig. 5-29 for the reference case at  $\phi = 0.8$ , and for  $\phi = 0.44$  which is smaller than

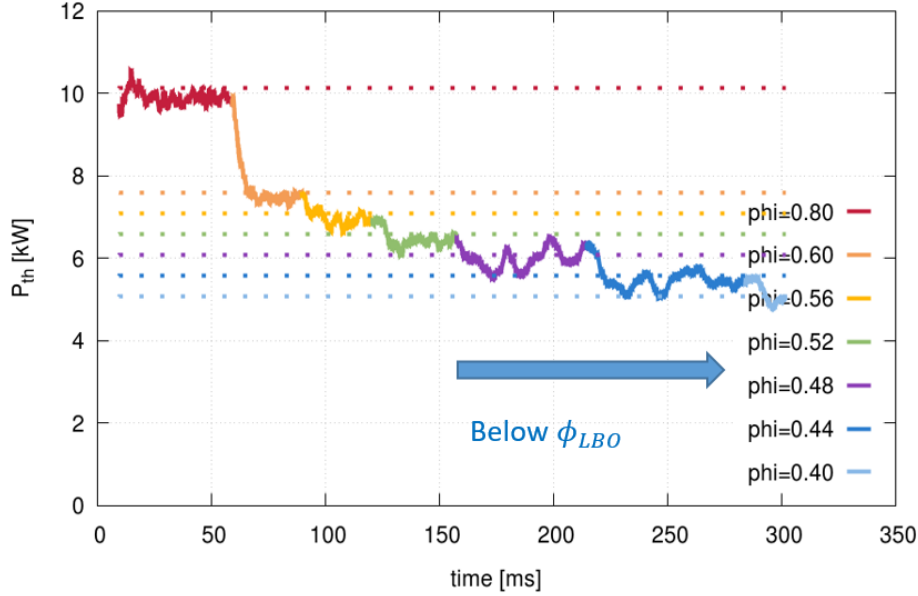


Figure 5-28: Total power during DLR-lbo simulation sequence

the experimental LBO value  $\phi_{LBO} = 0.49$ .

As the global gaseous fuel/air equivalence ratio decreases, the maximum temperature drops below  $1500K$ . While a clearly defined v-shape can still be observed at  $\phi = 0.44$ , the heat release rate reduces almost by a factor of two, is much more dispersed, and goes far downstream compared to the reference solution at  $\phi = 0.8$ .

One of the reasons that could potentially lead to the misprediction of  $\phi_{LBO}$  in the DLR-lbo sequence can be the temperature boundary conditions assigned at the burner walls. The reduction of the global gaseous fuel/air equivalence ratio must lead to a drop in resulting burned temperatures. Therefore, the wall heat flux during LBO becomes under-predicted with the assigned high wall temperatures of the reference flame, leading to over-estimated burned gas temperatures compared to the LBO experiment. In turn, these overestimated burned temperatures in the computed DLR-lbo sequence lead to a more stable flame than in reality.

DLR-lbo-scaled simulations with scaled temperatures at the walls are presented next to illustrate the importance of imposed boundary conditions at the burner walls. DLR-lbo-scaled simulations were done for  $\phi = 0.52$ ,  $\phi = 0.48$  and  $\phi = 0.44$ , each running for at least  $7FTT$ . At all three considered  $\phi$  values, the DLR-lbo-scaled configuration

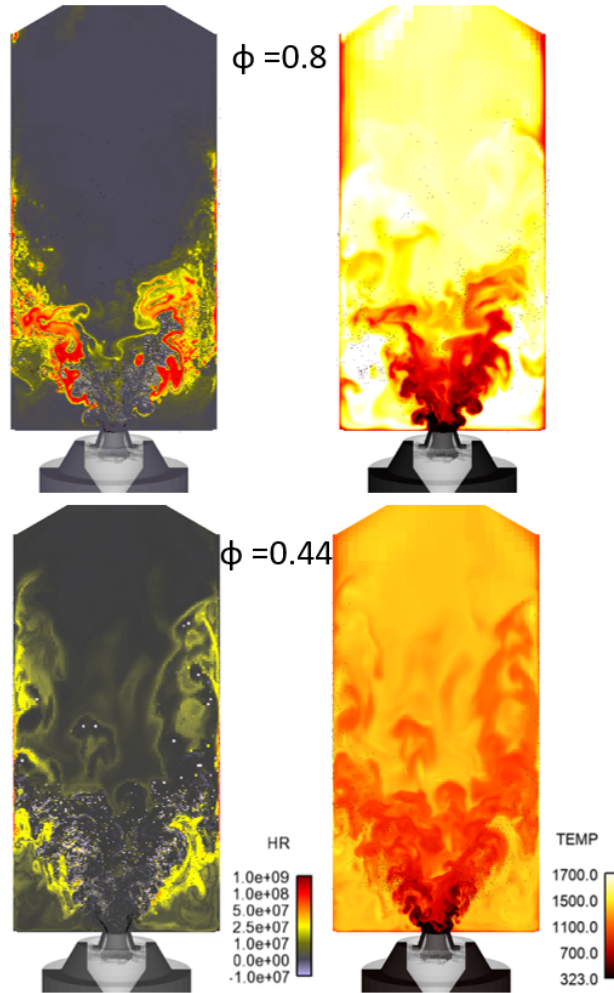


Figure 5-29: Instantaneous heat release rate and temperature fields at  $\phi = 0.80$  (top) and  $\phi = 0.44$  (bottom).

is initialized from the last time instance of the DLR-lbo case at corresponding  $\phi$ .

The results of the DLR-lbo-scaled sequence are illustrated in Fig. 5-30, where the lines correspond to the considered fuel/air equivalence ratios. The final instantaneous heat release rate and temperature fields are given on the left-hand side in Fig. 5-30. The computed burner powers are given on the right in Fig. 5-30 as a function of time. On the power plots, colored lines stand for the DLR-lbo-scaled cases, solid grey lines indicate the DLR-lbo configuration, and the grey dashed lines are the theoretical power value.

At  $\phi = 0.52$ , which is above  $\phi_{LBO}$ , the flame is stabilized in both DLR-lbo and DLR-lbo-scaled configurations. Even after the scaling of imposed temperature profiles

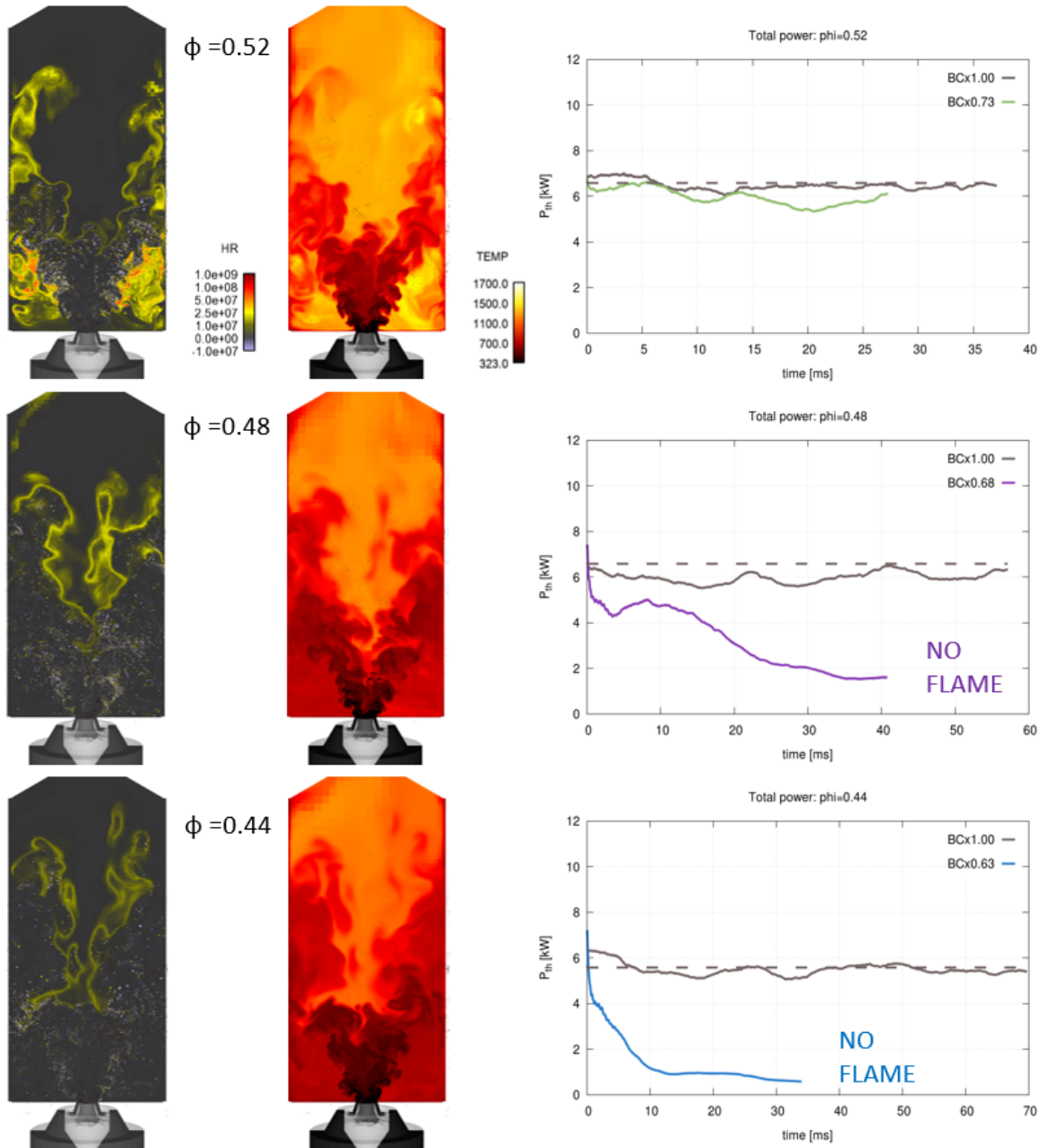


Figure 5-30: Instantaneous heat release rate and temperature fields (left), burner total power (right):  $\phi = 0.52$  (top),  $\phi = 0.48$  (middle) and  $\phi = 0.44$  (bottom).

is done, we can still recognize in Fig. 5-30 the typical V-shaped flame, common for this type of configuration. The total burner power also remains close to its theoretical value.

As it can be seen on the left in Fig. 5-30 for the  $\phi = 0.48$  and  $\phi = 0.44$  DLR-Ibo-scaled cases, the flame is not able to stabilize in the zone of interest and is blown away

towards the outlet. At the end of computed time, temperatures drop below  $1000K$  in the flame stabilization region in both these cases.

During the DLR-lbo simulation sequence, the flame stabilizes at  $\phi = 0.44$ , and the burner power remains close to the theoretical value, whereas the computed power goes towards zero directly after the scaling-down wall temperatures in the corresponding DLR-lbo-scaled case. The same trend with a slight delay can be observed for the DLR-lbo-scaled case at  $\phi = 0.48$ . The DLR-lbo-scaled results correlate with the experimental findings, since both  $\phi = 0.48$  and  $\phi = 0.44$  lie below  $\phi_{LBO}$ .

## 5.5 Conclusions

In this chapter, we investigated the DLR model combustor operated with n-dodecane at the reference conditions in Sec. 5.3.3 and during the lean blowout in Sec. 5.4. The computed flame results were then compared to the available experimental measurements.

Overall, a good agreement was reached for both gaseous and liquid phases between the experimental and the numerical results for the reference operating conditions in Sec. 5.3.3. Therefore, we conclude that the TFM-AMR modeling approach shows a great capability of predicting swirl-stabilized spray flames under atmospheric pressure.

In Section 5.3.3, we observed an under-prediction of the mean temperatures at the center-line of the combustor operated at the reference conditions. Since the same issues were present in the thickened and refined cases, we can exclude the influence of the flame thickening on the temperature field. This disagreement between the experimental and numerical results could be attributed to the simplified representation of the fuel injection, as well as the simplified droplets' treatment at the combustion chamber walls.

The parametric variation performed in Sec. 5.3.3 showed that the TFM correction considering spray/flame orientation has a minor effect on the simulation results. In addition, the parameter variation highlighted the importance of radiative heat losses in this burner configuration. Additional and more detailed analyses would have to be

carried out to strengthen this conclusion, which lies outside the present work's scope. Therefore, we decided here to neglect radiation in a first approximation.

The lean blowout simulation results using the TFM-AMR modeling approach were presented in Sec. 5.4. Here, we considered two cases of temperature boundary conditions at the combustion chamber walls: one with a constant temperature profile and the other with temperatures varying with the global equivalence ratio. The lean flame blowout was detected experimentally at an equivalence ratio of 0.49. Numerically, we observed no flame blowout even below  $\phi = 0.49$  for the case with constant wall temperatures, whereas we were able to reproduce the flame blowout with varying wall temperatures. In the second case, we obtained a stable burning flame at  $\phi = 0.52$ , while below  $\phi = 0.48$ , the total burner power rapidly decreases, and the flame is blown away from the combustion chamber. Thus, the fuel/air equivalence ratio at which the flame blows off must lie between  $\phi = 0.48$  and  $\phi = 0.52$ , that match very well the experimental value of  $\phi_{LBO} = 0.49$ . This confirms the suitability of TFM-AMR use for the LBO computations and the importance of the temperatures imposed at the combustion chamber walls.

In order to set up LBO numerical simulations accurately, it would be beneficial to have the wall temperature measurements during the entire run time of the LBO experiment. Alternatively, correct temporally and spatially varying wall temperature at all burner powers can be achieved by using Conjugate Heat Transfer (CHT) modeling approach. This, however, should be investigated in future work. Additionally, a more rigorous study is suggested to assess the effect of the boundary conditions in this burner configuration.

The standard TFM-AMR modeling approach presented in Chapter 2 demonstrated its shortcomings during the setup of the DLR model combustor simulations. In this burner configuration, the observed instantaneous heat release rates were significantly lower than the tabulated values, which obliged us to arbitrarily increase the sensor's sensitivity. Therefore, a new modeling approach is desired to compute such geometries avoiding such parameter tuning.

# Chapter 6

## Geometrical formulation of the thickened flame model

The TFM model presented in Chapter 2 relies on the tabulated data retrieved from the simulations of 1D premixed flames. While this modeling approach provides pretty accurate results in the case of purely gaseous premixed turbulent flames, some limitations arise when more complex setups are studied, as demonstrated in the previous chapters. For instance, we saw that the maximum heat release rate and the flame thickness differed significantly from the tabulated premixed flame values in the studied spray flame configurations. Another issue was faced in Chapter 5 when computing the DLR model combustor configuration. Here, we were forced to increase the sensor sensitivity to detect the flame front properly.

In the spray flames, the gaseous fuel/air equivalence ratio raises over the flame front as the liquid fuel evaporates, as demonstrated in Chapter 3. At the same time, laminar flame thicknesses are tabulated based on the gaseous fuel/air equivalence ratio according to the standard thickening approach given in Chapter 2. Therefore, the tabulated thicknesses become smaller as we approach the burned side in the spray flames, potentially leading to unnecessarily high values of the thickening factor. On the contrary, closer to the unburned side or even within the reaction zone, the spray flame can have steeper gradients than the premixed flame at the same local gaseous fuel/air equivalence ratio supported by a back-diffusion of intermediate combustion

products. The latter can cause an insufficient thickening and a flame under-resolution as a result.

The need to tune the model parameters depending on the flame configuration deteriorates the robustness of the model. Therefore, an alternative method to estimate laminar flame characteristics is proposed in this chapter. It relies on the local flame characteristics to derive these flame properties, avoiding using pre-tabulated heat release, laminar flame thickness, and laminar flame speed values. Since the new formulation does not rely on pre-computed tables, it is expected to generalize better on complex cases.

From a geometrical perspective, a flame front can be viewed as a function of a reduced variable that rises from zero to unity. As typically done in combustion studies, a progress variable can be used to describe the reaction progress. Since the method proposed below relies on the definition of a progress variable, it is referred to as a geometrical sensor or GS-TFM-AMR. To avoid any model confusion, we will refer to the previously used thickening approach, which details are given in Chapter 2, as to the standard sensor or SS-TFM-AMR.

In this chapter, the description of the modeling approach using the geometrical sensor is given first in Sec. 6.1. Then, GS-TFM-AMR is validated on simple 1D gaseous and spray flames in Sec. 6.2. Next, the academic burner configuration discussed in Chapter 4 is computed using the geometrical sensor, and the obtained results are compared to the results obtained with the standard sensor in Sec. 6.3. Finally, the proposed modeling approach is investigated in Sec. 6.4 in the context of the gas turbine model combustor described in Chapter 5.

## **6.1 Geometrical formulation of the thickened flame model: formulation**

In the proposed GS-TFM-AMR modeling approach, the estimation of the flame thickness is based on the local values of the progress variable. Therefore, it is important

first to define the progress variable properly. In the following, we define the progress variable based on the carbon monoxide and carbon dioxide mass-fractions, such that  $Y_C = Y_{CO} + Y_{CO_2}$  and:

$$C = \frac{Y_C - Y_{C,u}(\phi_g)}{Y_{C,eq}(\phi_g) - Y_{C,u}(\phi_g)}, \quad (6.1)$$

where  $Y_C$  indicates the sum of carbon monoxide and carbon dioxide mass-fractions within a computational cell,  $Y_{C,u}(\phi_g)$  their sum on the reactants side, and  $Y_{C,eq}(\phi_g)$  is the value tabulated at equilibrium conditions and stored as a function of the gaseous fuel/air equivalence ratio. The progress variable is limited between zero and unity. Note that the equilibrium  $Y_{C,eq}(\phi_g)$  is tabulated from 0-D homogeneous reactors and therefore does not depend on the choice of any specific combustion mode.

Depending on the flame, the computed progress variable can slightly deviate from its real value since  $Y_{C,eq}$  might not only depend on the local equivalence ratio. The enthalpy loss due to droplet evaporation and differential diffusion within the flame can also lead to composition differences compared to the homogeneous reactor considered for  $Y_{C,eq}$  tabulation. Thus, the real progress variable does not necessarily attain the same value as tabulated  $Y_{C,eq}(\phi_g)$ . For example, this can be the case for diluted or spray flames, the issue discussed in Sec. 6.2.

The geometrical sensor formulation relies on the flame properties that characterize the reaction flame zone. In order to thicken the entire flame front uniformly, we need to transfer this information from the reactive flame region to the entire flame front. The generic procedure of such property propagation over the flame front is described in Sec. 6.1.1.

### 6.1.1 Generic methodology to transfer information from the reaction zone

The transfer of information from the reaction zone to the surrounding flame region follows a procedure similar to the one used to transport the flame indicator given by Eq.(2.12). The transport of the variables is done at each time step and corresponds to

the algorithm subpart named "Transported quantities" in Fig. 6-2. To propagate the information from the reaction zone to the whole flame front, a variable  $\xi$  is defined by the following transport equation:

$$\frac{\partial \rho \xi}{\partial t} + \frac{\partial \rho u_j \xi}{\partial x_j} = \frac{\partial}{\partial x_j} \left( [\hat{S}(EF - 1) + 1] G_{diff,j} + [1 - \hat{S}] G_{diff,j}^{sgs} \right) + \frac{E}{F} \dot{\omega}_\xi, \quad (6.2)$$

where  $F$  is the thickening factor,  $E$  is the efficiency factor, and  $\hat{S}$  is the flame sensor. The terms on the left hand-side represent the temporal evolution of the variable  $\xi$  and its convection. The diffusive flux  $G_{diff,j} = \rho D_\xi \frac{\partial \xi}{\partial x_j}$  is defined with the diffusion coefficient  $D_\xi = \mu / (\rho Sc_\xi)$  with a Schmidt number set to 0.7. Similarly to the scalar transport, the sub-grid scale flux  $G_{diff,j}^{sgs}$  is computed using the turbulent diffusion coefficient  $D_t = \mu_t / (\rho Sc_t)$ . While all these terms are written in a generic way, the source term  $\dot{\omega}_\xi$  will be specific to every transferred property.

The general form of  $\dot{\omega}_\xi$  is given by Eq.(6.3) and is defined differently depending on whether we are within the reaction zone or not.

$$\dot{\omega}_\xi = \begin{cases} \rho \beta (\xi_{target} - \xi) \dot{\omega}_c & \text{reaction zone} \\ \rho \frac{0 - \xi}{\tau_{dest}} & \text{outside reaction zone} \end{cases} \quad (6.3)$$

Outside the reaction zone, the variable  $\xi$  relaxes towards zero with a characteristic time  $\tau_{dest}$ . The destruction relaxation time is defined as a product of an adjustable relaxation coefficient  $\alpha_*$  and a chemical time scale  $\tau_{destr} = \alpha_* \tau_{chem}$ . As in the definition of the Jaravel sensor,  $\alpha_*$  is set to different values in the cold and burned gas sides,  $\alpha_{cold} = 0.05$  and  $\alpha_{hot} = 0.005$ , respectively. The burned side is defined when the unburned temperature exceeds  $1000K$ . This is equivalent to what is done for the indicator  $\psi$  in the standard formulation of thickening described in Sec. 2.3.1.

Within the reaction zone, the variable  $\xi$  relaxes towards the desired target value  $\xi_{target}$  with a characteristic time  $1/\dot{\omega}_c$ , where  $\dot{\omega}_c$  is the progress variable reaction rate. With the local production rate computed as  $\dot{Y}_C = \dot{Y}_{CO} + \dot{Y}_{CO_2}$ , the progress variable reaction rate follows from Eq.(6.1) and computed using:

$$\dot{\omega}_c = \frac{\dot{Y}_C}{Y_{C,eq} - Y_{C,u}} \quad (6.4)$$

The stiffness parameter  $\beta$  in Eq.( 6.3) controls how fast the variable  $\xi$  relaxes to its target value. In the cases tested during this work,  $\beta = 1$  leads to an appropriate behavior of the relaxation procedure.

The progress variable reaction rate is homogeneous to the inverse of a time, and thus  $\dot{\omega}_c$  represents the inverse of this chemical time-scale. With  $\dot{\omega}_\xi$  defined in Eq. 6.3 the source term  $E/F\dot{\omega}_\xi$  in Eq. 6.2 equals to  $E/F\rho\beta(\xi_{target} - \xi)\dot{\omega}_c$  within the reaction zone. Here,  $E/F\dot{\omega}_c$  represents the inverse of the thickened flame time scale. This means that  $\xi$  is relaxed towards  $\xi_{target}$  in approximately this time. It was checked that using a time much smaller than the thickened flame time leads to divergence because the flame does not have enough time to adapt. This choice is, therefore, essential to the model.

The production of carbon monoxide and carbon dioxide can be non-zero in the regions where endothermic chemical reactions dominate and are characterized by negative heat release rates. In such regions,  $\dot{\omega}_c$  is set to zero to avoid flame detection. Additionally, we would like to exclude any other regions with non-zero  $\dot{Y}_C$  outside the flame-front. To achieve it,  $\dot{\omega}_c$  is considered zero when the progress variable values are above 0.9 and below 0.1.

The notable difference between the geometrical and the standard sensors concerns the relaxation of transported variables within the reaction zone. In the standard sensor formulation, the indicator relaxation time  $\tau_0$  is set intentionally small so that the indicator attains fast its maximum value  $\psi_{max}$ . In the geometrical sensor, the relaxation time is proportional to the chemical time. Therefore, we do not necessarily expect  $\xi$  to attain its target value  $\xi_{target}$  due to the reaction/diffusion competition taking place in premixed flames.

The definition of the reaction zone used to distinguish the cases in Eq.(6.3) is closely related to the definition of the progress variable reaction rate. The progress variable reaction rate multiplied with the non-thickened flame time  $\tau_{chem}$  gives

the reaction zone characteristic  $x_r = \tau_{chem}\dot{\omega}_c$  which compares an actual chemical activity characterized by  $\dot{\omega}_c$  with a chemical time scale given by the model  $\tau_{chem} = \delta_L^0/S_L^0$ . From an order of magnitude analysis,  $\dot{\omega}_c$  reaches a maximum of the order of  $1/\tau_{chem}$ . Hence,  $x_r$  reaches peak values of the order of unity. In practice, depending on the chemistry, it was found to be between 0.5 and 10. When  $x_r$  approaches unity, the chemical reactions attain maximum reaction rates, while very low  $x_r$  values indicate regions at the flame tail or in the preheat region. Thus, the reaction zone in Eq.(6.3) is defined when both conditions on the reaction zone characteristic  $x_r$  and the progress variable  $C$  are satisfied:  $x_r > 0.01$  and  $0.2 < C < 0.9$ .

### 6.1.2 Flame indicator

Dynamic thickening ensures that the thickening is applied only within the flame region and is avoided outside. In the standard sensor approach described in Sec. 2.3, the sensor  $S$  detects regions with high chemical activity, whereas the broadened sensor  $\hat{S}$  encloses the entire flame front and defines regions where the thickening is applied. This sensor extension is achieved through the transport of the flame indicator defined in Eq.(2.12).

In the geometrical sensor, the main role of the flame indicator  $\psi$  remains similar to the standard approach, which is to identify the location of the entire flame front. To achieve this goal, the flame indicator  $\psi$  uses information about the maximum chemical activity provided by the progress variable reaction rate defined in Eq.(6.4). Then, the flame indicator  $\psi$  is transported following the procedure described in Sec. 6.1.1.

As mentioned in Sec. 6.1.1, Eq.(6.2) remains the same for all the transported variables, and the main difference concerns the definition of the source term arising in this transport equation. While the generic source term is given in Eq.(6.3), it is defined for the flame indicator as follows:

$$\dot{\omega}_\psi = \begin{cases} \rho\beta(\psi_{max} - \psi)\dot{\omega}_c & \text{reaction zone} \\ \rho\frac{0-\psi}{\tau_{dest}} & \text{outside reaction zone} \end{cases} \quad (6.5)$$

Within the reaction zone, the target value for the flame indicator is set to the arbitrary value  $\psi_{max} = 20$ , the same as used in the standard sensor approach. However, due to the difference in the relaxation time definition addressed in Sec. 6.1.2, the flame indicator in the geometrical sensor should not necessarily reach the value of 20.

Flame indicator plays an essential role in the estimation of laminar flame properties as explained in the next section.

### 6.1.3 Flame properties

Flame properties, such as the flame thickness and the flame speed, are required to set up thickening and efficiency levels. In the standard sensor approach, these values are taken from the premixed flame tables. On the contrary, when thickening is done using the geometrical sensor, the model estimates these flame properties and does not require tabulation of 1-D laminar premixed flames.

To set an appropriate flame thickening, the laminar flame thickness and the laminar flame speed estimated by the model should characterize the reaction zone of the flame. Moreover, these properties must be constant within the flame front to ensure the robustness of the model. In order to fulfill these two conditions, flame properties are computed using a method described below.

Flame indicator  $\psi$  defined in Sec. 6.1.2 plays an essential role in propagating the desired flame characteristic. To obtain a flame property, designated with a variable  $f$ , we construct an additional variable  $\psi^* = f\psi$  that is transported using Eq.( 6.2) similarly to the flame indicator.

The transport equation of the variable to propagate  $f = \psi^*/\psi$  can be obtained by applying the product rule to the transport equation of  $\psi^*$  and consecutive subtraction of the transport equation of  $\psi$ . By doing so, we obtain the transport equation for variable  $f$  in the form of Eq.(6.2) with the source equal to:

$$\begin{aligned}\dot{\omega}_f &= \frac{1}{\psi}\dot{\omega}_{\psi^*} - \frac{f}{\psi}\dot{\omega}_{\psi} \\ &= \frac{1}{\psi}\dot{\omega}_{\psi^*} - \frac{\psi^*}{\psi^2}\dot{\omega}_{\psi}\end{aligned}\tag{6.6}$$

Within the reaction zone the source term of  $\psi$  has the following form:

$$\dot{\omega}_\psi = \rho\beta(\psi_{target} - \psi)\dot{\omega}_c, \quad (6.7)$$

while the source term of  $\psi^*$  is:

$$\dot{\omega}_{\psi^*} = \rho\beta(\psi_{target} f_{target} - \psi^*)\dot{\omega}_c \quad (6.8)$$

Thus, the source term of the variable  $f$  within the reaction zone :

$$\begin{aligned} \dot{\omega}_f &= \frac{1}{\psi}\dot{\omega}_{\psi^*} - \frac{\psi^*}{\psi^2}\dot{\omega}_\psi \\ &= \rho\beta(f_{target} - f)\frac{\psi_{target}}{\psi}\dot{\omega}_c, \end{aligned} \quad (6.9)$$

Equation (6.9) therefore shows that employing transport equations for  $\psi$  and  $\psi^*$  allows to relax  $f$  towards the desired value  $f_{target}$  and in a time proportional to  $1/\omega_c$ .

Following the same logic, we can derive the source term of  $f$  outside the reaction zone. The source term of  $\psi$  outside the reaction zone is defined with:

$$\dot{\omega}_\psi = \rho\frac{0 - \psi}{\tau_{dest}}, \quad (6.10)$$

while the source term of  $\psi^*$  outside the reaction zone is:

$$\dot{\omega}_{\psi^*} = \rho\frac{0 - \psi^*}{\tau_{dest}} = \rho\frac{0 - \psi f}{\tau_{dest}}, \quad (6.11)$$

Then the source term of the variable to propagate  $f$  outside the reaction zone equals to 0:

$$\begin{aligned} \dot{\omega}_f &= \frac{1}{\psi}\dot{\omega}_{\psi^*} - \frac{\psi^*}{\psi^2}\dot{\omega}_\psi \\ &= 0, \end{aligned} \quad (6.12)$$

meaning that  $f$  remains constant outside the reaction zone. Keeping  $f$  constant outside the reaction zone would be impossible using a transport equation Eq.( 6.2) for  $f$  directly because  $f$  gets diffused by molecular and turbulent diffusivities. On

the contrary, as shown by Eq.(6.12), using  $\psi$  and  $\psi^*$  allows to keep  $f$  constant in a simple way.

Next, we will go over all flame properties needed for the geometrical sensor formulation one by one, explaining the derivation of each in detail.

### Thickened flame thickness

The actual thickened flame thickness is denoted with  $\delta_L^1$ . It is obtained from the local flow characteristics, and it should not be confused with the real or non-thickened flame thickness denoted with  $\delta_L^0$ , which is defined later.

The estimation of the local thickened flame thickness in Eq.(6.13) is based on the local gradients of the progress variable  $C$  defined in Eq.(6.1). Here, we assume that shape of the progress variable profile  $C$  can be well approximated with the function  $C^*(x) = 0.5 \left( 1 + \tanh \left( \frac{2}{\delta_L} x \right) \right)$ . Then, the local flame thickness can be derived from the maximum slope of  $C^*(x)$ , as follows:

$$\delta_L^{local} = \beta_C \frac{4C(1-C)}{|\nabla C|} \quad (6.13)$$

The value of  $\beta_C = 1$  is used throughout this work which leads to good estimates of the thickness. However, the parameter  $\beta_C$  can be adjusted to assure a better fit with the function  $C^*(x)$  depending on flame characteristics. In cases where the progress variable profile is less steep than in the hyperbolic tangent function  $C^*(x)$  approximating it, it might require adjusting the  $\beta_C$  parameter by setting it below unity. Contrarily, when the  $C$  profile is sharper than  $C^*$ ,  $\beta_C$  can be set above unity for a better fit.

The steepest slope of the progress variable is observed within the reaction zone and defines the thickness of the flame. The thickened flame thickness indicator  $\psi^1$  is used to transport this information as described in Sec. 6.1.1 over the entire flame front. This allows to recover the thickness of the thickened flame from the flame indicator and the thickened flame thickness indicator using  $\delta_L^1 = \psi/\psi^1$ . The source term of the thickened flame thickness indicator is defined with Eq.(6.3) with  $\psi_{target}^1 = \psi_{max}/\delta_{target}^1$ .

Here, the target thickened flame thickness  $\delta_{target}^1$  is the local flame thickness given by Eq.(6.13).

Outside the flame front,  $\psi^1$  relaxes towards zero, which allows us to get an infinite flame thickness  $\delta_L^1$  so that no thickening is required. For this reason, the thickened flame thickness indicator is defined with  $\psi/\delta^1$ , not with  $\psi\delta^1$ .

### Non-thickened flame thickness

The non-thickened flame thickness is denoted with  $\delta_L^0$ , and its accurate prediction plays an essential role in determining the thickening factor.

A non-thickened flame thickness indicator  $\psi^0$  is introduced to compute the non-thickened flame thickness. It is recovered from the flame indicator and the non-thickened flame thickness indicator using  $\delta_L^0 = \psi/\psi^0$ .

The  $\psi^0$  indicator is transported as described in Sec. 6.1.1 and its target value within the reaction zone from Eq.(6.3) is defined with  $\psi_{target}^0 = \psi_{max}/\delta_{target}^0$ . The computation of the target non-thickened flame thickness  $\delta_{target}^0$  is based on the estimation of the equilibrium thickness  $\delta_L^{eq}$  and is done as follows:

$$\delta_{target}^0 = \delta_L^0 + \frac{\psi}{\psi_{max}}(\delta_L^{eq} - \delta_L^0), \quad (6.14)$$

where  $\psi$  is the flame indicator and  $\psi_{max}$  is its target value in the source term, both defined in Sec. 6.1.2.

The equilibrium thickness  $\delta_L^{eq} = \delta_L^1/F$  relates the thickening factor  $F$  with the thickened flame thickness. At the same time, the thickening factor is a function of the non-thickened flame thickness and can be expressed as  $F = \Delta_x n_{res}/\delta_L^0$ . If we combine these two, we get the definition of the equilibrium thickness:

$$\delta_L^{eq} = \delta_L^0 \frac{\delta_L^1}{\Delta_x n_{res}} \quad (6.15)$$

When the thickened flame thickness is equal to  $\Delta_x n_{res}$ , then  $\delta_L^{eq} = \delta_L^0$ , which means that  $\delta_L^0$  has reached the equilibrium value and does not need to be changed. Conversely, when the computed flame thickness is larger/smaller than  $\Delta_x n_{res}$ , then

the equilibrium thickness is larger/smaller than the estimated  $\delta_L^0$ , meaning that the real flame is thicker/thinner than the estimated one and  $\delta_L^0$  has to converge towards this equilibrium value.

The factor  $\psi/\psi_{max}$  in Eq.(6.14) comes from the derivation of the source term given in Eq.(6.9) and is required to correct the relaxation rate of the non-thickened flame thickness towards the desired value. If  $\delta_L^0$  has reached the equilibrium value, the target flame thickness will be equal to  $\delta_L^0$ . In the opposite case,  $\delta_L^0$  will gradually approach the equilibrium value.

For the same reasons as the thickened flame thickness  $\delta_L^1$ , the non-thickened flame thickness indicator is defined with  $\psi/\delta_L^0$ , not with  $\psi\delta_L^0$ .

### Laminar flame speed and reactive fuel/air equivalence ratio

The laminar flame speed is used in the determination of the efficiency factor, which is a function of  $u'/S_L^0$ , and is involved in the definition of the relaxation times for the transported variables. The non-thickened flame thickness  $\delta_L^0$  is used to evaluate the laminar flame speed. Flame thickness and speed may be related through the following formula  $\delta_L^{diff} = D_{th,u}/S_L^0$ , which comes from scaling laws. Here  $\delta_L^{diff}$  is the diffusive flame thickness, and  $D_{th,u}$  is the thermal diffusivity at the unburned side. However, we can not use  $\delta_L^{diff}$  to compute the laminar flame speed locally since it is not always precise and usually gives values that are smaller by a factor of the order of five [61]. Instead, we use Blint's correlation [9] that gives a better estimation for flame thicknesses characterizing the steepness of the temperature gradient, which is indeed crucial for numerical computations.

Blint's correlation relates the diffusive thickness  $\delta_L^{diff}$  to the actual flame thickness  $\delta_L^0$  as:  $\delta_L^0/\delta_L^{diff} = 2(\lambda/c_p)_b/(\lambda/c_p)_u$ , where subscripts  $b$  and  $u$  indicate the burned and unburned sides respectively. Then, the local laminar flame speed can be computed using:

$$S_{L,local}^0 = 2 \frac{(\lambda/c_p)_b}{(\lambda/c_p)_u} \frac{D_{th,u}}{\delta_L^0} \quad (6.16)$$

We assume that the Prandtl number is constant and equal to 0.7, and the dynamic viscosity  $\mu_b$  is estimated with Sutherland's law. In that case, the calculation of the local laminar flame speed reduces to:

$$S_{L,local}^0 = \frac{2\mu_b}{\rho_u \delta_L^0 Pr}, \quad (6.17)$$

where  $\mu_b$  is computed using the burned temperature  $T_b(\phi)$  tabulated as a function of local gaseous fuel/air equivalence ratio.

The local gaseous fuel/air equivalence ratio can vary a lot within spray flames. Moreover, we can also observe  $\phi_g$  peaks caused by the preferential diffusion within purely gaseous flames. Since the tabulated quantities depend on  $\phi_g$ , variation of  $\phi_g$  will also affect the local values of the progress variable given by Eq.(6.1) and the laminar flame speed computed using Eq.(6.17). We have also observed that low  $\phi_g$  values at the base of the flame can lead to incorrect relaxation time estimations in the spray flames with a low level of pre-evaporated fuel.

We considered two different solutions for this problem. The first one is to compute the laminar flame speed within the reaction zone and transfer it to the rest of the flame structure, following the procedure described in Sec. 6.1.3. The second solution is to evaluate the gaseous fuel/air equivalence ratio  $\phi_g$  in the reaction zone and then transfer this value to the rest of the flame front thanks to a transport equation for  $\psi\phi_g$ . In any of these cases, we need to introduce one additional indicator  $\psi^2$  transported according to the procedure described in Sec. 6.1.1. The source term for  $\psi^2$  depends on the selected option.

For the first version, we take the laminar flame speed defined in the reaction zone and transfer it to the rest of the flame. This model version is referred to as GS-sL-TFM-AMR. The laminar flame speed is recovered from  $S_L^0 = \psi^2/\psi$ . For the transported auxiliary variable, the target value within the reaction zone is computed using  $\psi_{target}^2 = S_{L,target}^0 \psi_{max}$ , where the target laminar flame speed  $S_{L,target}^0$  is computed locally using the expression given in Eq. 6.17.

The second model version, referred to as GS-phi-TFM-AMR, computes the fuel/air

equivalence ratio that characterizes the reacting zone of the flame and propagates it over the entire flame front. In the following, this characteristic fuel/air equivalence ratio is referred to as the reacting gaseous fuel/air equivalence ratio obtained from  $\phi_r = \psi^2/\psi$ . In this case, the target value within the reaction zone is computed using the local gaseous fuel/air equivalence ratio  $\psi_{target}^2 = \phi_g \psi_{max}$ .

In the GS-phi-TFM-AMR model version, all the tabulated quantities become a function of the reacting gaseous fuel/air equivalence ratio. Since the resulting  $\phi_r$  is uniform across the flame front, the local laminar flame speed computed in Eq.(6.17) becomes also uniform over the flame front and does not require any additional transport equation.

The differences between two model versions will be discussed in the context of 1D premixed and spray flames in Sec. 6.2.

Figure 6-1 summarize all transported variables that are required for geometrical sensor and discussed above. The flame indicator is given first, followed by the auxiliary transported variables needed to compute the flame properties. Here, the source term that arises in Eq.(6.2) is given in the third and the fourth column, corresponding to the reaction zone and the rest of the flame, respectively. While the source term remains similar for all transported variables, the target value  $\xi_{target}$  within the reaction zone differs for each variable and is given in the second column. The derivation of the flame property from the transported variable depends on the target value  $\xi_{target}$  and is noted in the last column.

### Flame sensor and flame thickening

The flame sensor  $\hat{S}$  employed in scalar transport equations depends on the flame indicator discussed in Sec. 6.1.2 and is defined by:

$$\hat{S} = \min(\psi; 1) \tag{6.18}$$

In the Jaravel sensor formulation given by Eq.(2.13), the flame detection requires the tabulation of the maximal heat release through the flame front. In contrast to the

$\xi$	$\xi_{target}$	Source term $\dot{\omega}_\xi$		Use
		Reaction zone	Outside reaction zone	
$\psi$	$\psi_{max} = 20$			
$\psi^0$	$\frac{\psi_{max}}{\delta_{target}^0}$ ; $\delta_{target}^0 = \delta_L^0 \frac{\psi}{\psi_{max}} (\delta_L^{eq} - \delta_L^0)$			$\delta_L^0 = \frac{\psi}{\psi^0}$
$\psi^1$	$\frac{\psi_{max}}{\delta_{target}^1}$ ; $\delta_{target}^1 = \beta_C \frac{4C - 4C^2}{ VC }$	$\beta \rho (\xi_{target} - \xi) \omega_C$	$\rho \frac{0 - \xi}{\tau_{destr}}$	$\delta_L^1 = \frac{\psi}{\psi^1}$
$\psi^2$	$\begin{cases} \psi_{max} S_L^0 \\ \psi_{max} \phi \end{cases}$			$S_L^0 = \frac{\psi^2}{\psi}$ $\phi_r = \frac{\psi^2}{\psi}$

Figure 6-1: Transported variables, their source terms and use.

standard TFM sensor formulation, we avoid the direct comparison to the premixed 1D flames in the geometrical sensor.

The flame thickening procedure detailed in Sec. 2.3.2 remains the same for the proposed modeling approach. The only difference in the geometrical sensor approach concerns the computation of the maximum thickening factor in Eq.(2.15) and the level of AMR in Eq.(2.16), where the estimated non-thickened flame thickness  $\delta_L^0$  is used instead of the tabulated value.

Figure 6-2 provides a global overview of the flame thickening algorithm and summarizes the model described above. The scheme for the geometrical sensor is given on the right in Fig. 6-2, whereas the scheme for the standard sensor formulation is shown on the left to compare both flame thickening approaches. The entire thickening algorithm is enclosed within a blue rectangle. It is divided into subparts, such as the initialization of the flame properties, the flame front detection, the flame thickening, and the transport of required properties, all shown with green rectangles. The interaction of variables within the model is given by the colored arrows, while the information that comes outside the model is shown with grey ones.

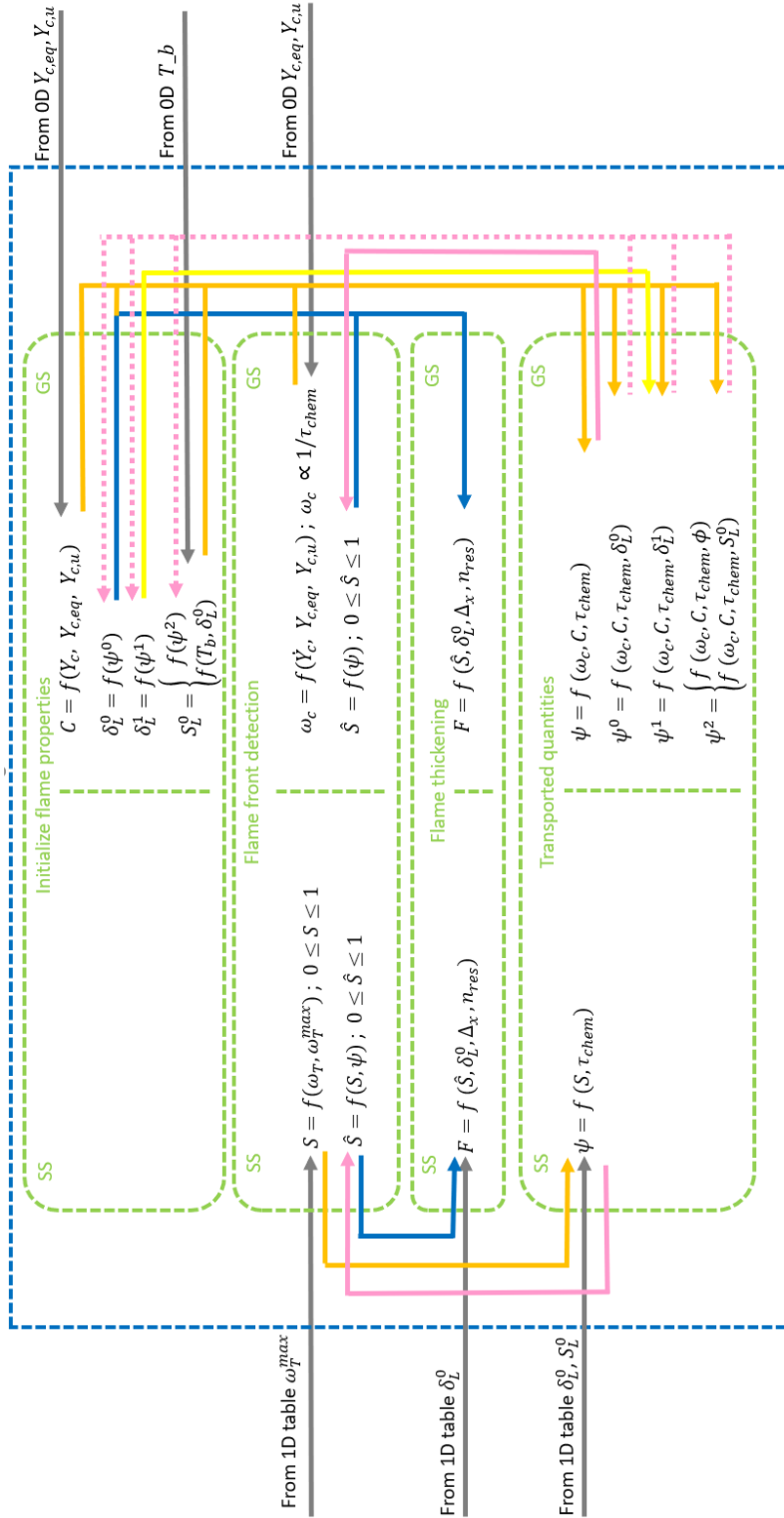


Figure 6-2: Flame thickening algorithm. Left: standard sensor formulation; right: geometrical sensor formulation.

## 6.2 Geometrical formulation of the thickened flame model: 1D Configuration

To validate the newly proposed model, we follow the procedure used for the standard TFM model by investigating a simple one-dimensional configuration first. For this purpose, the setup already considered in Section 3.2.2 is kept here. This configuration represents the 1D n-dodecane spray flames at  $T = 323K$ ,  $p = 1bar$ . The overall fuel/air equivalence ratio is set to  $\phi_o = 0.8$  for all gaseous and spray cases presented in Sections 6.2.2 and 6.2.3 respectively. In the two-phase flame configuration, the cell size is kept constant when the droplet size is varied.

In the reference non-thickened solution, we resolve the thinnest flame with at least seven points per flame thickness which is defined by the steepest progress variable gradient. The reference flame thickness and laminar speed values are given in Fig. 3-11.

### 6.2.1 Verification of model assumptions

Before analyzing the accuracy of the entire model, we would like to first verify the assumption that we make in Eq.(6.13) to estimate the local flame thickness. Here, we assume that the progress variable follows the profile of the analytical function  $C^*(x) = 0.5 \left( 1 + \tanh\left(\frac{2}{\delta_L}x\right) \right)$ , as described in Sec. 6.1.3. In Figure 6-3, we verify this assumption on non-thickened flames by plotting the profiles of progress variable  $C$  together with its approximations  $C^*$  given with black solid lines.

Figure 6-3 shows the progress variable and its approximation  $C^*(x)$  for the n-dodecane spray flames with the droplet sizes of  $10 \mu m$ ,  $20 \mu m$ ,  $30 \mu m$  and  $40 \mu m$ . The differences between the spray flame profiles with  $D_d = 10 \mu m$  and the gaseous flame are negligible, and, thus, only the  $D_d = 10 \mu m$  case is shown in Fig. 6-3.

We can observe a good agreement between the progress variable and the analytical function in most of the flame structures, except for the burned gases ( $C > 0.9$ ). However, for bigger droplet diameters,  $D_d > 20 \mu m$ , this agreement shrinks to the

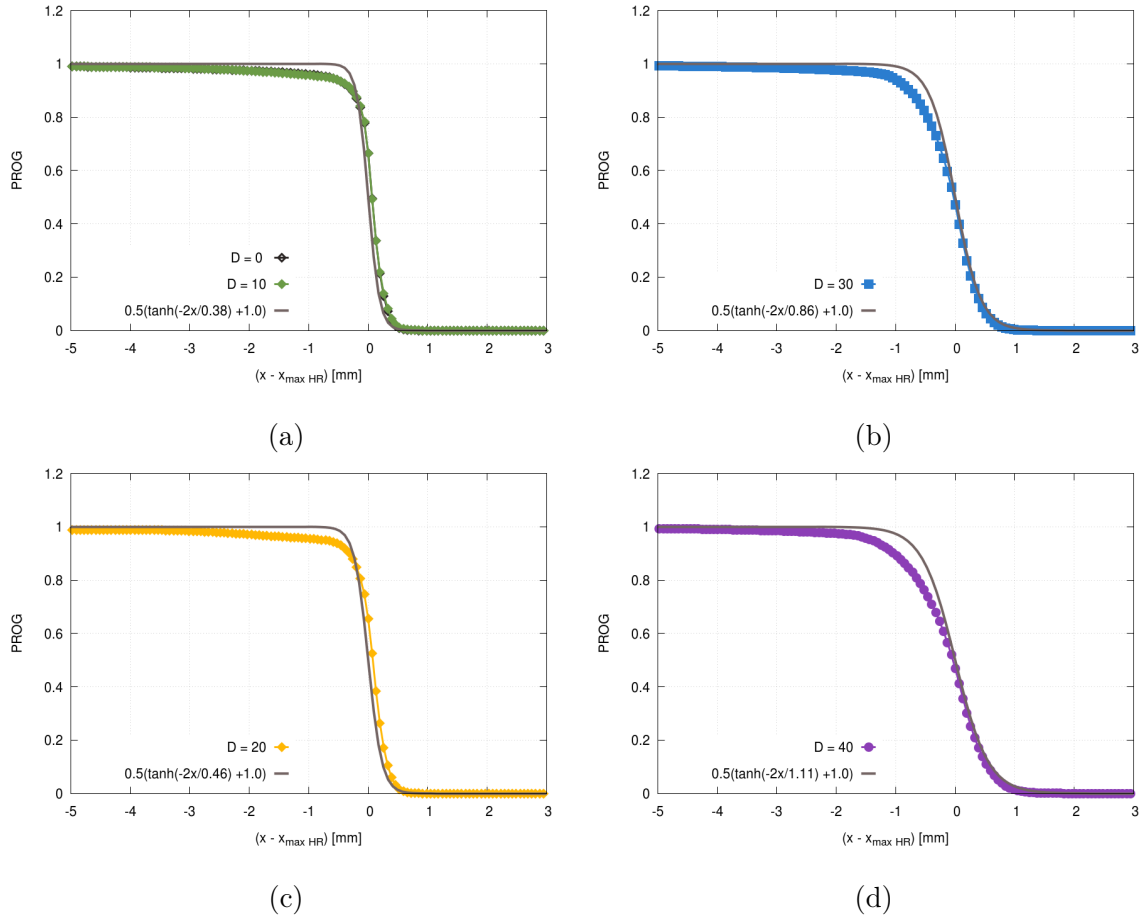


Figure 6-3: 1-D n-dodecane progress variable profiles versus  $C^*$  function,  $D_d = 0-40 \mu m$ , no TFM. (a): gaseous and  $D_d = 10 \mu m$ ; (b):  $D_d = 30 \mu m$ ; (c):  $D_d = 20 \mu m$  (d):  $D_d = 40 \mu m$ .

region where the progress variable is less than 0.6 approximately.

As the size of the droplets grows, the progress variable profile becomes less steep towards the burned gases, as seen in Fig. 6-3b and Fig. 6-3d. This can be explained by the slower evaporation rate of large droplets, which thus increases the flame thickness on the burned gases side. This non-symmetry in  $D_d > 20 \mu m$  cases cannot be captured with the selected analytical function. However, since the steepest flame region is approximated correctly, we can expect that the model provides a reasonable flame thickness estimation. The most significant deviation from the analytical function is observed for the largest droplets  $D_d = 40 \mu m$ . In this case, for instance, the flame thickness estimated by the model is 5–20% smaller than its actual value, as discussed in Sec. 6.2.3.

Configuration	Model	$\Delta_x$ [mm]	$\Delta_x$ AMR [mm]	$\beta$	$\alpha_{cold}/\alpha_{hot}$
G-REF	no	0.0625	-	-	-
G-TFM-sL	GS-sL-TFM-AMR	0.5	0.25	1	0.05/0.005
G-TFM-sL-ext	GS-sL-TFM-AMR	0.5	0.25	1	0.5/0.05
G-TFM-phi	GS-phi-TFM-AMR	0.5	0.25	1	0.05/0.005
G-TFM-phi-ext	GS-phi-TFM-AMR	0.5	0.25	1	0.5/0.05

Table 6.1: Computed 1D gaseous flame configurations.

In Sec. 6.1.3 it was mentioned, that the  $\beta_C$  parameter present in Eq.(6.13) can be adjusted to achieve a better match with the analytical function  $C^*(x)$ . Since we can observe a fairly good agreement between the progress variable and its approximation, we set the value of  $\beta_C$  to be equal to unity.

In the following, the resulting thickened flame profiles are compared against the reference non-thickened solutions. The target resolution  $n_{res}$  needed in Eq.(6.15) for all thickened flames is fixed to 9. Unless stated otherwise, the GS-TFM-AMR model uses the following settings:  $\beta = 1$ ,  $\beta_C = 1$ ,  $\alpha_{cold} = 0.05$  and  $\alpha_{hot} = 0.005$ .

## 6.2.2 Gaseous flame validation

The flame thickening using the geometrical sensor is analyzed first by computing a purely gaseous flame. The computed gaseous 1D cases are summarized in Table 6.1.

As mentioned in the model description in Sec. 6.1.3, two different model versions are available to obtain characteristic flame properties. Either the variable  $\psi^2$  is transported to get a uniform laminar flame speed over the flame front (GS-sL-TFM-AMR) or a uniform gaseous fuel/air equivalence ratio  $\phi_r$  (GS-phi-TFM-AMR). Below, we investigate these two modeling strategies corresponding to the G-TFM-sL and G-TFM-phi configurations listed in Table 6.1.

The reference non-thickened flame profiles are compared to thickened flame profiles in Figures 6-4 and 6-5. Thickened flame profiles obtained with GS-phi-TFM-AMR are represented in purple ( $\alpha_{cold} = 0.5$  and  $\alpha_{hot} = 0.05$ ) and green ( $\alpha_{cold} = 0.05$  and

$\alpha_{hot} = 0.005$ ), while the ones computed using GS-sL-TFM-AMR are in orange ( $\alpha_{cold} = 0.5$  and  $\alpha_{hot} = 0.05$ ) and yellow ( $\alpha_{cold} = 0.05$  and  $\alpha_{hot} = 0.005$ ).

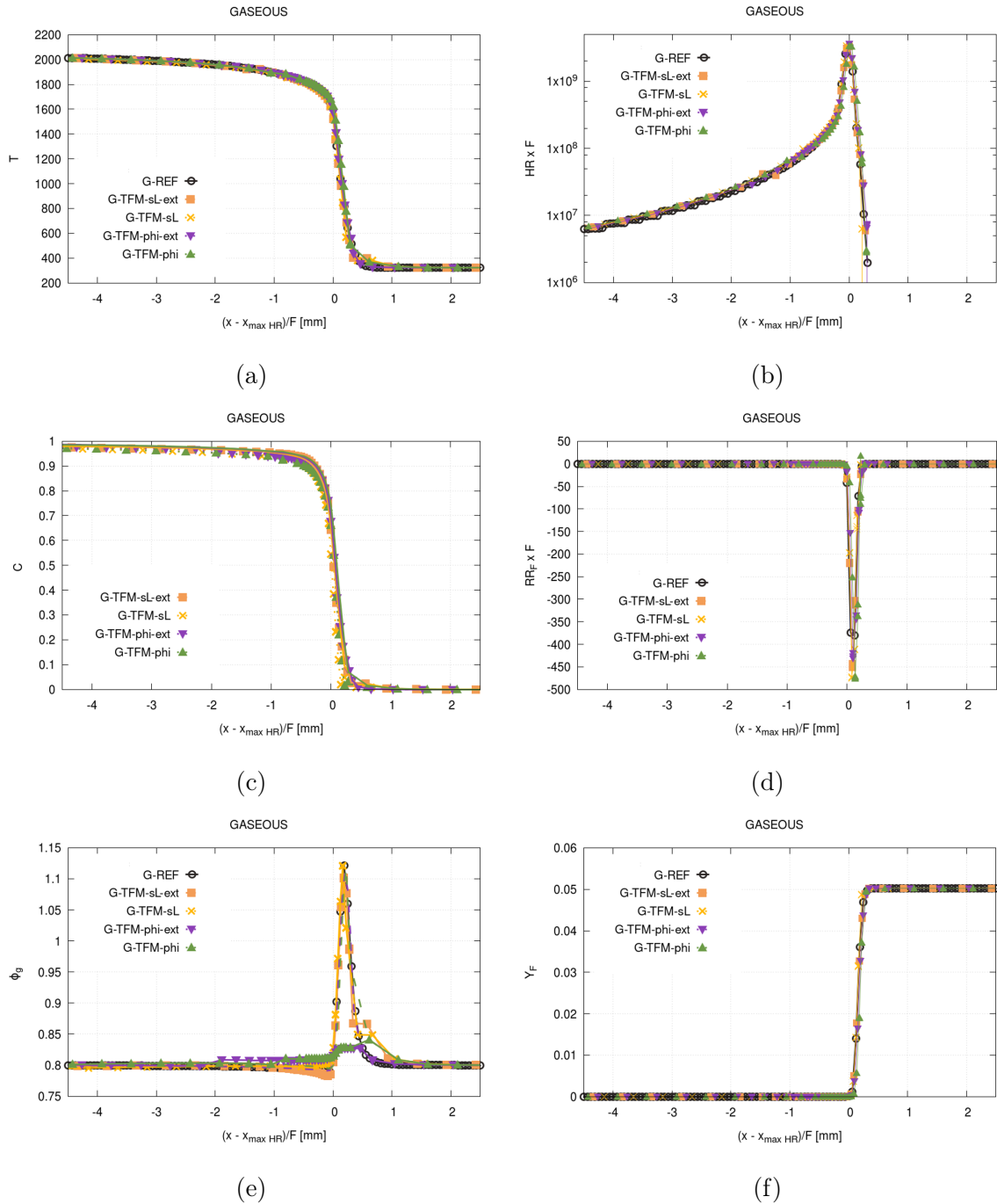


Figure 6-4: 1-D n-dodecane gaseous flame profiles, TFM-AMR with geometrical sensor. (a): gaseous temperature; (b): heat release rate; (c): progress variables: computed  $C$  - dashed lines with points, actual  $C$  - solid lines; (d): fuel reaction rate; (e): gaseous and reaction fuel/air equivalence ratio; (f): fuel mass fraction.

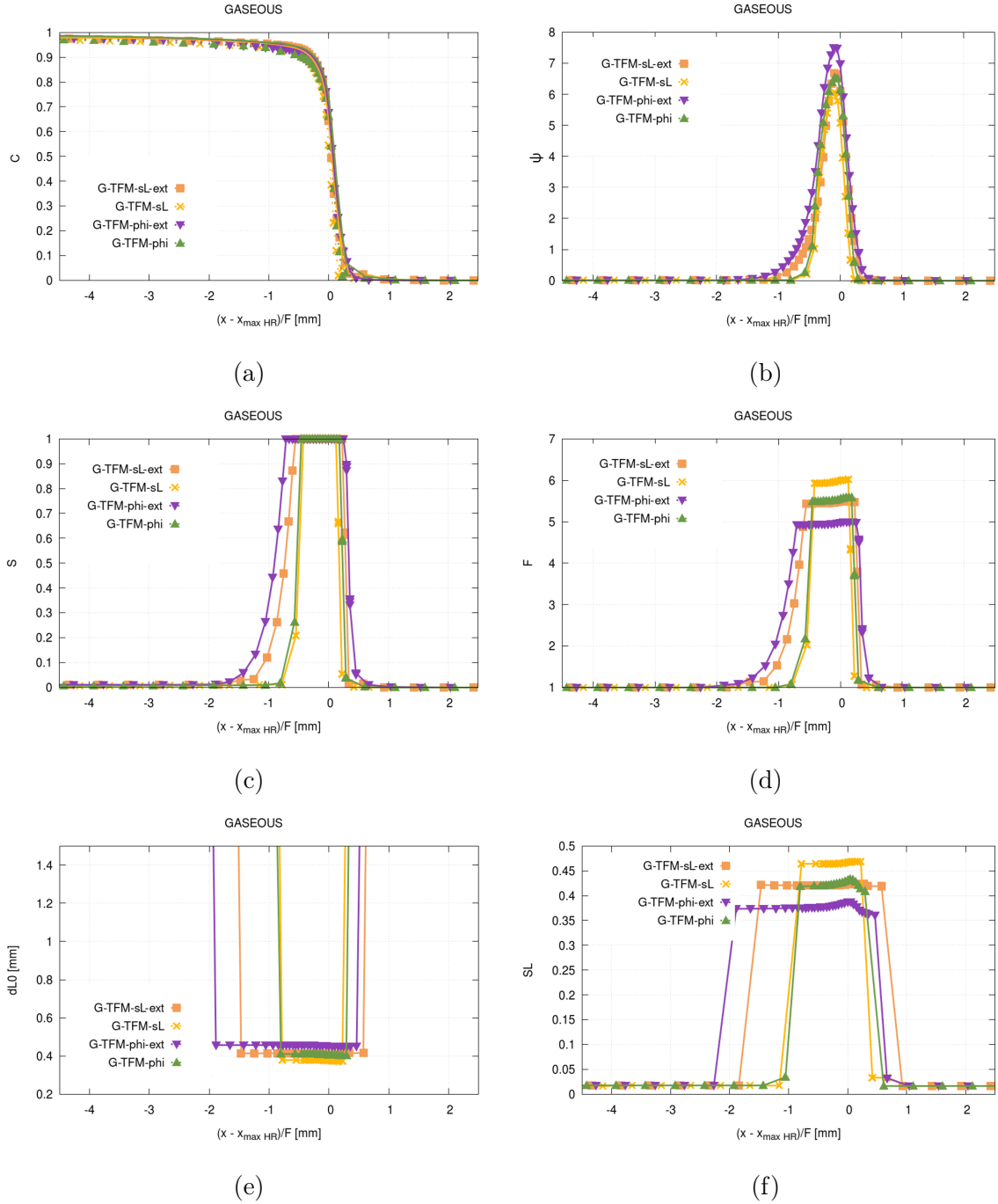


Figure 6-5: 1-D n-dodecane gaseous flame profiles, TFM-AMR with geometrical sensor. (a): progress variables: computed  $C$  - dashed lines with points, actual  $C$  - solid lines; (b): indicator  $\psi$ ; (c): final sensor  $\hat{S}$ ; (d): thickening factor  $F$ ; (e): flame thickness  $\delta_L^0$ ; (f): laminar flame speed  $S_L^0$ .

Regardless of the model choice, temperature, progress variable, heat release rate, fuel mass fraction and fuel reaction rate are perfectly predicted using the geometrical

sensor.

Figure 6-4e shows fuel/air equivalence ratio profiles obtained for purely gaseous flames. For the model version GS-phi-TFM-AMR, where the reactive fuel/air equivalence ratio  $\phi_r$  is computed,  $\phi_r$  is plotted together with the gaseous fuel/air equivalence ratio  $\phi_g$ . In this case, dashed lines represent the gaseous fuel/air equivalence ratio and lines with points the corresponding reacting one. The figure shows a peak of the gaseous fuel/air equivalence ratio due to preferential diffusion where  $\phi_g$  rises from 0.8 up to 1.1. At the same time,  $\phi_r$  computed in GS-phi-TFM-AMR is not perturbed by the preferential diffusion as desired and remains nearly constant and close to 0.8 over the entire flame, the value set at the inlet.

The progress variable profiles are shown in Fig. 6-4c. Here, dashed lines with points represent the  $C$  profiles, while the actual progress variable profiles are shown with the solid lines. Here, the actual progress variable profiles are computed at the post-processing step using the maximum  $Y_C$  observed within the computed flame. In this purely gaseous configuration, it is not easy to differentiate between the computed and actual progress variables because the lines overlap. Therefore, the use of computed progress variable  $C$  is justified to determine the thickened flame thickness.

Contrarily to the standard TFM indicator, we see here in Fig. 6-5b that the geometrical model indicator never reaches the maximal value. This behavior is expected from the model, as explained previously in Sec. 6.1.2.

Setting larger relaxation time coefficients helps investigate how sensitive the model is to this parameter. Therefore, we computed an additional flame with  $10\alpha_*$  for each model version. These are the configurations G-TFM-sL-ext and G-TFM-phi-ext in Table 6.1. As it can be seen in Fig. 6-5c, larger relaxation time coefficients broaden thickened regions, as expected. Moreover, larger relaxation time coefficients also lead to slightly lower thickening factors, as shown in Fig. 6-5d, which can be explained by the behavior of the progress variable. Figure 6-5a shows that the progress variable gradients, which directly affect the estimation of the flame thickness, become less steep as we approach the burned side. The further the sensor expands on the burned side, the larger region of the progress variable with less steep gradients is included in

Configuration	Model	$\Delta_x$ [mm]	$\Delta_x$ AMR [mm]	$\beta$	$\alpha_{cold}/\alpha_{hot}$
S-REF	no	0.0625	-	-	-
S-TFM-sL	GS-sL-TFM-AMR	0.5	0.25	1	0.05/0.005
S-TFM-sL-ext	GS-sL-TFM-AMR	0.5	0.25	1	0.5/0.05
S-TFM-sL-sens	GS-sL-TFM-AMR	0.5	0.25	10	0.05/0.005
S-TFM-phi	GS-phi-TFM-AMR	0.5	0.25	1	0.05/0.005
S-TFM-phi-ext	GS-phi-TFM-AMR	0.5	0.25	1	0.5/0.05
S-TFM-phi-sens	GS-phi-TFM-AMR	0.5	0.25	10	0.05/0.005

Table 6.2: Computed 1D spray  $D_d = 0 - 40 \mu m$  flame configurations.

the evaluation of  $\delta_L^0$  increasing its final value shown in Fig. 6-5e.

Although some tiny differences exist between the different models in the evaluation of  $\delta_L^0$ , all of them reproduce the reference value of  $0.38mm$  reasonably well, as can be seen in Fig. 6-5e.

The burning velocity estimated by the model  $S_L$  is shown in Fig. 6-5f. The predicted burning velocities exceed its actual value of  $0.3m/s$ . Depending on the parameter choice, this difference varies from 20% up to 50%. Such deviation is considered acceptable since  $S_L$  is not playing a crucial role in defining the final thickening factor. Within the model,  $S_L$  is used to define the relaxation rates of transported variables and for the efficiency factor computation. Therefore, it will impact the estimation of the efficiency factor, which should be evaluated.

### 6.2.3 Spray flame validation

Spray flame thickening using the geometrical sensor was performed for droplet diameters ranging from  $10 \mu m$  to  $40 \mu m$ . To demonstrate the model's behavior, we will analyze the case with the largest droplet size considering both modeling approaches: GS-phi-TFM-AMR and GS-sL-TFM-AMR. Additionally, we will investigate below the sensitivity of the model to the sensor slope  $\beta$  and to the relaxation time coefficients  $\alpha_*$ . All computed configurations are summarized in Table 6.2.

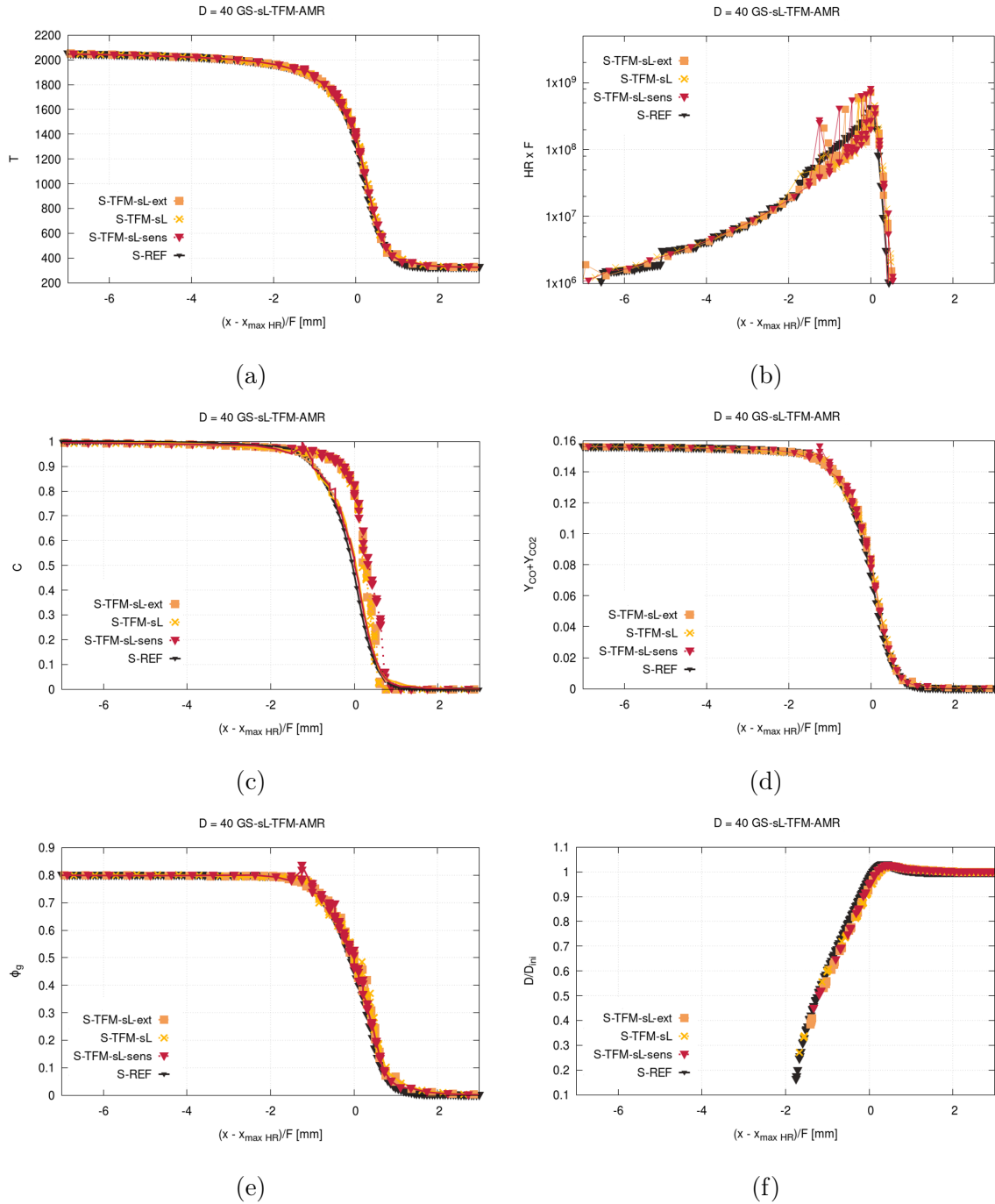


Figure 6-6: 1-D n-dodecane 40  $\mu\text{m}$  spray flame profiles, GS-sL-TFM-AMR. (a): gaseous temperature; (b): heat release rate; (c): progress variables: computed  $C$  - dashed lines with points, actual  $C$  - solid lines; (d): sum of  $\text{CO}$  and  $\text{CO}_2$  mass fractions; (e): gaseous fuel/air equivalence ratio; (f): normalized droplet diameter.

The results obtained for the droplets with  $D = 40 \mu\text{m}$  with GS-sL-TFM-AMR are shown first in Fig. 6-6 and Fig. 6-7. On the plots, the colored lines represent the

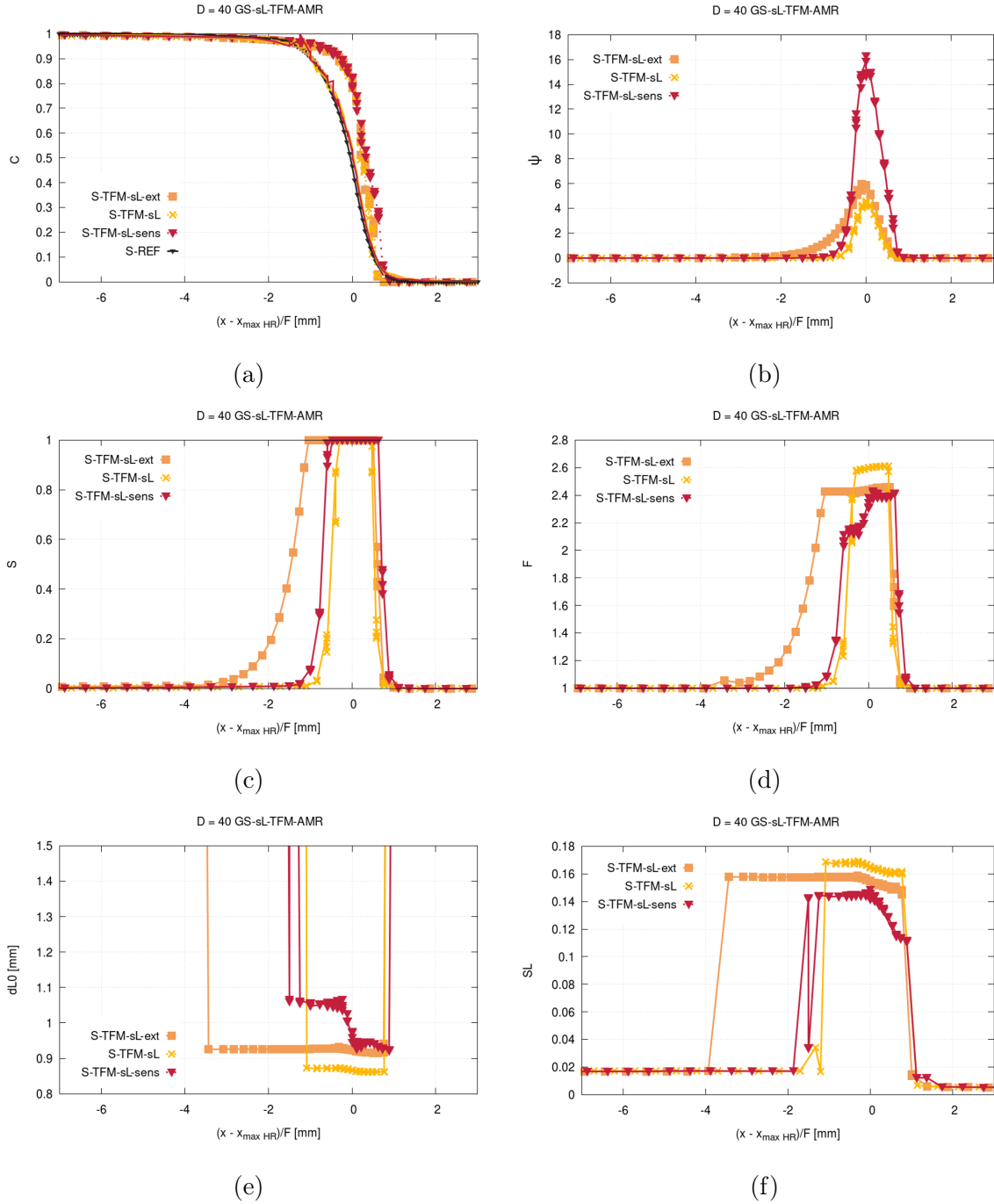


Figure 6-7: 1-D n-dodecane 40  $\mu\text{m}$  spray flame profiles, GS-sL-TFM-AMR. (a): progress variables: computed  $C$  - dashed lines with points, actual  $C$  - solid lines; (b): indicator  $\psi$ ; (c): final sensor  $\hat{S}$ ; (d): thickening factor  $F$ ; (e): flame thickness  $\delta_L^0$ ; (f): laminar flame speed  $S_L^0$ .

thickened profiles obtained with standard settings (S-TFM-sL, in yellow), with ten times increased sensor sensitivity (S-TFM-sL-sens, in red), with  $10\alpha_*$  (S-TFM-sL-ext, in orange).

The computed thickened profiles match the reference non-thickened solution very well. However, we can observe some discrepancies in the estimation of the local progress variable  $C$ . It is important to emphasize that this mismatch is related only to the  $C$  estimation and not its actual values. To illustrate this, the actual  $C$  profiles are shown in Fig. 6-7a with solid lines, while the estimated values are represented with symbols.

As explained in the model description in Sec. 6.1, the local estimation of the progress variable is used to compute the thickened flame thickness. These local estimations are obtained using Eq.(6.1) during the simulation run time, whereas the actual progress variable can be calculated only at the post-processing step for spray flames since it requires the knowledge of the entire flame structure. To retrieve the actual progress variable profiles in this 1D configuration, the tabulated  $Y_{C,u}$  in Eq.(6.1) is set to zero and  $Y_{C,eq}$  is replaced with  $Y_{CO} + Y_{CO_2}$  on the burned side.

In the studied spray flames, the computed during the simulation run time  $C$  profiles are steeper than the actual progress variable profiles. The difference between the actual progress variable and the one computed with Eq.(6.1) arises from the use of the tabulated properties of the gaseous flames. The latter explains why these discrepancies were not present in the purely gaseous computations previously discussed in Sec. 6.2.2. Steeper progress variable slopes directly affect the estimation of the flame thickness, giving values smaller than in reality. In such cases, we can expect that the model provides unnecessarily high thickening factors.

Indeed, the laminar flame thickness  $\delta_L^0$  predicted by the model is around  $0.9mm$ , as it can be seen in Fig. 6-7e, which is slightly lower than the actual thickness which is estimated at  $1.11mm$  in the reference case. Provided that the flame thickness estimation is exact, we should obtain a thickening factor of around 2. As we can observe in Fig. 6-7d, the computed thickening factor exceeds the theoretical value by approximately 20 percent.

When the sensitivity of the geometrical sensor  $\beta$  is multiplied by 10, the peak indicator rises, and the evaluation of the laminar flame thickness  $\delta_L^0$  and the laminar flame speed  $S_L^0$  becomes more sensitive to the local properties, making them slightly

vary across the thickened region.

The estimated burning velocities are given in Fig. 6-7f and range from 0.160 up to 0.210. The computed values are higher than the exact value of  $0.128m/s$ , even though they are still reasonably close.

Similarly to the flames computed with GS-sL-TFM-AMR, the thickened profiles obtained with GS-phi-TFM-AMR match very well the reference profiles. For the GS-phi-TFM-AMR cases, we can observe the same trends during the parameter variation as in the GS-sL-TFM-AMR cases.

Figure 6-8c illustrates that the characteristic reacting gaseous fuel/air equivalence ratio takes the value of around 0.5. This is the expected model behavior, since the gaseous fuel/air equivalence ratio  $\phi_g$  attains 0.5 when the heat release rate reaches its maximum, as can be seen in Fig. 6-8d.

In the GS-phi-TFM-AMR modeling approach, the maximum between  $Y_{C,eq}(\phi_g)$  and  $Y_{C,eq}(\phi_r)$  is taken to compute the local progress variable  $C$ . It results in slightly steeper  $C$  profiles compared to the GS-sL-TFM-AMR cases. And finally, stronger thickening is applied since the flame is estimated to be thinner.

The change in model parameters does not significantly affect the results. This emphasizes the robustness of the proposed thickening strategy. The geometrical sensor provides reasonable and uniform thickening across the entire flame front in the purely gaseous case and the spray flames.

Although the parameter variation did not affect the flame profiles, broader thickening regions improved the stability of simulations in general. For this reason, the flame consumption speeds plotted in Fig. 6-10 are computed with  $10\alpha_*$ , which corresponds to the previously discussed GS-TFM-phi-ext configuration. We can observe that an excellent agreement with the reference flames is achieved for all the computed cases.

In order to compare different model settings the thickened profiles were plotted only for one droplet diameter in Figures 6-6, 6-7, 6-8 and 6-9. Figure 6-11 shows how the thickening factor and gaseous fuel/air equivalence ratio vary with the droplet size in S-TFM-phi-ext configuration. The results obtained with the standard sensor

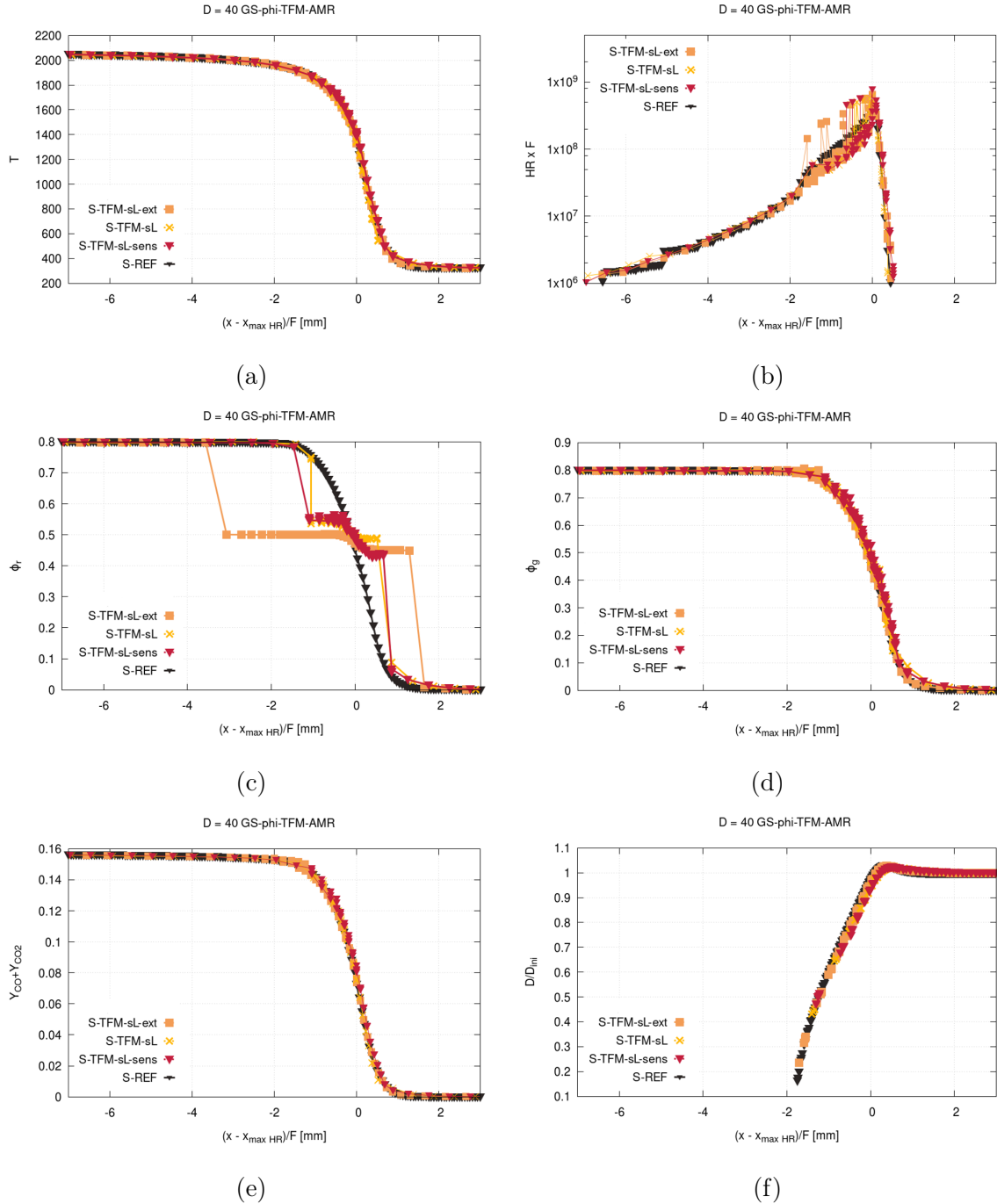


Figure 6-8: 1-D n-dodecane 40  $\mu\text{m}$  spray flame profiles, GS-phi-TFM-AMR. (a): gaseous temperature; (b): heat release rate; (c): reacting fuel/air equivalence ratio; (d): gaseous fuel/air equivalence ratio; (e): sum of  $\text{CO}$  and  $\text{CO}_2$  mass fractions; (f): normalized droplet diameter.

and presented in Sec. 3.2.4 in Fig. 3-17 are also shown in Fig. 6-11 to facilitate the comparison between the models.

In the selected simulation setup, the increase of the droplet size makes the flame

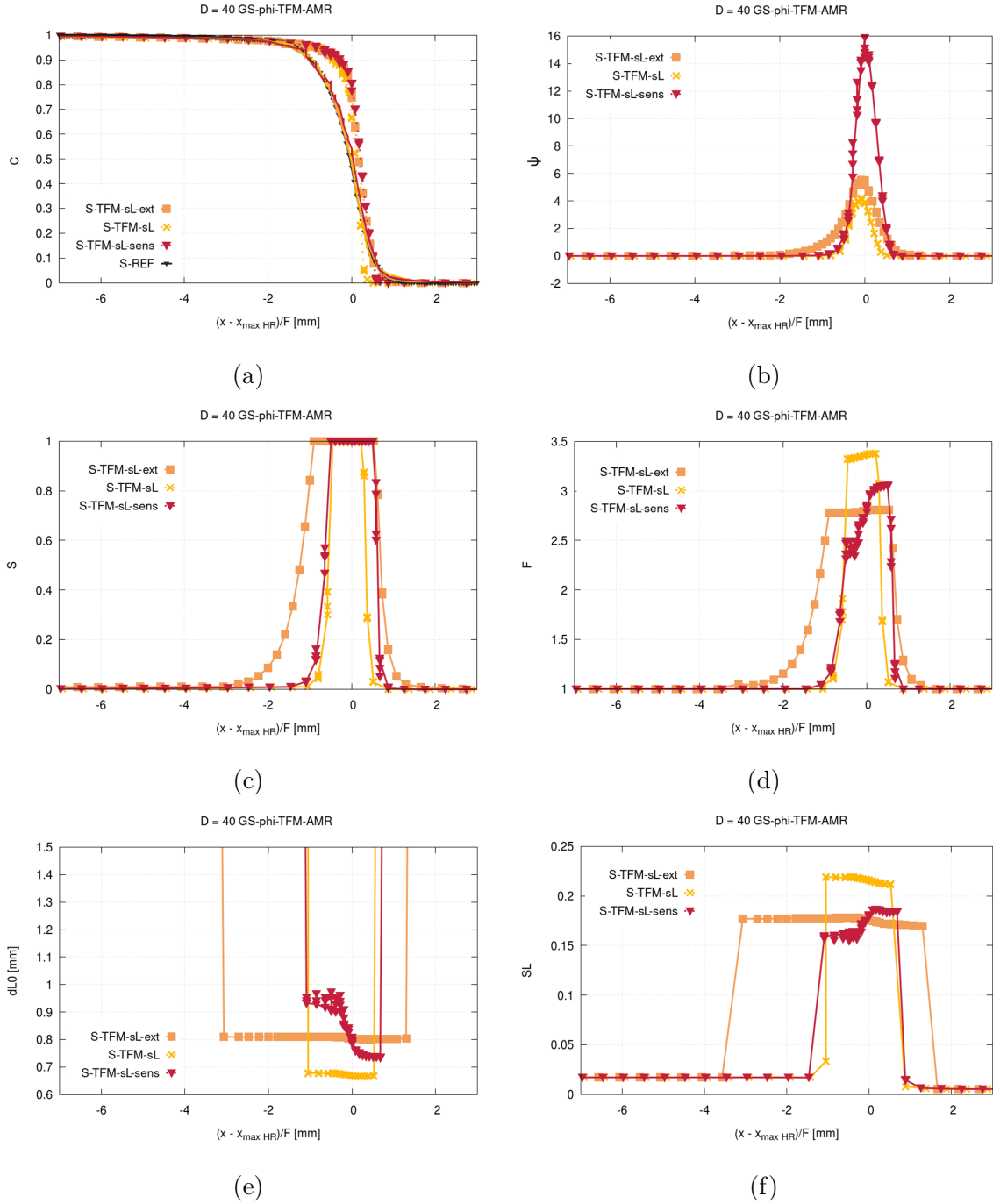


Figure 6-9: 1-D n-dodecane  $40 \mu\text{m}$  spray flame profiles, GS-phi-TFM-AMR (a): progress variables: computed  $C$  - dashed lines with points, actual  $C$  - solid lines; (b): indicator  $\psi$ ; (c): final sensor  $\hat{S}$ ; (d): thickening factor  $F$ ; (e): flame thickness  $\delta_L^0$ ; (f): laminar flame speed  $S_L^0$ .

thicker, as can be seen in Fig. 3-11b. Therefore, the thickening drops with an increase of the droplet diameter since the cell size is kept constant. As shown in Fig. 6-11c,  $F$  is not uniform in the flame with SS-TFM-AMR, especially when the droplet size

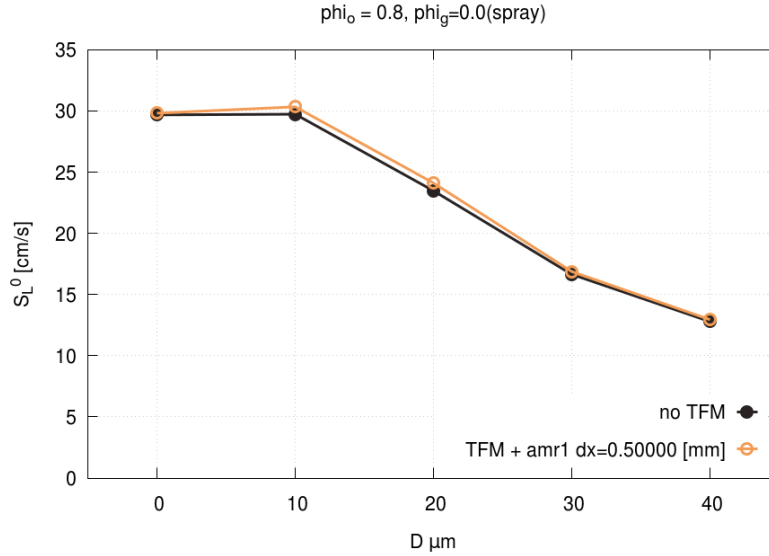


Figure 6-10: 1-D n-dodecane burning velocity as a function of droplet diameter. TFM-AMR with geometrical sensor, S-TFM-phi-ext configuration

increases, while  $F$  is nearly flat with GS-TFM-AMR. At the largest  $D_d$ ,  $F$  obtained with the geometrical approach keeps a value of 2.7, which is consistent with the real flame thickness, while SS-TFM-AMR shows an excessive thickening up to 5 on the burned gases side.

Even though the burning velocities computed with SS-TFM-AMR matched well the reference values, the cold gas side of the spray flames was not appropriately computed. The under-resolution issue is avoided with the geometrical sensor because the entire flame front is thickened uniformly. Therefore, the resulting profiles are smoother when approaching the fresh side, see Fig. 6-11d, than the ones obtained with the standard sensor in Fig. 6-11b.

## 6.2.4 Conclusions

As we saw in this section, the GS-TFM-AMR modeling approach correctly predicts the entire flame front and ensures a uniform thickening for both the gaseous and the spray flames. The model parameters variation did not significantly affect the results emphasizing the robustness of the proposed thickening strategy.

The most important advantage of using GS-TFM-AMR over SS-TFM-AMR is

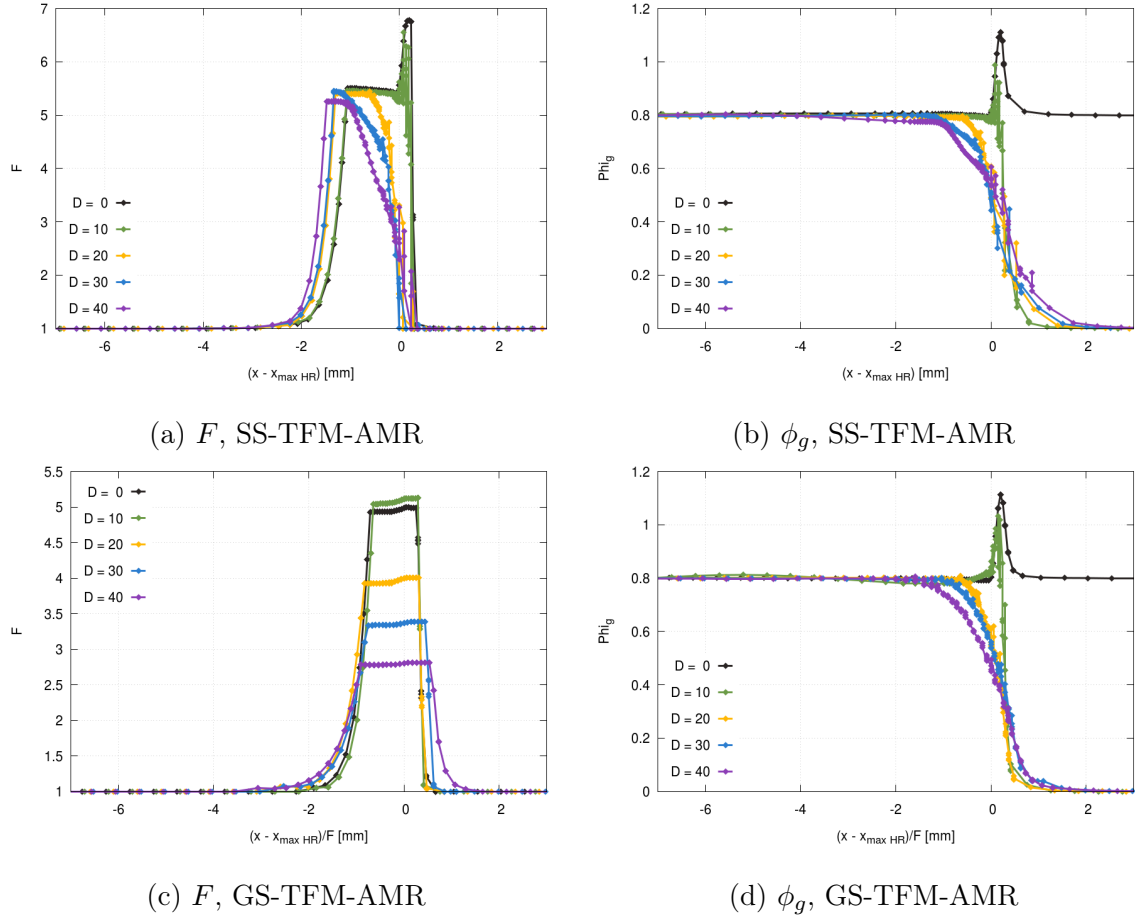


Figure 6-11: 1-D n-dodecane flame profiles,  $D_d = 0 - 40 \mu m$ , TFM-AMR. Top: SS-TFM-AMR, bottom: GS-TFM-AMR (S-TFM-phi-ext configuration). Left: Thickening factor, right: Gaseous fuel/air equivalence ratio

that the laminar flame thickness  $\delta_L^0$  and the laminar flame speed  $S_L^0$  are given by the model and are not tabulated values. GS-TFM-AMR estimations of  $\delta_L^0$  and  $S_L^0$  are pretty accurate for gaseous and spray flames, while the tabulated value in SS-TFM-AMR can be completely off for the spray flames. However, we can expect that the geometrical sensor can potentially lead to unnecessarily high thickening and efficiency factors in the spray flames with a low pre-evaporation and large droplet sizes.

## 6.3 Geometrical formulation of the thickened flame model: CORIA burner

The CRSB burner configuration described in Sec. 4.1 is also considered for the validation of the TFM-AMR modeling approach using the geometrical sensor (GS-TFM-AMR).

### 6.3.1 Numerical settings

While the CRSB results in Chapter 4 were obtained using CONVERGE 2.4 [66], all the computations presented below are conducted with updated code version CONVERGE 3.0 [67] which in particular includes a better algorithm for parallelization. To provide a fair comparison between GS-TFM-AMR results and the ones obtained with the TFM-AMR using the standard sensor definition given in Sec. 2.3.1 (SS-TFM-AMR), the latter ones were recomputed with CONVERGE 3.0. The results, however, are found to be the same.

The simulation domain, represented in Fig. 4-4, and the numerical settings remain the same as those described in Sec. 4.3. Additionally, all simulations presented below take into account the stretch correction for thickened flames and the TFM correction due to the spray/flame orientation explained in detail in Sec. 2.3.3 and Sec. 2.3.4 respectively.

The GS-TFM-AMR simulations are conducted for both modeling strategies defined in Sec.6.1.3: for GS-phi-TFM-AMR that uses the characteristic gaseous fuel/air equivalence ratio, and for GS-sL-TFM-AMR that uses the characteristic laminar flame speed. While the sensor sensitivity is set to  $\beta = 10$  to capture the flame front properly in the CRSB configuration, other geometrical sensor parameters are set to their default values  $\beta_C = 1$ ,  $\alpha_{cold} = 0.05$ ,  $\alpha_{hot} = 0.005$ .

The cell size reaches its largest value in the far-field and its lowest value of  $0.125mm$  within the nozzle. Additionally, adaptive mesh refinement is used in the flame front leading to a cell size of  $\Delta_x = 0.25mm$ . Thus, the resulting cell number

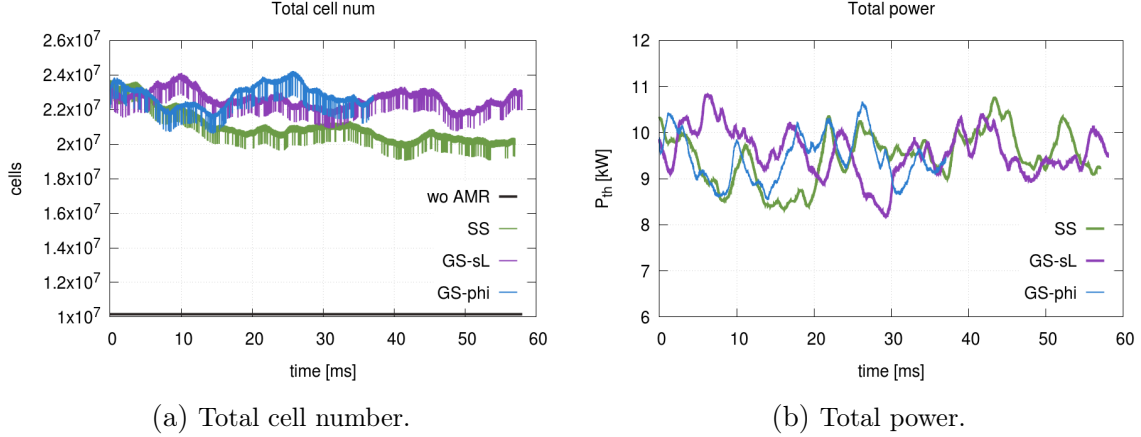


Figure 6-12: CRSB LES global parameters.

depends on how the thickening is defined and is different for the standard and the geometrical flame sensors, as it can be seen in Fig. 6-16.

The cell number without AMR reaches 10.2 million. The use of AMR doubles the number of cells in all considered cases, whereas the number of cells would need to be multiplied by a factor close to 8, if we would use the static mesh refinement to reach the same resolution within the flame region. As shown in Fig. 6-12b, the total cell number oscillates between 22 and 24 million when computed with the geometrical sensor, whereas it is approximately 2 million lower for the SS-TFM-AMR case.

The resulting total power of the burner is nearly the same for the two sensor definitions and is approximately 25% lower than the theoretical value. The incomplete droplet evaporation can explain this since some droplets cross the flame. The same behavior can be seen in the experimental flame shot in Fig. 4-1b, where droplets leave the flame.

Figure 6-13 shows the instantaneous fields of the final sensor  $\hat{S}$  and illustrates the impact of increased sensitivity of the sensor. Here, the elevated surface represents the gaseous temperature. Both images are obtained using GS-sL-TFM-AMR: the left one with the sensor slope  $\beta = 1$  and the right with  $\beta = 10$ . When  $\beta$  is set to one (Fig. 6-13 left), the sensor detects the steepest flame regions, but not the entire zone with strong temperature gradients. Multiplying the sensitivity of the geometrical sensor by a factor of 10 helps to capture better the flame regions with lower but still significant

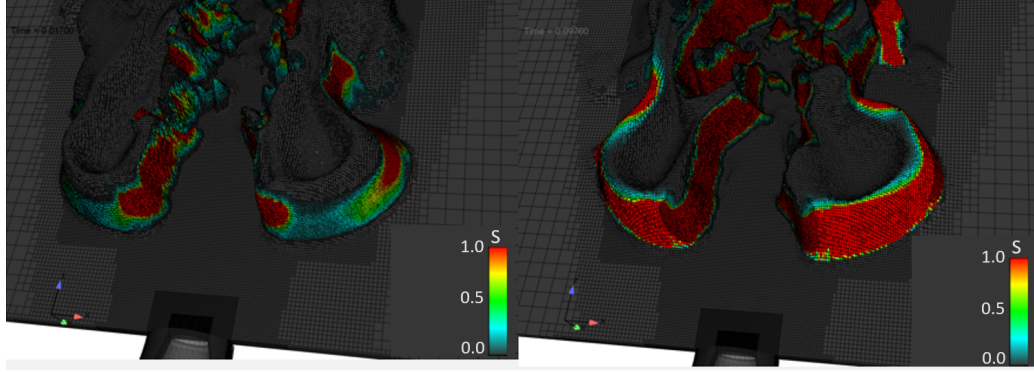


Figure 6-13: Instantaneous  $\hat{S}$  fields. Left: GS-sL-TFM-AMR  $\beta = 1$ ; right: GS-sL-TFM-AMR  $\beta = 10$

chemical activity. As we saw in the case of laminar spray flames in Sec. 6.2.3, the increased slope sensitivity does not significantly affect the resulting thickened flames. Therefore,  $\beta = 10$  is used in the GS-TFM-AMR simulations.

### 6.3.2 LES results

Instantaneous temperature and heat release rate fields computed with the standard sensor definition and the geometrical sensor, GS-sL-TFM-AMR and GS-phi-TFM-AMR, are shown in Fig. 6-14. Despite different flame sensor definitions, the obtained fields are pretty similar. In all cases, we can clearly distinguish two flame branches located in the inner reaction zone and the outer reaction zone, already discussed in Sec. 4.3.4. The region enclosed between these two flame branches is characterized by high temperatures and negative heat release rates.

The difference between the two TFM approaches becomes apparent when looking at the thickening factor fields in Fig. 6-15. Here, the elevated surface represents the temperature field. The temperature rise within the flame front promotes the fuel spray evaporation and thus leads to an increase of the gaseous fuel/air equivalence ratio. In the standard sensor definition, flame thicknesses are tabulated as a function of the local gaseous fuel/air equivalence ratio. Therefore, we can observe in Fig. 6-15 that the thickening factor raises across the flame in the SS-TFM-AMR case. At the same time,  $F$  computed with the geometrical sensor remains mainly uniform. Whereas the sensor changes the way the thickening is applied, the thickening factor

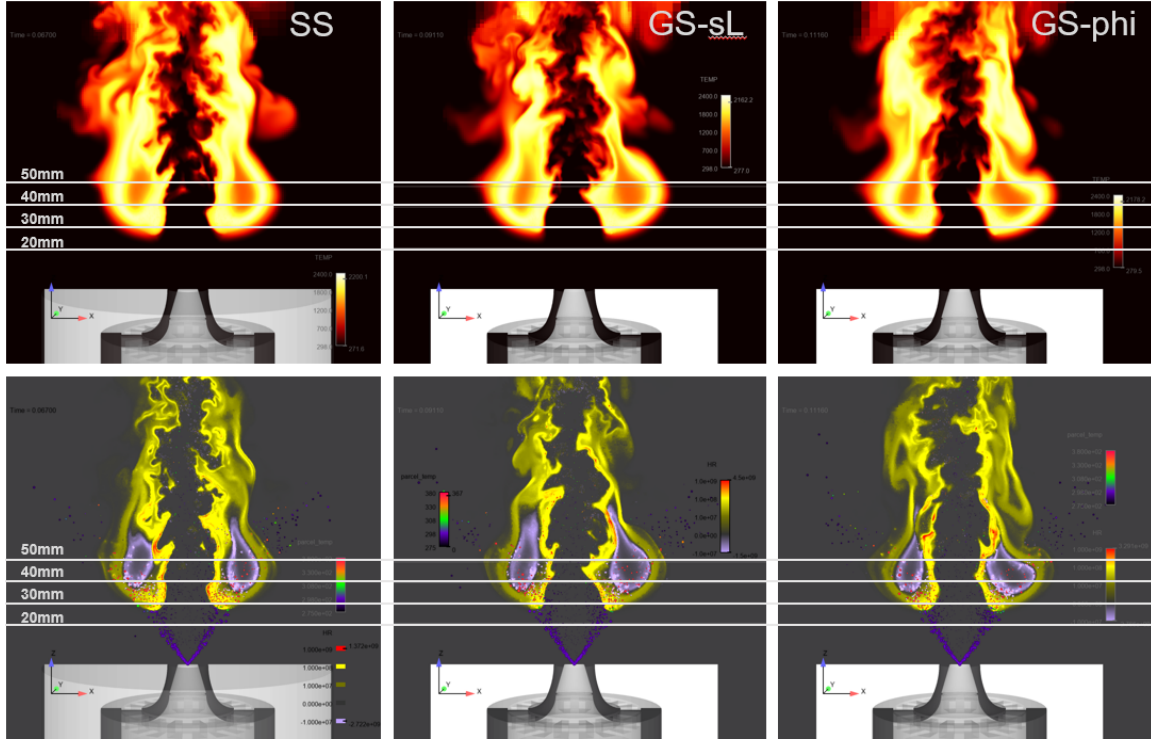


Figure 6-14: Instantaneous temperature and heat release rate fields. Left: SS-TFM-AMR; middle:GS-sL-TFM-AMR; right: GS-phi-TFM-AMR

values remain relatively close, thus leading to very similar flame shapes.

As discussed in Chapter 3, in two-phase flames, the estimation of the thickening factor based on gaseous flame tables can lead to an under-resolution of the flame. It can also result in excessively high  $F$  when approaching the burned side. However, in this particular case, the thickening levels are relatively low, and we do not notice a significant difference between the resulting flames computed with different thickening approaches.

The flame thickness estimated based on local properties by the geometrical sensor attains values between  $0.4mm$  and  $0.8mm$  within the inner branch increasing downstream. The thinnest flame portions are located below  $Z = 50mm$ , where the thickening factor reaches seven. The essential flame characteristics are summarized in the Table 6.3 for all computed cases.

Temperature gradients in the outer flame branch are much smoother than in the inner reaction zone, as it can be seen Fig. 6-16. As detailed in Sec. 4.3.4, the standard sensor yields low thickening levels due to the low heat release rates in this region, so

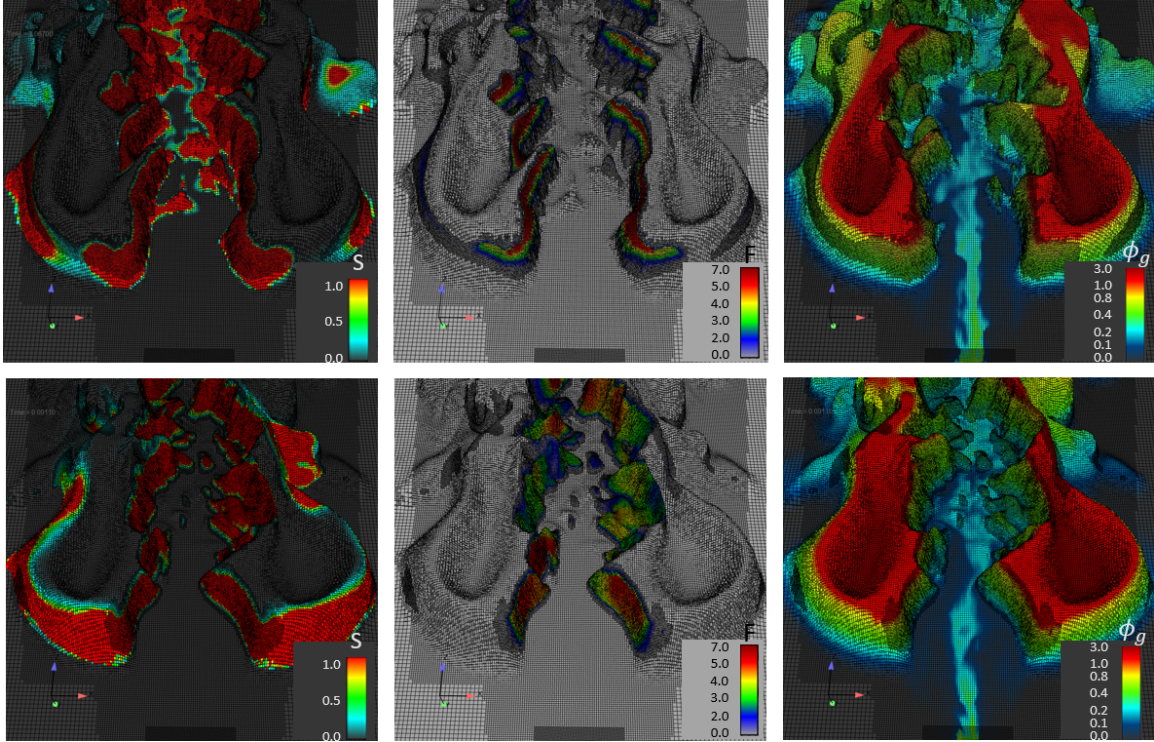


Figure 6-15: Instantaneous fields of final flame sensor  $\hat{S}$ , thickening factor  $F$  and gaseous fuel/air equivalence ratio. Top: SS-TFM-AMR; bottom: GS-sL-TFM-AMR

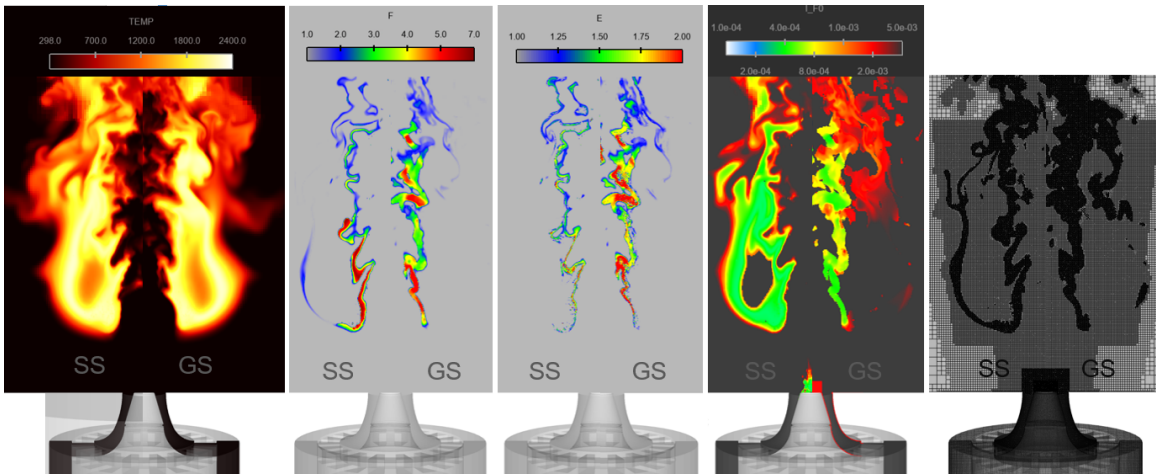


Figure 6-16: SS-TFM-AMR VS GS-sL-TFM-AMR. Instantaneous fields of temperature, thickening factor  $F$ , efficiency factor  $E$ , flame thickness  $\delta_L^0$  and AMR

that the flame can be resolved at  $F = 1$  thanks to AMR.

Based on the local properties, the geometrical sensor estimates the outer flame thicknesses close to or above  $4.5\text{mm}$ . Therefore, no thickening or refinement is required to resolve flames with  $\delta_L^0 > 4.5\text{mm}$ , as it can be seen in Fig. 6-16. The flames

Configuration	$\phi_g$	$F$	$\delta_L^0$	$S_L^0$
SS-TFM-AMR	0.4 – 1.0	1.0 – 5.0	0.35 – 3.8 mm	0.02 – 0.42 m/s
GS-sL-TFM-AMR	0.4 – 1.0	5.0	0.4 mm	0.2 – 0.3 m/s
GS-phi-TFM-AMR	$\phi_g$ : 0.4 – 1.0 $\phi_r$ : 0.4 – 0.5	7.0	0.3 mm	0.4 m/s

Table 6.3: The main CRSB flame characteristics, inner reaction zone,  $Z < 60mm$ .

with such thicknesses do not correspond to existing premixed n-heptane/air flames and represent more complex combustion regimes. In this situation, the GS-TFM-AMR modeling approach behaves appropriately and avoids thickening.

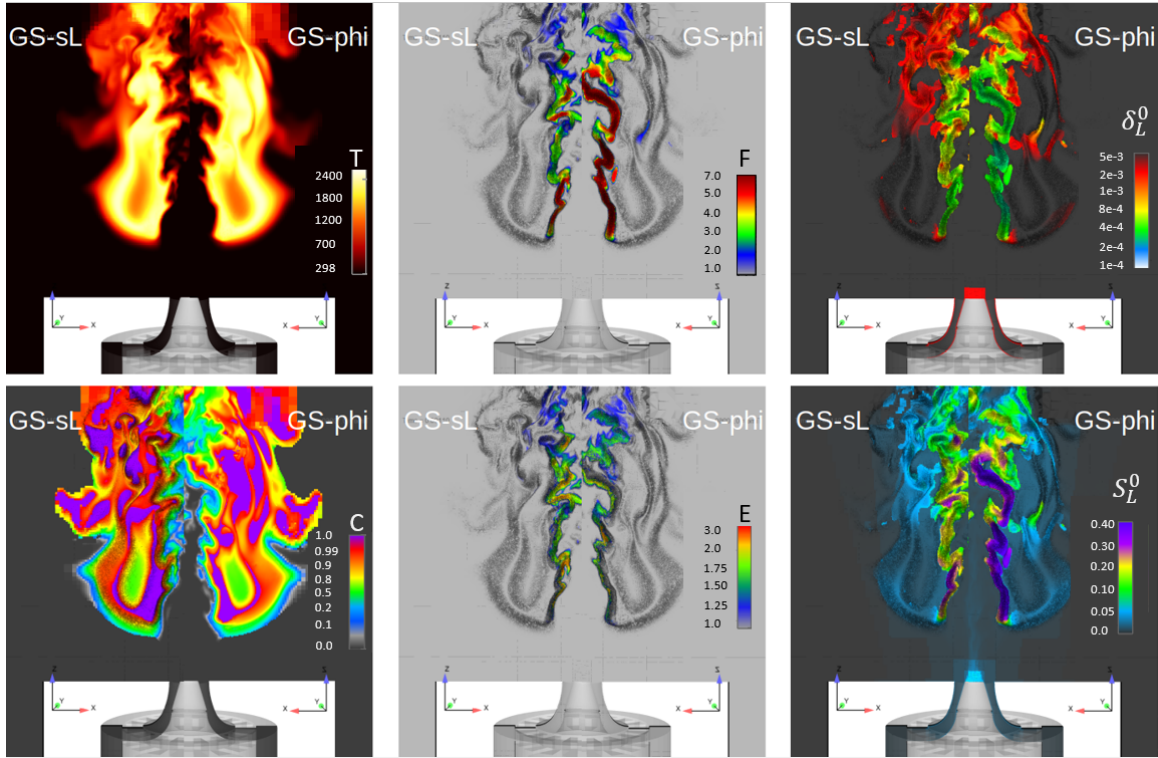


Figure 6-17: GS-sL-TFM-AMR (left) VS GS-phi-TFM-AMR (right). Instantaneous fields of temperature, thickening factor  $F$ , flame thickness  $\delta_L^0$ , progress variable  $C$ , efficiency factor  $E$ , and laminar flame speed

Although the mean radial profiles and the global flame shape are similar for both geometrical sensor approaches, some differences still exist in the model estimations of unthickened flame thicknesses and laminar burning velocities, see Table 6.3. To

illustrate those, Fig. 6-17 provides the instantaneous fields obtained with GS-sL-TFM-AMR on the left and with GS-phi-TFM-AMR on the right.

The main difference concerns the inner reaction zone, where both modeling strategies detect a broad flame-front which does not require any thickening and almost no additional refinement.

As we saw in Sec. 6.2.3, when we compute the gaseous fuel/air equivalence ratio characterizing the reacting zone and transport this information over the whole flame front in GS-phi-TFM-AMR, it results in steeper progress variable profiles compared to the thickening approach with transported laminar flame speed. Thus, the estimated laminar flame thickness  $\delta_L^0$  given by GS-phi-TFM-AMR is thinner than the one given by GS-sL-TFM-AMR, and the thickening factors are higher, which can also be observed in Fig. 6-17. Therefore, the instantaneous temperature fields computed with GS-phi-TFM-AMR are slightly smoother in the inner reaction zone compared to the case done with GS-sL-TFM-AMR, see Fig. 6-17.

The estimated laminar burning velocities are also higher in the GS-phi-TFM-AMR case. It is consistent with the 1D flames computations shown in Sec. 6.2, where the correlation used to compute  $S_L^0$  led to overestimated values but still provided a relatively good estimation of the laminar burning velocity. However, it does not significantly affect the resulting efficiency factor, which values depend mainly on the level of velocity fluctuations, see the  $S_L^0$  and  $E$  fields in Fig. 6-17.

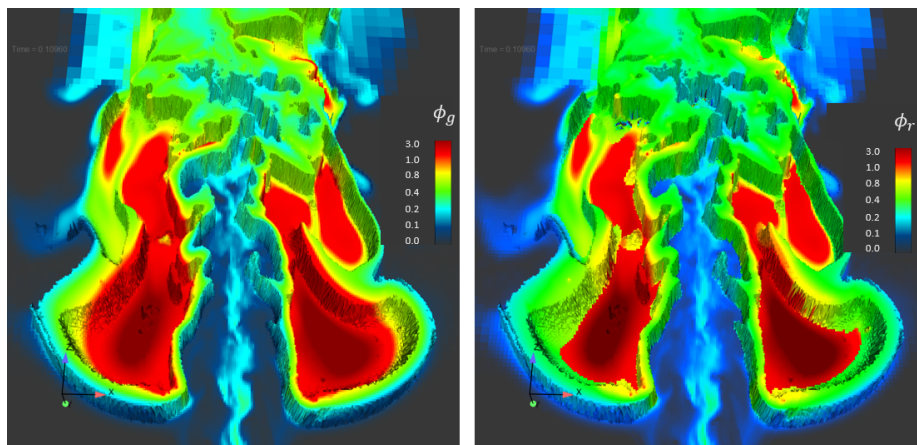


Figure 6-18: GS-phi-TFM-AMR: gaseous fuel/air equivalence ratio (left), reacting gaseous fuel/air equivalence ratio (right)

To illustrate the difference between gaseous fuel/air equivalence ratio and  $\phi_r$  characterizing the reacting zone, their instantaneous fields are shown in Fig. 6-18, where the elevated surface corresponds to the regions detected by the sensor. Compared to the  $\phi$  that varies from 0.3 up to 1.0 across the flame-front,  $\phi_g$  is more uniform and takes mainly values around 0.4 – 0.5.

Instantaneous fields are averaged first to perform a comparison with the averaged experimental fields. Then, the radial profiles are extracted at axial planes located 20mm, 30mm, 40mm and 50mm downstream of the fuel injector represented by the white horizontal lines in Fig. 6-14.

The flow-through time  $FTT = 2.3ms$  is defined as the time that the bulk air takes to reach the highest plane for which we have experimental data. The averaging is performed for more than  $25FTT$  for SS-TFM-AMR and GS-sL-TFM-AMR cases, while in the GS-phi-TFM-AMR case, the profile convergence is already reached after  $16FTT$ . The spray averaging procedure described in Sec. 5.3.3 is adapted below to present dispersed phase results.

Radial profiles that characterize the gaseous phase are given in Fig. 6-19. Each row represents a different axial plane location, and columns stand for the radial, axial velocity components, and temperature. The axial symmetry of the flame allows showing the mean and the fluctuating component on the same plot.

No significant differences can be observed in the resulting velocity fields for all flame sensor definitions. Fig. 6-19 demonstrates a very good agreement with the experimental data. The shape, as well as the magnitude of axial velocities, are very well reproduced numerically. We can notice a slight velocity under-prediction at 30mm and 40mm planes between  $X = -20mm$  and  $X = -10mm$  corresponding to the location of the inner flame branch that is illustrated by the first temperature peak on the temperature plots in the third column in Fig. 6-19.

Radial velocities are significantly lower than the axial ones. The radial velocities are slightly underpredicted upstream of the flame at 20mm and close to its stabilization point at 30mm, while the profile shape exactly matches the experiments. At the higher planes, we do not observe numerically the measured radial velocity drop that

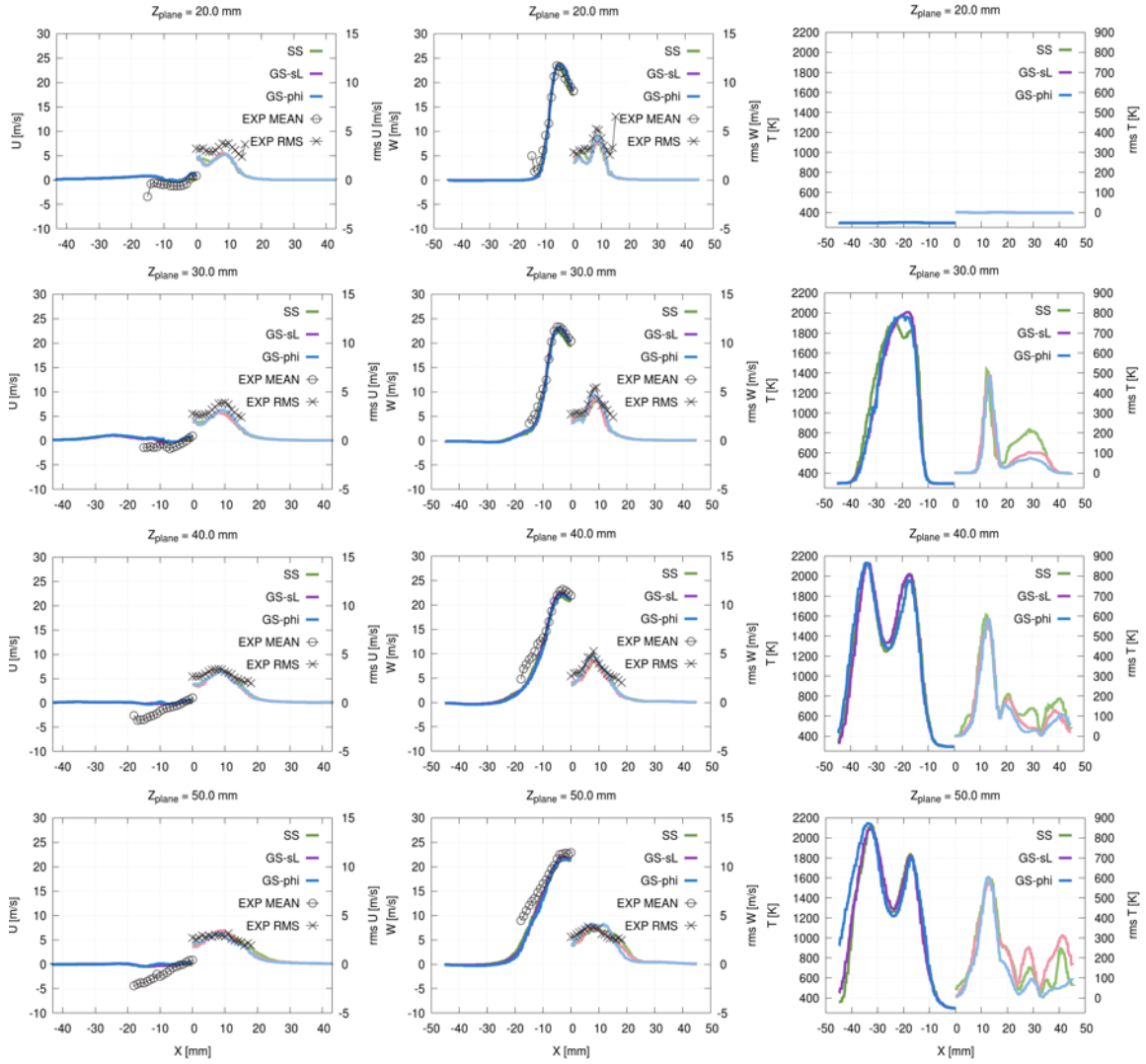


Figure 6-19: Radial profiles; gaseous phase; SS-TFM-AMR (—: mean, —: rms); GS-sL-TFM-AMR (—: mean, —: rms); GS-phi-TFM-AMR (—: mean, —: rms); experiments (o: mean, x: rms). Left: radial velocity component; middle: axial velocity component; right: temperature.

starts at  $X = -10\text{mm}$ . It is, however, difficult to conclude whether these discrepancies result from the flame thickening activated in this region, the simplified fuel injection, or are related to a possible decrease in the measurement accuracy in the high-temperature areas.

Temperature profiles are pretty similar for all cases, with only a difference at  $Z = 30\text{mm}$ , which is located close to the flame tip. While temperature profiles obtained with GS-phi-TFM-AMR and GS-sL-TFM-AMR exhibit a single peak, the flame computed with the standard sensor already develops the double shape form

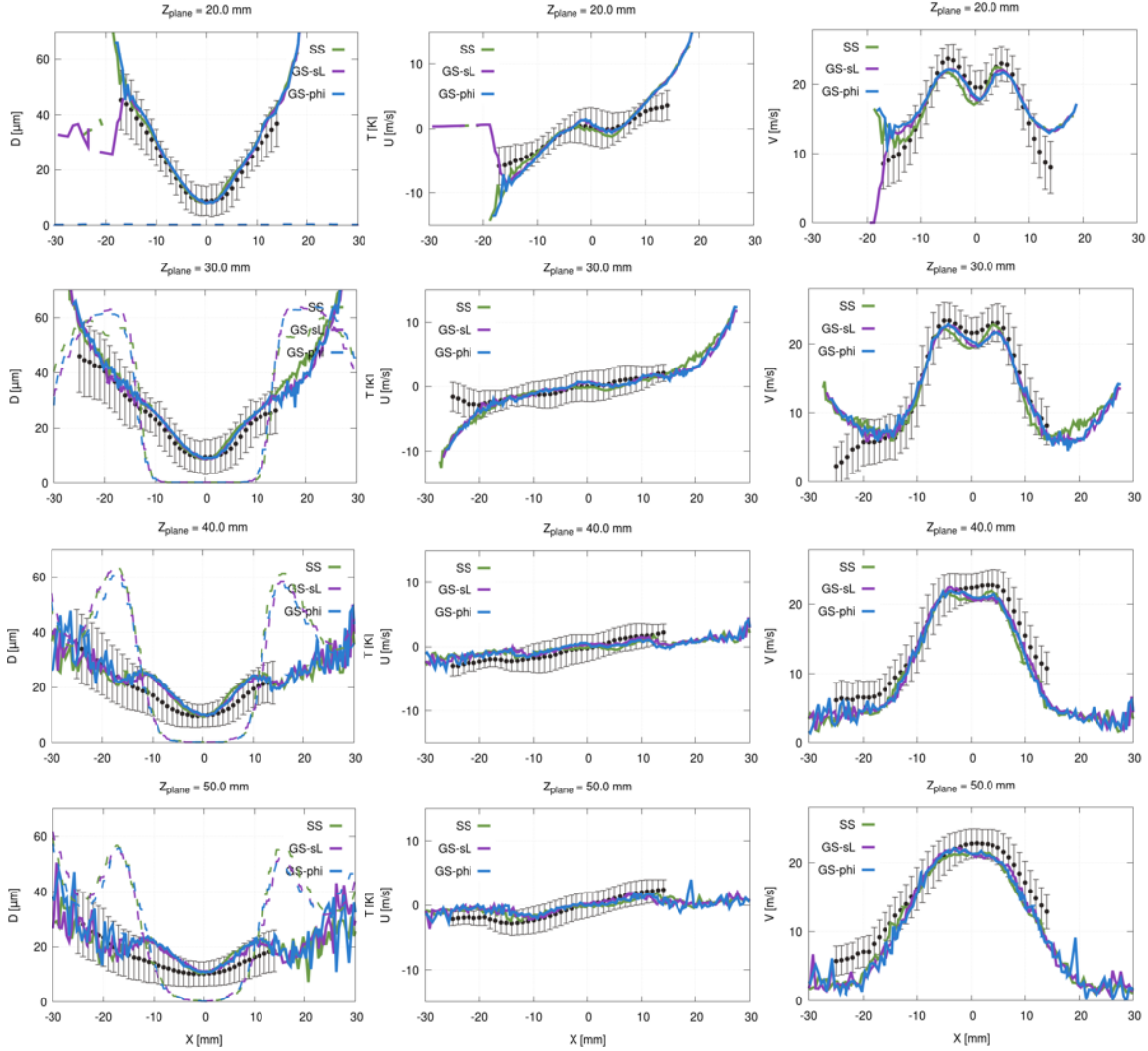


Figure 6-20: Mean radial profiles; dispersed phase; —: SS-TFM-AMR; —: GS-sL-TFM-AMR; —: GS-phi-TFM-AMR; —•—: experiments with error bars proportional to measured RMS-values [77]. Left: droplet diameter (solid lines), gaseous temperature (dashed lines); middle: radial velocity component; right: axial velocity component.

amplified downstream.

As discussed in Chapter 4, and it can be seen again in Fig. 6-19 and Fig. 6-14, that the inner reaction zone is characterized by lower temperatures and higher heat release rates, whereas the outer flame branch reveals higher temperatures and lower heat release rates.

The resulting mean spray characteristics, such as velocities and diameters, fully conform to the experimentally measured data. The gaseous temperature is plotted here together with the droplet diameters to visualize the flame front location.

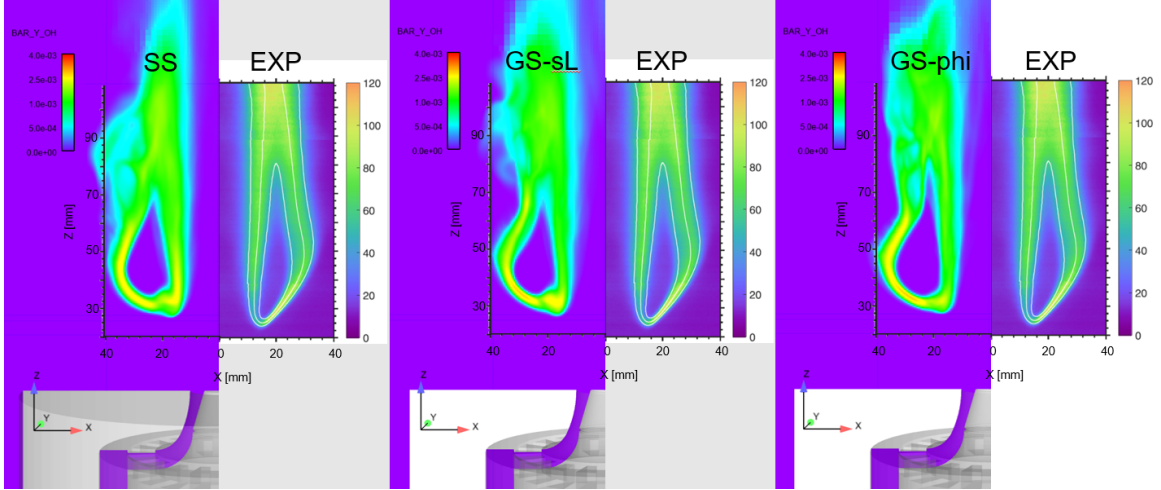


Figure 6-21: Mean  $Y_{OH}$  fields. Left: SS-TFM-AMR; middle: GS-sL-TFM-AMR right: GS-phi-TFM-AMR

The number of droplets reduces as they evaporate more intensively when reaching high-temperature regions. The increased profile oscillations come from the lower amount of droplets used for the averaging and are consistent with the gaseous temperature rise.

The liftoff length is deduced from the mean fields of  $OH$  mass fraction, which are given in Fig. 6-21. It is accurately reproduced by all thickening approaches and equals  $26.7mm$ , whereas the experimentally measured value is  $25mm$ . For further flame feature discussion, please refer to Sect. 4.3.4.

### 6.3.3 Conclusions

In this section the standard sensor (SS-TFM-AMR) was compared to the geometrical sensor (GS-sL-TFM-AMR and GS-phi-TFM-AMR) in the context of CRSB. All three cases reproduced well the experimental mean and rms profiles with a minor differences observed between the cases.

The main difference between the SS-TFM-AMR and GS-TFM-AMR modeling approaches concerns the way how the flame thickening is applied. While we get a nice uniform thickening across the flame front with the geometrical sensor, the thickening factor raises in the spray flame because of increasing  $\phi_g$  when the standard thickening approach is applied. Additionally, GS-TFM-AMR correctly predicts the thick outer

flame that does not require any thickening. In contrast, the flame thickness estimated in SS-TFM-AMR from the laminar premixed tables leads to an excessive refinement in the outer flame branch.

Despite the differences observed between the thickening approaches, all of them predict the investigated CRSB flame well. Exploring different burners at elevated pressures and temperatures should be the next step, since higher thickening factors might make the differences between SS-TFM-AMR and GS-TFM-AMR approaches more pronounced.

## 6.4 Geometrical formulation of the thickened flame model: DLR burner

The laboratory-scale gas turbine model combustor with some characteristics of real aero-engines was investigated with the standard TFM formulation in Chapter 5. It is considered here as the next validation target of the TFM-AMR modeling approach using the geometrical sensor (GS-TFM-AMR).

In contrast to the academic burner configuration discussed in Sec. 6.3, this burner features a confined geometry, a prefilming airblast atomization, and is operated with n-dodecane. While still operating under atmospheric conditions, the characteristics listed above make the gas turbine model combustor configuration one step closer to the real aero-engines.

The computations presented in Chapter 5 were performed with the standard sensor and included the reference flame and the LBO sequence. Below, only the reference n-dodecane flame is considered, which burns at the global equivalence ratio of  $\phi = 0.8$  with an air mass flow rate of  $\dot{m}_{air} = 4.3g/s$ .

The complete description of the numerical settings can be found in Sec. 5.3.1, and the non-reacting flow validation is discussed in detail in Sec. 5.3.2. In the following, the numerical settings specific to the geometrical sensor are summarized in Sec. 6.4.1, followed by the LES results in Sec. 6.4.2 and conclusions.

### 6.4.1 Numerical settings

In the computation below, we use the mesh shown in Fig.5-3 with one additional level of AMR leading to  $\Delta_x = 0.25mm$  within the flame front. As shown in Sec. 6.4.2, the resulting thickening levels with GS-TFM-AMR are lower than with SS-TFM-AMR. Therefore, the target thickening factor is reduced to 2 to enable the refinement within the flame. With these settings, the total number of cells reaches approximately 40 million.

The LES settings selected below are similar to those used for the reference case

computed with the standard sensor presented in Sec. 5.3.3 (DLR-rc-ref case in Table 5.1). Similar to DLR-rc-ref, the case computed with GS-TFM-AMR includes the correction due to the parcel/flame orientation and the correction of the thickening for stretched flames. In both these cases, the effect of radiative heat losses is not considered.

For the academic burner configuration, the GS-TFM-AMR simulations were conducted for both modeling strategies, GS-phi-TFM-AMR and GS-sL-TFM-AMR, defined in Sec.6.1.3. The corresponding LES results discussed in Sec. 6.3.2 demonstrated significant similarities and the ability to predict the CRSB flame correctly. Due to the limited computing resources, only the approach using the characteristic gaseous fuel/air equivalence ratio (GS-phi-TFM-AMR) is investigated in the context of the gas turbine model combustor. The geometrical sensor parameters are set to  $\beta_C = 1$ ,  $\beta = 1$ ,  $\alpha_{cold} = 0.5$ ,  $\alpha_{hot} = 0.05$ .

### Progress variable calculations

As explained in Sec. 6.1.3, the thickened flame thickness  $\delta_L^1$  estimation is based on the computation of progress variable gradients. Therefore, the computation of the progress variable plays an essential role in the modeling using the geometrical sensor. The confined geometry and the swirled flow result in strong recirculation regions in this burner configuration, promoting the mixing between fresh gases and burnt products. This mixing has to be taken into account in the progress variable calculations.

In the configurations computed in Sec. 6.2 and in Sec. 6.3 there was no premixing and the tabulated  $Y_{C,u}(\phi_g)$  arising in Eq.(6.1) was essentially zero. If we do not take into account the mixing with burned products, the progress variable would rapidly take the value of unity at the injector because burned gas recirculation is important in such a confined burner configuration. This makes the use of the geometrical sensor problematic.

In order to use GS-TFM-AMR in the cases involving mixing with burned products, we have to give an accurate value for  $Y_{C,u}$ , which cannot be tabulated anymore. Therefore, we transport  $Y_{C,u}$  using a procedure similar to the one described for an

arbitrary variable  $\xi$  in Sec. 6.1.1. For the freshly injected air,  $Y_{C,u}$  is set to zero and has to be updated when the mixture crosses the flame. Thus, the main equation Eq.( 6.2) remains the same, whereas the evaluation of the source term  $\dot{\omega}_{Y_{C,u}}$  differs from Eq.( 6.3) and is given by:

$$\dot{\omega}_{Y_{C,u}} = \begin{cases} \rho(Y_C - Y_{C,u})\frac{1}{\tau_{relax}} & \hat{S} < 0.9; T < 1100K; \tilde{C} > 0.1 \\ 0 & \text{else} \end{cases}, \quad (6.19)$$

where  $Y_C$  is a local sum mass-fraction of species involved in the progress variable definition. The relaxation time  $\tau_{relax} = 20\Delta_t$  is set to a multiple of the time step to ensure that the source term quickly relaxes towards a desired value in the region of interest. To limit sourcing to chemically active regions only, it is conditioned on the flame sensor and the progress variable, estimated from  $\tilde{C} = Y_C/Y_{C,eq}(\phi)$ . The source term for  $Y_{C,u}$  is conditioned on the local temperature to perform this relaxation only on the unburned gases side. Here,  $T = 1100K$  is chosen as an arbitrary value that allows distinguishing between the unburned and burned sides.

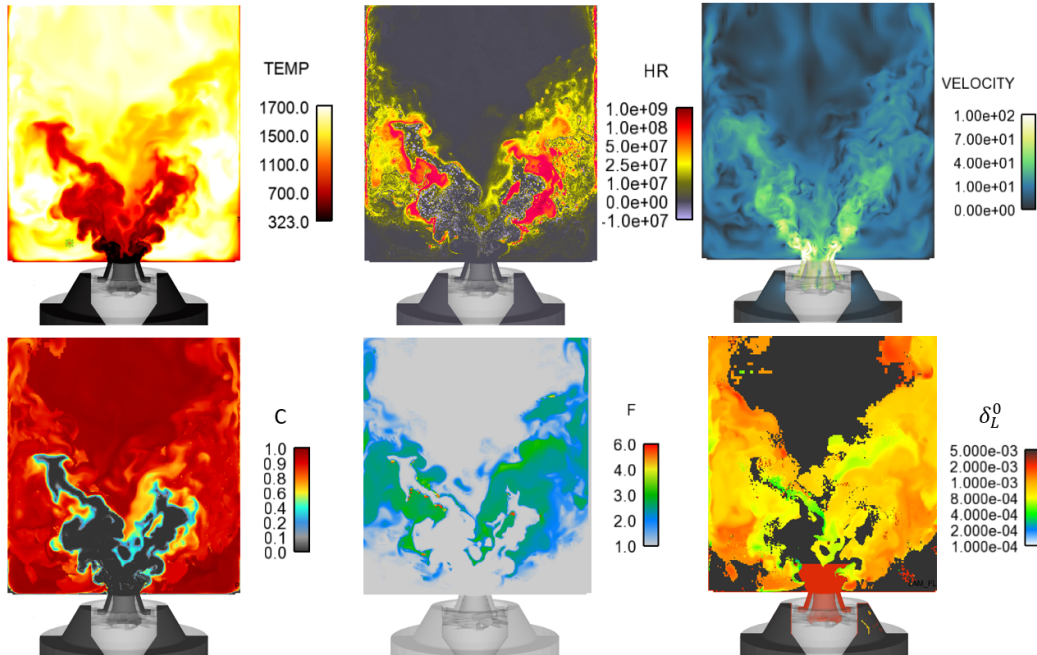
## 6.4.2 LES results

Due to the similarities with the DLR-rc-ref case computed with the standard sensor and mentioned in the previous section, the LES results obtained with GS-TFM-AMR are compared to the DLR-rc-ref case.

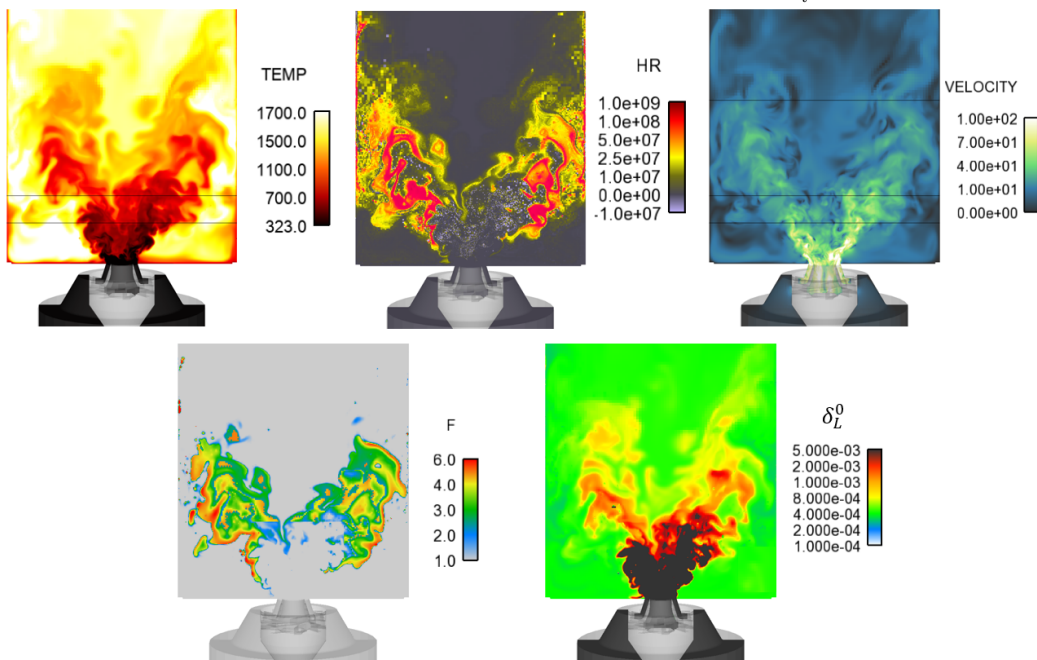
To compute averaged flow and spray characteristics, the data was collected over 7.5 FTT. The resulting total power of the burner is correctly predicted by the simulation and is similar to the DLR-rc-ref case.

The instantaneous fields obtained with the geometrical sensor are shown in Fig. 6-22a, while the ones obtained with the standard sensor are given for the comparison in Fig. 6-22b.

The resulting flame has a clearly defined V-shape. The lowest temperatures are found in the region with high gas velocities, whereas the hottest regions are located within recirculation zones. The flame is established in the shear layer between the



(a) GS-phi-TFM-AMR. Instantaneous fields of temperature, heat release rate, velocity, progress variable, thickening factor  $F$ , and laminar flame thickness  $\delta_L^0$ .



(b) SS-TFM-AMR (DLR-rc-ref case): temperature, heat release rate, velocity, thickening factor  $F$ , and laminar flame thickness  $\delta_L^0$ .

Figure 6-22: Instantaneous fields.

hot recirculation region and the fresh mixture flow promoted by the swirled flow.

The main difference between both simulations, as observed in Figures 6-22a and

6-22b, is the thickening factor field. While the thickening is mainly uniform across the GS-TFM-AMR flame and attains a value of 3 in the region with the highest heat release values, the thickening factor reaches the value of 6 within the flame computed with SS-TMF-AMR. The thickening factor increases when approaching the burned side with the standard sensor since  $F$  is directly related to the tabulated flame thickness. The latter becomes thinner as the droplets evaporate, increasing the local fuel/air equivalence ratio. A similar behavior we could also observe in the academic burner configuration in Sec. 6.3.2.

Lower thickening levels in the GS-TFM-AMR cases are explained by the larger values of the laminar flame thickness. With the standard sensor, the tabulation based on the local  $\phi_g$  values gives a value of  $0.4mm$ . At the same time, the geometrical sensor predicts values based on the local flow properties which are nearly two times larger.

Figure 6-23 shows the instantaneous sensor and thickening factor fields on the surface elevated by temperature values, as well as the efficiency factor with AMR. In both cases, the efficiency factor is relatively low and does not exceed the value of 2. As discussed in Sec. 6.3.2,  $E$  values depend mainly on the computation of the velocity fluctuations and less on the laminar burning velocity, which explains the similarities between the cases. The enlarged AMR region is related to the choice of the target thickening, as described in the discussion of numerical settings in Sec. 6.4.1.

The sensor is broader towards burned gases with GS-TFM-AMR than with SS-TFM-AMR. While the flame sensor in the SS-TFM-AMR case covers the entire high-gradients temperature region, the geometrical sensor is relatively low at the flame base. This, however, can be improved by setting a higher sensor sensitivity value. As noted above,  $F$  shows less variations in space with GS-TFM-AMR than with SS-TFM-AMR because it relies on a transported laminar flame thickness  $\delta_L^0$ , and not on a value read from a table.

Since the GS-phi-TFM-AMR modeling approach is selected to run this configuration,  $\phi_r$  is computed to get the gaseous fuel/air equivalence ratio characteristic to the reaction zone. Figure 6-24 shows the gaseous fuel/air equivalence ratio and

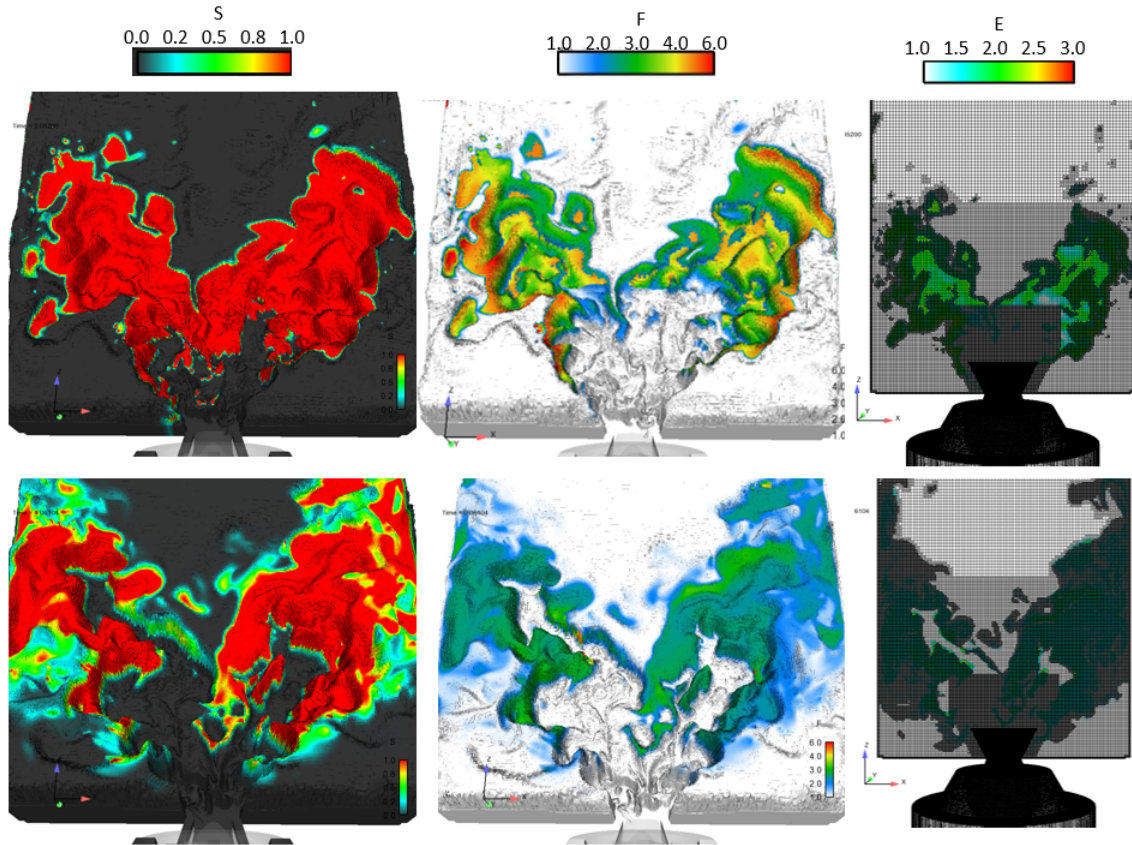


Figure 6-23: Instantaneous fields of the flame sensor  $\hat{S}$ , thickening factor  $F$ , and efficiency factor  $E$  with AMR. Top: SS-TFM-AMR (DLR-rc-ref case), bottom: GS-TFM-AMR. Elevation is based on the temperature field.

the reacting gaseous fuel/air equivalence ratio. Here, the elevated surface represents the sensor values. Compared to the  $\phi_g$  field, the  $\phi_r$  is slightly smoother within the sensor active regions and does not have the spots introduced by the intense droplet evaporation, which could deteriorate the results.

The averaged radial temperature profiles are compared against the experimental data at  $Z = 15mm$ ,  $Z = 25mm$  and  $Z = 35mm$  for both modelling approaches. The dashed lines on the right of Fig. 6-25 indicate the considered planes.

The gaseous temperatures are also compared against the experiments along the entire combustion chamber length at  $X = -20mm$ ,  $X = 0mm$  in Fig. 6-26.

Figures 6-25 and 6-26 reveal that the main difference between the flames computed using the standard modeling approach and the geometrical sensor concerns the central region defined between  $X = -10mm$  and  $X = 10mm$ . Mean temperatures were

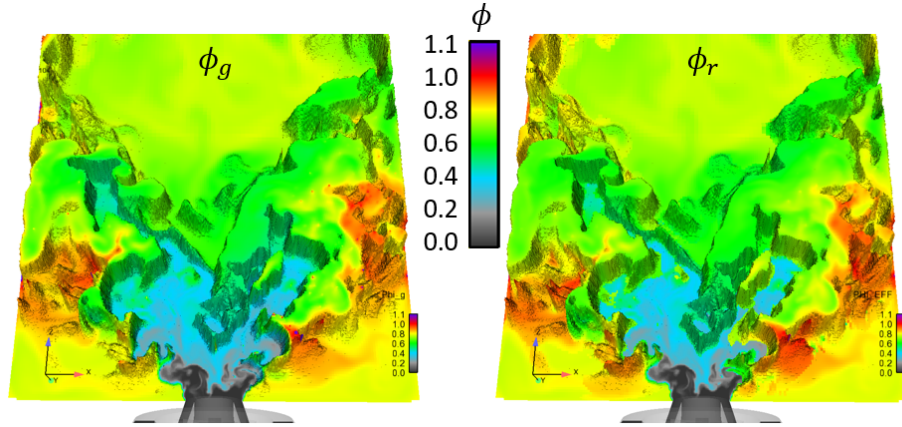


Figure 6-24: GS-phi-TFM-AMR. Gaseous fuel/air equivalence ratio (left), reacting gaseous fuel/air equivalence ratio (right). Elevation is based on the sensor field.

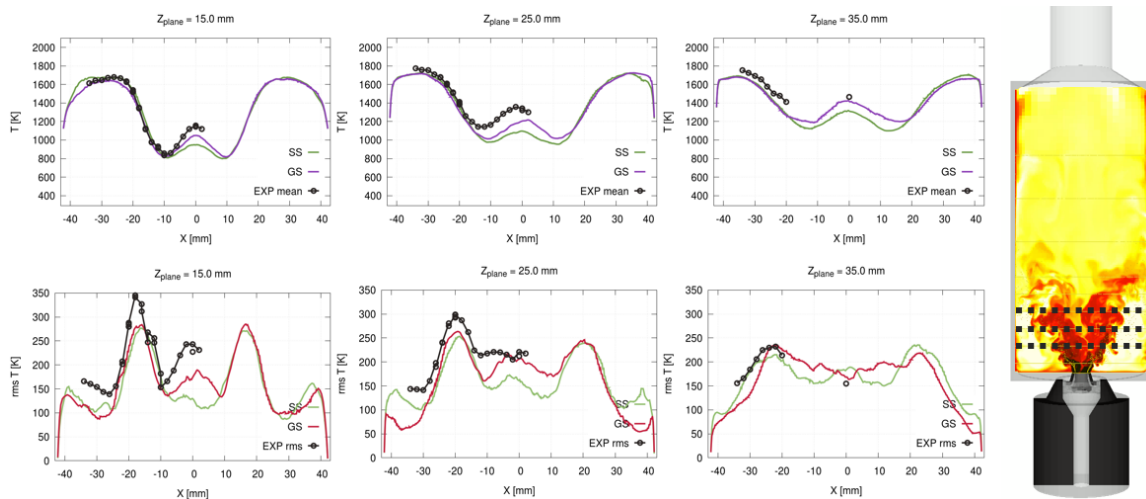


Figure 6-25: Temperature radial profiles at  $Z = 15\text{mm}$ ,  $Z = 25\text{mm}$  and  $Z = 35\text{mm}$ ; GS-TFM-AMR vs SS-TFM-AMR.

under-predicted in the central region using the standard modeling approach, which is discussed in Sec. 5.3.3. As seen in both figures, using the geometrical sensor reduces the discrepancy with the experiments by a factor of two, making this under-prediction less prominent. At the same time, the mean temperature attained above  $Z = 50\text{mm}$  is similar in both cases, and the temperature profiles at  $|X| > 10\text{mm}$  almost overlap.

The time-averaged spray characteristics, such as the droplet Sauter mean diameter and its three velocity components, are shown in Fig. 6-27. The radial profiles are compared against the experimental data at the planes located at  $Z = 15\text{mm}$  and  $Z = 25\text{mm}$ . Here, the averaging is performed using the procedure described in Sec. 5.3.3.

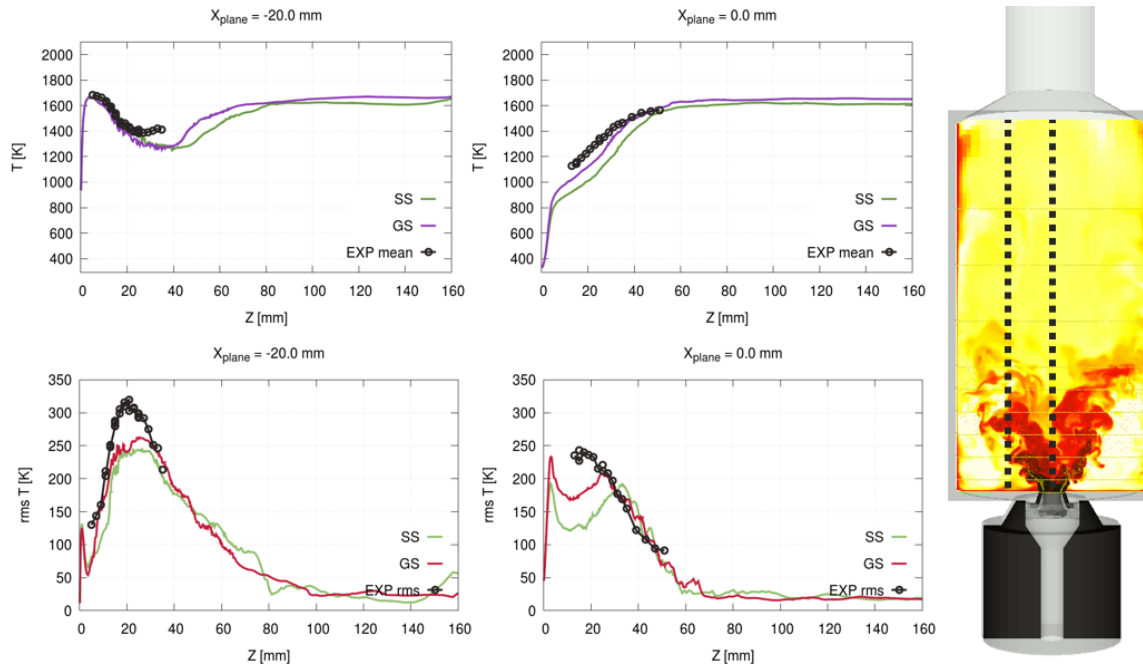


Figure 6-26: Temperature axial profiles at  $X = -20\text{mm}$  and  $X = 0\text{mm}$ ; GS-TFM-AMR vs SS-TFM-AMR.

Both simulations achieve an overall good agreement with experiments. The droplet diameters obtained with the geometrical sensor become slightly smaller than in the SS-TFM-AMR case. At the same time, all three droplet velocity components remain very much alike.

The fraction of evaporated liquid fuel defined in Sec. 5.3.3 is plotted for SS-TFM-AMR and GS-TFM-AMR modeling approaches in Fig. 6-28, where the black horizontal line represents the total amount of the injected fuel. While in both cases, the entire fuel evaporates before reaching the  $120\text{mm}$  height, the droplet evaporation is slightly more intense between  $Z = 20\text{mm}$  and  $Z = 50\text{mm}$  in the case computed with the geometrical sensor. This can be explained by the higher temperatures in the GS-TFM-AMR case that promote the droplets' evaporation.

### 6.4.3 Conclusions

In this section, the modeling approach using the geometrical sensor was investigated in the context of the DLR gas turbine model combustor. The GS-TFM-AMR modeling approach shows a great potential of predicting swirl-stabilized spray flames under

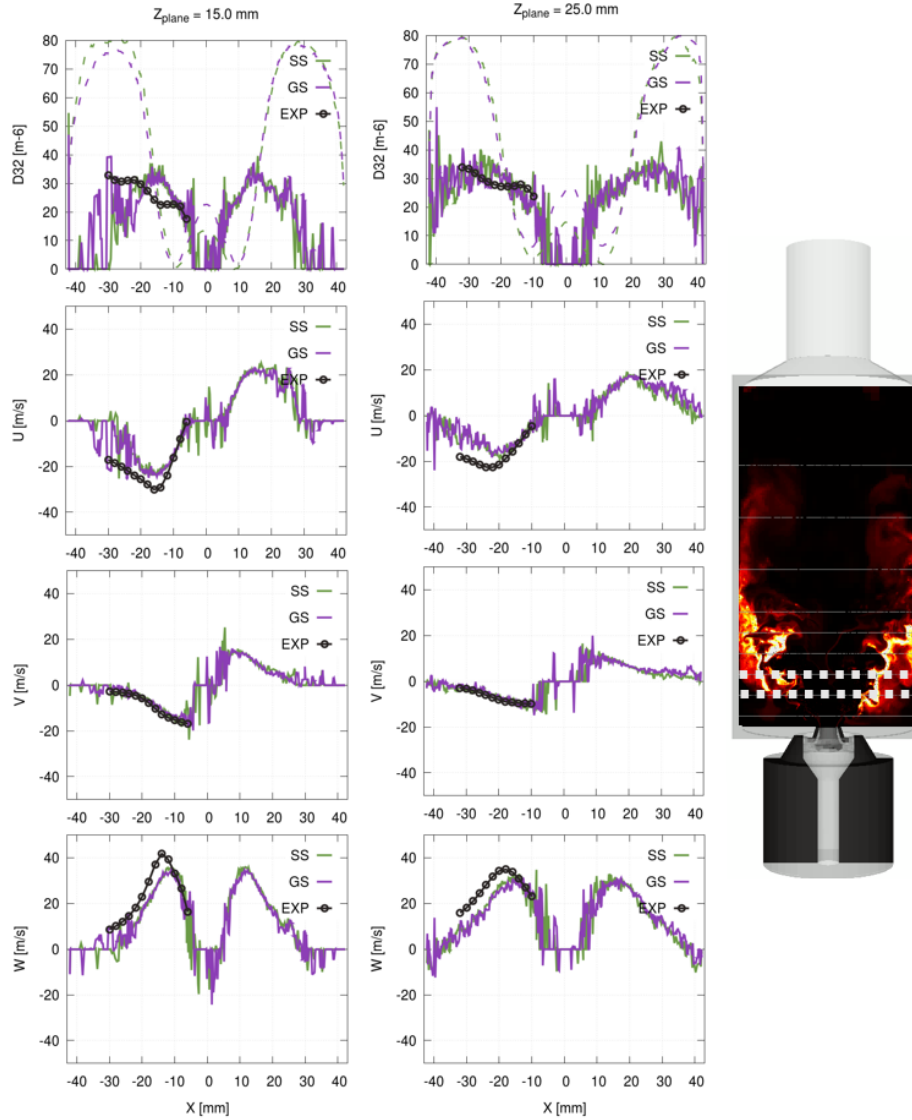


Figure 6-27: Averaged axial profiles of droplet diameter  $D_{32}$  and spray velocity components: radial  $U$ , circumferential  $V$ , axial  $W$ ;  $Z = 15\text{mm}$  and  $Z = 25\text{mm}$ ; GS-TFM-AMR vs SS-TFM-AMR.

atmospheric pressure since we observed an overall good agreement with the experimental data. Like in the academic burner configuration, GS-TFM-AMR allows to recover realistic laminar flame thickness  $\delta_L^0$  in such a complex configuration close to an industrial one. Compared to the standard thickening method described in Chapter. 2, the maximum thickening levels are reduced by a factor of two, and the thickening is applied more uniformly across the flame, which better reflects the resulting flame.

Although mean temperatures remain slightly under-predicted in the central region, the discrepancy with the experimental results was reduced using GS-TFM-AMR. As

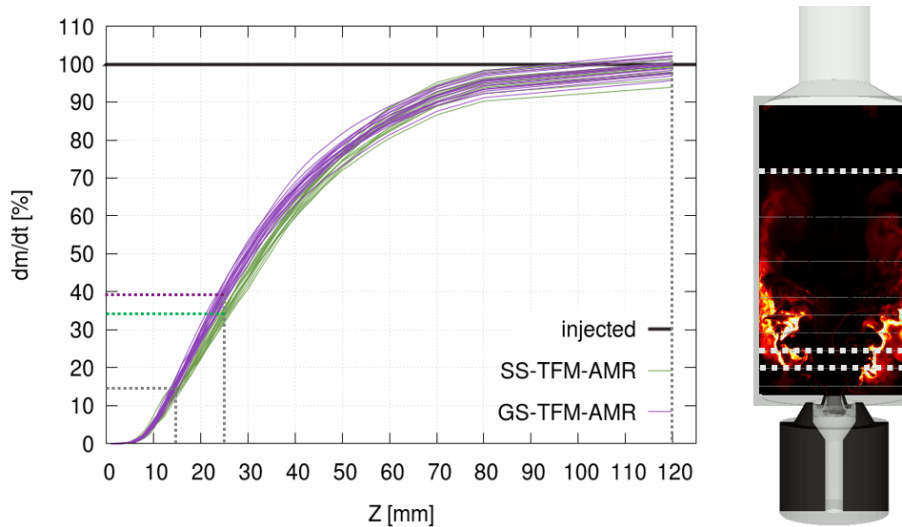


Figure 6-28: Instantaneous fraction of evaporated liquid fuel; GS-TFM-AMR vs SS-TFM-AMR.

was mentioned in Sec. 5.3.3, this deviation from the experiments might also come from the simplified fuel injection as well as the the simplified droplet treatment at the combustion chamber walls.

While GS-TFM-AMR with selected model parameters was able to predict the flame reasonably well, it would be interesting to explore in a future work the effect of model parameter variation on the resulting flame. As demonstrated on the 1D n-dodecane flames, mixing with burned products can require elevating the sensor sensitivity, so higher sensor sensitivity might be the next option. Together with the increase of the sensor sensitivity, the relaxation time coefficients can be reduced to shrink the thickened regions and thus the AMR region. This would decrease the total number of cells and reduce computational costs.

Due to the very small thickening, it is difficult to show differences between the different thickening approaches. To our knowledge, the experimental investigation of the gas turbine model combustor at higher pressures and temperatures is planned in the future. In that case, the comparison between SS-TFM-AMR and GS-TFM-AMR might reveal more significant differences, considering larger thickening levels predicted by SS-TFM-AMR.

# Conclusions

The development of industrial aero engines requires a more profound understanding of the processes that take place inside gas turbine combustors. This can be achieved by means of numerical simulations. Therefore, this work has focused on the two-phase flow combustion modeling using the TFM-AMR approach. First, we have introduced the flame thickening technique for premixed gaseous flames. Then, the existing model extension on spray flames was discussed and implemented within CONVERGE framework.

In the next step, we investigated and evaluated the performance of the presented modeling approach in different flame configurations. We have started the validation on simple laminar spray flames and assessed the corrections in the Lagrangian equations that govern the spray evolution. The results showed that these corrections are essential to obtain correct spray evaporation and propagation rates in thickened flames.

To continue validating the existing modeling approach, we have used two different burner geometries of increased complexity; both operated under atmospheric conditions. While the first burner, designed in CORIA, was unconfined, the second one, designed in DLR, was confined, resulting in a swirled recirculating flow, which is typical for gas turbine combustion chambers. In both cases, TFM reproduced the important flame characteristics reasonably well. Moreover, we could predict the lean blowout in the second burner correctly.

Nevertheless, the use of tabulated properties of laminar premixed flames limited the model application in the considered complex two-phase flame configurations and required some parameter adjustments. Therefore, we have proposed a novel TFM-

AMR formulation in the second part of this work. Instead of tabulation, laminar flame thicknesses and laminar flame speeds are derived here by the model and are not tabulated anymore.

The new model does not rely on the tabulated 1D flame properties and thus is better suited to compute complex flames. To validate this modeling approach, we have applied it to laminar gaseous and spray flames and to two burner configurations used for the standard TFM-AMR validation. The obtained results matched the experimental data very well, thus proving the great potential of the proposed modeling approach to compute complex spray flames.

In realistic operating conditions, we can expect thickening levels that will be at least by a factor of 4 higher than in the considered atmospheric cases. As a result, the effect of flame thickening will be more pronounced, and the influence of the model parameters could be better evaluated. Therefore, a further investigation of the proposed modeling approach is required to justify its use in high-temperature, high-pressure vessels.

# Bibliography

- [1] *Comparison of the Combustion Characteristics of Liquid Single-Component Fuels in a Gas Turbine Model Combustor*, volume Volume 4A: Combustion, Fuels and Emissions of *Turbo Expo: Power for Land, Sea, and Air*, 06 2016. V04AT04A010.
- [2] *Experimental Investigation With Optical Diagnostics of a Lean-Premixed Aero-Engine Injection System Under Relevant Operating Conditions*, volume Volume 4B: Combustion, Fuels and Emissions of *Turbo Expo: Power for Land, Sea, and Air*, 06 2017. V04BT04A022.
- [3] *Gas Turbine Model Combustor Emissions of Liquid Single-Component Fuels*, volume Volume 4A: Combustion, Fuels and Emissions of *Turbo Expo: Power for Land, Sea, and Air*, 06 2017. V04AT04A011.
- [4] *World Energy Outlook 2019*. IEA, Paris, 2019.
- [5] *Experimental Investigation on NO Pollutant Formation in High-Pressure Swirl-Stabilized Kerosene/Air Flames Using NO-, OH- and Kerosene-PLIF and PIV Laser Diagnostics*, volume Volume 4A: Combustion, Fuels, and Emissions of *Turbo Expo: Power for Land, Sea, and Air*, 09 2020. V04AT04A052.
- [6] A.A. Amsden, P.J. O'Rourke, and T.D. Butler. Kiva-ii: A computer program for chemically reactive flows with sprays. 1989.
- [7] A. Babajimopoulos, D. N. Assanis, D. L. Flowers, S. M. Aceves, and R. P. Hessel. A fully coupled computational fluid dynamics and multi-zone model with detailed chemical kinetics for the simulation of premixed charge compression ignition engines. *International Journal of Engine Research*, 6(5):497–512, 2005.
- [8] J Blasco, N Fueyo, C Dopazo, and J-Y Chen. A self-organizing-map approach to chemistry representation in combustion applications. *Combustion Theory and Modelling*, 4(1):61–76, March 2000.
- [9] R. Blint. The relationship of the laminar flame width to flame speed. *Combustion Science and Technology*, 49:79–92, 1986.
- [10] M. Boileau. *Simulation aux grandes échelles de l'allumage diphasique des foyers aéronautiques*. Theses, Institut National Polytechnique de Toulouse - INPT, October 2007.

- [11] T. D. Butler and P. J. O'Rourke. A numerical method for two-dimensional unsteady reacting flows. *International Symposium on Combustion*, 16:1503–1515, 1977.
- [12] D.E. Cavaliere, J. Kariuki, and E. Mastorakos. A comparison of the blow-off behaviour of swirl-stabilized premixed, non-premixed and spray flames. *Flow, Turbulence and Combustion*, pages 347–372, 2013.
- [13] F. Charlette, C. Meneveau, , and D. Veynante. A power-law flame wrinkling model for les of premixed turbulent combustion. part i: non-dynamic formulation and initial tests. *Combust. Flame*, 131(1):159–180, 2002.
- [14] A. Chatelier. *Modeling questions for numerical simulations of aeronautical combustors*. PhD thesis, Paris Saclay, 2019.
- [15] C. Chi, G. Janiga, and D. Thévenin. On-the-fly artificial neural network for chemical kinetics in direct numerical simulations of premixed combustion. *Combustion and Flame*, 226:467–477, April 2021.
- [16] O. Colin, F. Ducros, D. Veynante, and T. Poinso. A thickened flame model for large eddy simulations of turbulent premixed combustion. *Physics of Fluids*, 12(7):1843–1863, 2000.
- [17] CONVERGE. *CONVERGE manual v2.4*. Convergent Science, 2019.
- [18] S.G. Davis and C.K. Law. Determination of and fuel structure effects on laminar flame speeds of  $c_1$  to  $c_8$  hydrocarbons. *Combustion science and technology*, 140:427–449, 1998.
- [19] P. Dirrenberger, P.A. Glaude, R. Bounaceur, H. Le Gall, A. Pires da Cruz, A.A. Konnov, and F. Battin-Leclerc. Laminar burning velocity of gasolines with addition of ethanol. *Fuel*, 115:162–169, 2014.
- [20] L. Dressler, F. L. Sacomano Filho, A. Sadiki, and J. Janicka. Influence of thickening factor treatment on predictions of spray flame properties using the atf model and tabulated chemistry. *Flow, Turbulence and Combustion*, 106:1573–1987, 2021.
- [21] G. Eckel, J. Grohmann, L. Cantu, N. Slavinskaya, T. Kathrotia, M. Rachner, P. Le Clercq, W. Meier, and M. Aigner. Les of a swirl-stabilized kerosene spray flame with a multi-component vaporization model and detailed chemistry. *Combustion and Flame*, 207:134 – 152, 2019.
- [22] A. Felden, L. Esclapez, E. Riber, B. Cuenot, and H. Wang. Including real fuel chemistry in les of turbulent spray combustion. *Combustion and Flame*, 193:397–416, 2018.

- [23] A. Felden, E. Riber, and B. Cuenot. Impact of direct integration of analytically reduced chemistry in les of a sooting swirled non-premixed combustor. *Combustion and Flame*, 191:270–286, 2018.
- [24] F. L. Sacomano Filho, G. Kuenne, M. Chrigui, A. Sadiki, and J. Janicka. A consistent artificially thickened flame approach for spray combustion using les and the fgm chemistry reduction method: Validation in lean partially pre-vaporized flames. *Combustion and Flame*, 184:68 – 89, 2017.
- [25] B. Fiorina and S. Candel. Modeling combustion chemistry in large eddy simulation of turbulent flames. *Flow, Turbulence and Combustion*, pages 3–42, 2015.
- [26] B. Fiorina, R. Mercier, G. Kuenne, A. Ketelheun, A. Avdić, J. Janicka, D. Geyer, A. Dreizler, E. Alenius, C. Duwig, P. Trisjono, K. Kleinheinz, S. Kang, H. Pitsch, F. Proch, F. Cavallo Marincola, and A. Kempf. Challenging modeling strategies for les of non-adiabatic turbulent stratified combustion. *Combustion and Flame*, 162(11):4264–4282, 2015.
- [27] L.Y.M. Gicquel, G. Staffelbach, and T. Poinsot. Large eddy simulations of gaseous flames in gas turbine combustion chambers. *Progress in Energy and Combustion Science*, 38(6):782 – 817, 2012.
- [28] A. Giusti and E. Mastorakos. Turbulent combustion modelling and experiments: Recent trends and developments. *Flow, Turbulence and Combustion*, pages 847–869, 2019.
- [29] D.A. Goussis and U. Maas. *Model Reduction for Combustion Chemistry*, pages 193–220. Springer Netherlands, Dordrecht, 2011.
- [30] J. Grohmann. *Experimentelle Untersuchungen zum Einfluss von Kohlenwasserstoffen auf das Verbrennungsverhalten drallstabilisierter Sprayflammen. VT-Forschungsbericht 2019-01*. Deutsches Zentrum für Luft- und Raumfahrt Institut für Verbrennungstechnik Stuttgart, 2019.
- [31] J. Grohmann, W. O’Loughlin, W. Meier, and M. Aigner. Comparison of the combustion characteristics of liquid single-component fuels in a gas turbine model combustor. *ASME Turbo Expo 2016: Turbomachinery Technical Conference and Exposition*, Volume 4A: Combustion, Fuels and Emissions, 2016.
- [32] J. Grohmann, B. Rauch, T. Kathrotia, W. Meier, and M. Aigner. Influence of single-component fuels on gas-turbine model combustor lean blowout. *Journal of Propulsion and Power*, 34(1):97–107, 2018.
- [33] L. Guedot. *Development of numerical methods for the characterization of large scale structures in aeronautical swirl burners. Application to multi-points injectors*. PhD thesis, INSA Rouen Normandie, 2015.
- [34] Y. Huang, C.J. Sung, and J.A. Eng. Laminar flame speeds of primary reference fuels and reformer gas mixtures. *Combustion and Flame*, 139:239–251, 2001.

- [35] R.I. Issa. Solution of the implicitly discretised fluid flow equations by operator splitting. *Journal of Computational Physics*, 62(1):40–65, 1986.
- [36] T. Jaravel. *Prediction of pollutants in gas turbines using large eddy simulation*. PhD thesis, INPT Toulouse, 2016.
- [37] P. Jenny, D. Roekaerts, and N. Beishuizen. Modeling of turbulent dilute spray combustion. *Progress in Energy and Combustion Science*, 38(6):846 – 887, 2012.
- [38] W.P. Jones and R.P. Lindstedt. Global reaction schemes for hydrocarbon combustion. *Combustion and Flame*, 73(3):233–249, 1988.
- [39] W.P. Jones and R.P. Lindstedt. Turbulent combustion modeling. *Progress in Energy and Combustion Science*, 28(3):193–266, 2002.
- [40] E. Knudsen, Shashank, and H. Pitsch. Modeling partially premixed combustion behavior in multiphase les. *Combustion and Flame*, 162(1):159–180, 2015.
- [41] K. Kumar, J.E. Freeh, C.J. Sung, and Y. Huang. Laminar flame speeds of preheated iso-octane/ $o_2/n_2$  and n-heptane/ $o_2/n_2$  mixtures. *Journal of propulsion and power*, 23, 2007.
- [42] A. H. Lefebvre and D. R. Ballal. *Gas Turbine Combustion. Alternative Fuels and Emissions*. CRC Press, 2010.
- [43] A. H. Lefebvre and V. G. McDonell. *Atomization and Sprays*, chapter 3. Taylor Francis, CRC Press, 2nd edition, 2017.
- [44] J. Legier. *Simulations numériques des instabilités de combustion dans les foyers aéronautiques*. PhD thesis, Toulouse, INPT, 2001.
- [45] A.B. Liu, D.K. Mather, and R.D. Reitz. Modeling the effects of drop drag and breakup on fuel sprays. *SAE Technical Paper 930072*, 1993.
- [46] M. Matalon, C. Cui, and J.K. Bechtold. Hydrodynamic theory of premixed flames: Effects of stoichiometry, variable transport coefficients and arbitrary reaction orders. *Journal of Fluid Mechanics*, pages 179–210, 2003.
- [47] C. Mehl, S. Liu, Y.C. See, and O. Colin. Les of a stratified turbulent burner with a thickened flame model coupled to adaptive mesh refinement and detailed chemistry. *Joint Propulsion Conference, AIAA Propulsion and Energy Forum*, 2018.
- [48] R. Mugele and H. D. Evans. Droplet size distributions in sprays. *Ind. Eng. Chem.*, 43(6):1317–1324, 1951.
- [49] I. A. Mulla, G. Godard, G. Cabot, F. Grisch, and B. Renou. Quantitative imaging of nitric oxide concentration in a turbulent n -heptane spray flame. *Combustion and Flame*, 203:217–229, 2019.

- [50] I. A. Mulla, G. Godard, and B. Renou. Instantaneous planar measurements of nitric oxide concentration in a turbulent n -heptane spray flame. *Combustion and Flame*, 208:451–471, 2019.
- [51] I. A. Mulla and B. Renou. Simultaneous imaging of soot volume fraction, pah, and oh in a turbulent n-heptane spray flame. *Combustion and Flame*, 209:452–466, 2019.
- [52] K. Narayanaswamy, P. Pepiot, and H. Pitsch. A chemical mechanism for low to high temperature oxidation of n-dodecane as a component of transportation fuel surrogates. *Combustion and Flame*, 161(4):866–884, 2014.
- [53] NASA. Cfd vision 2030 study. URL<http://www.cfd2030.com/>.
- [54] A. Neophytou and E. Mastorakos. Simulations of laminar flame propagation in droplet mists. *Combustion and Flame*, 156:1627–1640, 2009.
- [55] F. Nicoud, H. Baya Toda, O. Cabrit, S. Bose, and J. Lee. Using singular values to build a subgrid-scale model for large eddy simulations. *Physics of Fluids*, 23, 2011.
- [56] D. Noh, S. Gallot-Lavallée, W. P. Jones, and S. Navarro-Martinez. Comparison of droplet evaporation models for a turbulent, non-swirling jet flame with a polydisperse droplet distribution. *Combustion and Flame*, 194:135–151, 2018.
- [57] P.J. O’Rourke and A.A. Amsden. The tab method for numerical calculation of spray droplet breakup. *SAE Paper 872089*, 1987.
- [58] D. Paulhiac. *Modeling of spray combustion in an aeronautical burner*. PhD thesis, CERFACS, 2015.
- [59] D. Paulhiac, B. Cuenot, E. Riber, L. Esclapez, and S. Richard. Analysis of the spray flame structure in a lab-scale burner using large eddy simulation and discrete particle simulation. *Combustion and Flame*, 212:25–38, 2020.
- [60] C. Pichard, Y. Michou, C. Chauveau, and L. Gökalp. Average droplet vaporization rates in partially prevaporized turbulent spray flames. *Proceedings of the Combustion Institute*, 29(1):527–533, 2002. Proceedings of the Combustion Institute.
- [61] T. Poinso and Denis Veynante. *Theoretical and numerical combustion*. 3rd edition.
- [62] P. Quillatre. *Simulation aux grandes échelles d’explosions en domaine semi-confiné*. PhD thesis, 2014.
- [63] M. Raju, M. Wang, P. K. Senecal, S. Som, and D. E. Longman. A reduced diesel surrogate mechanism for compression ignition engine applications. *ASME 2012 Internal Combustion Engine Division Fall Technical Conference*, pages 711–722, 2013.

- [64] W. E. Ranz and W. R. Marshall. Evaporation from drops. parts i ii. *Chem. Eng. Progr.*, 48:141–146; 173–180, 1952.
- [65] C.M. Rhie and W.L. Chow. Numerical study of the turbulent flow past an airfoil with trailing edge separation. *AIAA Journal*, 21(11):1525–1532, 1983.
- [66] K. J. Richards, P. K. Senecal, and E. Pomraning. *CONVERGE 2.4*. Convergent Science, Madison, WI (2019), 2019.
- [67] K. J. Richards, P. K. Senecal, and E. Pomraning. *CONVERGE 3.0*. Convergent Science, Madison, WI (2019), 2019.
- [68] M. Rieth, F. Proch, O.T. Stein, M.W.A. Pettit, and A.M. Kempf. Comparison of the sigma and smagorinsky les models for grid generated turbulence and a channel flow. *Computers Fluids*, 99:172 – 181, 2014.
- [69] B. Rochette. *Modeling and simulation of two-phase flow turbulent combustion in aeronautical engines*. PhD thesis, INPT Toulouse, 2019.
- [70] B.A. Sen and S. Menon. Turbulent premixed flame modeling using artificial neural networks based chemical kinetics. *Proceedings of the Combustion Institute*, 32(1):1605–1611, 2009.
- [71] P. K. Senecal, E. Pomraning, K. J. Richards, T. E. Briggs, C. Y. Choi, R. M. McDavid, and M. A. Patterson. Multi-dimensional modeling of direct-injection diesel spray liquid length and flame lift-off length using cfd and parallel detailed chemistry. In *SAE 2003 World Congress Exhibition*. SAE International, mar 2003.
- [72] F. Shum-Kivan. *Large Eddy Simulation of spray flames and modelling of non-premixed combustion*. PhD thesis, Toulouse, INPT, 2017.
- [73] F. Shum-Kivan, J. Marrero Santiago, A. Verdier, E. Riber, B. Renou, G. Cabot, and B. Cuenot. Experimental and numerical analysis of a turbulent spray flame structure. *Proceedings of the Combustion Institute*, 36:2567–2575, 2017.
- [74] P. Sitte and E. Mastorakos. Large eddy simulation of a spray jet flame using doubly conditional moment closure. *Combustion and flame*, 199:309–323, 2019.
- [75] S.Jerzembeck, N.Peters, P.Pepiot-Desjardins, and H.Pitsch. Laminar burning velocities at high pressure for primary reference fuels and gasoline: Experimental and numerical investigation. *Combustion and Flame*, 156:292–301, 2009.
- [76] J.P.J. van Lipzig, E.J.K. Nilsson, L.P.H. de Goey, and A.A. Konnov. Laminar burning velocities of n-heptane, iso-octane, ethanol and their binary and tertiary mixtures. *Fuel*, 90:2773–2781, 2011.
- [77] A. Verdier. *Experimental study of dilute spray combustion*. PhD thesis, INSA Rouen Normandie, 2017.

- [78] K. Wan, C. Barnaud, L. Vervisch, and P. Domingo. Chemistry reduction using machine learning trained from non-premixed micro-mixing modeling: Application to DNS of a syngas turbulent oxy-flame with side-wall effects. *Combustion and Flame*, 220:119–129, October 2020.
- [79] H. Yamashita, M. Shimad, and T. Takeno. A numerical study on flame stability at the transition point of jet diffusion flames. *Symposium (International) on Combustion*, 26:27–34, 1996.



# Synthèse

L'augmentation constante du trafic aérien et les réglementations environnementales strictes exigent d'améliorer les systèmes de propulsion modernes. Actuellement, les avions civils sont propulsés par des turbines à gaz, où le carburant est injecté sous forme liquide pour assurer leur fonctionnement en toute sécurité. La mécanique des fluides numérique (CFD, "Computational Fluid Dynamics") joue un rôle essentiel dans le développement des chambres de combustion des turbines à gaz, car les simulations numériques sont beaucoup moins coûteuses que les essais expérimentaux. Par conséquent, la simulation précise de la combustion en écoulement diphasique est cruciale pour la conception des chambres de combustion aéronautiques.

Afin de mieux comprendre les interactions complexes entre la flamme, l'écoulement et la phase liquide, le présent travail porte sur la modélisation de la combustion pour les simulations aux grandes échelles (LES, "Large Eddy Simulation") d'écoulements diphasiques turbulents. Les tailles de cellule LES généralement utilisées sont supérieures à l'épaisseur de la flamme. Comme la combustion a généralement lieu au niveau de la sous-maille, elle nécessite un traitement spécifique. Le modèle de flamme épaissie (TFM, "Thickened Flame Model") est l'une des approches robustes et bien connues pour calculer les flammes turbulentes.

Pour résoudre une flamme sur les mailles LES, le modèle TFM applique un épaississement artificiel du front de flamme tout en préservant la vitesse de la flamme. Le modèle TFM couplé au raffinement de maillage adaptatif (AMR, "Adaptive Mesh Refinement") fournit des résultats de haute précision sans coûts de calcul prohibitifs et donne lieu à l'approche de modélisation TFM-AMR étudiée dans ce travail.

Le modèle TFM a été initialement conçu pour des flammes prémélangées, qui ne

sont pas toujours représentatives de la combustion ayant lieu dans les sprays. De plus, l'évolution des gouttelettes de combustible liquide est suivie dans un cadre lagrangien séparément de la phase gazeuse. Par conséquent, l'approche de modélisation doit être adaptée pour inclure l'effet de l'épaississement de la phase moyenne sur la phase dispersée afin de garantir une évaporation et une propagation correctes du spray.

Le cadre de modélisation utilisé dans ce travail est résumé au chapitre 2. Nous avons d'abord introduit les équations gouvernantes pour les phases gazeuse et liquide. Ensuite, la description de l'approche de modélisation TFM-AMR est donnée. Le chapitre 2 fournit également un résumé des modifications TFM existantes pour calculer les flammes diphasiques turbulentes.

Dans le chapitre 3, l'extension du TFM-AMR aux écoulements diphasiques présentée dans le chapitre 2 a été validée sur des cas de flammes laminaires diphasiques unidimensionnelles. Deux combustibles différents ont été examinés. Tout d'abord, nous examinons un combustible n-heptane hautement volatil qui est utilisé dans la configuration de brûleur confiné discutée dans le chapitre 4. Ensuite, nous considérons un combustible n-dodécane peu volatil utilisé dans la configuration confinée étudiée au chapitre 5.

Il a été montré sur des flammes diphasiques 1D de n-heptane que la correction des termes sources lagrangiens permet de retrouver les résultats de flammes non épaissies avec précision. Un excellent accord avec les solutions non-épaissies de référence a été démontré d'abord pour l'épaississement constant et un maillage statique, puis pour l'épaississement dynamique et un maillage statique, et enfin pour l'épaississement dynamique avec AMR.

La fraction de combustible gazeux a été réduite à zéro dans les flammes laminaires de n-dodécane. Ceci, ainsi que la volatilité plus faible du carburant n-dodécane, a révélé certaines déficiences possibles de l'approche de modélisation TFM-AMR lorsqu'elle est appliquée à la flamme diphasique.

Tout d'abord, nous avons observé que le dégagement de chaleur dans une flamme diphasique peut s'écarter des valeurs de dégagement de chaleur tabulées pour les flammes prémélangées. Par conséquent, le détecteur de flamme peut avoir des dif-

difficultés à couvrir la totalité du front de flamme. La dilution d'un réactif avec des produits brûlés, couramment rencontrée dans les turbines à gaz, peut amplifier les divergences avec les valeurs tabulées.

Deuxièmement, de faibles niveaux de prémélange, combinés à de grosses gouttelettes de combustible peu volatile, peuvent conduire à une faible teneur en combustible à la base de la flamme. Ainsi, le détecteur de flamme peut avoir du mal à couvrir la base de la flamme malgré le réajustement des paramètres du détecteur.

Troisièmement, nous avons vu que l'épaississement des flammes diphasiques n'est pas uniforme et augmente au-dessus du front de flamme lorsque le rapport carburant/air augmente. Cette dépendance des propriétés tabulées peut également conduire à des niveaux d'épaississement inutilement élevés dans les flammes diphasiques lors de l'approche du côté brûlé.

L'approche de modélisation TFM-AMR a été appliquée au brûleur CORIA au Chapitre 4, comme première étape vers de véritables applications industrielles de turbine à gaz. Ce brûleur diphasique à l'échelle du laboratoire n'est pas confiné et fonctionne avec du n-heptane aux conditions atmosphériques.

Le LES capture correctement les vitesses du gaz et des gouttelettes ainsi que la distribution de la taille des gouttelettes pour les cas froids et réactifs. La longueur de décollement et la forme globale de la flamme sont correctement récupérées. Seule la partie amont de la flamme présente un rayon de courbure excessif. Cette observation, partagée avec les LES d'autres groupes de recherche, n'est pas comprise aujourd'hui et nécessite une étude plus approfondie.

Comme prévu, l'épaississement appliqué n'était pas uniforme à travers la flamme et augmentait avec un rapport carburant/air croissant. De plus, le détecteur de flamme avait des difficultés à détecter la base de la flamme caractérisée par de faibles rapports carburant/air.

Le chapitre 5 augmente la complexité de la flamme considérée et se concentre sur la géométrie pertinente pour la pratique. Le brûleur DLR étudié ici est confiné et reproduit une flamme stabilisée par tourbillonnement.

Globalement, un bon accord a été atteint pour les phases gazeuse et liquide entre

les résultats expérimentaux et numériques pour les conditions de fonctionnement de référence. Par conséquent, nous concluons que l’approche de modélisation TFM-AMR montre une grande capacité à prédire les flammes diphasiques stabilisées par tourbillon sous pression atmosphérique.

La variation paramétrique a montré que la correction TFM prenant en compte l’orientation du spray et de la flamme a un effet mineur sur les résultats de la simulation. En outre, la variation des paramètres a mis en évidence l’importance des pertes thermiques radiatives dans cette configuration de brûleur.

Le soufflage de la flamme est également abordé dans ce chapitre. Le soufflage maigre (LBO) a été prédit avec précision en utilisant l’approche de modélisation TFM-AMR. En outre, les résultats de la simulation démontrent la sensibilité des résultats au traitement des parois.

L’approche de modélisation standard TFM-AMR a montré ses défauts lors de la configuration des simulations de la chambre de combustion du modèle DLR. Dans cette configuration de brûleur, les taux de dégagement de chaleur instantanés observés étaient nettement inférieurs aux valeurs tabulées, ce qui nous a obligés à augmenter arbitrairement la sensibilité du détecteur.

Les propriétés tabulées des flammes laminaires prémélangées utilisées dans le TFM-AMR standard ont limité l’application du modèle dans les configurations de flammes diphasiques complexes considérées et ont nécessité certains ajustements de paramètres. Par conséquent, nous avons proposé une nouvelle formulation TFM-AMR dans le chapitre 6. Au lieu d’être tabulées, les épaisseurs de flamme laminaire et les vitesses de flamme laminaire sont dérivées ici par le modèle et ne sont plus tabulées.

Le nouveau modèle ne repose pas sur les propriétés de flamme 1D tabulées et est donc mieux adapté au calcul de flammes complexes. Pour valider cette approche de modélisation, nous l’avons appliquée à des flammes laminaires gazeuses et diphasiques et à deux configurations de brûleurs utilisées pour la validation standard du TFM-AMR. Les résultats obtenus correspondent très bien aux données expérimentales, prouvant ainsi le grand potentiel de l’approche de modélisation proposée pour le

calcul de flammes diphasiques complexes.